Role of Colored Organic Matter in the Photochemical Fate and Removal of Contaminants of Emerging Concern

Davide Palma

Role of Colored Organic Matter in the Photochemical Fate and Removal of Contaminants of Emerging Concern

This dissertation is submitted to the

University of Clermont Auvergne

For the degree of

Doctor of Philosophy

By the candidate

Davide Palma

Faculty: **Fundamental Sciences**

Specialization: **Physical, theoretical, and analytical chemistry**

Date of PhD defense: **30 April 2021**

Composition of the jury:

Rapporteurs:	Stéphane Bouchonnet, Ingenieur de recherche at Polytechnical University of Paris, France
	Silvio Canonica, Senior Scientist at Eawag, Switzerland
Examiners:	Alessandra Bianco Prevot, Professor at University of Torino, Italy
	Maria Luisa Marin, Professor at Polytechnical University of Valencia, Spain
	Mohamed Sarakha, Professor at University of Clermont Auvergne, France
Thesis director:	Claire Richard, CNRS Research Director, France
Thesis co-director:	Mohamad Sleiman, Maitre de Conference at Sigma-Clermont, France

Acknowledgements

First of all, I wish to express my deepest gratitude to my supervisor Claire for her precious guidance throughout all my thesis. Her professional commitment and her passion for the scientific research made my PhD a truly unique and fruitful experience.

I would like to thank my supervisor Mohamad for his scientific and personal support during these years. His inspiring vision of science represented a precious help in the difficult moments of my thesis.

I wish to thank Guillaume, Gilles, Xavier, Harout, Mohamed and all the people of the equipe Chimie 6 for their professional help but especially for their friendship and support. They all contributed into making my working environment a welcoming and serene place that I will always remember with the greatest affection.

My most sincere thank you go to Arezou, Camille, Daching, Anaëlle, Peng, Yara, Luna, Astrid, Margot, Amina and all the PhD students and postdoc researchers for the beautiful moments we spent together both inside and outside the laboratory.

A special thank goes to Nicola and Paola (and Leonardino!) for their beautiful friendship that made Clermont feel less like a stranger place, and more like home. The memories of the joyful time we spent together will always be with me.

I will never thank Marcello and his family enough for all they have done for me. We got to know each other as colleagues, we then became friends, and ended up being family. I honestly cannot imagine the years of my PhD without them.

A very special thank goes to Alessandra because if I reached this important milestone is also thanks to her who believe and invested in me since when we first met during my master.

I wish to thank Jenny with all my heart for sharing with me this winding road across France, Spain and Italy both in the happy and in the difficult times. She taught me that me that friendship and love really know no boundaries and her presence was, and still is, an infinite source of motivation.

I eventually wish to thank my parents and my sister Erika for their wholehearted support and for always being there for me. They made it easy for me to take difficult decisions even when we had conflicting ideas and I will always be extremely grateful to them all.

This PhD thesis has received funding from the European Union's Horizon 2020 research and innovation programme under the Marie Skłodowska-Curie grant agreement No 765860.

Table of contents

Abbreviations

^{3}DOM*	Triplet Excited States of DOM
CDOM	Chromophoric Dissolved Organic Matter
CHL	Copper chlorophyllin
DBPs	Disinfection By-Products
DOM	Dissolved Organic Matter
EOY	Eosin Y
FAs	Fulvic Acids
FFA	Furfuryl Alcohol
GLY	Glyphosate
HAAs	Haloacetic Acids
HAs	Humic Acids
IC	Inorganic Carbon
IMD	Imidacloprid
MW	Molecular Weight
NOM	Natural Organic Matter
PAR	Photosynthetic Available Radiation
PFAS	Perfluoroalkyl Compounds
PFHxA	Perfluorohexanoic Acid
PFOA	Perfluorooctanoic Acid
PFOS	Perfluorooctanesulfonic acid
POC	Particulate Organic Carbon
POM	Particulate Organic Matter
RS	Reactive Species
SOM	Soil Organic Matter
TC	Total Carbon
THMs	Trihalomethanes
TMP	2,4,6-Trymethylphenol
TOC	Total Organic Carbon
WEOM	Water Extractable Organic Matter

Introduction

Introduction

This PhD thesis is part of the Marie Skłodowska-Curie grant N. 765860 named AQUAlity, born to develop innovative tools and technologies to respond to the water emergency observed today worldwide. The rapid deterioration of the quality of water resources and the increasing need of water reuse due to water scarcity, requires the availability of technologies capable of efficiently removing the anthropogenic footprint observed in the vast majority of natural water bodies. The AQUAlity project arises from the collaboration between multiple European universities and industrial partners, active in the field of water research and willing to collaborate for the development of novel efficient technologies for water treatment, analytical methods for untargeted environmental screening, or focusing on a better understanding of fundamental aspects related to water treatment.

This thesis was carried out in the Photochemistry group of the Institute of Chemistry of Clermont-Ferrand (Université Clermont Auvergne), in France, under the supervision of Drs Claire Richard and Mohamad Sleiman. It focuses on the study of the effect of Natural Organic Matter (NOM) in the photochemical fate and removal of micropollutants of anthropogenic origin often referred to as Contaminants of Emerging Concern (CECs). Over the course of this three years thesis, a total duration of ten months was spent working in collaboration with international partners of both academic and industrial nature. Specifically, three months were spent working at Universitat Politecnica de Valencia in Spain, three months at Università degli studi di Torino and other four months at Iris s.r.l. company located near Torino in Italy. Each working unit was carefully planned to approach the study of NOM and its interaction with water contaminants, both in the environment and in water treatment processes, from different perspectives. NOM is in fact a ubiquitous constituent of terrestrial and aquatic environments that plays a fundamental role in many biological and physico-chemical processes affecting plants, macro and microorganisms, soil and water and pollutants. An exhaustive comprehension of its biogeochemical functions as well as of its problematic role in water treatment processes is therefore essential for an efficient and sustainable water management worldwide.

In the aquatic environment, NOM influences the photo-reactivity of surface water exposed to sunlight and plays a key role in the formation of reactive species, such as triplet excited states of NOM, singlet oxygen, hydroxyl radicals, that are responsible for the degradation of water contaminants under natural conditions. Due to their environmental significance these photochemical processes have been widely studied in the literature. However, essential aspects such as the identification of the NOM

chromophores responsible for its photo-reactivity and the establishment of correlations capable of predicting NOM reactivity on the basis of its physicochemical properties are still leaving a lot of unanswered questions. In the attempt to give new insights on these topics, samples of DOM collected from the nearby aquifer of Allier river, were characterized in terms of spectral properties (i.e. absorption and fluorescence properties) and photoreactivity (i.e. production of excited triplet states, singlet oxygen, hydroxyl radicals and hydrogen peroxide) as a function of temporal and spatial distribution. Our objective was to search for relationships between chemical and physical characteristics on the one hand, and photochemical properties on the other hand and to analyze data with regard to the hydrological functioning of the aquatic system under study.

While the effect of NOM on the environmental fate of water pollutants has been widely studied, the mutual effect of pollutants on NOM chemical structure is another scarcely documented aspect; due to the complexity of NOM itself this type of induced modifications are in fact very difficult to study. We decided to approach the issue by studying the photodegradation of the neonicotinoid insecticide imidacloprid (IMD) reported in the literature as able to release the nitro group under photolysis. The aqueous photolysis of IMD alone and in presence of aromatic probes, selected to represent NOM aromatic moieties, was investigated in detail to find possible mutual interactions between NOM and IMD or its photoproducts.

In water treatment processes instead, the role of NOM as the main precursor of toxic disinfection by-products, especially when chlorine-based disinfectants are used, is a very well documented phenomenon. Because of this, the removal of DOM represents today a fundamental step of every process of drinking water production. However, for UV-based treatment processes, the presence of DOM could potentially be beneficial as it could actively participate to pollutants degradation through the photo-induced formation of reactive species. If on one hand the inhibitory effect of DOM on the removal of water contaminants has been widely covered by countless publications, its positive contribution is a poorly studied phenomenon. In this regard, we studied the photodegradation of the Suwannee River NOM from International Humic Substances Society under UV-C irradiation to investigate how pre-irradiation can modify its photodegrading properties. In parallel, a detailed analytical study was undertaken to characterize Suwannee River NOM phototransformation products.

At Universitat Politecnica de Valencia instead, a different kind of water treatment technology aimed to photo-catalytically reduce CECs using compounds of natural origin was investigated. Profiting from the expertise of Prof. Maria Luisa Marin's group, simple molecules selected to represent NOM, were used to reduce IMD under irradiation with visible light.

Iris s.r.l. company was the industrial partner of this PhD thesis and it gave me the unique opportunity to conduct scientific research in a more market-oriented way than the one typically adopted in academic laboratories. The company is developing a non-thermal plasma device for water treatment applications and during the months spent at their facility, great effort was put in understanding the chemistry behind plasma discharges and their possible applications in the field of water treatment. The transformation of NOM during plasma processes is poorly documented in the literature and therefore an effort was put into filling this gap. The effect of NOM on the degradation of different classes of pollutants was also studied. The planning of the experimental work as well as the analyses of the water samples produced at Iris s.r.l. and the interpretation of the results was conducted at Università degli studi di Torino in the department of analytical chemistry under the supervision of Prof. Marco Minella.

In conclusion, the goal of this work was to study the DOM under different points of view, not only analyzing its photo-sensitizing properties, but also following its transformation when submitted to oxidative water treatment processes, focusing on those aspects poorly documented in the literature.

Bibliographic study

1 Bibliographic study

1.1. Generalities about Natural Organic Matter

Natural organic matter (NOM) can be defined as a complex mixture of organic compounds formed in soils, sediments, and natural waters through microbial and chemical transformation of plant tissues and microbial residues. This set of processes is commonly referred to as humification, a process during which cellulose, lignin, polysaccharides as well as proteins, lipids and nucleic acids undergo oxidation at a rate that is strongly dependent on temperature, humidity, and oxygen availability. During the first year of decomposition, around 60 to 80% of the starting material organic carbon in converted to CO_2 which is released to the atmosphere [1]. The remaining non-mineralized carbon undergoes a slower oxidation that can take up to several years to be completed. Another important source of NOM are wildfires, where incomplete combustion of biomasses generates big amounts of pyrolysis compounds that significantly modify NOM composition; furthermore, the high temperatures reached can induce thermal modification of pre-existing organic matter.

Considering the great heterogeneity of the starting material and the variety of transformation pathways this material undergoes, the resulting NOM can have very diverse chemical structures and molecular weights. Nevertheless, three different main fractions have been identified on the basis of their physical-chemical properties that are remarkably similar despite the different sources, namely, **humic acids** (HAs), **fulvic acids** (FAs) and **humin**; these three families of compounds are generally grouped under the name of **humic substances** (HS). All other NOM constituents that do not fall within one of these three groups are considered as non-humic substances. Non-humic constituents include carbohydrates, peptides, fatty acids, waxes, hydrocarbons, and residual materials of non-humified plant and microbial residues. The elemental composition of humic substances by weight is approximately 40-60% carbon, 30-50% oxygen, 4-5% hydrogen, 1-4% nitrogen, 1-2% sulfur and 0-0.3% phosphorus [2]. In general, considering carbon to be accounting for half the molecular weight of NOM, measured TOC values can be multiplied by two to estimate the concentration of NOM in mg/L.

Considering the heterogeneity of humic substances, providing a proper definition of what they are on the basis of their molecular structure is a very problematic, if not impossible, goal. For this reason, it is a common practice to identify HAs, FAs and humin fractions according to their solubility at different

pH values. Humin is considered to be insoluble at any pH and it is therefore impossible to extract it from soil with water. HAs and FAs, on the other hand, are commonly extracted in basic solution (typically 0.1–0.5 M NaOH) together with the water soluble fraction of non-humic substances; the set of these compounds is often referred to as Water Extractable Organic Matter (WEOM). Common isolation of humic and fulvic acids can be done as follows:

- HAs are identified as the fraction that can be precipitated at pH 1 while forming a dark brown precipitate; solutions are typically acidified with diluted HCl. The average molecular weight of HAs is in the range of 2,000 to 10,000 Da and their chemical structure dominated by phenolic groups and long carboxylic fatty acids and they are in general more hydrophobic in comparison with fulvic acids.

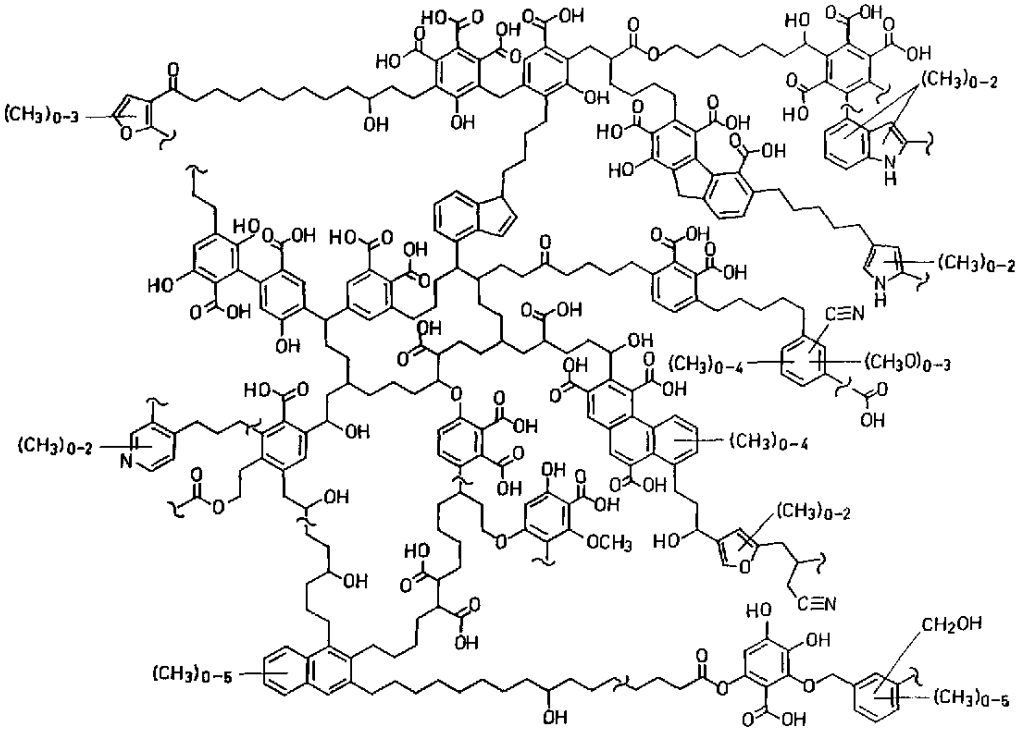

Figure 1. Humic acid model extracted from Schulten and Schnitzer [3].

- FAs are considered soluble at any pH value and are commonly isolated passing the supernatant of the acidified solution through a column packed with XAD resins. At pH 1 the acid moieties of FAs are in fact fully protonated and they get adsorbed on the hydrophobic resin while non-humic substances are not retained. FAs are eventually recovered from the separation column by reverse elution with alkaline solution (typically 0.1 M NaOH) [4,5]. The average molecular weight of FA is typically between 500 and 2000 Da [6].

Solid samples of HAs and FAs suitable for storage are commonly obtained by freeze-drying. A simple protocol for NOM fractionation is reported in figure 1.

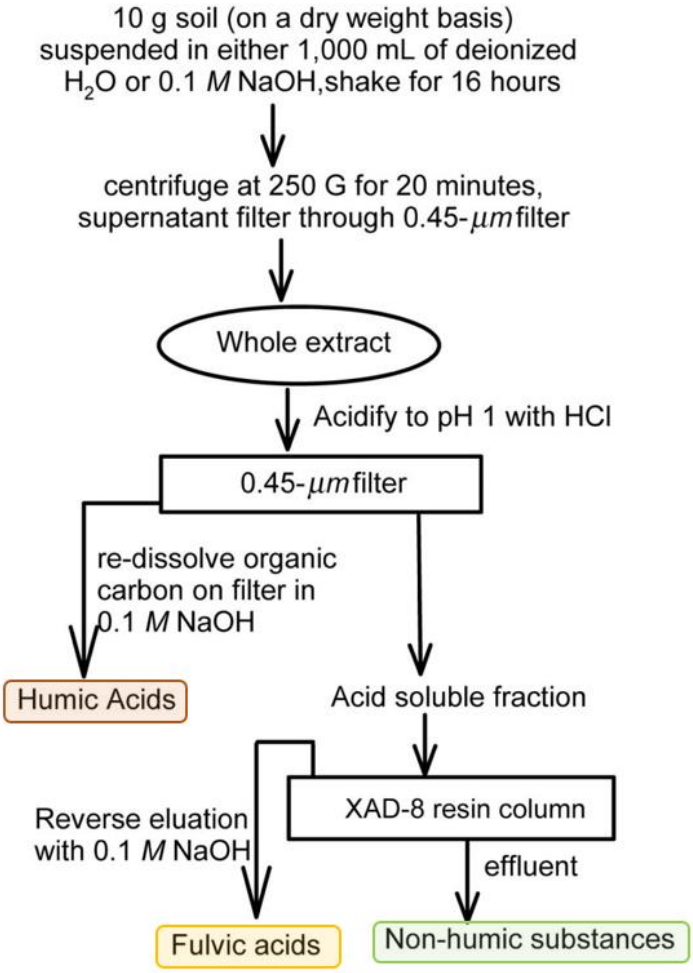

Figure 2. Scheme for NOM fractionation extracted from Chow et al. [7].

Soil NOM (or soil organic matter, SOM), commonly contains both water soluble and insoluble fractions of NOM with humin accounting for around 50% of total SOM. In natural waters on the other hand, we commonly find only the water soluble fraction of NOM composed by HAs, FAs and soluble non-humic compounds such as low MW organic acids, sugars, amino acids [8].

1.2. Aquatic NOM

Natural organic matter is a ubiquitous component of surface, underground or marine waters; its concentration can range from less than 1 mg/L to hundreds of mg/L according to the type of water body, its surrounding ecosystem, its geographical location, the climate, and the period of the year. Despite this wide range of values, most concentration values generally stay under 10 mg/L; as a matter of facts, worldwide median concentration for lake, river and sea waters lies below this value.

Aquatic NOM exists under two physical states: we call **dissolved organic matter (DOM)** the solubilized fraction of NOM, and **particulate organic matter (POM)** the fraction of NOM suspended in water as supramolecular aggregates. DOM is considered to be the larger pool of organic matter in natural water accounting for over 90% of aquatic total organic matter. From a practical point of view, DOM has been defined by convention as the fraction of NOM that can pass through filters having pore size 0.1-0.7 µm while POM is the fraction that is retained by such filters [9,10]. The most common DOM constituents are HAs and FAs of terrestrial origin, FAs containing both hydrophobic and hydrophilic components. The largest fraction is generally hydrophobic acids, which makes up approximately 50% of the TOC in water (figure 3) [11]. The mass range of these complex mixture of compounds goes from low molecular weight compounds like organic acids to macromolecules like HAs that can reach over 300,0000 Daltons. However, it has been estimated that only around 20% of HAs fall in the very high MW category and that 75% of HAs have MW <100,000 Da.

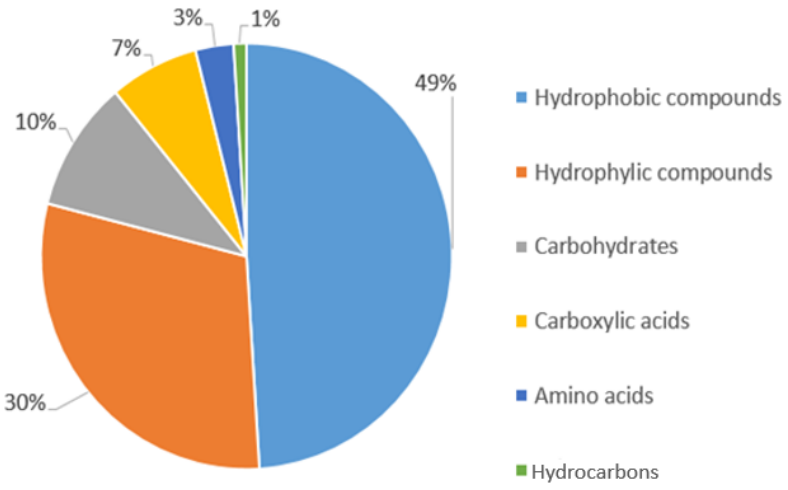

Figure 3. Generic DOM composition of a natural surface water suggested by Thurman [11].

According to its origin, NOM can be divided into, i) **autochthonous NOM** mainly produced by microbial and algal metabolism and by their biomass degradation taking place directly in water, ii) **allochthonous NOM** that is formed in the soil during the breakdown of terrestrial organism and plant material and that is later introduced to the water body through soil drainage, and iii) **anthropogenic OM** of man-made or industrial origin.

1.2.1. Biogeochemical functions of aquatic NOM

Both dissolved and particulate NOM, of allochthonous and autochthonous origin, can play multiple functions in the photochemical, chemical, microbial and geochemical processes occurring in natural waters. These NOM induced modifications of the natural water characteristics can be classified as follows.

1. Optical properties: the light absorbing fraction of DOM is called colored or **chromophoric dissolved organic matter (CDOM)** and it is largely responsible for the yellowish-brownish color observed for many natural waters. Water color is mostly imparted by humic substances of soil origin and autochthonous FAs of algal or phytoplankton origin capable of absorbing light in the visible (400-800 nm), UVA (320-400 nm) and UVB region (280-320 nm) therefore controlling the penetration of solar light in the water column. Depending on DOM concentration UVB penetration can vary from a few centimeters, in lakes with high DOM content, to dozens of meters in the oceans. In lakes having concentration DOC content ranging from 5 to 10 mg/L, 99% of the UV-B radiation is generally attenuated in the first 50 cm of the water column while the corresponding attenuation for UV-A at 380 nm occurs in the first meter [12]. DOM is thus responsible for UV attenuation in the water column and for the related protection of aquatic organisms in natural waters. As a consequence, CDOM can affect water transparency, temperature and thermal stratification in the surface water of lakes and oceans [13,14]. By absorbing photosynthetically available radiation (PAR, 400-700 nm) CDOM also determines the depth of the euphotic zone [14–16].

2. Photochemical reactivity of natural waters: under solar radiation CDOM is capable of producing highly reactive species like hydroxyl radicals, singlet oxygen ($^1O_2$) and triplet excited states of organic matter (^{3}CDOM*) as well as less reactive and long-lived radicals [17]. These species determine the capacity of natural waters to promote the degradation of dissolved molecules such as pollutants, compounds of

natural and anthropogenic origin or the NOM itself [18–21]. Photochemical reactivity of natural waters will be discussed in more detail in the dedicated section 1.8.

3. Microbial activity: DOM can influence microbial growth in two different ways: 1) by modifying the physical and chemical aquatic environment like for example determining the depth of the euphotic zone or the amount of photosynthetically available radiation; 2) by acting as a direct energy source for metabolic chains. POM and DOM are biologically decomposed by aquatic biota and, at the same time, autochthonous DOM and nutrients are produced as a result of microbial metabolic activity therefore contributing to microbial loop [22–24]. Some researchers have suggested that the fluorescence emission of DOM at specific wavelengths (*Ex* = 310-320 nm, Em=380-410 nm) could be used as a tool to estimate biological activity. Nature and size of DOM have been observed to play a significant role on its bioavailability and microorganism have been observed to prefer non-humic fractions of DOM having MW lower than 3000 Da as a source of nutrients [25]. Humic substances have also been observed to influence phytoplankton reproduction by chelating important nutrients like iron and phosphorous; while iron uptake by phytoplankton increases in presence of HS, presumably due to improved metal chelation in the medium, growth inhibition of phytoplankton by high concentrations of humic substances has been observed as a consequence of iron over chelation leading to its reduced availability [26,27].

4. Cycling of nutrients: humified macromolecules are quite stable and refractory compounds and nutrients like nitrogen and phosphorous embedded inside them are very little available for microbial and plant uptake. Degradation of DOM via microbial respiration or photochemical transformations can help breaking down these macromolecules into smaller and simpler fragments making these nutrients accessible for uptake mainly under the form of dissolved organic nitrogen (DON) or dissolved organic phosphorous (DOP) [28–30]. As a result, nutrients released by DOM and POM can indirectly control photosynthesis in natural waters and affect water productivity enhancing the cyanobacterial or algal blooms [31–33]. As a matter of facts, the occurrence of chlorophyll *a,* an indicator of photosynthetic activity in natural water, has often been reported to be significantly correlated to DOC contents [34–36].

5. Metal ions complexation: DOM has been reported to be the most important source of organic ligands capable of forming stable complexes with major and trace metal ions (M) in natural surface waters [37,38]. Most of the DOM components in fact, such as allochthonous FAs and HAs of plant origin but especially autochthonous FAs of algal or phytoplankton origin, contain strong π-electron bonding systems such as oxygen, sulfur, phosphorous or nitrogen groups, but, the formation of covalent type

interactions between metal ions and DOM has been observed as well [39–44]. The formation of these complexes is of fundamental importance in metal ion chemistry and can control the occurrence of free metallic ions, their transport or migration, their solubility in water, occurrence of the photo-Fenton reaction in surface water, biological effects as well as the bioavailability and toxicity to organisms in water, sediment and soil environments [45]. As the fluorescence emission of CDOM has been observed to be quenched by M complexation, the study of fluorescence excitation-emission matrices (EEMs) has often been proposed as a valid tool for identification and quantification of such interactions [38,46–48].

6. Influence of DOM on drinking water quality: drinking water is typically obtained by the treatment of different kind of natural water sources such as riverine water or groundwater and DOM is commonly present, at different concentrations, in all these sources. Knowledge on the type and concentration of the DOM present in treated water is a key aspect of the whole water treatment process as DOM, even if non-toxic by itself, can heavily affect the quality of resulting drinking water in different ways. 1) DOM is the main precursor of toxic disinfection by-products (DBPs) such as haloacetic acids (HAAs) formed from the reaction of DOM constituents with chlorine based disinfectants (e.g. chlorine dioxide or hypochlorite); 2) DOM can vehiculate toxic compounds and protect them from being efficiently removed under water disinfection treatments and it can also enhance the transport of complexed toxic metals; 3) DOM can modify water color as well as its organoleptic parameters. The role of DOM in water treatment processes will be discussed with further details in section 1.4; 4) furthermore, DOM is excellent radical scavenger (especially for $HO^{\bullet}$ radicals) therefore lowering the overall treatment efficiency.
7. Influence on global carbon cycle: aquatic NOM is one of the most important carbon pools containing roughly the same amount of carbon as terrestrial biomass or CO_2 in the atmosphere, and it strongly influences production, transformation and distribution of carbon compounds in the biosphere [49]. Marine primary production of organic carbon for example, with an estimated gross production of 5×10^{16} g/year is responsible of roughly 40% of total carbon biogeochemical cycles [50]. The photodegradation of DOM is strongly dependent on the nature of the DOM itself but, for light absorbing and fluorescent fractions (CDOM and FDOM), the weight loss can be larger than 50% of its original carbon content therefore representing a significant source of CO_2, CO and dissolved inorganic carbon [51].

1.3. NOM and water treatment

NOM content in drinking water is not typically regulated by law, however, national and international organizations have defined some general guidelines: the U.S. Environmental Protection requires removal of total organic carbon (TOC) for waters having TOC above 2 mg/L. The World Health Organization suggests optimized NOM removal as a means to minimize biofilm growth in the distribution system. The European Union regulations include TOC as a general water quality indicator. In Canada, guidance has been developed for water utilities to help them understand and control the impact of NOM [52].

The production of drinking water is typically based on surface water bodies like rivers, artificial reservoirs and groundwater; the relative importance of these sources varies significantly from country to country or depending on the time of the year considered. Denmark and Austria for example use exclusively groundwater for the production of drinking water while Ireland relies on surface water bodies at almost 90% of their production. A report published by the European Environment Agency (EEA) in 2016 showed that about 50% of total drinking water in Europe comes from underground water bodies while 37% comes from surface water. Other sources of drinking water are bank filtration water (that represents the most important source in Hungary), artificial groundwater recharge (largely adopted in Sweden), or, in particular cases where freshwater source are particularly scarce (e.g. Cyprus), desalinated coastal water may be used.

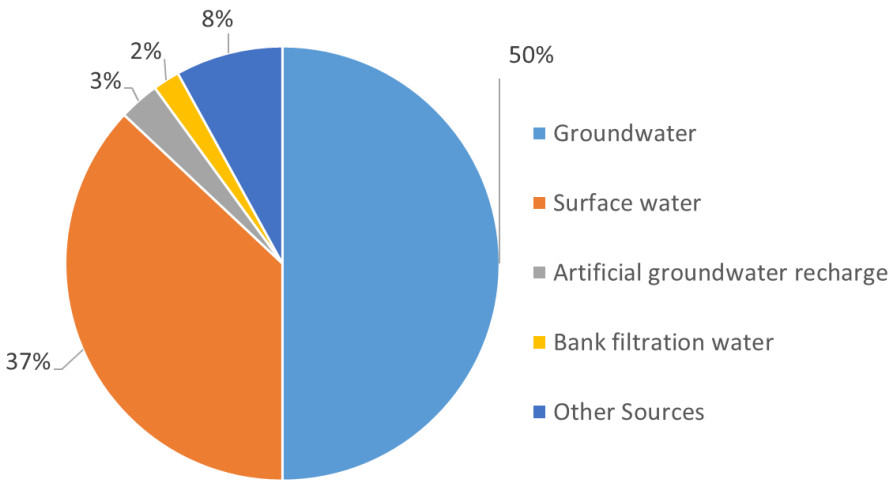

Figure 4. Sources of drinking water in the European Union in the years 2011-2013 extracted from the European Environment Agency report.

DOM and POM are ubiquitous components of all these waters with DOM usually being the most abundant of the two accounting for up to 90% of TOC. NOM gives the yellowish-brownish color of natural waters and it can act as a substrate for the microbial growth [33]. Starting from the 1980s, as a consequence of global temperature increase and modification of the quality and quantity of atmospheric precipitation, an increase of NOM concentrations in surface water bodies has been reported by various sources [53–55]. This increment in the concentrations of aquatic NOM contributes to the rapid deterioration of water quality and represents a critical aspect for the production of high-quality drinking water. NOM removal is an essential step in any process of drinking water production and it presents two main critical aspects; the first is related to the nature of NOM, the second to its concentration. Because of the heterogeneity of NOM in terms of chemical structures, molecular weights and solubility values, the development of an efficient technology for its removal is a very challenging task. In general, the complete removal of NOM does not occur and the most soluble fraction of DOM proceeds therefore to the disinfection step where it is the main responsible for the formation of toxic DBPs. Secondly, because of the fluctuations in the concentration and type of aquatic NOM, the removal process needs to be finely and rapidly tuned according to the characteristics of treated water. These fluctuations can be divided in three different classes; 1) sudden variations mainly dependent on storm events; when intense precipitations occur rivers flow can significantly increase and the turbulent nature of the flow increases as well with a consequent increase in the concentrations of transported NOM [56–58]; 2) seasonal variations depending on the climatic factors like floods, draughts, rainfalls, snowmelt runoffs as well as microbial and algal activity than can influence both the type and the concentration of aquatic NOM [59]; 3) long term variations in the concentration of aquatic NOM have already been observed over the last few decades as a consequence of climate change and land use and it is expected that in the future the overall increase of temperatures and enhanced biodegradation of SOM will lead to a further increase in the production of DOM, while the flooding and runoff will export it from soil to rivers, lakes, and groundwater [53–55]. Knowing the concentration of organic matter present in the water at every time is therefore an essential information to the treatment process; the classical measure to determine the amount of NOM in water is the measure of the total organic carbon (TOC) but the absorbance at 254 nm or fluorescence spectroscopy are used as well for fast estimation of NOM concentration. The latter techniques have the advantage of being usable for real time data acquisition and live monitoring using simple and robust equipment.

1.3.1. NOM as a precursor for toxic DBPs

NOM itself is not considered to be harmful for living organisms and, generally, numerical limits for its concentration in drinking water have not been established. However, in water disinfection processes, NOM was found to be responsible for the formation of the most common toxic DBPs such as trihalomethanes (THMs), haloacetic acids (HAAs), chlorinated ketones and haloacetonitriles, by reaction with free chlorine added as a disinfectant. Chlorine is the most widespread disinfectant used worldwide, and THMs and HAAs are formed at the highest concentrations after chlorination [60]. In figure 5 it is shown what happens when chlorine (either Cl_2 or HClO) is added to water; it can be seen how the concentration of chlorine residual, as well as DBPs formation, does not linearly increase with added chlorine dose and that a minimum, called breakpoint, can be identified. Breakpoint is not a universal value and optimal chlorine dose must be identified according to water parameters such as type and concentration of NOM and pH.

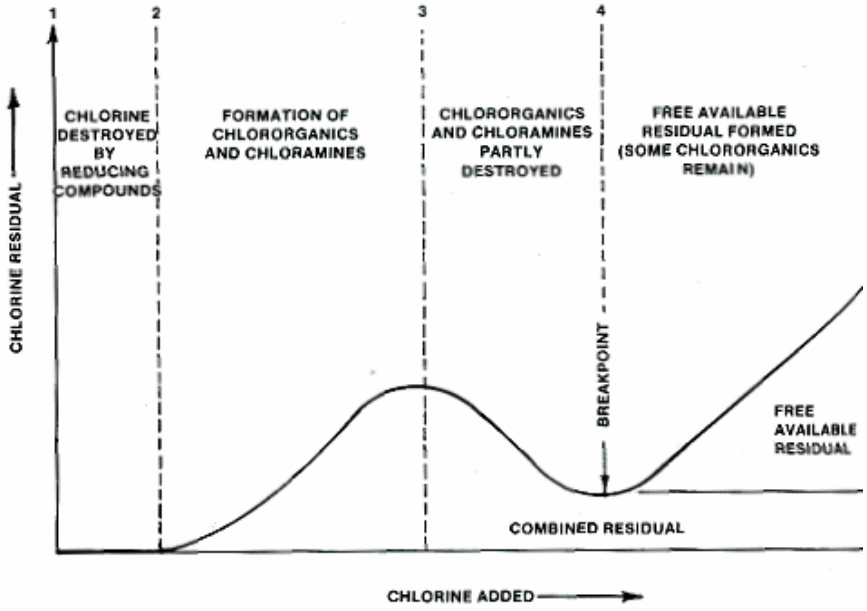

Figure 5. Formation of DBPs as a function of added chlorine dose in water disinfection processes. Figure extracted from www.thewatertreatments.com/disinfection/chlorination.

The identification of readily measurable water quality parameters providing a reliable indication of DBPs formation potential (DBPFP) is therefore essential for a correct estimation of the disinfection

breakpoint. Generally, it has been reported that DBPFP correlates well with UV 254 nm absorption or DOC content. In recent years, fluorescence spectroscopy has also been employed in an attempt to improve this correlation [61,62].

Trihalomethanes (THMs)

The presence of THMs in chlorinated drinking waters was first observed in the United States at the beginning of the 1970s. A survey published in 1975 by *Symons et al.*, containing the analysis of drinking water in 80 north American cities, showed that four trihalomethanes, i.e., trichloromethane ($CHCl_3$), bromodichloromethane ($CHBrCl_2$), dibromochloromethane ($CHBr_2Cl$), and tribromomethane ($CHBr_3$), and carbon tetrachloride (CCl_4) were widely spread in chlorinated drinking waters in the US due to chlorination processes. These compounds were not found or were present in low concentrations in the raw waters and their total concentration in finished waters was found to be strongly dependent on the concentration of NOM in the water supply [63]. In 1976, the National Cancer Institute identified chloroform as a carcinogenic compound (NCI 1976), leading ultimately to the regulation of THMs by the Environmental Protection Agency (U.S. EPA 1979) whose total concentration was fixed to a maximum 100 µg/L as an annual average. Today, the same valued is applied for drinking water in the EU (even if some member states have set lower limits on a national level) while in the US it was lowered to 80 µg/L.

As indicated earlier, NOM is the principal organic precursor with which the halogens react to form these by-products. In the absence of bromide ion, only chlorinated by-products are formed. In the presence of bromide, hypochlorous acid (added as disinfectant) rapidly oxidizes bromide to hypobromous acid (HOBr), which then, along with the residual hypochlorous acid, reacts with the NOM to produce mixed chloro-bromo derivatives. The extent of bromine incorporation into the by- products depends upon the bromide ion concentration relative to the amount of free chlorine applied; as the bromide concentration increases, the extent of bromine incorporation increases. In waters with very high bromide concentrations (typically > 1 mg/L), it is possible to form primarily the brominated species [64].

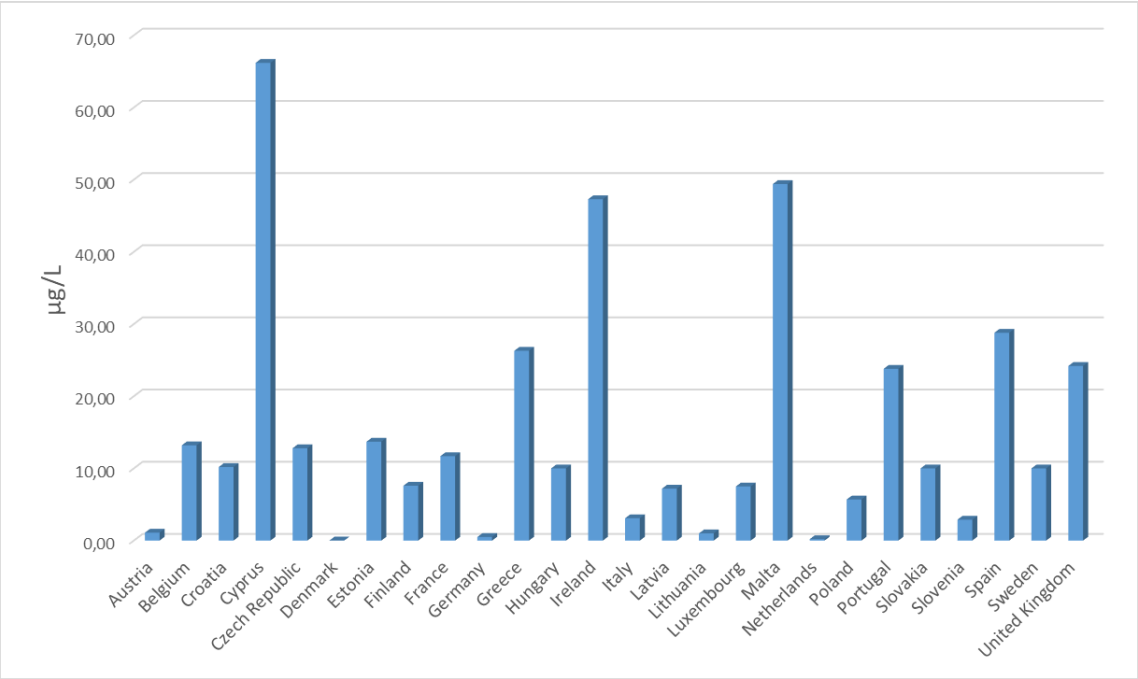

Figure 6. Average total THMs levels in drinking water in European Union countries. Data extracted from Evlampidou et al. [65].

Other disinfectants may be used alone or in combination with chlorine. Chlorine dioxide for example is widely used in Italy, leading to lower levels of THMs but higher levels of chlorite and chlorate [66]. Ozone is often used in combination with chlorine-based disinfectants to produce a lower volume of THMs, HAAs, and chlorine-based DBPs, but results in the production of aldehydes, ketones, carboxylic acids, alcohols, and esters, and can also form bromate when the raw water contains bromide [67].

Haloacetic acids (HAAs)

HAAs are the second most important class of DBPs in terms of occurrence and concentration in drinking waters. This group consists of nine different chlorinated/brominated acetic acids. The five most common HAAs, commonly referred to as HAA_5, are monochloroacetic acid (MCA), dichloroacetic acid (DCA), trichloroacetic acid (TCA), monobromoacetic acid (MBA) and dibromoacetic acid (DBA). The other four are bromodichloroacetic acid (BrCl2AA), dibromochloroacetic acid (Br2ClAA), tribromoacetic acid (Br3AA) and bromochloroacetic acid (BrClAA). In the U.S., the limit for total concentration of HAA_5 has been fixed to 60 µg/L while in the EU individual limit values for each HAA have been identified [68].

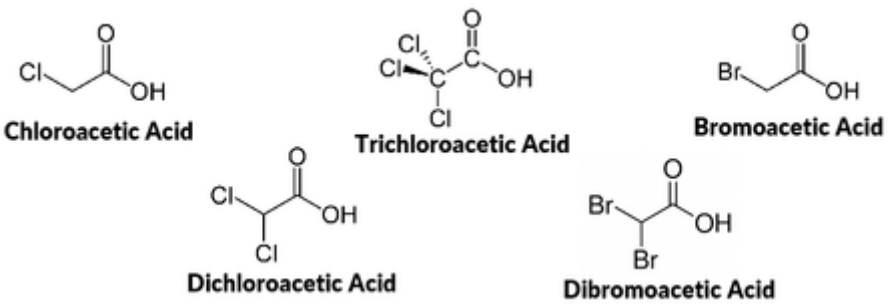

Figure 7. Chemical structures of HAA_5.

The rate and extent of HAAs formation is impacted by the chlorine dose and free chlorine residual. Higher doses and free residual chlorine have been found to favor the formation of HAAs over THMs, the formation of the trihalogenated HAAs over the di- and monohalogenated HAAs, and the formation of the chlorinated THMs and HAAs over the brominated and mixed bromo-chloro species [64].

1.3.2. NOM removal techniques

Different technologies have been developed over the years for the removal of NOM from water, nevertheless, the research for an optimal removal method is far from being concluded. Today's water emergency is increasing the pressure over the availability of efficient technologies which enable to ensure high-quality drinking water. This is not only a challenge for those countries having scarce freshwater resources, but also for densely populated regions like Europe where an efficient water reuse has become imperative.

Coagulation

The oldest and most widely adopted method for NOM removal is coagulation, a physical-chemical process aiming at reducing the electrostatic repulsion potential of colloids bearing electrical charges using various coagulants. As a result, colloidal microparticles start to develop and then agglomerate into larger particles or flocs that can precipitate and, therefore, be removed. NOM can be seen as a colloid due to the presence of charged functional groups such as deprotonated carboxylic groups but the variability of its organic content in terms of molecular and electrical properties, requires adaptation of the removal from one water source to the other and even within the same source due to seasonal variations or storm events. This makes the application of coagulation in the treatment of drinking

water supplies challenging [69,70]. The most important two operational parameters in such processes are **pH** and **concentration and type of the coagulant** used; the tuning of these parameters must be done according to the type and concentration of NOM entering the treatment process. The understanding of its characteristics and the variability patterns of its compositions and amounts in drinking water sources is therefore essential for the enhancement of NOM removal efficiencies of any water treatment process. Practically, coagulation processes are carried out by adding a determined amount of coagulants that dissociate in water carrying multiple positive charges and interact with the negatively charged NOM. Al^{3+} (aluminum sulfate, aluminum chloride) and Fe^{3+} (ferric sulfate, ferric chloride) salts are the most used ones because of their efficiency in removing color and turbidity, high availability and affordable price, but polymeric cationic polyelectrolytes (e.g. polydiallyldimethyl ammonium chloride and cationic polyacrylamide) have also been proven to be effective in NOM removal [71,72]. The highest percentages of DOC removal by coagulation/flocculation reported in the literature are around 80%; this corresponds to a significant portion of NOM, however, the most hydrophilic and low-MW fraction is not removed and reaches the disinfection step where it can act as a precursor of toxic DBPs.

Membrane filtration

Other treatments have therefore been developed to reach better removal efficiency of NOM and one of them is membrane filtration**.** In this case, the main technical problem is the frequent fouling that is responsible for the high maintenance costs and rapid decrease of filtration performances. Despite the possibility of periodical cleaning of the membranes by backward flushing, NOM has been observed to cause irreversible fouling that reduces membranes lifespan [73,74]. In order to mitigate the membrane fouling phenomenon, the application of membrane processes is generally coupled with a pre-treatment step; in this optic, coagulation processes can be seen as a pre-treatment for membrane filtration [75–77]. Recent studies have shown that coupling coagulation and membrane nanofiltration could remove more than 90% of the dissolved organic carbon (DOC) with a consequent reduction of 96% of the UV absorbance at 254 nm from lake water [78]. The fundamental mechanism of membrane fouling lies in the intermolecular interaction between the membrane surface and the various feed components; these interactions involve short range attraction forces, electrostatic interactions, and polarization forces. The interactions lead to adsorption processes and particles deposition and therefore to pore blockage, pore constriction and cake filtration. The characteristics of membranes surface play therefore a major role in determining the fouling rate and it has been observed that in general negatively charged, hydrophilic membranes represent the best option for surface water treatment [79]. Most membranes used so far for nanofiltration and ultrafiltration applications are polymeric membranes but, over the last decade, alternative ceramic membranes have received

increasing attention in the drinking water industry. Ceramic membranes are superior to their polymeric counterpart in their mechanical and chemical characteristics allowing the use of higher fluxes and backwash pressures and of more aggressive cleaning approaches without risk of damaging the membrane integrity [80]. Furthermore, ceramic membranes structural and chemical stability result in an expected lifespan that is considerably longer than the one of polymeric membranes (20 years compared to a typical 7–10 years of polymeric membranes) therefore reducing maintenance costs [79]. A more recent approach involves the development of functionalized membranes bearing a photocatalytic layer, responsible for the degradation of organic compounds, that helps reducing the fouling phenomenon [81,82].

Advanced Oxidation Processes (AOPs)

Additional technologies that can be used to remove NOM from drinking water are advanced oxidation processes (AOPs). There is a considerable interest in the use of AOPs not only for the treatment of drinking water, but for wastewater treatment and soil remediation as well [83–86]. Various oxidants (O_3, H_2O_2), catalysts (TiO_2, Fe^{2+}), radiations (UVA, UVB, UVC) alone or in combination (O_3/H_2O_2, UV/H_2O_2, UV/O_3, UV/TiO_2 or Fe^{2+}/H_2O_2) have been developed for the removal of NOM and organic pollutants [87–89]. These processes rely on chemical and/or physical processes generating highly reactive radical species, the most important being the hydroxyl radical ($HO^{\bullet}$), able to react non selectively with almost all organic compounds present in solution, including NOM [90–93].

Table 1. Oxidation potentials of some oxidants.

Species	Oxidation potential (V)
Fluorine	3.03
Hydroxyl radical	2.80
Atomic oxygen	2.42
Carbonate radical	2.10
Ozone	2.07
Hydrogen peroxide	1.78
Perhydroxyl radical	1.70
Permanganate	1.68
Hypobromous acid	1.59
Chlorine dioxide	1.57
Hypochlorous acid	1.49
Hypoiodous acid	1.45
Chlorine	1.36
Bromine	1.09
Iodine	0.54

As it can be seen in Table 1, HO• is one of the most powerful oxidants known and its reaction rate with organic compounds (typically 10^8-10^{10} $M^{-1}s^{-1}$) is usually several orders of magnitude higher than the one of ozone under the same conditions [94]. HO• radicals can react with organic compounds following three different reaction pathways: addition to double bonds (reaction 1), H-atom abstraction (reaction 2), electron abstraction (reaction 3).

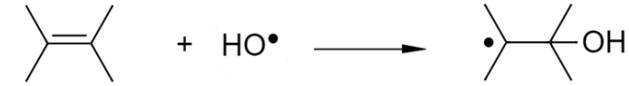

(1)

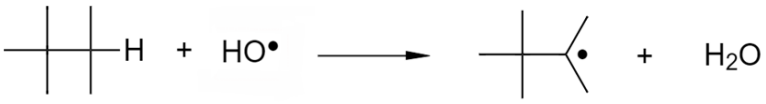

(2)

(3)

Once the radical reaction chain has been initiated, countless degradation pathways can simultaneously take place; the carbon centered radicals formed in reactions (1) and (2) for example, can very rapidly react with oxygen to form organic peroxyl radicals and the reactions of peroxyl radicals among themselves can lead to production of ketones, aldehydes and/or carbon dioxide [95]. The overall rate of NOM oxidation therefore depends on the amount of radicals initially formed, on the concentration of dissolved oxygen, on the concentration of NOM itself and on the concentration of radical scavengers the most important ones being carbonate and bicarbonate anions (reactions 4-5) [94].

$$HO^{\bullet} + HCO_3^- \rightarrow H_2O + CO_3^{\bullet-} \qquad k_4=1.5\times10^7\ M^{-1}s^{-1} \qquad (4)$$

$$HO^{\bullet} + CO_3^{2-} \rightarrow OH^- + CO_3^{\bullet-} \qquad k_5=4.2\times10^8\ M^{-1}s^{-1} \qquad (5)$$

Estimating an exact rate constant for the reaction between NOM and HO• is not possible since it changes according to the molecular structure of the NOM itself but as a general rule it is possible to say that the higher the aromatic character of NOM, the higher is its reactivity with HO•; indole derivatives for example exhibit rate constant >10^8 M^{-1} s^{-1} in neutral aqueous solution [96]. For Suwannee river fulvic acids, a value of 1.6 × 10^8 $M_C^{-1}s^{-1}$ was determined by pulse radiolysis [97].

As mentioned before, estimating the concentration of aquatic NOM can be done both by measuring the TOC concentration and then multiplying this value by two (assuming that carbon contributes for about 50% of NOM weight) or, in a more indirect way, by means of spectroscopic measurements such as measuring the absorbance at 254 nm (A_{254}) or measuring the intensity of NOM fluorescent emission

[98–100]. However, when determining the efficiency of an AOP in the removal of NOM, it has been reported by several works that A_{254} decreases at a higher rate than TOC values [101–103]; this is because the light absorbing fraction of NOM (CDOM) is mainly composed by large macromolecules, containing aromatic rings and conjugated double bonds, that are rapidly fragmented into smaller molecules that do not absorb light (or at least many of them do not absorb at 254 nm) while mineralization of NOM carbon necessarily requires longer time. These smaller fragments are in fact more refractory for two reasons: they are little sensitive to photodegradation as their absorbance in the UV-Vis region is small and, being poorly aromatic, they are less susceptible to attacks by $HO^{\bullet}$ radicals. Complete mineralization is therefore seldom achieved [102,104]. The main types of AOPs commonly adopted for water treatment and for NOM removal are described below.

UV-induced production of $HO^{\bullet}$ radicals

UV-light based AOPs are among the oldest and most widely adopted water treatment processes. UV radiation can in fact induce direct photolysis of large number of organic compounds. The efficiency of direct photolysis obviously depends on the chemical structure of these compounds as it determines their chemical stability, reactivity, and their light absorbing properties; a compound that does not absorb the UV radiation adopted for the treatment is in fact insensitive to direct photolysis and will not be degraded. In Table 2, some typical single bonds energies and their corresponding wavelength are reported. Theoretically, a C-C bond could be cleaved using light at 344 nm but that does not mean that a C-C bond itself is capable of absorbing light at 344nm; furthermore, the absorption of a photon does not necessarily lead to the cleavage of a chemical bond as several non-dissociative relaxation pathways are possible.

Table 2. Typical energies for some single bonds and the approximate light wavelengths corresponding to this energy.

Bond	Bond energy (kJ/mol)	Corresponding λ (nm)
O-H	465	254
H-H	436	274
C-H	415	288
N-H	390	307
C-O	360	332
C-C	348	344
C-Cl	339	353
Cl-Cl	243	492
Br-Br	193	620
O-O	146	820

The cleavage of a chemical bond by direct photolysis depends in the first place on the probability of a photon having a certain energy to be absorbed by a molecule therefore inducing an electron transition and secondly on the probability that this molecule in its excited state would follow a dissociative relaxation pathway. On a macroscopic level, the first phenomenon is described by the Lambert-Beer law:

$$A(\lambda)=\varepsilon_i(\lambda)\cdot b\cdot C_i \qquad \text{Eq. 1}$$

where $A(\lambda)$ is the absorbance of the solution at a specific wavelength, ε is the *molar absorption coefficient* (expressed in $M^{-1}cm^{-1}$) and represents the probability of a compound *i* to absorb light at that wavelength, C_i is the concentration of the compound in the solution expressed in M, and *b* is optical path length of the light in the solution expressed in cm. The second phenomenon is governed by the *quantum yield of photolysis* $\phi_{Pi}(\lambda)$ that can be described as follows:

$$\phi_{Pi}(\lambda) = \frac{\text{number of molecules } i \text{ undergoing transformation during } t}{\text{total number of photons (of wavelenght } \lambda) \text{ absorbed by the compound } i \text{ during } t}$$

Once a molecule has been promoted to an excited state by light absorption, fragmentation is only one of the relaxation pathways it can undergo. These pathways can be divided into physical processes (such as fluorescence emission) than do not cause structural modification of the compound, and chemical reaction (such as fragmentation) that lead to the formation of products different from the original light absorbing compound. A schematic representation of these processes proposed by *Schwarzenbach et al*. is shown in figure 8 [105].

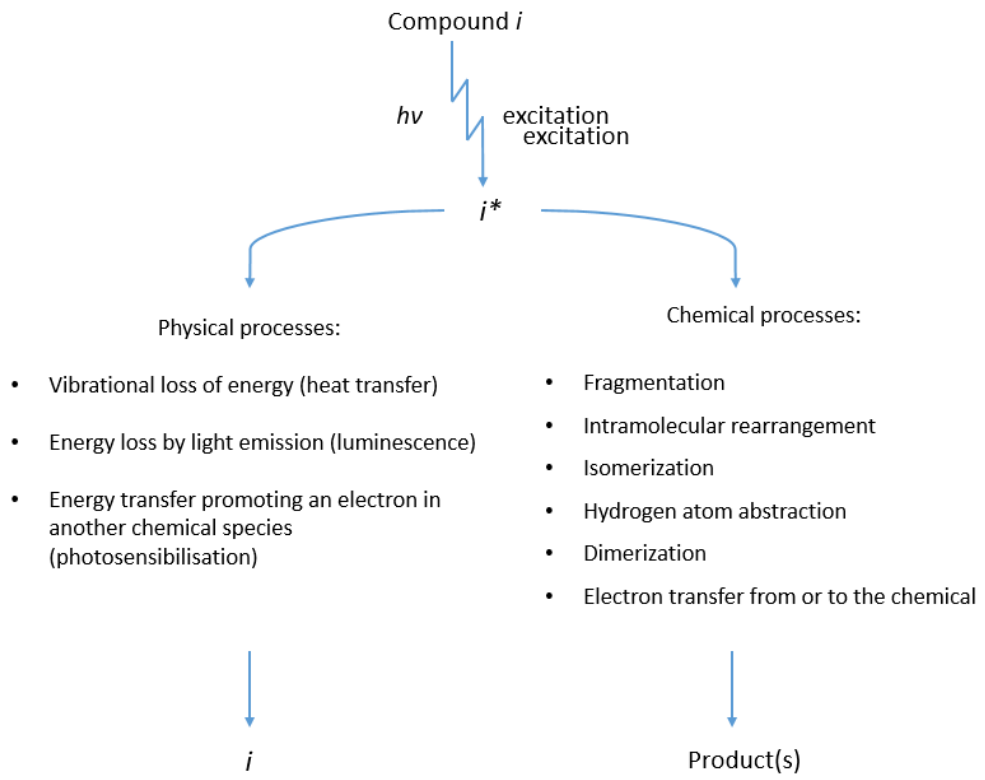

Figure 8. Possible physical processes and chemical reactions for a photochemically excited organic species. Extracted from Schwarzenbach et al.

Typical wavelengths used for AOPs fall within the UVC region (<280 nm) with 254 nm being one of the most classical ones even if less energetic radiation, such as 365 nm, can be used (often in combination with catalysts such as TiO_2) [101,102,106–108]. Many authors however reported that UV 254 nm is not energetic enough to achieve degradation of more stable compounds as well as NOM and proved that using 185 nm vacuum UV (VUV) leads to better TOC removal [109–111]. The efficiency of the VUV-based AOP relies not only on the increased rate of direct photolysis of NOM, but especially on the capacity of this type of radiation to induce homolytic cleavage of water O-H bond resulting in the generation of $HO^{\bullet}$ and hydrogen atoms. Typical VUV sources are xenon excimer lamps (emission maximum at λ=172 nm) and standard low-pressure mercury lamps (part of its emission spectra λ=185 nm). The main drawback encountered when using VUV radiation is that it is strongly absorbed by both air and water and its penetration in the volume of treated water is limited, furthermore, short-living $HO^{\bullet}$ and $H^{\bullet}$ cannot diffuse far outside the irradiated area and treated volume is therefore restricted. This leads to an extreme heterogeneity between the irradiated solution in direct proximity of the lamps, where the treatment is actually taking place, and the non-irradiated bulk that is not affected by the water treatment [109]. Coupling VUV with ozone injection in water has been reported to

significantly improve treatment performances; conveniently, ozone can be produced irradiating oxygen in the gas phase using the same VUV sources [112].

Another way to improve the performances of UV 254 nm is to add hydrogen peroxide in solution (typically referred to as UV/H_2O_2). At this wavelength hydrogen peroxide is in fact efficiently photolyzed producing $HO^\bullet$ (reaction 6) that, once generated, can initiate the degradation mechanisms as indicated by reactions 1-3. At the same time if used in excess, hydrogen peroxide can react with $HO^\bullet$ to produce hydroperoxyl radicals (reaction 7) that are much less reactive and do not appear to significantly contribute to the degradation of organic compounds therefore lowering treatment efficiency [89].

$$H_2O_2 + h\nu \rightarrow 2\,HO^\bullet \quad (6)$$

$$H_2O_2 + HO^\bullet \rightarrow H_2O + HOO^\bullet \quad (7)$$

$$H_2O_2 \rightleftarrows HO_2^- + H^+ \quad pK_a=11.6 \quad (8)$$

$$H_2O_2 + HO_2^- \rightarrow H_2O + O_2 + HO^- \quad (9)$$

There are several advantages in using H_2O_2 as an oxidant such as its commercial availability, the possibility to store it on-site due to its stability, minimal capital investment and simple operation procedure. Its decomposition does not produce harmful byproducts that would require additional treatment steps to be removed and it is a very efficient source of $HO^\bullet$ ($\phi \approx 1$). The main obstacle encountered with UV/H_2O_2 processes is that the rate of chemical oxidation of contaminants depends on the rate of formation of $HO^\bullet$ and this is limited by the very small absorption coefficient of H_2O_2 at 254 nm (table 3). The rate of photolysis of aqueous H_2O_2 was observed to be pH-dependent and to increase in basic environment because of the higher absorption coefficient of the peroxide anion (pK_a=11.6). On the other hand, hydrogen peroxide is known to decompose by a dismutation reaction (reaction 9) with a maximum rate at the pH of its pK_a [89].

Several authors reported significant changes in NOM structural characteristics during UV/H_2O_2 processes: generally NOM was observed to be fragmented into lower MW fractions with significant reduction in absorbance and aromaticity without observing significant drop in TOC values [113]. According to another study carried out by *Kruithof et al*. instead, over 60% of NOM was removed using a UV dose of 540 mJ/cm^2 and H_2O_2 concentrations of 6 mg/L [114]. Despite the overall good efficiency of UV/H_2O_2 processes in the removal of organic compounds, it has been observed that under the photon flux and with H_2O_2 concentrations typically used for water treatment (400 mJ/cm^2 and 5-20 mg/L respectively), NOM is not significantly removed. At a concentration of 0.0082 M, H_2O_2 can absorb most of the energy in the UVC range (200-280 nm) and it was calculated that its optimal concentration

for efficient HA removal for surface waters having high DOC values would lie between 0.0032 M and 0.0163 M [115].

Ozone based AOPs

Ozone has a long history in water treatment with the first preliminary applications dating back to the end of 19th century when its disinfecting properties were discovered. Shortly after, it was observed that ozone-treated waters exhibited a distinctive improvement in both taste and odor. By 1915 about 50 ozonation plants for drinking water treatment had been installed across Europe but, during World War I, the research conducted on poisonous gases, that led to the production of inexpensive chlorine, drastically limited ozone applications for water disinfection. The discovery in 1973 of the formation of carcinogenic trihalometanes (THMs) as by-products of chlorination processes was probably the main driving force leading to a renovated interest in the use of ozone in water treatment applications. Today, most applications of ozone are in fact oriented to DBPs control due to the reduced amount of toxic by-products formation in ozonation treatments compared to chlorination [116].

Ozone reacts with NOM by selective electrophilic addition to double bonds leading to the cleavage of the double bond and to the formation carboxylic acids, alcohols, and aldehydes (figure 6).

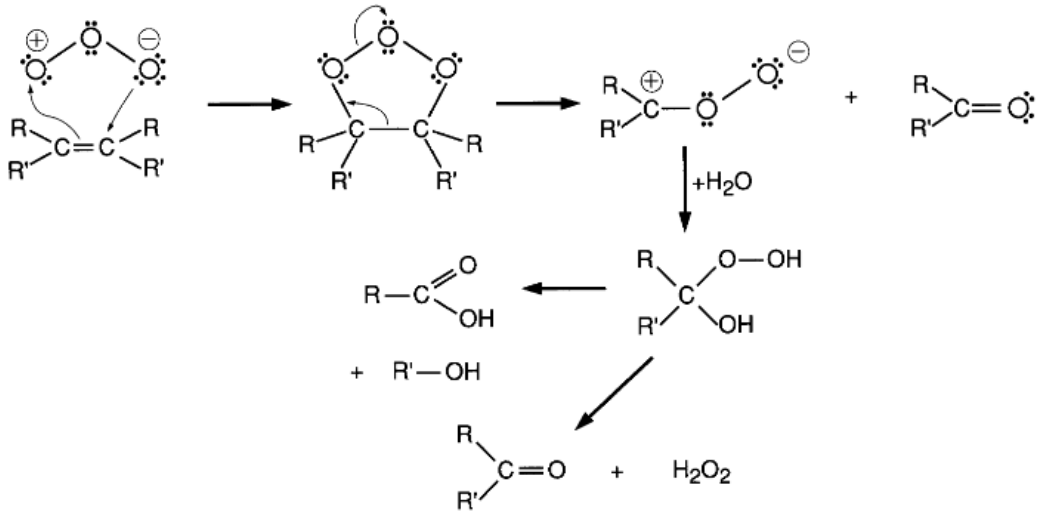

Figure 9. Mechanism of ozone electrophilic addition to double bonds studied by Criegee [117].

In addition, HO• radicals can be formed by ozone decomposition in water even though the amount of radicals produced in this way is low compared to AOPs [118]. In order to improve the conversion of ozone to HO• several methods have been developed. The simplest way is to increase water pH as ozone decomposition is more efficient in alkaline environment (reactions 10-14) [119].

$$O_3 + OH^- \rightarrow HO_2^- + O_2 \qquad k_{10} = 7\times10^1\ M^{-1}s^{-1} \qquad (10)$$

$$O_3 + HO_2^- \rightleftarrows HO^\bullet + O_2^{\bullet-} + O_2 \qquad (11)$$

$$O_3 + O_2^{\bullet-} \rightarrow O_3^{\bullet-} + O_2 \qquad k_{12} = 1.6\times10^9\ M^{-1}s^{-1} \qquad (12)$$

$$O_3^{\bullet-} + H^+ \rightarrow HO_3^\bullet \qquad k_{13} = 5.2\times10^{10}\ M^{-1}s^{-1} \qquad (13)$$

$$HO_3^\bullet \rightarrow O_2 + HO^\bullet \qquad k_{14} = 1.1\times10^5\ s^{-1} \qquad (14)$$

In modern AOPs however, ozone is typically used in combination with H_2O_2 (O_3/H_2O_2), UV light (O_3/UV) or with both of them at the same time (O_3/H_2O_2/UV). HO• production initiated by hydrogen peroxide or UV radiation is in fact largely superior than the one initiated by hydroxide ions. Ozone reacts very slowly with the H_2O_2 molecule but it strongly reacts with hydroperoxide anion produced by reaction 8.

The set of reactions for ozone decomposition in presence of hydrogen peroxide is shown in figure 10.

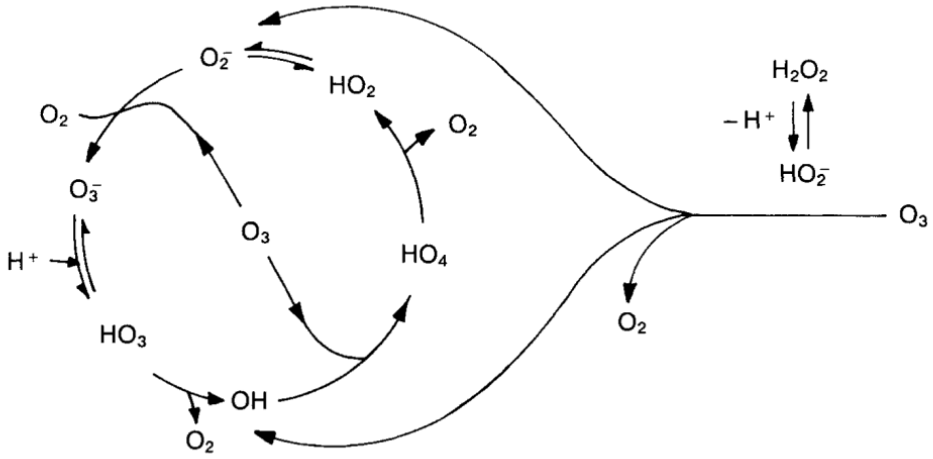

Figure 10. Ozone decomposition process in presence of H_2O_2 extracted from Langlais et al [119].

Another advantageous initiator for ozone decomposition is UV light. From a photochemical point of view, the absorption spectrum of ozone in both gaseous and aqueous phase provides a much higher absorption cross section at 254 nm than H_2O_2, and inner filter effects by CDOM are less problematic (see table 3). In a gaseous phase enriched with water vapor, the mechanism of ozone photolysis involves the release of one molecule of oxygen and one oxygen atom (reaction 15); the latter can then react with water to generate two HO• (reaction 16) [120].

$$O_3 + h\nu \rightarrow O_2 + O(^1D) \qquad (15)$$

$$O(^1D) + H_2O \rightarrow 2\ HO^{\bullet} \quad (16)$$

Furthermore, under UV irradiation ozone can react with water to form hydrogen peroxide and molecular oxygen (reaction 18); in situ-formed H_2O_2 is itself a source of $HO^{\bullet}$ by reaction with ozone according to reaction 15, or being photolyzed (reaction 6).

The process of ozone decomposition under UV 254 nm is shown in figure 8. Ozone driven degradation of NOM occurs following two main pathways: 1) direct selective electrophilic addition of ozone to NOM double bonds and, 2) $HO^{\bullet}$-mediated degradation as a consequence of ozone decomposition in presence of H_2O_2, UV light, and to a lesser extent, hydroxide anion. The set of these processes has been reported by several authors to cause an overall reduction in NOM aromaticity and MW [119,121,122]. *Westerhoff et al.* observed that this reduction in aromaticity was due to selective decrease of phenolic carbon content resulting in an increase in aliphatic compounds, carboxylic acids, aldehydes and ketones with a consequent reduction in NOM hydrophobicity; DOC removal however was limited to 2-10% of pre-treatment values [122]. In a study published by *Chin et al.,* it was shown that individual application of ozone or UV did not have any significant effect in TOC removal; however, simultaneous application of O_3 and UV led to a 50% TOC removal [123]. *Zhang et al.* instead, studied the photocatalytic degradation of NOM in different drinking water sources using a combined O_3/TiO_2/UV AOP and obtained good TOC removal, especially for the high-MW NOM fractions (about 80% of TOC removal for MW>10k). They also observed that high concentration of bicarbonate greatly inhibited TOC removal and aromaticity loss [124].

Photocatalysis

Using *heterogeneous photocatalysts* for the removal of CECs and DBPs precursors has been proven to be a valid alternative for both drinking water and wastewater treatment. Photocatalysts are typically semiconductors in the form of nanometric or micrometric particles that get suspended in water and irradiated with near-UV or visible light to promote the formation of reactive species such as superoxide radical anion, $HO^{\bullet}$ and electron holes. When a semiconductor particle absorbs a photon of appropriate wavelength in fact, an electron is promoted from its valence band to its conduction band leaving an electron hole in the valence band; from here, the reduction of molecular oxygen at the conduction band and the oxidation of water at the valence band can simultaneously take place. A simplified mechanism for these processes, proposed by *Bekbolet and Ozkosemen* using TiO_2 as model photocatalyst, is shown in figure 11.

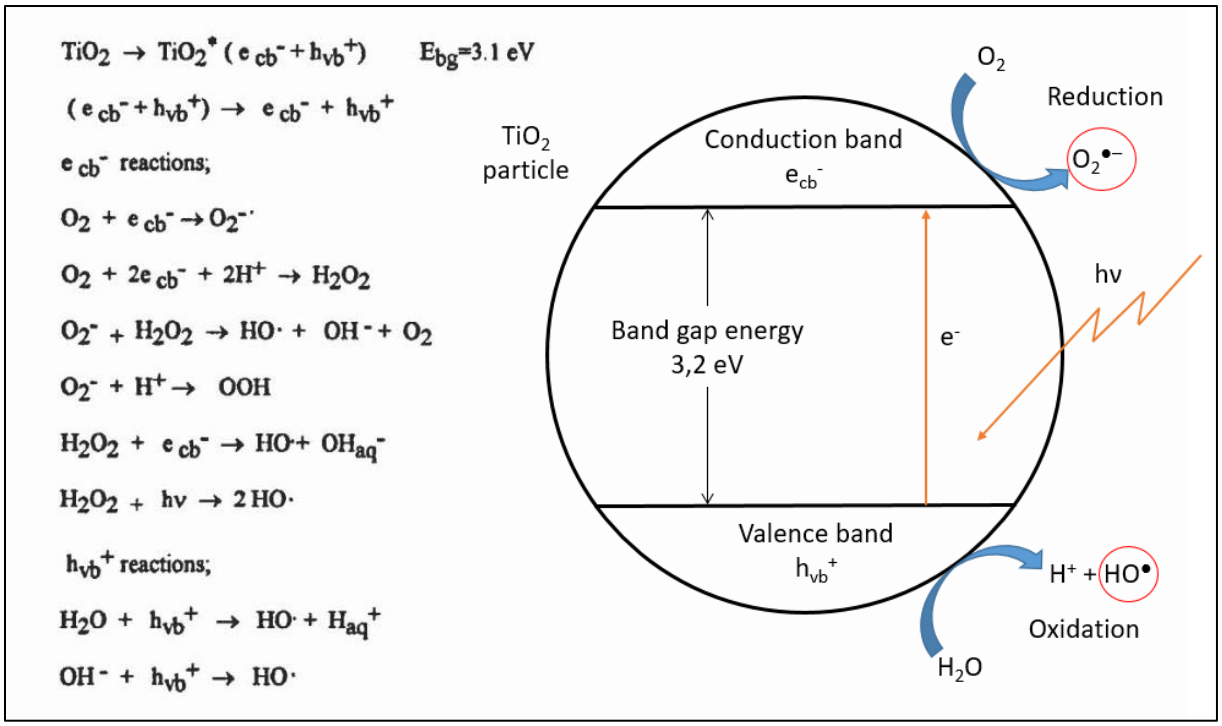

Figure 11. Simplified mechanism for reactions occurring in the presence of a photocatalyst extracted from Bekbölet et al. [125].

TiO_2 is one of the oldest and most commonly used photocatalysts, due to its high photocatalytic activity, commercial availability and low cost, but many other semiconductors such as ZnO, ZnS, WO_3, $SrTiO_3$ have been proven to be effective in water treatment applications [126,127]. The relative importance of the surface reactions in the whole treatment process strongly depends on the strength of the interactions between the catalyst and the pollutant and physical adsorption was found to greatly promote surface degradation of pollutants. This process was found to be of particular importance for NOM in acidic conditions where carboxylic groups have been noted to be rapidly adsorbed onto TiO_2 [128,129]. *Huang et al.* observed that for a solution of NOM 10 mg/L, about 80% of NOM was adsorbed on the catalyst when this was added at the concentration of 0.3 g/L or more (figure 12a). When UV lamps were turned on, TOC removal efficiency was found to be dependent on TiO_2 concentration and about 80% of TOC was removed with a TiO_2 dose of 2 g/L (figure 12b). They concluded that hydrophobic, high-MW NOM is preferably adsorbed onto TiO_2 surface, and more hydrophilic intermediate oxidation products having lower MW are then released; as a consequence, the application of photocatalytic treatment before membrane filtration, was found to significantly reduce membrane fouling [128].

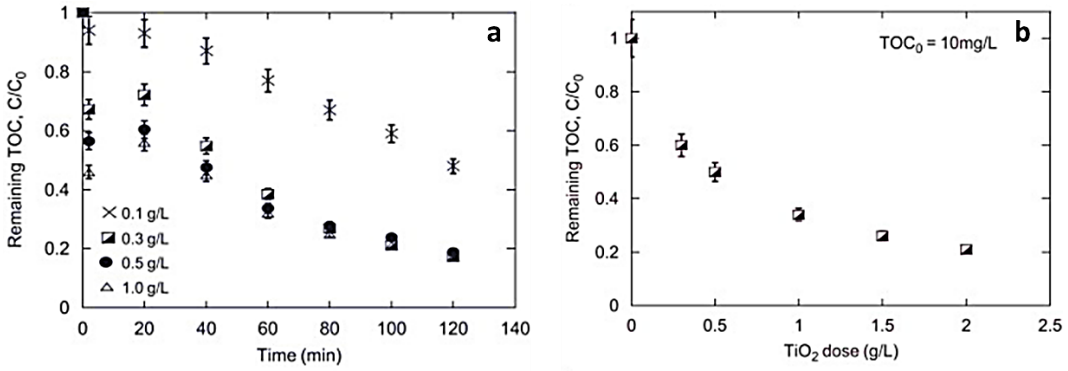

Figure 12. NOM adsorption on TiO_2 at different catalyst concentrations (a); NOM removal in photocatalytic treatment using different TiO_2 concentrations extracted from Huang et al. [128].

Another interesting and highly innovative approach to water depollution is *homogeneous photocatalysis* where heterogeneous catalysts are replaced by light-absorbing organic compounds, or organo-metal complexes, in solution. In contrast with heterogeneous photocatalysts that typically work best under UV light, the photocatalysts typically used in homogeneous photocatalysis absorb light in the visible range therefore introducing a series of advantages such as the possibility to use solar light and the fact that visible radiation is safer to use and cheaper to produce. Another interesting difference is that, while the other treatments generally rely on pollutants oxidation, homogeneous photocatalysis can be used to selectively reduce water contaminants. To do so, a suitable photocatalyst P, irradiated at the proper wavelength, gets excited to its singlet and triplet states from where it can react with an electron donor to form the radical anion $P^{\bullet-}$ than, in turn, reacts with a pollutant R via electron transfer to form the corresponding radical anion $R^{\bullet-}$. The reduced form of the pollutant can then undergo different degradation pathways according to its molecular structure and to the reaction with surrounding chemicals. Such mechanism has recently been used by *Martinez-Haya et al.* to perform the selective reductive dehalogenation of brominated compounds using riboflavin as photocatalyst and amines as electron donors and the reaction mechanism is shown in figure 12 [130].

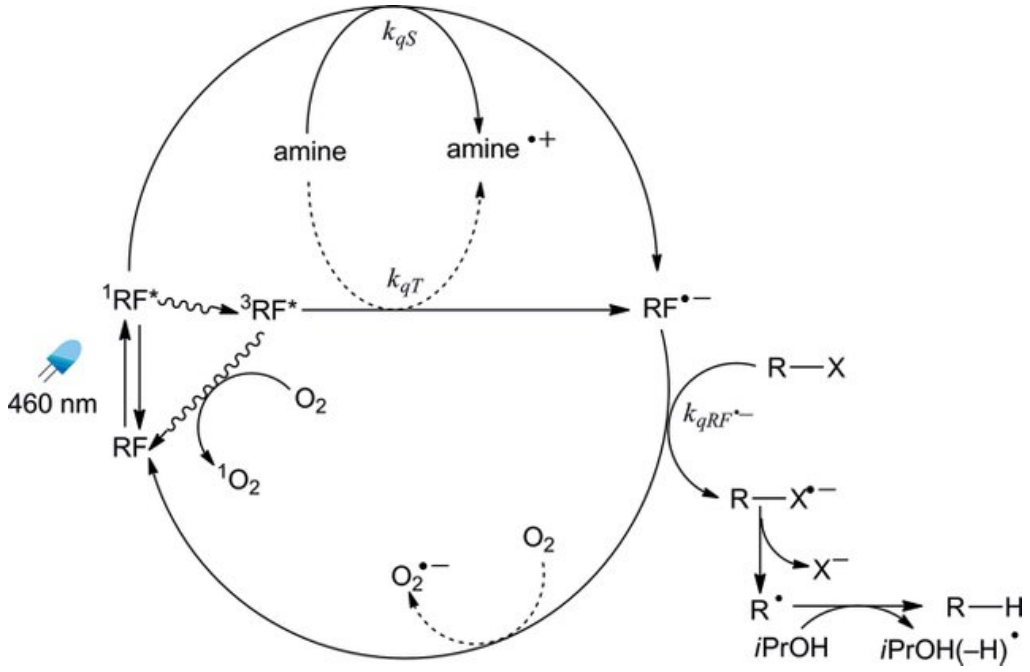

Figure 12. Reaction mechanism for the selective debromination of benzyl bromide and α-bromoacetophenone (indicated as R-X) in the presence of riboflavin (RF) used as photocatalyst, and isopropanol (iPrOH) used as proton donor. Extracted from Martinez-Haya et al. [130].

Plasma based AOPs

The application of plasma technology to water treatment processes is considered as a non-conventional AOP. However, plasma-initiated reactions lead to the simultaneous formation of highly reactive species such as high-energy electrons, H_2O_2, $HO^\bullet$ and O_3, in analogy with the other AOPs. Non-thermal plasmas such as streamer or corona discharges, are particularly interesting for water treatment applications because of the small energy input required. In general, a high-voltage pulsed generator is connected to two or multiples electrodes in order to generate an electrical discharge in contact with water. The production of high-energy electrons in the discharge, and their interaction with water or molecular oxygen, can lead to the production of $HO^\bullet$ and O_3, respectively (reactions 17 and 18).

$$e^- + H_2O \rightarrow e^- + HO^\bullet + H^\bullet \quad (17)$$

$$e^- + 3O_2 \rightarrow e^- + 2O_3 \quad (18)$$

At the same time, a series of physical phenomena such as UV light emission, shockwave generation and electrohydraulic cavitation can take place. This mix of physical and chemical effects often makes plasma processes effective even for those particularly refractory CECs, such as perfluoroalkyl compounds (PFAS), that are poorly destroyed by conventional AOPs [131–133]. Despite the large

amount of information available on water plasma for CECs removal, very few studies have focused on NOM transformation and removal in such processes. *Panorel et al.* observed that upon nebulization of a solution of HAs over pulsed corona discharges (figure 13a), effective HAs oxidation was achieved with consistent reduction of energy consumption compared to ozonation. As already seen for other AOPs, TOC removal rate was found to depend on NOM initial concentration but it was generally slower than the water discoloration rate (figure 13b) [134].

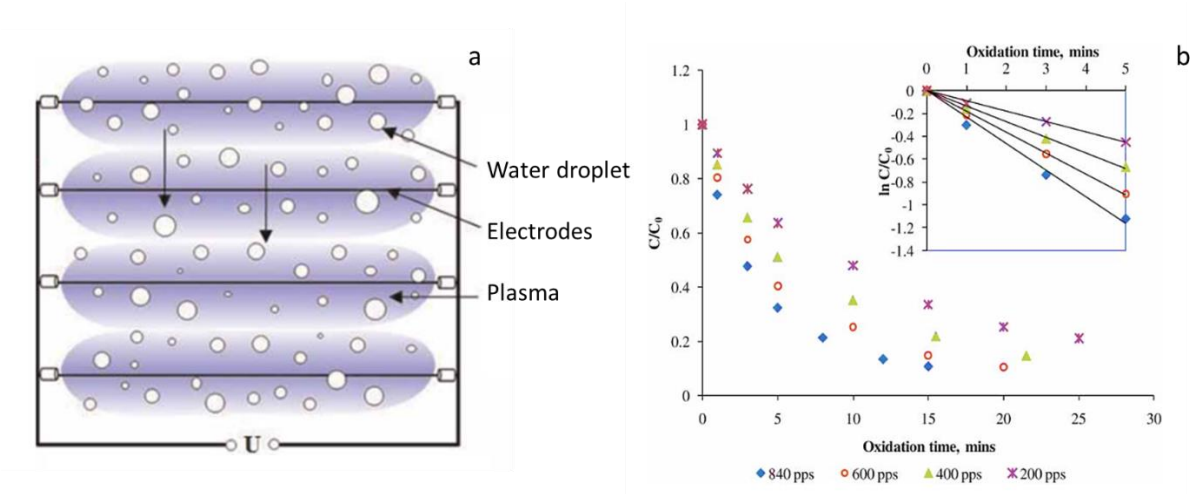

Figure 13. Plasma reactor utilized for NOM removal by Panorel et al. (a), and, NOM removal at different discharge pulse frequencies (b). Extracted from Panorel et al. [134].

1.4. NOM CHARACTERIZATION

Different characterization approaches can be followed to collect information on DOM chemical composition and MW, but the measure of optical properties, such as UV-Vis absorbance and fluorescence emission, is probably the most utilized. The obvious requirement for the application of this approach is that DOM must absorb light in the UV-visible range. This approach is therefore limited to the study of chromophoric or **colored dissolved organic matter (CDOM)** [99,100,135,136]. Since non-colored organic matter typically plays a secondary role in the photochemical processes occurring in natural waters, we will focus our attention on the study of CDOM.

UV-Visible parameters

UV-visible absorption spectra of CDOM do not have characteristic maxima and the absorbance is typically increasing approximately exponentially with decreasing wavelength [137]. To extract

information about CDOM composition and structure from these spectra, several spectral parameters have been defined:

- **E_2/E_3** is the ratio of the absorbance at 250 nm to the absorbance at 365 nm and it is typically used to track changes in the **relative size of CDOM** [136]. In fact, CDOM fractions having higher MW exhibit stronger absorption at longer wavelengths due to the presence of larger conjugated systems; consequently, E_2/E_3 increases as average CDOM MW decreases.
- **E_4/E_6** is the ratio of the absorbance at 465 nm to the absorbance at 665 nm. Similarly to E_2/E_3, E_4/E_6 is also dependent on the MW, but it has been observed to better correlate with the atomic ratios O/C and C/N, the content of carboxylic functions and total acidity of CDOM; it is therefore commonly used to estimate the **degree of humification** of the OM [136,138]. In case the absorbance at 665 nm is too little to be used, the absorbance at 254 nm or at 280 nm have alternatively been used as an indicator of humification and aromaticity [139,140].
- **$SUVA_{254}$** is defined as the absorbance at 254 nm (in m^{-1}) divided by the TOC measured in mg/L and it is commonly used to estimate **CDOM aromaticity** [141]. The most accurate measurement of NOM aromaticity is provided by ^{13}C NMR spectroscopy, but this method requires expensive and sophisticated instrumentation. However, it has been observed that a strong correlation exists between NMR data and $SUVA_{254}$ values (figure 15) making this latter a reliable, fast and cheap alternative to determine NOM aromaticity [140].

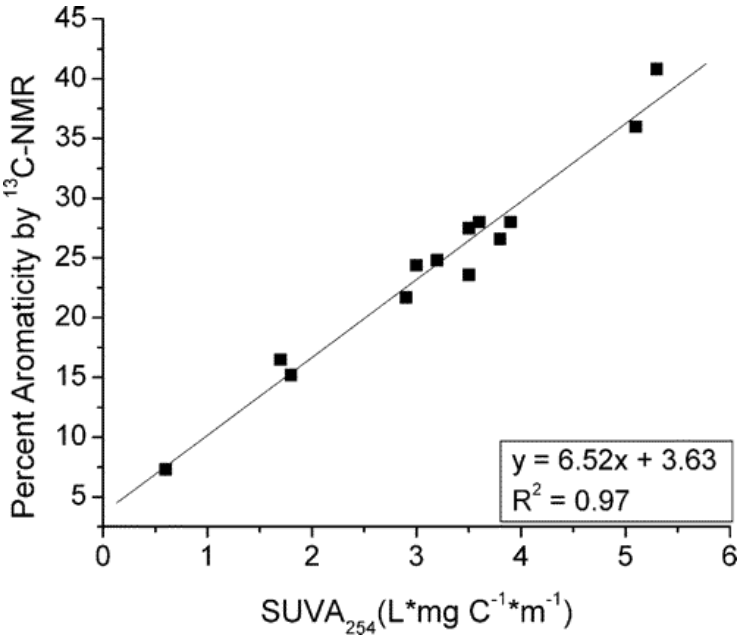

Figure 14. Correlation between $SUVA_{254}$ values and percent aromaticity of DOM determined by ^{13}C NMR extracted from Weishaar et al [140].

CDOM fluorescence

NOM is typically fluorescent regardless of its origin and age, and the characteristics of its fluorescence emission primarily depend on NOM molecular structure. External factors such as temperature, pH, concentration of metal ions and presence of other solutes, can also influence the fluorescence emission in terms of intensity and quantum yield but these are in general minor modifications. Fluorescence spectroscopy represents one of the most powerful tools to obtain information about the origin and composition of both soil and aquatic organic matter. The most common measures of CDOM fluorescence are:

- **Excitation Emission Matrices (EEMs):** EEMs are a 3D representation of CDOM fluorescence emission obtained by moving the excitation wavelength by fixed increments (typically 5 or 10 nm) and by scanning, for each λ_{Ex}, all emission wavelengths obtaining distinctive NOM fluorescence fingerprints. Two main types of CDOM fluorescence signals were initially distinguished: the humic-like signal and the protein-like one. However, over the course of the years, a more precise identification of the diverse CDOM chromophores has been proposed by several authors and other distinctive NOM chromophores have been identified, even though their exact nature remains unknown; a common classification of CDOM fluorescence signals is reported in table 4 [142,143].

Table 3. Main NOM fluorophores and their corresponding names according to different authors.

Ex_{max} (nm)	Em_{max} (nm)	Component type	Coble **(1996)** [143]	Parlanti et al. **(2000)** [142]
330-350	420–480	Humic and fulvic-like	C	α
230-260	380-480	Humic and fulvic-like	A	α'
310-320	380-420	Autochthonous production	M	β
270-280	300-320	Tyrosine-like, protein-like	B	γ
270-280	320-350	Tryptophane-like, protein-like or phenol-like	T	δ

An example of fluorescence EEM containing humic and fulvic-like fluorophores for a riverine water is shown in figure 16. Fluorescence emissions of HAs and FAs normally fall within very

similar ranges in terms of both excitation and emission wavelength and are therefore difficult to differentiate. The protein-like fluorescence is instead easily recognizable as it appears at shorter excitation and emission wavelength; it arises from the fluorescence of aromatic amino acids, either as free molecules or as protein constituents, and is commonly divided into a tyrosine-like signal at 300-320 nm, and a tryptophan-like signal at 320-350 nm (Ex at 220 and 275 nm for both fractions) [144]. The study of EEMs is therefore a powerful tool to obtain information about the chemical composition and origin of CDOM.

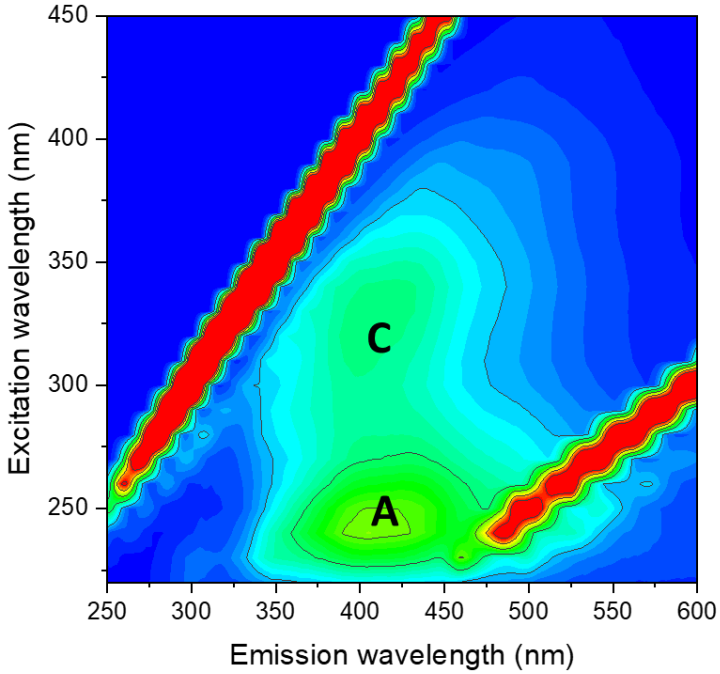

Figure 15. Typical humic and fulvic-like fluorescence signals measured for a sample of riverine water.

In recent years, the development of mathematical algorithms for the deconvolution of EEMs allowed to extract much more information from fluorescence matrices than the one obtainable by simple visual interpretation. Such algorithms allow in fact to identify single fluorescent components and to keep track of their evolution as NOM undergoes chemical transformation [145]. The parallel factor analysis (PARAFAC) algorithm is probably the most used one and it has been widely applied to keep track of the changes in NOM in the aquatic environment. This led to the creation of libraries of fluorescence data such as OpenFluor that contains over 500 published PARAFAC individual components corresponding to recurring fluorophores previously reported in the literature [146].

- **Fluorescence index (FI)** is an indicator of relative contribution of aquatic and terrestrial CDOM proposed by *McKnight et al.* in 2001. It is obtained by dividing the emission intensity at 450 nm by that at 500 nm with excitation at 370 nm. In the original study, FI values of ≈1.9 were assigned to autochthonous fulvic acids (mainly of microbial origin) while lower values of ≈1.4 were assigned to fulvic acids of terrestrial origin [147]. However, considering the variety in NOM chemical composition and the resulting fluorescence signals, it is complicated to use *FI* to undoubtedly determine the predominant source of CDOM.

- **Humification index (HIX)** was introduced in 1999 by *Zsolnay et al.* who proposed the use of HIX for the estimate the degree of humification of SOM but it has been later extensively used for the study of CDOM samples as well [59,148]. HIX is calculated as the ratio H/L of two areas underlying the fluorescence emission spectrum obtained with λ_{EX}=254 nm. The H region goes from 435 nm to 480 nm and the L region goes from 300 nm to 345 nm. *Huguet et al.* measured HIX values for a series of riverine and seawater samples and observed that high HIX values (between 10 and 16) corresponded to strongly humified organic material mainly of terrestrial origin, whereas low values (<4) were associated with autochthonous OM [149].

- **Biological Index (BIX)** is a newer parameter introduced by *Huguet et al.* in 2009 to determine with better accuracy the presence of the β (or M depending on the authors) fluorophore, typical of autochthonous DOM and therefore to use it as an indicator of biological activity in natural waters. BIX is obtained by dividing the emission intensity at 380 nm to that at 430 nm with λ_{EX}=310 nm. The authors observed that values of BIX>1 corresponded to DOM of mainly autochthonous origin while lower values of BIX (0.6–0.7) indicated the presence of NOM freshly released from soils [149].

Other techniques

- **Nuclear Magnetic Resonance (NMR) spectroscopy:** ^{13}C and ^{1}H NMR spectroscopies, and in particular solid-state NMR spectroscopy, have been intensively used for the study of NOM of terrestrial and aquatic origin and still represents some of the most accurate analytical techniques to determine NOM composition. Some of the advantages of this technique are the

absence of solvent effect and the possibility to analyze highly insoluble fractions such as humin [150–152].

- **High-resolution Mass Spectrometry (HRMS):** High-resolution mass spectrometry is another powerful tool commonly used for the study of NOM [153]. Fourier Transform Ion Cyclotron Resonance Mass Spectrometer (FTICR-MS) represents, among mass spectrometers, the one with the highest resolution available and it makes possible the identification of single NOM fragments therefore helping to better understand complex DOM mixtures across aquatic systems; despite its lower resolution, orbitrap-MS has proven to be a valid alternative to FTICR-MS [154–156]. To facilitate the interpretation of the huge amount of data produced by HRMS analysis, graphical representation of data is often adopted. Van Krevelen diagrams, for example, are obtained by plotting the occurrence frequency versus the elemental ratios H/C and O/C and allow to identify different classes of NOM constituents such, e.g., proteins, cellulose, condensed hydrocarbons, lignin and lipids [157,158].

- **Size Exclusion Chromatography (SEC):** Size exclusion chromatography coupled with high performance liquid chromatography (SEC-HPLC) is a widely used analytical technique to fractionate NOM according to its MW. The idea behind SEC chromatography is that smaller molecules have stronger interactions with the column stationary phase and are therefore eluted at higher elution volumes (Ve) while bigger molecules, that are excluded by the pores of the stationary phase to a bigger extent, are eluted sooner. The coupling of SEC-HPLC with multi-wavelength absorbance (PDA) and fluorescence detectors allows the simultaneous evaluation of NOM MWs and fluorophores distribution [159].

1.5. Photo-reactivity of natural waters

The photochemical processes occurring in irradiated surface waters can be divided into two main groups: the direct photochemical processes and the indirect ones. To the first group belong the **direct photolysis** reactions, however, as the UV light typically responsible for the photolysis of organic compounds only represents a limited portion of the solar spectrum, this pathway is commonly activated only for the most photo-labile compounds. As a result, most part of CECs, and their transformation products, are not photolyzed in the environment at a significant rate. The second group of photochemical processes is governed by the **photo-sensitized reactions** where the absorption of a photon in the UV or visible light by a chromophore can promote the formation of reactive species or energy transfer process, capable of inducing the transformation of water contaminants. The efficiency of such reactions depends on the number of reactive species produced by excitation of the chromophores as well as on the ability of these species to react with the contaminant. DOM represents the largest source of chromophores in natural water and is therefore the protagonist of photo-sensitized processes occurring in the environment. A schematic representation of direct and indirect photochemical transformations occurring in natural waters is shown in figure 16.

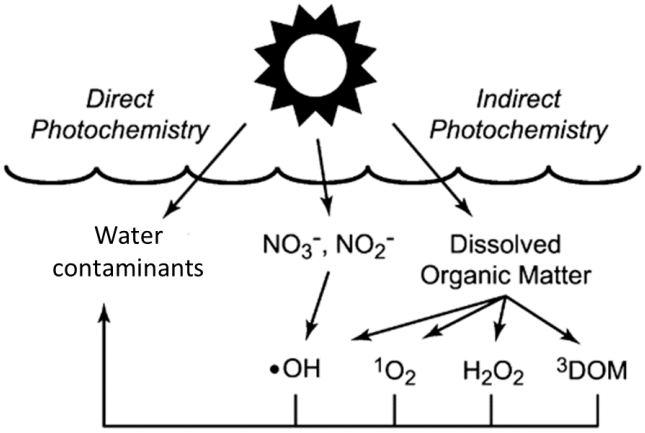

Figure 16. Photochemical processes of surface waters extracted from William and McNeill [160].

The rate of CDOM-driven transformation reactions occurring in a surface water depends in the first place on the amount of solar radiation absorbed by CDOM itself and therefore, on CDOM nature and concentration, as well as on weather conditions and geographical location. Higher concentrations of CDOM obviously lead to higher absorption of solar light at the top layer of water, however, it also results in a shorter penetration of light in the water column. Furthermore, as CDOM acts both as a

producer and a scavenger of reactive species, a universally valid correlation between CDOM concentration and water reactivity cannot be drawn.

Light absorption by NOM is associated with the presence of a delocalized electron systems. Hence, NOM chromophores are typically formed by aromatic rings and conjugated double bonds and the heterogeneous nature of CDOM results in great heterogeneity of chromophores; as a result, CDOM typically exhibits continuous absorption spectra in the range 200-600 nm having a nearly exponential shape and a shoulder in the 250-300 nm region. Above about 290 nm, the spectra can be reasonably fit using a single exponential function of the form:

$$a(\lambda)=a(\lambda_0)exp^{-S(\lambda-\lambda 0)} \qquad \text{Eq. 2}$$

where a is the absorption coefficient, λ the wavelength, λ_0 a reference wavelength and S is the spectral slope [161]. The typical absorption spectrum for a riverine water (water sample was taken in July 2018 in the Allier River, central France, 1cm optical path) is reported in figure 18 together with the standard spectrum of solar irradiance at the sea level.

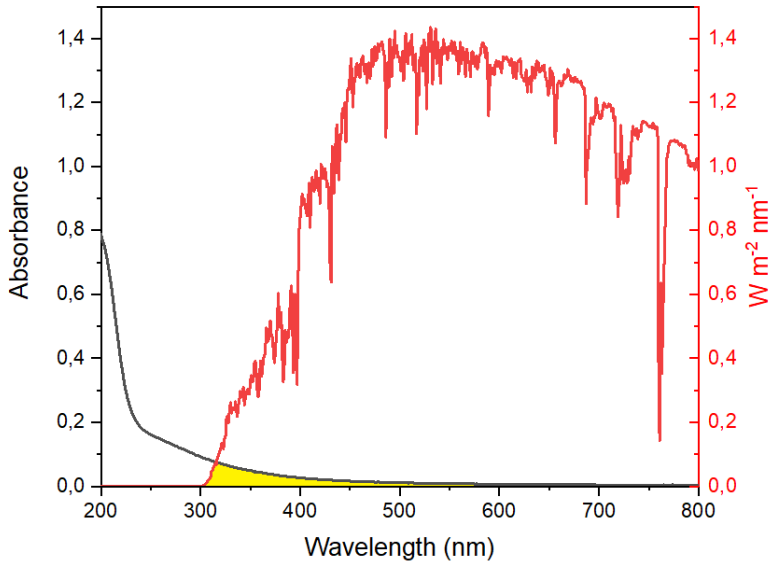

Figure 17. Absorption spectrum of a water sample of Allier River (black) and solar irradiance at the sea level (red). The fraction of the solar spectrum absorbed by CDOM is highlighted in yellow.

1.5.1. Formation of reactive species

Absorption of UV and visible light by CDOM can lead to the production of reactive species (RS) including, singlet oxygen ($^1O_2$), excited triplet states (^{3}CDOM*), superoxide radical anion ($O_2^{\bullet-}$), the hydroxyl radical ($HO^\bullet$), and hydrogen peroxide (H_2O_2). These RS can react with water pollutants present in natural waters and promote their degradation but, at the same time, can react with DOM itself contributing to its natural transformation. A schematic representation of the processes occurring in irradiated surface waters in the presence of CDOM, proposed by *Richard et Canonica,* is shown in figure 19 [162].

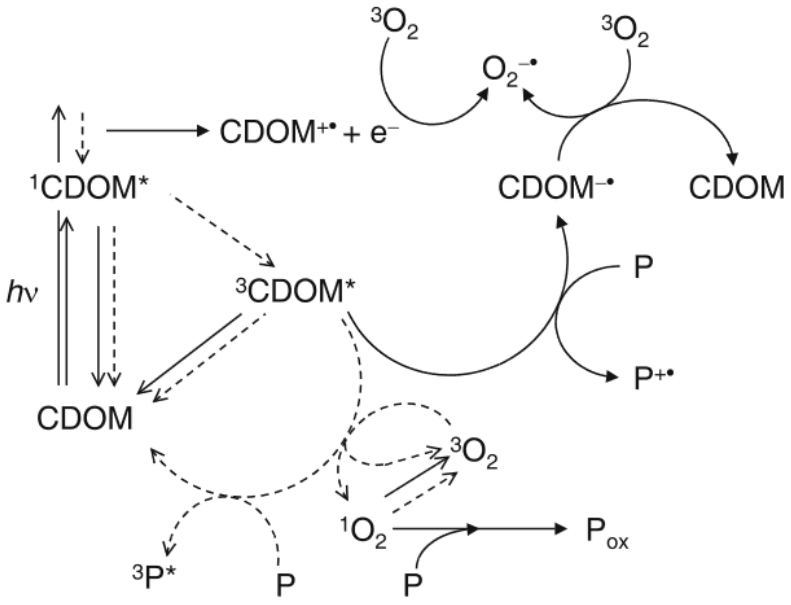

Figure 18. Major photochemical processes of coloured dissolved natural organic matter (CDOM) that may lead to the transformation of organic contaminants (P), extracted from Richard et Canonica [162].

Excited triplet states (^{3}CDOM*)

The absorption of a photon by CDOM leads, in the first place, to the formation of singlet excited states of OM (^{1}CDOM*) but, the lifetime of these intermediates is so short (in the order of nanoseconds or less) that their direct involvement in photochemical processes is usually negligible. ^{1}CDOM* , in fact, undergoes rapid deactivation via radiative processes or intersystem crossing: the first pathway is responsible of fluorescence emissions while, the second, leads to the formation of triplet excited states

^{3}CDOM* whose lifetime is typically over 1000 times longer than their singlet counterpart. They can therefore undergo several types of reactions with organic water contaminants, or oxygen, such as triplet-triplet energy transfer or redox reactions. The deactivation of ^{3}CDOM* leads to the formation of a triplet excited state of the pollutants, while, in the second scenario, ^{3}CDOM* gets reduced by abstracting one electron from the pollutant to form $CDOM^{-\bullet}$ and the corresponding oxidized pollutant $P^{+\bullet}$. This second reaction pathway is considered to be the main responsible for the transformation of electron-rich phenols [163]. For this reason, the degradation rate of 2,4,6-trimethylphenol (TMP), irradiated in presence of DOM, is commonly used to assess the formation of ^{3}CDOM*. The molecular structure of TMP is shown in figure 19. Typical steady-state concentrations of ^{3}CDOM* in irradiated natural waters lie in the range 10^{-14} -10^{-12} M [164].

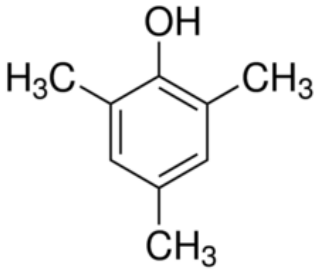

Figure 19. Molecular structure of 2,4,6-trimethylphenol.

Singlet oxygen ($^1O_2$)

Singlet oxygen is produced by reaction of ^{3}CDOM* with the dissolved oxygen typically present under common environmental conditions. Molecular oxygen has in fact the peculiarity to have an electron configuration of triplet when at the ground state and therefore efficiently reacts with ^{3}DOM* generating oxygen in an excited singlet state (reaction 19).

$$\underset{\text{excited state}}{^3\text{CDOM}^*} + \underset{\text{ground state}}{O_2\,(^3\Sigma_g)} \longrightarrow \underset{\text{ground state}}{\text{CDOM}} + \underset{\text{excited state}}{^1O_2\,(^1\Delta_g)} \qquad (19)$$

Since the concentration of dissolved oxygen in the surface layer of natural water bodies (5-12 mg/L) is normally higher than that of other chemicals acting as triplet-energy acceptors, the reaction with O_2 is the main deactivation pathway for ^{3}CDOM*. A kinetic scheme illustrating the connection between ^{3}DOM* and $^1O_2$ is shown in figure 20.

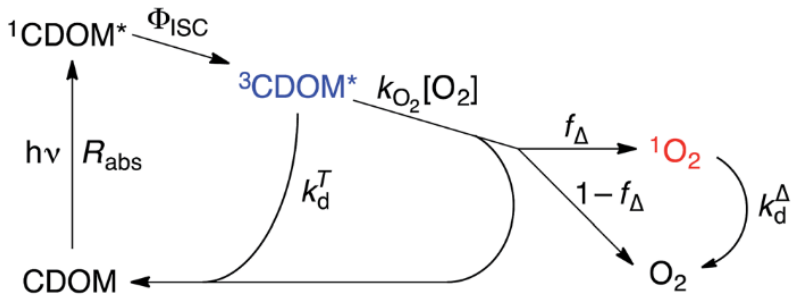

Figure 20. Kinetic scheme illustrating the connection between ^{3}DOM and $^1O_2$ published by McNeil and Canonica [164].*

Although direct measurement of $^1O_2$ is achievable using Laser Flash Photolysis measurements, its stationary-state concentrations are typically measured using probe compounds, the most used one being furfuryl alcohol, whose structure is reported in figure 21 (FFA).

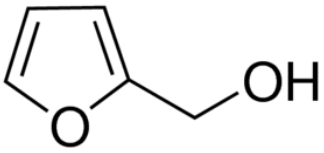

Figure 21.Molecular structure of furfuryl alcohol.

Hydroxyl Radical

Despite its prominent role in AOPs, HO• is considered a minor oxidant in the great majority of surface waters due to low formation rates and its efficient scavenging by DOM itself, bicarbonate, and carbonate anions (reactions 4 and 5) [165]. In most surface waters, DOM is at the same time the main source (reactions 22 and 23) and the main sink of HO• (reactions 1-3).

$$DOM + h\nu \rightarrow DOM^* \quad (22)$$

$$DOM^* + H_2O \rightarrow DOM\text{-}H^\bullet + HO^\bullet \quad (23)$$

However, when high concentrations of nitrate ions are present and the ratio NO_3^-/DOM is higher than 3.3×10^{-5} (mol NO_3^-)(mg C)$^{-1}$, nitrate would prevail over DOM as HO• source (reaction 24) [18]. In this scenario, substantial photo-transformation of DOM, i.e. photo-mineralization and photo-nitration, can occur as a consequence of the high HO• production rate [18].

$$NO_3^- + H_2O + h\nu\ (\leq 340\ nm) \rightarrow NO_2^\bullet + HO^- + HO^\bullet \quad (24)$$

Typical steady-state concentrations of $HO^{\bullet}$ in irradiated surface waters lie in the range 10^{-17} M to 10^{-15} M.

Carbonate radical

Carbonate radicals are mainly produced by the reaction of $HO^{\bullet}$ with carbonate and bicarbonate anions naturally present in water.

$$HO^{\bullet} + HCO_3^- \rightarrow H_2O + CO_3^{\bullet-} \qquad k_4=1.5\times10^7\ M^{-1}s^{-1} \qquad (4)$$

$$HO^{\bullet} + CO_3^{2-} \rightarrow OH^- + CO_3^{\bullet-} \qquad k_5.2\times10^8\ M^{-1}s^{-1} \qquad (5)$$

The carbonate radical, with a redox potential of 2.1 V (slightly higher than the one of ozone), is potentially a very good oxidant, however, the kinetic constants of reaction with the vast majority of water contaminants are so low that their contribution in pollutants transformation is generally negligible. Furthermore, as carbonate radicals are efficient scavengers of $HO^{\bullet}$, high concentrations of carbonate and bicarbonate anions have an overall negative effect on the photo-oxidizing properties of natural waters [18,162]. In analogy with $HO^{\bullet}$, the main sink of carbonate radicals is once more the reaction with DOM but, due to their lower reactivity, stationary-state concentration of $CO_3^{\bullet-}$ is typically about two orders of magnitude higher than the one of $HO^{\bullet}$ [166].

Superoxide Radical Anion and hydrogen peroxide

The formation of hydrogen peroxide in irradiated waters samples containing NOM is a well-known phenomenon since the 1960s, however, the mechanism of H_2O_2 formation has not been fully elucidated. A two-steps mechanism involving the one-electron reduction of O_2 by ^{3}CDOM* to produce superoxide (O_2^-) followed by the dismutation of O_2^- to form H_2O_2 has been proposed (reactions 21, 25, 26) [19].

$$^3CDOM^* + O_2 \rightarrow CDOM + {}^1O_2 \qquad (21)$$

$$CDOM + {}^1O_2 \rightarrow CDOM^{\bullet+} + O_2^{\bullet-} \qquad (25)$$

$$O_2^{\bullet-} + 2H^+ \rightarrow 2H_2O_2 + O_2 \qquad (26)$$

Hydrogen peroxide plays an important role in natural water reactivity as it contributes to the formation of $HO^{\bullet}$ in two different ways: in presence of solar light, H_20_2 undergoes in fact direct photolysis (reaction 6), while, in dark conditions, it can react with iron(II) according to the Fenton reaction (reaction 27) [167].

$$Fe^{2+} + H_2O_2 \rightarrow Fe^{3+} + HO^{\bullet} + HO^- \qquad (27)$$

Moreover, H_20_2 can directly react with both water pollutants and naturally occurring water constituents therefore contributing to the transformation of NOM itself.

Materials and methods

2 Materials and Methods

2.1. Chemicals

Suwannee River NOM (2R101N) was purchased from International Humic Substances Society (IHSS). The main chemicals used were: imidacloprid (PESTANAL, analytical standard), glyphosate (PESTANAL, analytical standard), PFOA (Perfluorooctanoic acid, analytical standard), PFHxA (perfluorohexanoic acid, analytical standard), PFOS, (Perfluorooctanesulfonic acid, solution 40% w/w), furfuryl alcohol (FFA, 98%), 2,4,6-trimethyphenol (TMP, certified reference material), terephthalic acid (purity 98%), 2,4-dinitrophenylhydrazine (DNPH, purity 97%). They were purchased from Sigma-Aldrich and were used without further purification.

Water was purified using a reverse osmosis RiOs 5 and Synergy (Millipore) device (resistivity 18 MΩ cm, DOC < 0.1 $mg \cdot L^{-1}$). All solvents or other reactants were of the highest grade available.

2.2. Water sampling and sample preparation

Water samples studied in Manuscript 1 and Manuscript 2 were collected in the aquifer of river Allier near the city of Brioude located about 70 km south of Clermont-Ferrand in France. Three types of water samples were collected: 1) riverine water samples from river Allier and its tributary river Vendage, 2) two samples of stagnant water B4 and B7 from the dead branch of river Allier and, 3) two samples of groundwater named PZ1 and PZ5. Three sampling campaigns were carried out during the year 2018 in the months of March, July, and October. In every campaign, water samples were taken to evaluate the temporal evolution of water parameters for each sampling site. The samples of riverine water and stagnant water were sampled by manually filling 1 liter Pyrex glass bottles around 20 cm below the water surface while groundwater was extracted using a pump equipped with polyethylene tubes from a depth varying between 8 and 11 m. Water temperature, pH and oxygen saturation were measured on site using a multiparameter probe. A more detailed description of the aquifer as well as the map of sampling sites location are provided in Manuscript 1.

After reaching the laboratory, water samples were vacuum filtered using 1.2 µm pore size mixed cellulose esters filters (RAWP, Merk Millipore) and then again using filters of the same type having

pore size of 0.45 µm. After filtering, all samples were put in clean Pyrex glass bottles, purged by nitrogen bubbling for 15 minutes, and stored in the fridge at 4°C until use.

2.3. Degradation techniques

2.3.1. Steady state irradiations

Steady state irradiations had a fundamental role in the development of this thesis. Three types of light sources were used according to the wavelength desired for each experiment:

1. For UVA irradiations, tubular lamps model Sylvania F15W/BL 368, 438 mm × 26 mm emitting between 300 and 450 nm with emission maximum at 365 nm were used. Six of these tubes were installed on the internal wall of a cylindrical stainless-steel irradiation device equipped with a fan to maintain the temperature into the reactor at 23±2°C. A cylindrical Pyrex glass reactor (14 mm internal diameter) containing the solutions to irradiate was placed at the center of the cylinder. A schematic representation of the setup is displayed in figure 22.

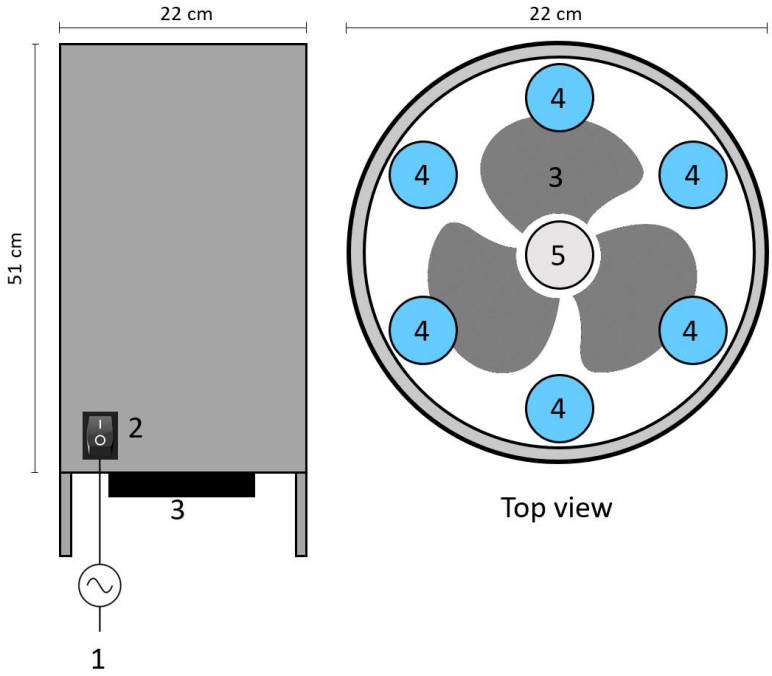

Figure 22. Irradiation setup used for UVA and UVC irradiations composed of: 1) power supply, 2) power switch, 3) fan, 4) lamp mounts, 5) Pyrex glass or quartz reactor.

In Manuscript 3 aqueous solutions of imidacloprid were irradiated in a big Pyrex glass flow reactor (0.65 L), allowing to continuously analyze the reactor headspace during irradiation. The gas inlet of the reactor was connected to O_2 and N_2 bottles and the flow of the two gases was controlled by two flow controllers (model Brooks 4800 Series) while the outlet was connected to an NO_X analyzer. A bypass also allowed to exclude the reactor from the flow line and therefore to accumulate volatile compounds in the headspace of the reactor. A schematic representation of the setup is displayed in figure 23.

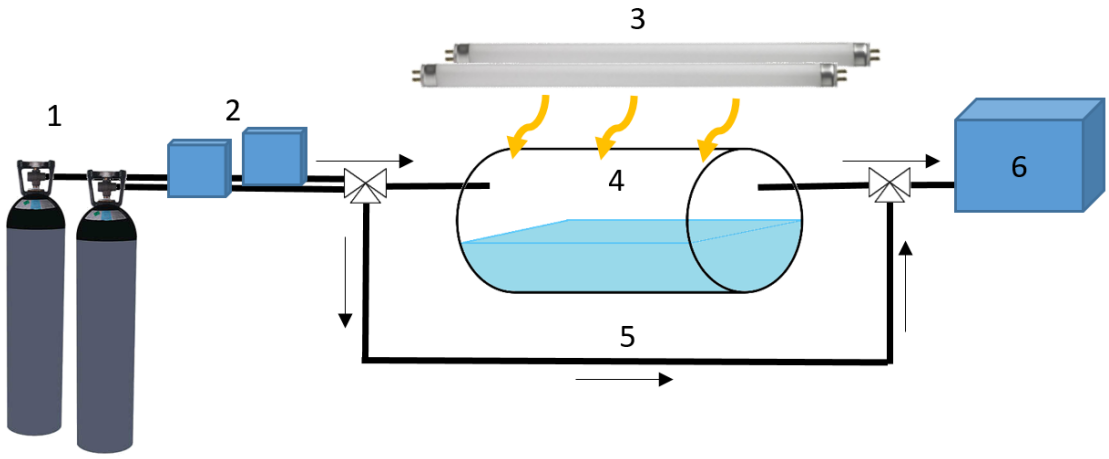

Figure 23. Irradiation setup for NO_X monitoring composed of: 1) O_2 and N_2 bottles, 2) O_2 and N_2 flow controllers, 3) UVA lamps, 4) Pyrex glass reactor, 5) bypass, 6) NO_X analyzer.

2. For UVC irradiations, tubular lamps model General Electric G15T8 (15W) with monochromatic emission at 253.7 nm were used. The same irradiation device displayed in figure 21 was used but, in this case, four tubes were installed. A cylindrical quartz reactor (20 mm internal diameter) containing the solutions to irradiate was placed at the center of the cylinder.

3. For the photo-reduction of imidacloprid, 288 mm 5W green LED tubes having a narrow emission band centered at 520 nm were used. 10 of these tubes were installed in a Luzchem Photoreactor model LZC-4V equipped with a rotating carousel allowing to homogeneously irradiate up to 16 tubes (16 mm of diameter) at the same time.

2.3.2. Plasma generator and water treatment setup

The plasma generator developed by Iris s.r.l. (European Patent n 14194376.1) consists of a custom-built Marx generator capable of generating high voltage discharges having peak voltage of 100-130 kV and peak current values of 20-40 A. The generator hardware includes a high-voltage transformer, four 990 pF capacitors and a pulse-width modulation circuit allowing the operator to select the frequency of the plasma discharge (5-17 Hz). The discharge was supported between two metal electrodes consisting in a stainless-steel bar (diameter 10 mm) on one side and a tungsten sintered electrode (diameter 3 mm) on the other side. A flow of compressed air was used to stabilize the generator's internal atmosphere making it less sensitive to fluctuations of air temperature and humidity.

Water samples were treated using two different reactors: a 20 mL cylindrical polypropylene (PP) reactor was initially used for the optimization of the generator working conditions, while, for pollutants abatement, a 50 mL Pyrex glass (PG) was used. We decided to switch to the PG reactor because of a problem of TOC contamination caused by the PP reactor. For both reactors, the same electrodes were used. A more detailed description of both the plasma generator and the experimental setup are provided in Manuscript 4.

2.4. Spectroscopic techniques

UV-Visible absorbance of solutions was measured using a Varian Cary 3 UV-Visible spectrophotometer and a 1 cm quartz cell. For natural water samples however, since their absorbance was generally low, the measurement was performed using a 5 cm optical path quartz cell. Purified water was used as a reference.

Fluorescence spectra and 3D excitation-emission fluorescence matrices (EEMs) were recorded on a Perkin Elmer LS-55 luminescence spectrophotometer with excitation and emission slits set at 10 nm. For the recording of EEMs, excitation wavelength was increased from 220 nm to 450 nm with 10 nm increments and, for every excitation wavelength, the fluorescence emission was recorded from 250 nm to 600 nm. The deconvolution of the three-dimensional spectra by the parallel factor analysis (PARAFAC) approach was done using the multi-way PARAFAC model and the DOMFluor toolbox (ver. 1.7) for MATLAB (R14-6.5). These decompositions were performed by the team of Edith Parlanti (EPOC laboratory, Université de Bordeaux) in the framework of a collaboration.

2.5. Chromatographic techniques

HPLC-UV, HPLC-FLD

Liquid chromatography separations were performed on a Water Alliance 2695 equipped with a column oven maintained at 30°C, a UV-visible diode array detector model Waters 2998 and a fluorescence detector model Waters 2475. The column was a Nucleodur C8ec 4.6×150 mm.

UHPLC-HRMS

Liquid chromatography-mass spectrometry analyses were performed using a high resolution Thermo Scientific Orbitrap Q-Exactive spectrometer (HR-MS) with ESI ionization source coupled to an ultra-high performance liquid chromatograph (UHPLC) model Thermo Scientific Ultimate 3000 RSLC. The resolution of the instrument was 35000 and the ESI voltage was 3.2 kV for the positive mode and -3.0 kV for the negative one. The chromatographic separation was performed using a Phenomenex column model Kinetex EVO C18 (100 x 2.1mm; 1.7µm) maintained at 30°C and using acidified water (0.1% formic acid) and acetonitrile as mobile phase components; the used chromatographic gradient is reported in table 5. Injection volume was between 5 and 15 µL and solvent flow was set at 0.45 mL/min.

Table 4. Chromatographic gradient used for UHPLC-MS analyses.

Run time (min)	% H2O + 0.1% F.A.	% ACN + 0.1% F.A.
0	95	5
7.5	1	99
8.5	1	99
9	95	5
11	95	5

In some cases, the high resolving power of the orbitrap allows the identification of unknown compounds by providing their exact molecular formula. The molecular structure was often identified by calculating the number of double bonds using the equation 3:

$$DoU = \frac{2C+2+N-X-H}{2} \quad \text{Eq. 3}$$

where *DoU* is the Degree of Unsaturation, *C* is the number of carbon atoms, *N* is the number of nitrogen atoms, *X* is the number of halogens atoms (F, Cl, Br, I), and *H* is the number of hydrogen atoms contained in the molecular formula.

GC-MS

GC-MS analyses were performed using a Shimadzu GCMS-QP2010 SE gas chromatograph-mass spectrometer. Column type was a capillary column MEGA-5 MS (length 30 m, thickness 0.25 µM, diameter 0.25 mm) and column oven was heated from 60 °C to 300 °C with a temperature ramp of 10 °C/min; temperature was then maintained at 300 °C for 5 min. Masses were scanned in the range 50-600 m/z using a scan speed of 2000 amu/s.

IC

The ionic chromatography analyses performed on the plasma-treated water samples were performed using a Dionex DX 500 ion chromatograph equipped with an electrochemical suppression unit (ASRS 300 for anions and CERS 500 for cations), an ED40 detector; the injection volume was 100 µL. The separation column used for anions was a Dionex Ion Pac AS9-HC while a column model Dionex CS12A was used for cations. The mobile phases were a 9 mM K_2CO_3 water solution for anions and 20 mM methanesulfonic acid solution for cations. In both cases, the flow rate was set to 1 mL/min.

HPIC-MS

The ionic chromatography analyses of irradiated SRNOM samples were performed on a Thermo Fisher ICS6000 HPIC coupled with both a conductivity detector and a single quadrupole detector equipped with a ESI ionization source operating in negative mode with a -3 kV potential. Detection in full scan mode was performed in the range 10-500 m/z and in single ion detection mode (+/- 0.5 amu). The column was a Dionex IonPack AS11-HC-4µm (2x250 mm) with a 50 mm pre-column of the same type

and the mobile phase was an aqueous solution of KOH with a concentration gradient from 1 mM to 60 mM (table 6).

Table 5. Chromatographic gradient used for HPIC-MS analyses.

Run time (min)	[KOH] (mM)
0	1
5	1
25	30
31	60
35	60
35.1	1

2.6. Photochemical calculations

2.6.1. Actinometric methods

The intensity of the radiation reaching the irradiated solutions in the cylindrical irradiation device, equipped with UVA or UVC lamps, was calculated using two different actinometric methods.

For UVA lamps, the spectral distribution of the emission was measured using an Ocean Optics radiometer model QE65000 equipped with an optic fiber probe that was inserted directly inside the reactor. However, due the geometry of the device, an absolute irradiance value was impossible to be determined precisely in this way. For this reason, the rate of metamitron photo-deamination (reaction 28) was used to estimate the photonic flux accurately as recommended by Palm [168]. This reaction has in fact a well-known quantum yield of photolysis of $\phi = 0.022 \pm 0.002$ that has been reported to be independent on the wavelength in the range 270-376 nm, and has negligible dependence on both the pH and on the starting concentration of metamitron [169].

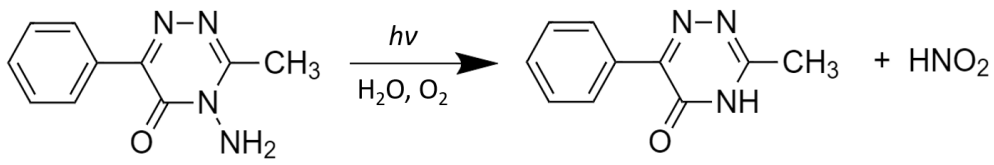

metamitron deaminometamitron (28)

A solution of metamitron 1.7×10^{-5} M, buffered at pH 6.7 using phosphate buffer 0.1 M, was irradiated for 4 minutes and its photolysis rate was 1.09×10^{-8} M/s. From this value we calculated that the total number of photons entering in the photoreactor in the range 280-380 nm corresponded to $I_0=2.1\times10^{16}$ Einstein/s.

For UVC lamps, I_0 was evaluated from the rate of glyphosate consumption in the presence of H_2O_2 in the device. In this case, considering the lamps narrow emission band at 253.7 nm, the use of spectrometer was not necessary. From the rate of glyphosate degradation that corresponded to R_{gly} = (9.3± 0.5) $\times10^{-8}$ min^{-1} we estimated that the total number of emitted photons corresponded to $I_0=2.9\times10^{6}$ Einstein/s. The calculation is reported in the supplementary material of Manuscript 5.

2.6.2. Measurement of triplet excited states (^{3}CDOM*)

2,4,6-Trimethylphenol is probably the most commonly used probe to quantify the formation of triplet excited states. From the rate of TMP degradation (R_{TMP}), the rate of *^{3}CDOM** formation was calculated by applying the relationship described in *equation 4*, where R_{a-DOM} is the rate of light absorption of the solution, Φ_T is the quantum yield of *^{3}CDOM** formation, k_1 (≈2×10^9 $M^{-1}s^{-1}$) is the bimolecular rate constant of reaction between ^{3}CDOM* and TMP leading to TMP transformation, k_d (5×10^5 s^{-1}) is the first order rate constant for the deactivation of ^{3}DOM* by the solvent and oxygen and $[TMP]_0$ (in this work $[TMP]_0$= 50 µM) is the initial concentration of TMP [170].

$$R_{TMP} = R_{a-DOM} \times \Phi_T \frac{k_1[TMP]_0}{k_d + k_1[TMP]_0} \quad \text{Eq. 4}$$

The rate of light absorption R_{a-DOM} was calculated using equation 5:

$$R_{a-DOM} = \Sigma I_0^{\lambda} \left(1 - 10^{-A(\lambda)}\right) \times \Delta\lambda \times 1000N^{-1} \quad \text{Eq. 5}$$

where I_0^{λ} is the amount of photons at λ reaching the solution in the interval λ ±2.5 nm (photons cm^{-3} nm^{-1} s^{-1}); $A(\lambda)$ is the averaged absorbance of the solution at λ ±2.5 nm (for the path length of the reactor used), N is the Avogadro number, and Δλ is the wavelength interval chosen at 5 nm.

R_{TMP} values were calculated by irradiating 10 mL of water sample for 30 min using the cylindrical irradiation device equipped with 6 UVA lamps at room temperature (21 ± 2 °C). TMP was added at the concentration of 50 µM and its concentration was monitored by HPLC-UV at time 0 (lamps off), 10, 20 and 30 min.

Eq. 4 supposes that all the triplet generated show the same absorption spectrum, the same quantum yield of formation and the same rate constant of reaction with TMP which might not be the case. Comparing the photosensitizing properties of different NOM solution can be also done on the basis of the rate of TMP photolysis, f_{TMP}, that is obtained using Eq. 6:

$$f_{TMP} = \frac{k_{TMP}}{R_{a-DOM}} \qquad \text{Eq. 6}$$

where k_{TMP} is the apparent first-order rate constant for TMP loss [170].

2.6.3. Measurement of singlet oxygen formation ($^1O_2$)

The rate of singlet oxygen formation was calculated using furfuryl alcohol (FFA) as a probing compound and monitoring the formation of its main transformation product (P) generated by reaction 29.

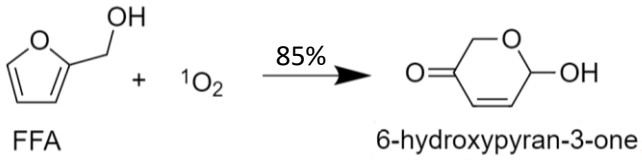

FFA 6-hydroxypyran-3-one (29)

In analogy with e*quation 3*, R_{a-DOM} is the rate of light absorption of the solution, Φ_{SO} is the quantum yield of $^1O_2$ formation, k_2 (1.2×10^8 M^{-1}s^{-1}) is the bimolecular rate constants of reaction between $^1O_2$ and FFA, k_d(2.5×10^5 s^{-1}) is the first order rate constant for the deactivation of $^1O_2$ with the solvent and $[FFA]_0$ (in this work $[FFA]_0$= 100 µM)is the initial concentration of furfuryl alcohol. The rate of FFA disappearance is equal to:

$$R_{FFA} = R_{a-DOM} \times \Phi_{SO} \frac{k_2[FFA]_0}{k_d + k_2[FFA]_0} \qquad \text{Eq. 7}$$

To improve the sensitivity of the measurements, we generally monitored the formation of 6-hydroxypyran-3-one (P). Its rate of formation is equal to:

$$R_P = 0.85 \times R_{FFA} \qquad \text{Eq. 8}$$

2.6.4. Other techniques

TOC

The organic carbon content of water samples was measured using a Shimadzu TOC-L Total Organic Carbon Analyzer equipped with a OCT-L 8 port auto-sampler. For inorganic carbon (IC) measurement, sample solution is automatically acidified with HCl in order to convert carbonate and bicarbonate anions into CO_2 that is then purged using clean compressed air from a gas bottle and measured in a NDIR detector. For total carbon content (TC), the sample solution is directly sent to a high temperature furnace (680°C) where, in presence of a platinum catalyst, both organic and inorganic carbon are converted to CO_2 that is measured in the same NDIR detector. The total organic carbon content (TOC) is therefore obtained by subtracting the concentration of IC from the concentration of TC measured independently. A scheme of the measurement steps performed by the machine is shown in figure 24.

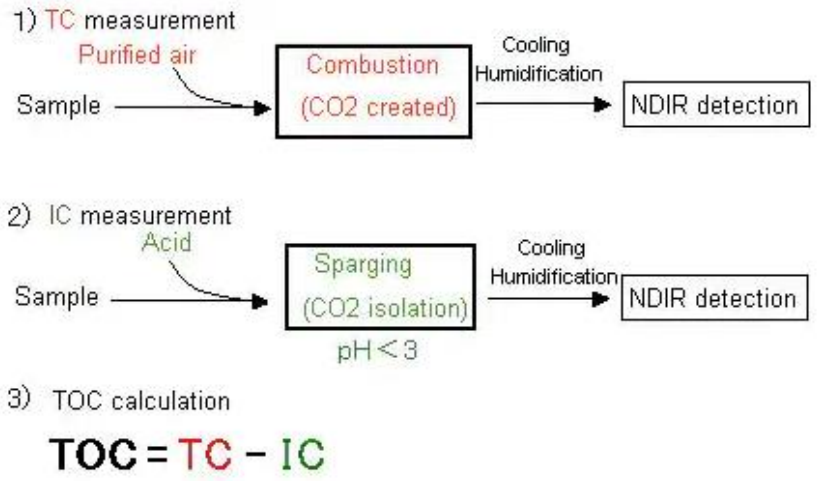

Figure 24. Analytical procedure for TC and IC measured extracted from www.shimadzu.com.

External calibration for total carbon was performed preparing standard solutions of potassium hydrogen phthalate (Naclai Tesque, Kyoto, Japan) in the range 1-15 mg/L of carbon. External calibration for inorganic carbon was performed preparing standard solutions of sodium carbonate and sodium hydrogen carbonate (Naclai Tesque, Kyoto, Japan) in the range 1-5 mg/L of carbon. Injection volume was typically 50 µL and reported results were the average value of at least two repetitions whose relative standard deviation was inferior to 2%.

NO_X and ozone measurement

Two different types of gas phase analysis setups have been developed during the course of this thesis; one of them was designed to measure the NO_X formation in the headspace of a cylindrical reactor used for the irradiation of imidacloprid solutions, while a second setup was installed at Iris s.r.l. to measure the formation of NO_X and ozone during plasma treatment of water samples.

In the first case a Thermo Scientific NO_X analyzer Model 42i was used while in the second case NO_X and O_3 formations were followed simultaneously using a Horiba APNA-370 Ambient NO_x Monitor and a Horiba APOA-360 Ambient Ozone Monitor, respectively.

From an analytical standpoint, the NO concentrations are measured by monitoring the chemiluminescence generated from the oxidation reaction of NO to NO_2 by reaction with ozone (produced internally in the NO_X detector). The measurement of NO_X (NO + NO_2) concentration is performed by preliminary reducing NO_2 to NO and then measuring again the chemiluminescence produced by the reaction with ozone, this time representative of both NO and NO_2 species. To do so, the volume of sampled air is split in two and while one part is directly sent to the ozone chamber, the other undergoes the additional step of reduction before being sent to the ozone chamber. The concentration of NO_2 is therefore obtained as the difference between the NO_X and NO concentrations measured independently.

Measurement of hydrogen peroxide, hydroperoxides and organic peroxides formation

H_2O_2, ROOH and ROOR species are commonly formed during the irradiation of NOM solutions and they are involved in the formation of hydroxyl radicals in irradiated solutions. The concentration of these species was determined according to the spectrofluorometric method described by Miller that uses the dimerization of the 4-hydroxyphenylacetic (HPAA) acid in the presence of horseradish peroxidase [171]. The resulting dimer is a highly fluorescent compound whose formation is directly proportional to the concentration of H_2O_2, ROOH and ROOR species present in solution (reaction 30).

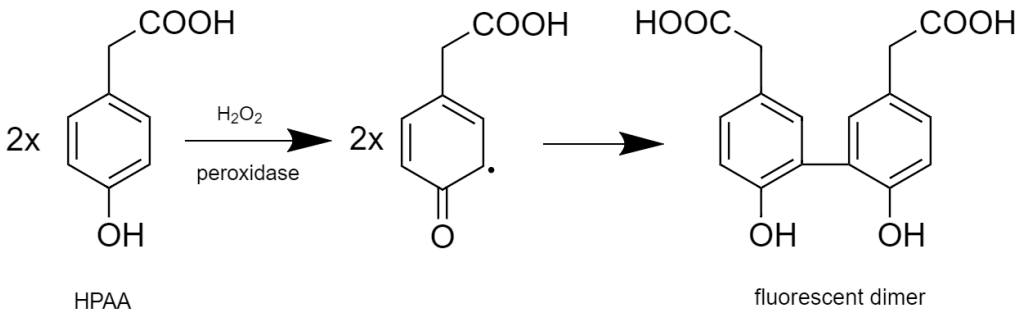

(30)

When the bovine enzyme catalase is added to the sample before the peroxidase, the fluorescence reading represents the contribution of ROOH and ROOR species alone. H_2O_2 concentration is therefore

determined as the difference of two fluorescence measurements performed with and without catalase.

The sample preparation requires three reagent solutions:

a) 0.894 g of Na_2HPO_4 were dissolved in a 50 mL flask with ultrapure water and 0.788 g of NaH_2PO_4 were dissolved in another 50 mL flask. Solution *a* was obtained mixing 40.5 mL of the Na_2HPO_4 solution with 9.5 mL of the NaH_2PO_4 solution and adding 3 mg of horseradish peroxidase to the mix.

b) 4-hydroxyphenylacetic acid at the concentration of 10^{-3} M in ultrapure water.

c) bovine catalase solution at the concentration of 1 mg/mL in ultrapure water.

- The measurement for **H_2O_2 + ROOH + ROOR** was performed by mixing in a 10 mL beaker in the following order:

  2 mL of solution *a* + 4 mL of solution *b* + 120 µL of sample

- The measurement for **ROOH + ROOR** was performed by mixing in a 10 mL beaker in the following order:

  2 mL of solution *a* + 4 mL of solution *b* + 5 µL of solution *c* + 120 µL of sample

After the sample preparation, 2 mL of solution were placed in a 1 cm quartz fluorescence cell and the fluorescence emission of the dimer was measured at 408 nm with an excitation wavelength of 320 nm.

Derivatization with DNPH

The formation of low molecular weight carbonyl compounds originating from the photo-transformation of NOM was monitored using 2,4-dinitrophenylhydrazine (DNPH) as derivatizing agent. DNPH efficiently reacts with aldehydes and ketones according to reaction 31 and the derivatized compounds can be analyzed by HPLC coupled with a UV or MS detector.

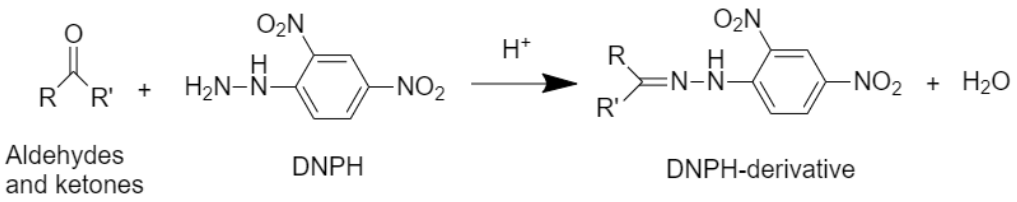

(31)

To perform the analysis, 200 µL of DNPH solution (1 mg/mL in acetonitrile) and 20 µL of phosphoric acid 1.67 M were added to 1 mL of sample solution. After 30 minutes of mechanical shaking 1 mL of acetonitrile was added to the mix and the solutions were analyzed by HPLC-MS in negative ESI mode using an injection volume of 15 µL.

Derivatization with BSTFA

A parallel approach to the one followed for carbonyl compounds analysis was used to monitor the formation of low molecular weight carboxylic acids and alcohols using, in this case, N,O-bis-(trimethylsilyl)trifluoroacetamide (BSTFA) containing 1% of trimethylchlorosilane (TMCS) as a derivatizing agent. The derivatization reaction is shown below.

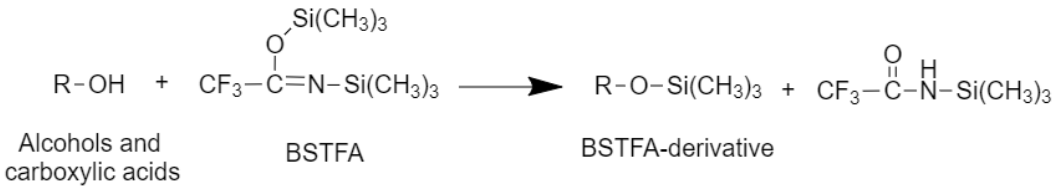

(32)

Since BSTFA rapidly decomposes in presence of water, all NOM solutions were freeze-dried, and the solid residue was redissolved using the lowest volume possible of acetonitrile. Then 1 mL of sample was put in a 1.5 mL vial, spiked with 0.5 mL of BSTFA + TMCS derivatizing agent, and capped right away. Samples were let stand for at least 10 minutes and then analyzed by GC-MS. The adopted procedure is available at https://static.thermoscientific.com/images/D00376~.pdf.

2.7. Software

PCA analysis investigating the relationship between NOM fluorophores and the rate of production of reactive species, presented in Manuscript 2, were performed with the statistical software *R*

(Foundation for Statistical Computing, version 3.6.1) by the team of Edith Parlanti (EPOC laboratory, Université de Bordeaux) in the framework of a collaboration.

The Design of Experiment (DOE) used to optimize the performances of the plasma water treatment, presented in Manuscript 4, was developed using the statistics software *Ellistat* (6.4 2020/11). The results obtained from the DOE, used to obtain the predictive model, were analyzed with the same software.

Summary of the main results

3 Summary of the main results

Note to the reader: This chapter represent a summary of results that have been published during this thesis and does not contain bibliographic references. References can be found in the corresponding articles attached at the end of this manuscript.

3.1. NOM characterization and NOM-driven processes

In natural surface waters, NOM governs the auto-remediation processes occurring under exposure of solar radiation through the generation of short-lived reactive species. Furthermore, since NOM properties are strongly dependent on its age, type of surrounding soil, microbial and algal activity and atmospheric events, it can represent a useful indicator to gather information on the history on the water sample as well as on the hydrology of the area under study. These aspects have been investigated in Manuscripts 1 and 2 by studying the water samples collected in the Auzon site. Studied samples included 2 riverine waters (Allier and Vendage), 2 samples of stagnant water collected in the dead branch of Allier river (B4 and B7), and 2 samples of groundwater sampled from the piezometers PZ1 and PZ5 located near the dead branch. Three sampling campaigns performed in March, July and October 2018, allowed to monitor the temporal evolution of the water chemical parameters.

3.1.1. Photoreactivity of NOM of the Auzon site (Manuscript 1)

At first, water samples were characterized in terms of their spectral properties (A_{280}, SUVA, E2/E3, spectral slope and fluorescence emission), ability to produce ^{3}DOM* and singlet oxygen under UVA irradiation, and organic carbon content. Average molecular weight, estimated from spectral parameters, was found to be relatively stable all year round with higher values observed for surface water samples (0.91-1.80 kDa) and lower values observed for groundwater samples (0.54-0.89 kDa). All these values, however, fall in the lower range of the size distribution observed for natural waters and correspond to little humified organic matter. The fluorescence indices, and in particular the high values obtained for the biological index BIX (0.812-2.25), also confirmed a predominant autochthonous

origin of NOM with the highest values measured for the samples of stagnant water B4 collected in July; during the summer, the surface of the stagnant dead branch was covered by aquatic plants and their release of freshly produced NOM might explain the observed results. TOC values reached their maximum in July for all sampling locations. For all water samples, the quantum yield of ^{3}DOM* and $^1O_2$ formation were found to reach the highest value for the groundwater samples PZ1 and PZ5 and lower values for surface water samples. They were more affected by the sampling sites than by the sampling period.

In a second step, correlations between water samples spectral properties and photoreactivity properties were investigated using Principal Components Analysis (PCA). Correlations obtained along the Principal Component 1 (PC1) highlighted that the water samples reactivity (^{3}CDOM* and $^1O_2$ formation rate) increased when the NOM average MW and the absorbance at 280 nm decreased; in fact, high MW macromolecules are expected to reduce the sensitizing properties due to internal deactivation processes and more efficient scavenging of reactive species [172]. Principal Component 2 (PC2) instead, was positively correlated to the rate of production of ^{3}DOM* and $^1O_2$ and negatively correlated to BIX and seemed associated to the degree of conjugation of chromophores. Results also provided information on the site hydrodynamic functioning, revealing that the dead branch and the piezometer located on the right bank are probably fed by the River Allier, contrary to the piezometer located on the left bank. We decided to further investigate the relationship between the chromophores nature and the oxidative properties of irradiated NOM.

3.1.2. Correlation between fluorophores nature and photoreactivity of NOM (Manuscript 2)

Fluorescence Excitation-Emission matrices (EEMs) were recorded for all water samples from the Auzon site and were then decomposed using a parallel factor algorithm (PARAFAC). As a result, 7 individual components were obtained and similarities were searched within the fluorescence database OpenFluor obtaining successful matches for components C1 to C5 (similarities scores >0.95).

The 7 components identified with the PARAFAC analysis are:

C1 (λ_{exc} <250 and 300 nm; λ_{em}=390 nm) assigned to low MW substances.

C2 (λ_{exc}= 280 nm; λ_{em}=300-340 nm) assigned to the protein-like (i.e. tryptophan-like and tyrosine-like) fluorophores.

C3 (λ_{exc}= 245 and 315 nm; λ_{em}=400 nm) assigned to fluorophores of terrestrial origin possibly produced by photo-degradation of NOM.

C4 (λ_{exc}= 260 and 370 nm; λ_{em}=480 nm) assigned to high MW fluorophores produced during bacterial processing of NOM; furthermore, component C4 also had strong analogies with the component SQ2 assigned by Cory and McKnight (2005) to reduced quinone-like component [173].

C5 (λ_{exc}= 270 and 325 nm; λ_{em}=345 nm) assigned to 2-naphthoxyacetic acetic by comparison with a pure reference. 2-naphthoxyacetic acid is a highly fluorescent compound typically used to reduce the pre-harvest fruit drop on strawberries and tomatoes crops and its presence in our water samples can be explained by the presence of vegetable farming near the site.

C6 (λ_{exc} <245 nm; λ_{em}=345 nm) did not find any match in the OpenFluor database, but was likely connected, optically and temporarly, to **C5**.

C7 (λ_{exc} =265 and 345 nm; λ_{em}=412 nm) presented strong analogies with the component SQ3 assigned one again t0 reduced quinone-like component by Cory and McKnight (2005) [173].

Once the 7 PARAFAC components were identified, the relationship between these components and NOM photoreactivity was investigated with a PCA analysis. The 10 variables used for the PCA included the components C1 to C7, the rate of ^{3}DOM* formation (R^{3DOM*}), the rate of singlet oxygen formation (R^{SO}) and the rate of light absorption (R_a). A strong correlation was found between DOM photoreactivity and the 2 PARAFAC components C4 and C7 identified as DOM reduced quinonic moieties. This shows that these components play a role in the photosensitizing properties and suggests that fluorescence EEMs could be used for a rapid estimation of the overall DOM sensitizing properties.

3.1.3. Photolysis of imidacloprid: mechanism of degradation and effects on NOM (Manuscript 3)

In Manuscript 3 instead, we decided to follow an opposite approach to the one followed in Manuscripts 1 and 2 and we investigated the possible modifications occurring to NOM when irradiated in presence water contaminants. In particular, we investigated the transformations of NOM aromatic moieties

occurring when irradiated in presence of the pesticide imidacloprid (IMD) under UVA. Due to NOM complexity, we chose to replace the actual NOM with 3 aromatic model compounds, phenol, resorcinol, and tryptophan, chosen to simulate the aromatic moieties of NOM . This choice made it possible to identify the transformation products obtained during the irradiation that would have been extremely challenging if we used real NOM samples.

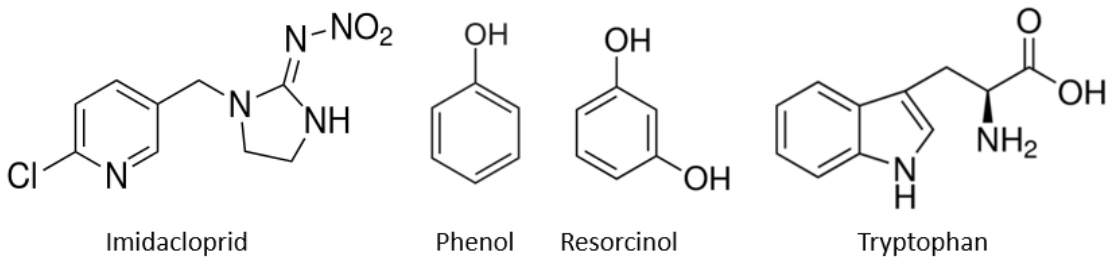

Figure 25. Chemical structures of imidacloprid and of the three aromatic probes.

At first, we studied the degradation pathway of IMD under UVA light and it was observed that its two main photoproducts originated from the loss of its nitro group. Quantum calculations (performed by prof. Pascal de Sainte-Claire at the lab) showed that, upon light absorption, IMD gets excited to the triplet state T1 from where the homolytic cleavage of the RN–NO_2 bond takes place generating NO_2 as major product and NO as the minor one. To gather experimental evidence on the NO_X formation, IMD 10^{-4} M was irradiated in a closed reactor and the gas phase was continuously analyzed using a NO_X chemiluminescence detector. During the first 2 h of irradiation, the total quantities of 24 ± 5 µg and 0.88 ± 0.20 µg were respectively measured for NO_2 and NO. Simultaneously, as NO_X undergo rapid hydrolysis, the accumulation of nitrate and nitrite anions in the liquid phase was also observed.

In the literature it has been reported that the irradiation of NO_2^- and NO_3^- solutions generates HO•, NO and NO_2 radicals capable of inducing the nitration and nitrosation of phenolic aromatic substrates present in the mixture [174]. To verify if IMD could also contribute to the formation of such toxic compounds, we irradiated IMD in presence of phenol, resorcinol, and tryptophan in separate experiments; the concentration of both IMD and the probes was 10^{-4} M. For all three tested probes, the formation of nitro and nitroso derivatives was confirmed by UHPLC-HRMS analyses and their estimated yields of formation, in relation to IMD disappearance, are reported in table 7.

Table 6. Yield of formation of phenol, resorcinol, and tryptophan nitro/nitroso derivatives in presence of IMD.

Compound	% yield of formation
Nitro-resorcinol	3.3
Nitroso-resorcinol	5.1
Nitro-phenol	2.6
Nitroso-phenol	0.5
Nitro-tryptophan	0.08
Nitroso-tryptophan	0.14

The much lower yield of formation observed for tryptophan derivatives are probably because of the much higher rate of direct photolysis of tryptophan itself. When IMD was replaced with the equivalent amount of nitrite and nitrate anions produced by IMD itself after 2 h of irradation, the formation of nitro/nitroso-derivatives was drastically reduced therefore showing that NOx released upon irradiation of IMD played a major role in the reaction.

Eventually, the influence of real NOM (IHSS Suwannee River NOM, 2R101N) on the formation rate of nitro/nitroso-derivatives of resorcinol, in presence of IMD and of NO_2^-/NO_3^-, was investigated. NOM was added at the concentration of 11 mg/L while the concentration of the other chemicals was maintained the same as for precedent experiments. In the IMD-resorcinol system, the formation of nitro-resorcinol and nitroso-resorcinol increased by a factor of 2.0 and 1.3 respectively when solutions were irradiated in the presence of NOM. For the system NO_2^-/NO_3^--resorcinol, the formation of nitro-resorcinol and nitroso-resorcinol increased by a factor of 35 and 2.8 respectively. Due to the complexity of the system, the catalytic effect of NOM on resorcinol transformation is difficult to rationalize. The generation of $HO^\bullet$ and $^3DOM^*$ by irradiated NOM can, on the one hand, favor the formation of phenoxyl radicals of aromatic substrates therefore increasing their reactivity but, on the other hand, NOM can also act as a radical scavenger. The overall effect of NOM will therefore depend on the relative concentration and reactivity of the species involved in the transformation reactions.

3.2. NOM and water treatment

During the course of this thesis, the relationship between NOM and water treatment has been explored using three different approaches. At first we investigated how the chemical modifications induced in NOM by UVC irradiation affect its photodegrading properties on the herbicide glyphosate;

the simultaneous presence of NOM, glyphosate and UVC radiation is in fact likely to be observed in water treatments since glyphosate is a widely used herbicide in agriculture and UVC is commonly adopted technology for water disinfection. Then, the effect of NOM on the efficiency of water plasma treatments was studied in collaboration with the industrial partner Iris (Turin, Italy) who is currently developing a novel plasma-generating device for water treatment applications. The use of non-thermal plasma for water decontamination has been explored in recent times and very encouraging results were obtained. An exhaustive comprehension of the chemistry behind plasma processes and the ability to predict the performances of such treatments in different water matrices have not been fully achieved. Eventually, at Polytechnical University of Valencia, we investigated the possibility of using environmental-friendly compounds of natural origin, chosen as NOM replacement, to photochemically reduce imidacloprid upon irradiation with visible light.

3.2.1. Effect of NOM on glyphosate photodegradation under UVC light (Manuscript 5)

NOM undergoes important transformation when irradiated with UVC light. Together with TOC loss, the destruction of chromophores, resulting in reduced absorbance and fluorescence of irradiated solutions, is typically observed; as a consequence of these structural modifications, NOM photosensitizing properties also evolve along irradiation. We decided to investigate about these modifications by irradiating Suwannee River NOM (SRNOM) samples under UVC light. UHPLC-HRMS and GC-MC coupled to derivatization allowed the identification of several transformation products that were not present in the original sample. In particular, we observed a consistent formation of low MW carbonyl compounds in the C_1-C_6 range and we calculated that the total contribution of these compounds to the TOC after 3h of irradiation corresponded to 46%. Then, we tested the ability of original and pre-irradiated SRNOM to induce the photo-degradation of glyphosate (GLY). The chemical structures of glyphosate and of its main degradation product aminomethylphosphonic acid (AMPA) are reported in figure 25. When glyphosate 10^{-5} M was irradiated at 254 nm in presence of the pre-irradiated NOM, its disappearance rate was 29 times faster than the one obtained in the presence of the original NOM (0.038 min^{-1} and 0.004 min^{-1} respectively).

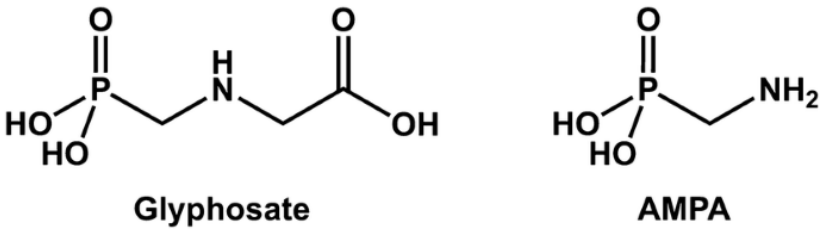

Figure 26. Chemical structure of glyphosate and of its main degradation product aminomethylphosphonic acid (AMPA).

Considering the high chemical stability of glyphosate, it is reasonable to assume that it was degraded only by the reaction with highly oxidant species like $HO^{\bullet}$ radicals; the inhibition of degradation observed in presence of 2-propanol supports this hypothesis. We therefore calculated that the quantum yield of $HO^{\bullet}$ production for SRNOM was 0.024 while for $SRNOM_{3h}$ it was between 0.21 and 0.55. Considering the great amount of carbonyl compounds formed during the irradiation, we postulated that these molecules were responsible for the increased reactivity of $SRNOM_{3h}$ by photosensitizing the formation of $HO^{\bullet}$ radicals. To verify this hypothesis, we irradiated glyphosate in presence of acetone 10^{-4} M and we observed that glyphosate disappeared with an auto-accelerated profile. During the first 10 minutes of irradiation the rate constant was 0.002 min^{-1} but, from 10 to 30 min, the rate increased by a factor of 12 reaching the value of 0.024 min^{-1}; we therefore made the hypothesis that key intermediates, likely hydroperoxides, needed to be formed and accumulated in the first stage of the irradiation. We proposed a mechanism, shown in scheme 1, in which the homolytic α-cleavage of the C—C bond of acetone (or other carbonyl compounds) from its triplet state leads, in presence of oxygen, to the formation of hydroperoxides. The photolysis and/or the thermal decomposition of these hydroperoxides produce $HO^{\bullet}$ radicals that can both react with GLY and with an H donor molecule RH to induce the formation of a catalytic cycle leading to other hydroperoxides. To explain the high rate of glyphosate degradation we need to make the hypothesis that these hydroperoxides are instable at room temperature and provide an additional source of $RO^{\bullet}$ and $HO^{\bullet}$ radicals contributing to further accelerate the reactions chain. As 2-propanol does not inhibit entirely the reaction, GLY might also react with other radicals than $HO^{\bullet}$, likely, the two chain-carrying radicals $R^{\bullet}$ and $ROO^{\bullet}$ or $RO^{\bullet}$.

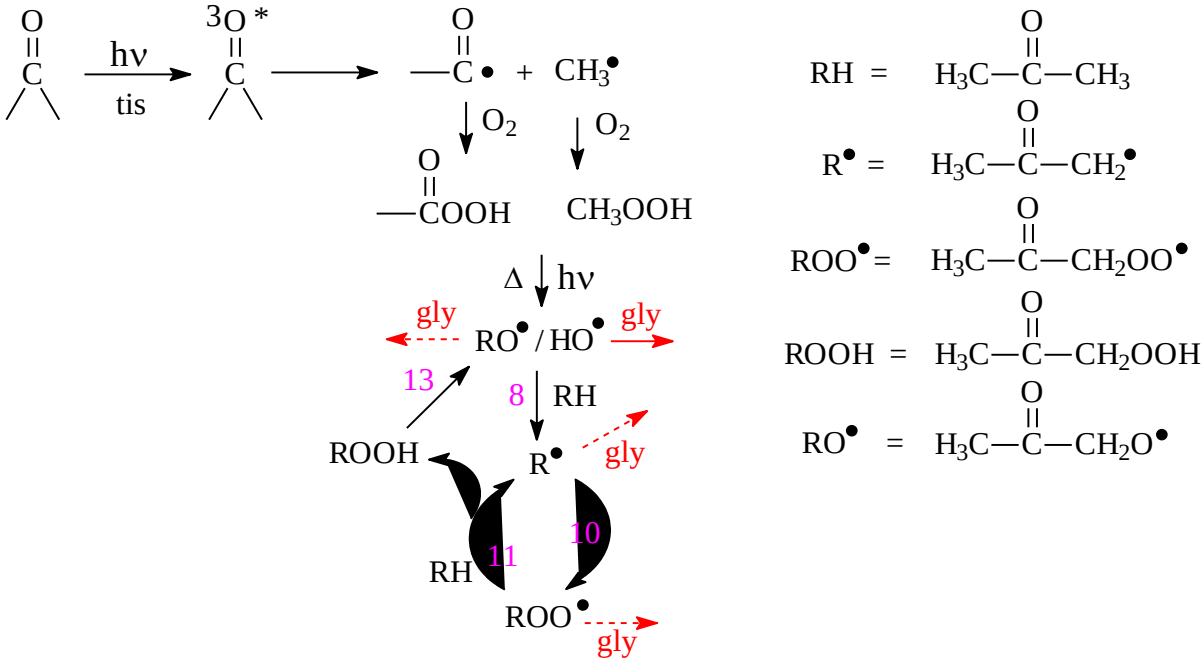

Scheme 1. Proposed mechanism of $HO^\bullet$ formation upon irradiation of carbonyl compounds in presence of oxygen, and H-donor molecules RH.

3.2.2. NOM and non-thermal plasma water treatment (Manuscript 4)

3.2.2.1. Plasma device parameters optimizations

At first, to gain preliminary information on the functioning of the plasma system developed by Iris (European Patent n EP 3 023 392 B1), a full factorial experimental design, investigating the effect of plasma discharge frequency, electrodes distance and water conductivity on the treatment efficiency, was used. The monitored response was the rate of discoloration of methylene blue (MB) solutions (initial absorption coefficient at 665 nm =0.7) and the DOE highlighted that better performances were obtained with higher discharge frequency and lower water conductivity. The distance between electrodes was not a significant parameter when water conductivity was low, however, when water conductivity was raised to about 300 µS/cm, higher electrodes distance hindered the formation of the discharge. The following experiments were therefore performed with a frequency discharge of 17 Hz (maximum frequency allowed by the generator), an intermediate electrodes distance of 5 mm, and without increasing the conductivity of treated solutions.

3.2.2.2. Effect of pollutant concentration and role of HO•

After these preliminary tests, we tested the performance of the plasma treatment to abate the concentration of aqueous diclofenac (DCF), a compound having a higher relevance from an environmental point of view. Different concentrations of DCF in ultrapure water, ranging from 50 µM to 500 µM, were tested and degradation profiles are reported in figure 27. The treatment efficiency did not seem to linearly depend on DCF concentration and the best results were obtained with an initial concentration of 100 µM while, at 500, µM the calculated constant rate was 5.6 times smaller.

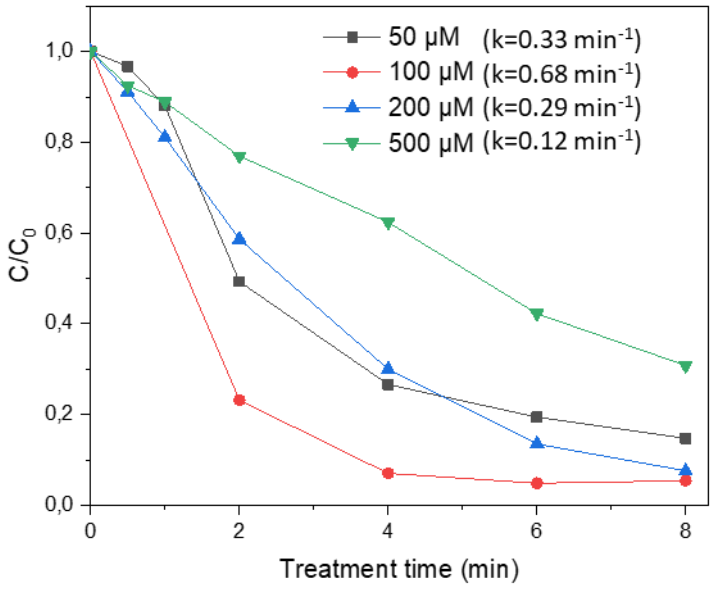

Figure 27. Degradation of DCF at different concentrations using the plasma device.

To better understand the mechanism of pollutants degradation, both MB (initial absorbance at 665 nm =0.7) and DCF (100 µM) were degraded in presence of 2-propanol, allowing to evaluate the role played by HO• on the degradation of these compounds. Interestingly, very different results were obtained in the two cases; MB degradation rate strongly diminished in presence of 2-propanol and, when the latter was added in large excess, the rate was about 70% smaller than the one obtained in absence of 2-propanol. HO• radicals were therefore one of the most important species responsible for MB degradation even though the incomplete inhibition in presence of large excess of 2-propanol suggests that other mechanisms of degradation are involved. For DCF on the other hand, despite its degradation kinetic measured in absence of scavengers was comparable to the one of MB, the

presence of 2-propanol did not affect its degradation rate. These results show that different pollutants may therefore undergo different degradation pathways that not only involve $HO^{\bullet}$, but also free electrons, cavitation, high-density electric field, NO_x, and photolysis. The degradation profiles obtained for the two compounds are shown in figure 28.

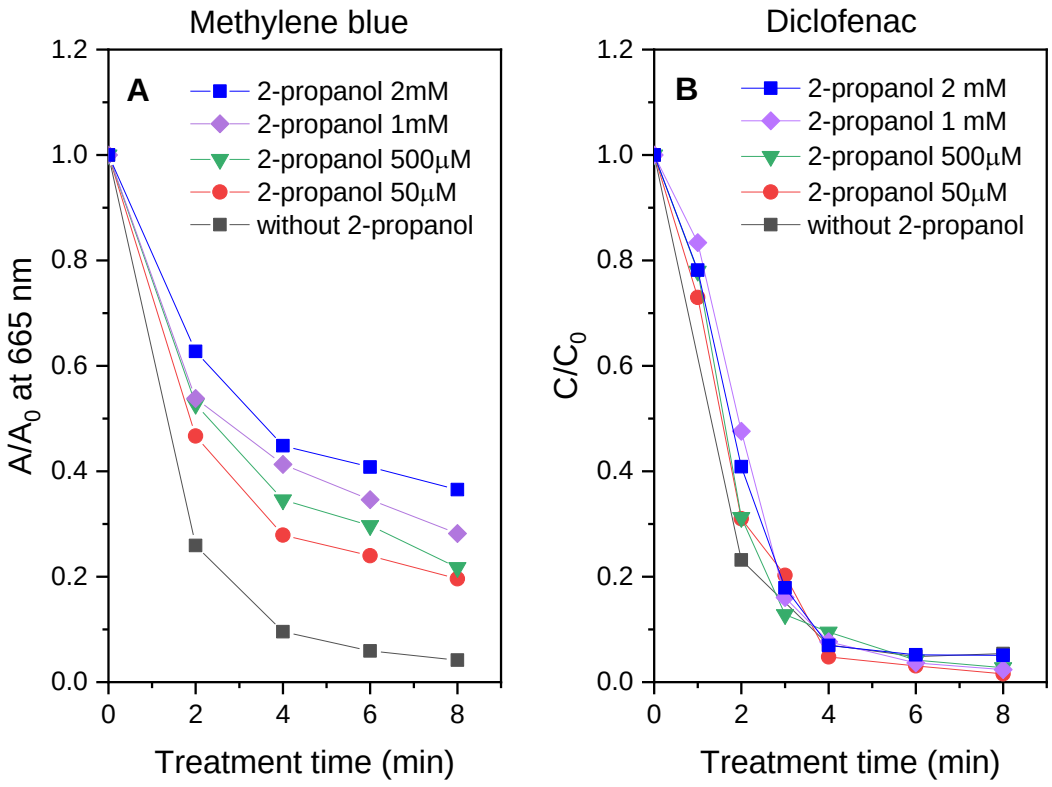

Figure 28. Degradation of methylene blue (A) having initial absorbance at 665 nm = 0.7, and diclofenac (B) having initial concentration 100 µM, in presence of different concentrations of 2-propanol obtained with plasma treatment.

3.2.2.3. NOM and matrix effect on pollutants degradation

Then, to investigate the role of NOM on treatment efficiency, the pseudo first-order rate constant of discoloration of methylene blue solutions in presence of different concentrations of Suwannee Rive NOM (IHSS Suwannee River NOM, 2R101N) was measured. 10 mL of solution were treated using the polypropylene (PP) reactor and the initial rate constant, measured during the first 4 minutes of treatment, was 0.60 min^{-1} in absence of NOM, 0.28 min^{-1} in presence of 5 mg/L NOM, and 0.21 min^{-1} in presence of 10 mg/L NOM. Treatment efficiency was therefore heavily affected by NOM presence

that was reasonably trapping most part of reactive species produced by the plasma discharge. When TOC was measured along treatment to evaluate the extent of NOM mineralization, we realized that TOC values were actually increasing with treatment time. Since the source of organic carbon was unlikely to come from the metal electrodes, we concluded that the PP reactor was either releasing plastics into treated solutions because of the extreme solicitations that it was exposed to, or, the problematic washing of the reactor caused, with use, an accumulation of organic compounds on the reactor walls that were then released in solution; the replacement of the PP reactor with a new one of the same type only partially improved the reliability of measured TOC values but did not entirely solve the issue. For this reason, the PP reactor was eventually replaced with a Pyrex glass (PG) reactor having no plastic parts.

Using the PG reactor, we could verify that TOC of solutions containing NOM was not modified during plasma treatment and that mineralization was not significant under studied conditions.

The effect of NOM on the degradation of DCF was also tested and, in addition, the removal performances in tap water and wastewater matrices was evaluated; the results are shown in figure 29. Similarly to what had been observed for MB, the presence of NOM at the concentration of 10 mg/L strongly slowed down DCF degradation but, when tap water and wastewater matrices were used, the degradation was almost entirely inhibited. Although poorer treatment performances were expected when working with real matrices, these results were very surprising; TOC content alone in fact, for both wastewater and tap water, could not justify a complete inhibition of DCF degradation. Further investigation would therefore be required to understand the influence of water parameters on treatment efficiency and therefore develop a predictive model.

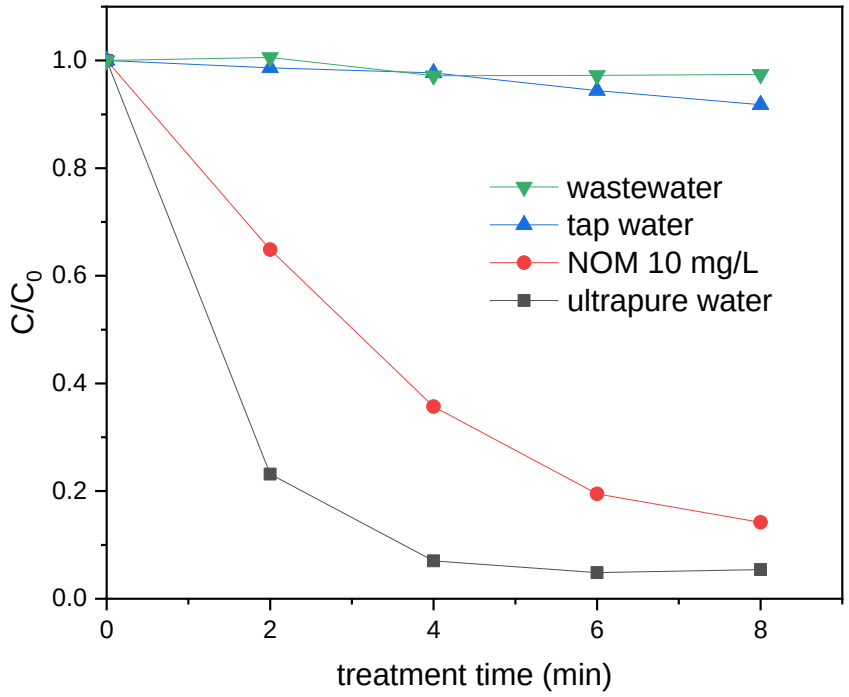

Figure 29. Degradation of diclofenac 10^{-4} M in different matrices using plasma discharge treatment.

In Manuscript 4 we eventually investigated the degradation of three perfluoroalkyl substances (PFAS) using the plasma treatment. PFAS have been intensively studied in recent years because, due to their exceptional chemical stability, their efficient removal in water treatment processes represents a challenging task. Perfluorooctanoic acid (PFOA), Perfluorohexanoic acid (PFHxA) and perfluoroctanesulfonic acid (PFOS) were treated in ultrapure and groundwater matrices, both in individual solutions and in mixture; the structures of the selected PFAS are reported in figure 30.

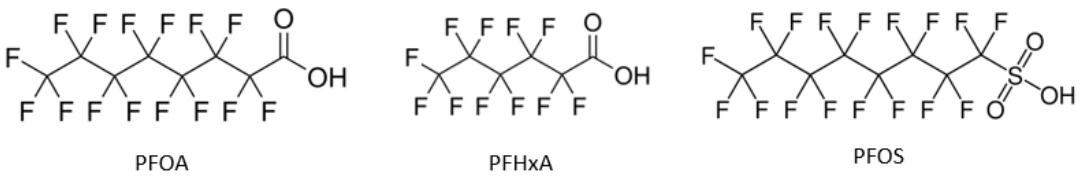

Figure 30. Chemical structures for PFOA, PFHxA and PFOS.

Treatment duration was 30 minutes when compounds were treated individually and was extended to 60 min when treated in mixture. Plasma treatment was capable of promoting the degradation of all three PFAS in both ultrapure and groundwater matrices and the results are summarized in figure 31.

The small matrix effect observed in this case could be explained considering the low TOC value of the groundwater used for the tests (<1mg/L); chemical parameters of the groundwater and the rate constant of degradation obtained for PFASs can be found in the supporting material of Manuscript 4.

To conclude, the studied non-thermal plasma seems to be a promising technology for water treatment applications since it was able to efficiently degrade all the contaminants tested, included the highly refractory PFAS. However, at the moment, treated volumes are very low and the treatment efficiency is highly dependent on the properties of the matrix such as NOM content and water conductivity and additional studies are required.

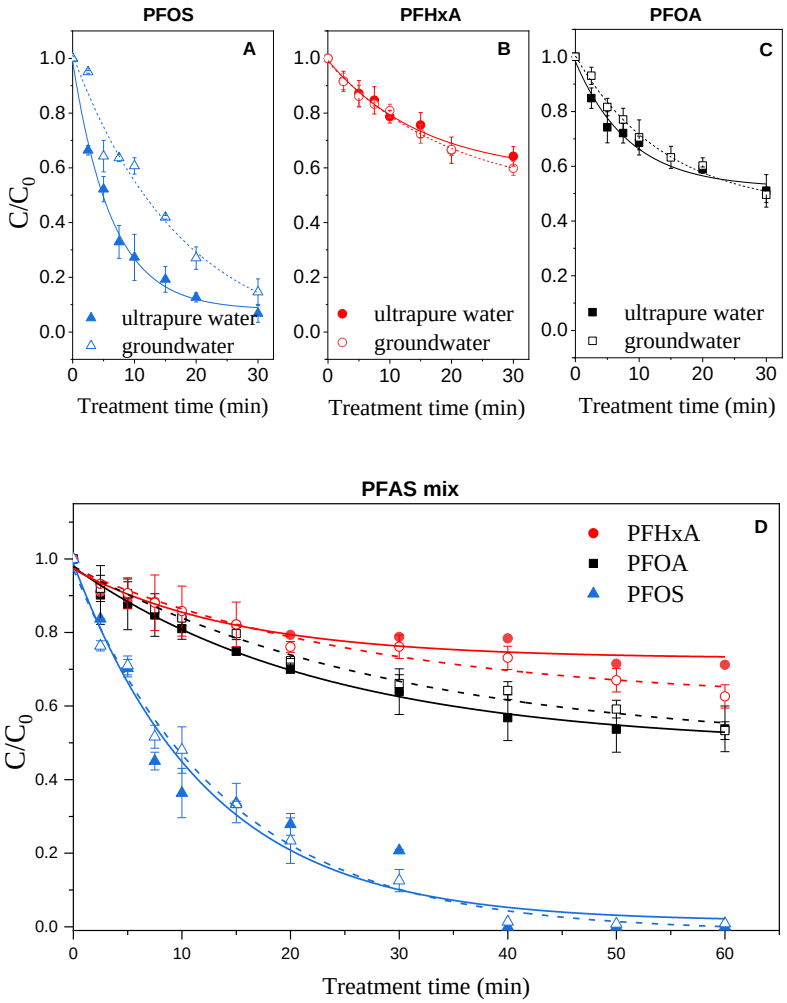

Figure 31. Degradation profiles obtained for the three tested PFAS having individual initial concentration of 10^{-6} M in ultrapure water (closed symbols) and groundwater (open symbols) matrices. Extracted from manuscript 4.

3.2.3. Photoreduction of imidacloprid

During this 3-month secondment at Polytechnical University of Valencia, the possibility to photoreduce the pesticide imidacloprid (IMD) in aqueous solution was investigated. Our goal was to use compounds of natural origin as substituents of NOM and copper chlorophyllin (CHL) as photocatalyst (PC), and ascorbic acid (AA) as electron donor, to create the catalytic photoinduced electron transfer shown in scheme 3.

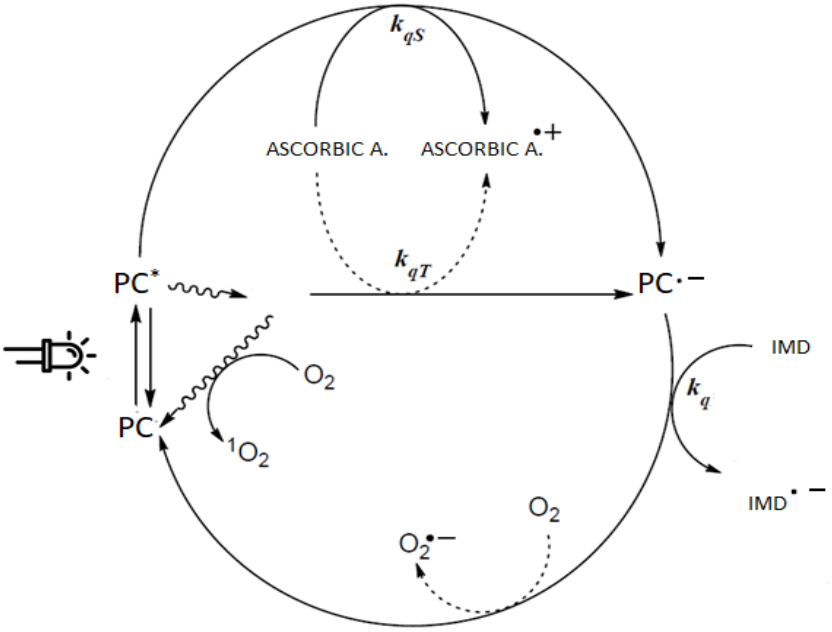

Scheme 2. Reaction scheme for imidacloprid reduction in presence of ascorbic acid and copper chlorophyllin.

The advantage of using copper chlorophyllin as NOM replacement is that its molecular structure is known and the compound is available at high purity therefore making the photochemical system much easier to study. As a starting point, UV-visible spectra of the 3 compounds have been recorded (see figure 32).

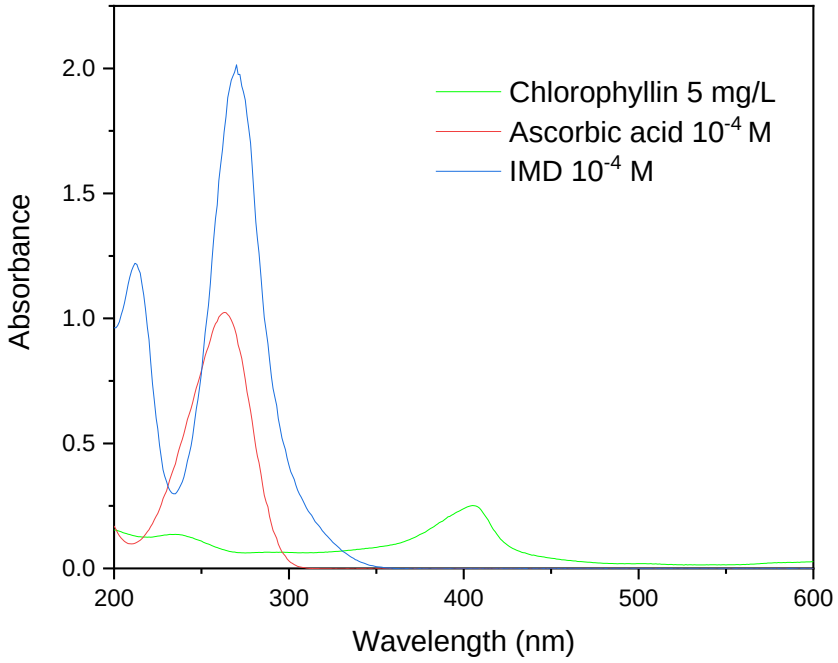

Figure 32. UV-visible absorption spectra of copper chlorophyllin, ascorbic acid and imidacloprid registered in a 1 cm quartz cell.

For steady state irradiation we selected the wavelength 420 nm, where only chlorophyllin is absorbing. The performances of chlorophyllin as a photocatalyst were also compared to the ones obtained with the two classical photocatalysts rhodamine B (RhB) and eosin Y (EOY) irradiated at 520 nm. With all three tested photocatalysts (10^{-5} M), the concentration of imidacloprid was 10^{-4} M and the concentration of ascorbic acid was 10^{-3} M. In all experiments, 10 mL of solution were irradiated in cylindrical Pyrex glass tubes. The degradation profiles obtained for IMD during 3 h of irradiation with the different catalysts are reported in figure 33. Promising results were obtained using CHL as photocatalyst and IMD rate of degradation in the first hour of irradiation was considerably faster than the ones obtained using RhB and EOY; the fact that the degradation stopped after the first hour suggests that a problem of limiting reagent was present and the measurement of AA concentration during irradiation confirmed that it was no longer detected after one hour of irradiation. Since AA was added in large stoichiometric excess, its high rate of consumption was probably not due to his reaction in the cycle of photo-induced electron transfer but it was rather oxidized by atmospheric oxygen. The high consumption of AA measured when solutions were kept in the dark seems to support this hypothesis.

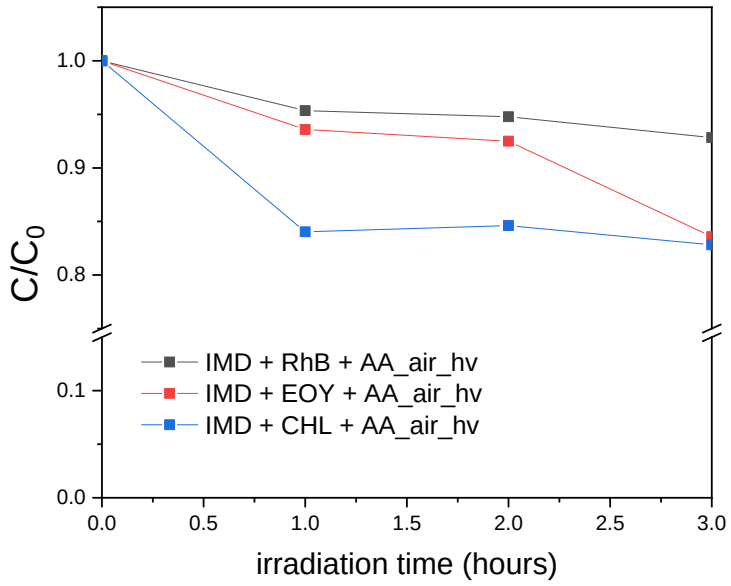

Figure 33. Degradation of imidacloprid (10^{-4} M) in presence of ascorbic acid (10^{-3} M) and different photo-catalysts (10^{-5} M).

The fast oxidation of AA is responsible for its loss of electron donor properties and therefore represent a big limitation in such experiments. For this reason, AA was replaced with the better electron donor DABCO (1,4-diazabicyclo[2.2.2]octane) using again Chlorophyllin and Eosin Y as photocatalysts. The concentration of the catalysts was in both case increased to 10^{-4}M since the solutions in the previous experiments were very lightly colored and DABCO was used at the concentration of 10^{-2} M. The imidacloprid concentration was again 10^{-4}M. This time we also investigated the effect of oxygen on the degradation of IMD and experiments were repeated both under air and under nitrogen atmosphere; the results are shown in figure 34. Very low IMD abatement (<5%) was obtained for all sample exception made for the sample IMD + DABCO + EOY (N_2) in which IMD concentration was reduced of ~65% at the end of the 3h irradiations.

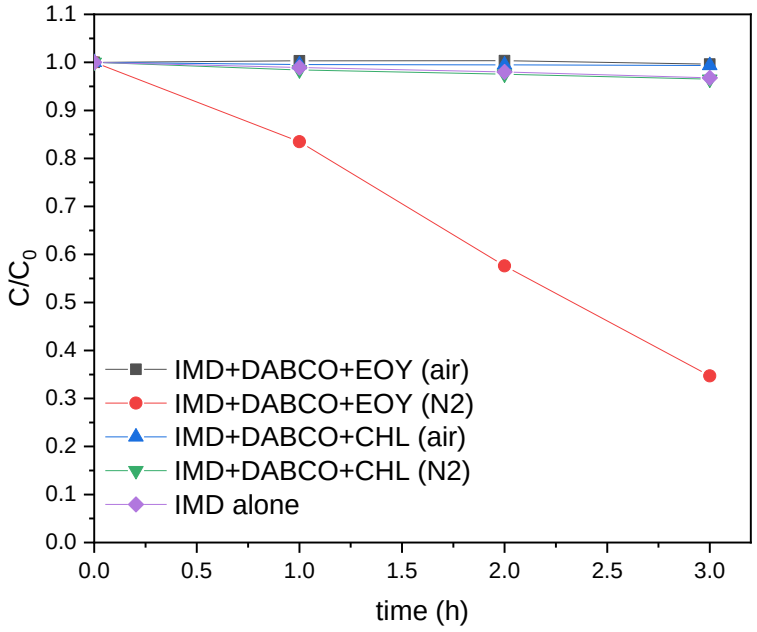

Figure 34. Degradation of IMD in presence of CHL and EOY as photocatalysts and DABCO 10^{-2}M working as electron donor.

Despite the positive results obtained using DABCO as an electron donor, the use of compounds of synthetic nature deviated from the original idea of using compounds of natural origin to promote the degradation of IMD. For this reason, a new series of steady state irradiations were performed testing tryptophan and phenol as electron donors to be paired with Eosin Y. Tryptophan is a compound of natural origin commonly found in natural waters, especially when strong microbial or photosynthetic activities are present; phenol was instead selected to represent the aromatic moieties of NOM as previously done for the study of nitro and nitroso derivatives formation in presence of aqueous IMD (Manuscript 3). An additional experiment in which DABCO concentration was lowered from 10^{-2} M to 10^{-3} M was also performed. The concentrations of both IMD and EOY was 10^{-4} M and degradation profiles of IMD are shown in figure 35.

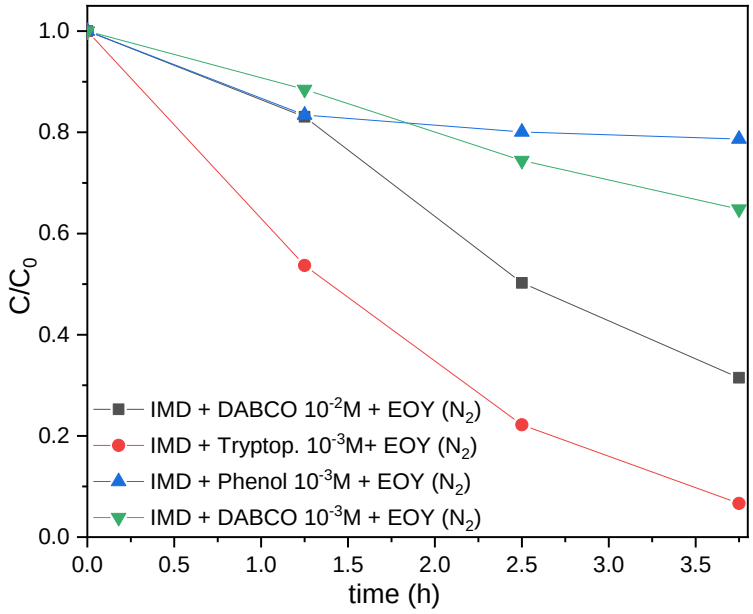

Figure 35. Degradation profiles of IMD obtained under nitrogen in the presence of DABCO, phenol and tryptophan as electron donors and in presence of EOY as photocatalyst.

Of all tested combinations of electron donors, photocatalysts and atmosphere the best results were obtained with the combination tryptophan 10^{-3} M + EOY 10^{-4} M + IMD 10^{-4} M under nitrogen atmosphere; in this case in fact, almost complete degradation of imidacloprid was achieved in the 3h45min of irradiation (red curve in figure 31). The gray line reports the results obtained with DABCO 10^{-2}M while the green curve was obtained with DABCO concentration 10^{-3}M and shows a clear effect of the concentration of the electron donor on IMD degradation rate. The worst performances, in this last set of experiments, were obtained when phenol was used as an electron donor (blue curve). In this case IMD degradation was reduced of about 20% during the first hour of irradiation and then remained relatively stable for the rest of the irradiation, similarly to what had been observed in presence of ascorbic acid.

In conclusion, good performances using chlorophyllin as a photocatalyst were obtained working under air while the use of tryptophan as electron donor of natural origin worked better under nitrogen. However, despite the reduction of IMD using the mechanism of photo-induced electron transfer has shown promising results, the development of an ideal system that uses both photocatalyst and electron donor of natural origin would require further investigation.

General conclusions

General conclusions

This PhD thesis studied the NOM and its interaction with water contaminants from different perspectives, both in the environment and in water treatment processes, with the objective to document non or poorly studied aspects in this field of research. The studied NOM was sampled in the Auzon wetland or, in the case of the Suwannee River NOM, was purchased from the international Humic Substances Society. NOM mimicking chemicals such as phenol, resorcinol or tryptophan were also used to evidence the occurrence of specific NOM transformation reactions that would have been difficult to observe on NOM itself. Water contaminants were chosen among chemicals classified as Contaminants of Emerging Concern (CECs) and whose study has been prioritized by the NORMAN international network. The main ones were the insecticide imidacloprid that absorbs solar light and undergoes photolysis under solar light, the herbicide glyphosate that does not absorb solar light and was used as a probe molecule to monitor the formation of hydroxyl radicals in UVC, and the perfluoroalkyl compounds that are very recalcitrant to oxidation and that were tested in the promising application of non-thermal plasma technology to water treatment.

In the first part of dissertation, I investigated the photochemical processes taking place in natural waters exposed to solar light in two different situations: when NOM acts as a producer of reactive species, which is the most studied case, and, when NOM is potentially transformed by reactive species produced by water contaminants, here imidacloprid. Natural water samples were collected at different places and periods of the year in the Auzon site and NOM was characterized both in terms of its spectral properties and in terms of ability to produce reactive species under irradiation. NOM fluorescence emission was also studied to gather information about the nature of NOM fluorophores with the goal of identifying a correlation between the fluorophores nature and NOM reactivity. NOM from the Auzon site was found to be generally little humified and mainly constituted by compounds of microbial origin falling in the lower part of the size distribution typically observed for NOM (generally around 1000 Da or less). Water samples reactivity was found to be inversely proportional to NOM molecular weight and directly proportional to the concentration of quinonic moieties. *We therefore suggested that the selective monitoring of such moieties using fluorescence could represent a valid tool for a rapid estimation of the photoreactivity of natural waters.*

Then, I investigated the possible transformations occurring on NOM aromatic structures when it is irradiated in presence of imidacloprid. Imidacloprid photolysis, under UVA radiation, proceeds via the loss of the nitro group and generation of NO_X radicals that were proved to be capable of inducing the formation of toxic nitro and nitroso derivatives of the aromatic probes phenol, resorcinol, and tryptophan, selected to represent the aromatic moieties of NOM. *These results highlight how the simultaneous presence in irradiated surface waters of NOM and water contaminants, can ignite complex transformation processes not only of water contaminants but of NOM itself too. Such processes can be of particular importance in water bodies found in the proximity of agricultural or industrial areas and where the concertation of water pollutants can be considerably higher.*

In the second part of this dissertation, I investigated the role of NOM in three different types of water treatment process: UVC irradiation, non-thermal plasma treatment, and homogeneous photocatalysis. In an attempt to obtain as much information as possible on the role played by NOM in water treatment process, a different approach was used for each type of water treatment under study. For UVC irradiation, we investigated the effect of NOM photodegradation on its photoreactivity and therefore on the transformation rate of water contaminants present in the mixture. In plasma treatment, we studied the inhibiting effect of NOM on treatment performances; eventually, we investigated the possibility to use compounds of natural origin for homogeneous photocatalysis applications oriented to water contaminants reduction.

UVC pre-irradiation was found to greatly increase the oxidizing properties of Suwannee River NOM. Pre-irradiated SRNOM could in fact photoinduce the degradation of the herbicide glyphosate under irradiation at 254 nm, while, the original SRNOM could not. Up to 46% of the solution TOC of low MW carbonyl compounds were produced after 3h of irradiation as a result of NOM breakdown. We investigated the photoreactivity of these compounds in a series of parallel experiments and we eventually proposed a photochemical mechanism in which these carbonyls act as photo-sensitizers capable of inducing the formation of hydroperoxides and organic peroxides that represent an important source of $HO^{\bullet}$ and $RO^{\bullet}$ radicals that are responsible for glyphosate degradation. *In the literature NOM is mostly reported to reduce the performances of water treatment processes; however, the results obtained here suggest that the photosensitizing properties of NOM could be used to remove refractory water contaminants.*

As for the investigation on the possible use of homogeneous photocatalysis for the reduction of imidacloprid, the optimal system was searched testing different combinations of electron donor

compounds and photocatalysts. Copper chlorophyllin used as photocatalyst under irradiation at 420 nm gave promising results under air using ascorbic acid as electron donor. However, the fast oxidation of ascorbic acid limits its applications is such systems. By replacing ascorbic acid with tryptophan, excellent results were obtained using Eosin Y as photocatalyst (irradiation at 520 nm) and imidacloprid concentration was reduced of over 90% in less than 4 hours of irradiation. *Even though these data only represent the result of some preliminary tests, the use of non-toxic photocatalysts and electron donors of natural origin to induce the photo-reduction of suitable substrates seems to be an interesting alternative for water depollution applications. Such treatments could be of particular interest in industrial realities where the optimal combination of photocatalyst and electron donor could be searched according to the type of contamination present in the industrial waste.*

In non-thermal plasma treatment, the presence of NOM in treated water at the concentration of 5-10 mg/L was found to strongly reduce treatment performances for the different contaminants tested. The plasma system under study was not able to efficiently mineralize NOM whose concentration was therefore relatively stable for all treatment duration. However, when groundwater samples having low TOC values (<1mg/L) were spiked with different PFAS, the plasma treatment was found to efficiently abate PFAS concentration. *In ultrapure water, the treatment system was indeed able to efficiently degrade all the pollutants tested, but the interference of NOM on treatment efficiency probably represents the biggest limitation to be overcome in order to make this technology efficient for the treatment of waters of heterogeneous nature.*

To conclude, if on the one hand the photosensitizing properties of NOM in irradiated surface waters and the problematic role of NOM in water treatment process represent two well documented topics in the literature, little information concerning the transformation of NOM itself in these two scenarios is available. The goal of this dissertation was therefore to provide an overview on NOM, in both natural systems and in water treatment processes, focusing on such poorly studied aspects. In the environment, we proved that high concentrations of water contaminants could induce the formation of toxic NOM derivatives, hence highlighting the importance of studying the reciprocal interactions between NOM and water contaminants in such complex systems. In water treatment processes instead, the detection of high amounts of carbonyl compounds during UVC irradiation, providing new insights in the NOM degradation pathways under highly oxidative conditions, together with the unexpected increase of NOM photosensitizing properties with irradiation, represent two interesting starting points for future research.

Publications

List of publications

Manuscript 1: Palma, D., Sleiman, M., *et al.* Study of the dissolved organic matter (DOM) of the Auzon cut-off meander (Allier River, France) by spectral and photoreactivity approaches. *Environ Sci Pollut Res* **27,** 26385–26394 (2020).

https://doi.org/10.1007/s11356-020-09005-7.

Manuscript 2: Palma, D., Parlanti, E., *et al.* Fluorescence analysis allows to predict the oxidative capacity of humic quinones in dissolved organic matter: implication for pollutant degradation. *Environ Chem Lett* (2020).

https://doi.org/10.1007/s10311-020-01137-z

Manuscript 3: Palma, D., Arbid, Y., *et al.* New Route to Toxic Nitro and Nitroso Products upon Irradiation of Micropollutant Mixtures Containing Imidacloprid: Role of NOx and Effect of Natural Organic Matter. *Environmental Science & Technology 2020 54 (6)*, 3325-3333.

https://doi.org/10.1021/acs.est.9b07304

Manuscript 4: Palma, D., Papagiannaki, D., *et al.* PFAS Degradation in Ultrapure and Groundwater Using Non-Thermal Plasma. *Molecules* 2021, *26*, 924.

https://doi.org/10.3390/molecules26040924

Manuscript 5: Evolution of SRNOM photoxidant properties under UV-C irradiation: role of carbonyls in the production of OH radicals

Accepted for publication on June 24th 2021 on the journal Water Research.

MANUSCRIPT 1

Study of the dissolved organic matter (DOM) of the Auzon cut-off meander (Allier River, France) by spectral and photoreactivity approaches.

Publishing journal: Environmental Science and Pollution Research

Date of acceptance: 22 April 2020

Environmental Science and Pollution Research
https://doi.org/10.1007/s11356-020-09005-7

RESEARCH ARTICLE

Study of the dissolved organic matter (DOM) of the Auzon cut-off meander (Allier River, France) by spectral and photoreactivity approaches

Davide Palma[1] · Mohamad Sleiman[1] · Olivier Voldoire[2] · Aude Beauger[2] · Edith Parlanti[3] · Claire Richard[1]

Received: 3 December 2019 / Accepted: 22 April 2020

Abstract
Wetlands are recognized for the importance of their hydrological function and biodiversity, and there is now a consensus to protect and restore them as well as to complete the knowledge on their functioning. Here, we studied the dissolved organic matter (DOM) of a wetland composed of the Auzon cut-off meander, the Allier River, the alluvial fluvial flow, and watershed aquifer. Water was sampled at different locations, in spring, summer, and autumn. For each sample, DOM was characterized for its chemical and optical properties and its photooxidant capacity through its ability to generate DOM triplet excited states (^{3}DOM*) and singlet oxygen upon simulated solar light exposure. UV-visible and fluorescence indices revealed that DOM was mainly microbial-derived whatever the sampling sites with spatial and temporal variations in terms of aromaticity (5.5–22%), specific UV absorbance at 254 nm (0.28–2.82 L $m^{-1}mgC^{-1}$), ratio of the absorbance at 254 and 365 nm (4.6–10.8), fluorescence index (1.35–166), and biological index (0.812–2.25). All the samples generated ^{3}DOM* and singlet oxygen, rates of formation of which showed parallel variations. Using principal component analysis (PCA), we found positive correlations between the sensitizing properties of DOM samples and parameters associated to the abundance of low molecular weight and low absorbing chromophores. Moreover, the parameter variation across the wetland reinforced the hydrological movements observed in a previous study, suggesting that these parameters could be used as water connection tracers.

Keywords Riverine DOM · Absorption · Fluorescence · Reactive species · Photoreactivity · Correlations

Introduction

In the past, wetlands were considered as unhealthy areas and largely drained leading to a loss of about 64 to 71% of natural wetlands since 1900 because of human activities (Davidson 2014). Moreover, during the last decades, pollution intensification led to water body's contamination with effects on aquatic ecosystems, human health, productive activities, water system reliability, and operating costs for water use (Gleick 1998; Sutton et al. 2013). Today, the importance of their hydrological function and biodiversity has been recognized, and there is a consensus to protect and restore them. Actions have therefore been implemented in order to preserve or restore wetlands, to complete the knowledge on their functioning, and to communicate about the necessity of maintaining that kind of environments.

Dissolved organic matter (DOM) that consists of water-soluble organic chemicals deriving from the decomposition of plants and living organisms is an important constituent of wetlands. DOM has different roles in freshwater systems. It has an effect on the speciation, transport, and availability of chemical elements and pollutants. Besides, DOM absorbs solar light and an important and largely documented property of DOM components is their capacity to degrade organic pollutants under solar light exposure (Shang et al. 2015). This property is based on their ability to generate reactive species under

Responsible Editor: Philippe Garrigues

Electronic supplementary material The online version of this article (https://doi.org/10.1007/s11356-020-09005-7) contains supplementary material, which is available to authorized users.

✉ Claire Richard
Claire.richard@uca.fr

[1] Université Clermo Auvergne, CNRS, SIGMA-Clermont ICCF, 63000 Clermont-Ferrand, France

[2] Université Clermont Auvergne, CNRS, GEOLAB, 63000 Clermont-Ferrand, France

[3] Université Bordeaux, CNRS, UMR EPOC, 33405 Talence, France

Published online: 03 May 2020

irradiation (Zepp et al. 1977; Cooper and Zika 1983; McCabe and Arnold 2016).

Our first objective in this work was to explore the relationships between the spectral properties of DOM and its capacity to generate reactive species under irradiation. Some correlations were reported in the literature. Parameters connected to the amount of DOM (organic carbon content, absorbance, or intensity of fluorescence at specific wavelengths) were found to be positively correlated to the formation rate of oxidant species such as singlet oxygen ($^1O_2$) and triplet excited states (^{3}DOM*) (Coelho et al. 2011; Peterson et al. 2012; Timko et al. 2014; McCabe and Arnold 2016) while those linked to DOM quality (average molecular weight of DOM components, antioxidant activity) negatively correlated to the quantum yields of formation of these species (Dalrymple et al. 2010; McKay et al. 2017).

Spectral properties of DOM give useful information about the chemical characteristics and origins of their components. The specific UV absorbance at 254 nm ($SUVA_{254}$) gives the aromatic carbon content of DOM (Weisshar et al. 2003). The spectral slope ($S_{275–295}$) and the ratio of the absorbance at 254 and 365 nm (E_2/E_3) are both linked to the relative size of DOM molecules (De Haan and De Boer 1987; Peuravouri and Pihlaja 1997). Fluorescence indices such as the fluorescence index (FI), the biological index (BIX), and the humification index (HIX) are related to the terrestrial versus aquatic source of DOM (Stedmon and Markager 2005; Coble 2007; Huguet et al. 2009; Birdwell and Engel 2010), and the humification degree (Zsolnay et al. 1999). On the other hand, the rate of reactive species photoproduction can be obtained using probe molecules (Rosario-Ortiz and Canonica 2016).

The present study was carried out on a wetland including the Auzon cut-off meander, the Allier River and its tributary Vendage, as well as two aquifers, the alluvial fluvial flow and the watershed ones (Fig. 1). This site looked very appropriate to the study because it offers diversity regarding some parameters among those affecting quality and quantity of DOM: hydrologic conditions, vegetation cover, organic matter inputs, and photochemical and biological degradation processes (Sobek et al. 2007; Gao et al. 2018; McCullough et al. 2019; Queimaliños et al. 2019). This wetland DOM is therefore expected to vary quantitatively and qualitatively with the location and could also change over the season (McCabe and Arnold 2016).

Previous results showed that the connection degree is high between the cut-off meander and both the main stream and alluvial aquifer (Beauger 2008). Indeed, a non-negligible supply of the cut-off meander by the alluvial groundwater is observed, especially in its downstream part. Our second objective, here, was to use the results on the variations of DOM in the site in terms of chemical and spectral characteristics to better understand the hydrological movements of the site.

To achieve this work, surface water was taken at 6 places: three in the Auzon cut-off meander, one in the Allier River and two in boreholes, in spring, summer, and fall. Chemical and spectral characteristics of DOM as well as their ability to generate ^{3}DOM* and $^1O_2$ were determined for all samples across seasons and locations. Then, principal component analysis (PCA) was performed to explore the relationships between all the variables.

Materials and methods

Site description and samplings

The study area is a cut-off meander of the Allier River, a tributary of the Loire River situated in the temperate zone (Massif central, France) (Fig. 1a). A complete description is given in SI text 1. The Auzon cut-off meander was formed when the Allier River captured a gravel-pit and modified the course of the stream (Beauger 2008; Beauger et al. 2015) (Fig. 1b). The cut-off meander approximates 560 m length and is divided into three distinct zones (Fig. 1c): (1) the upstream zone disconnected from the river and similar to a pond, with an important development of macrophytes; (2) the intermediate zone corresponding to a geomorphological riffle characterized by the alternation of lentic and lotic areas with dominant mineral substrates; (3) the downstream zone characterized by bedload deposits coming from the river and macrophytes. For the present study, we retained two sampling sites of surface water in the cut-off meander: B4 situated in the intermediate zone in the middle of the lentic area where solar irradiation is high, and B7 situated in the uppest part of the upstream zone where the riparian forest induced less light penetration. Moreover, two of the boreholes: one on the right bank (PZ1) that collected the alluvial fluvial flow at 5 m depth and the other on the left bank (PZ5) that collected the groundwater of the watershed at 12 m depth were also retained as well as one in the Allier River, and another in the Vendage River, a small tributary of the Allier River. Samples were collected in March, July, and October 2018 allowing us to study seasonal variations in the ability of DOM to produce reactive species. They were taken from surface water (between 10 and 30 cm) in pre-rinsed glass bottles and transported in ice to the laboratory. All samples of natural water underwent a 2 steps vacuum filtration at 1.2 μm and at 0.45 μm using cellulose membranes filters. The filtered samples were placed in cap sealed Pyrex-glass bottles and stored at 4 °C until uses.

Chemicals

Furfuryl alcohol (FFA, 98%) and 2,4,6-trimethyphenol (TMP, certified reference material) were purchased from Sigma-

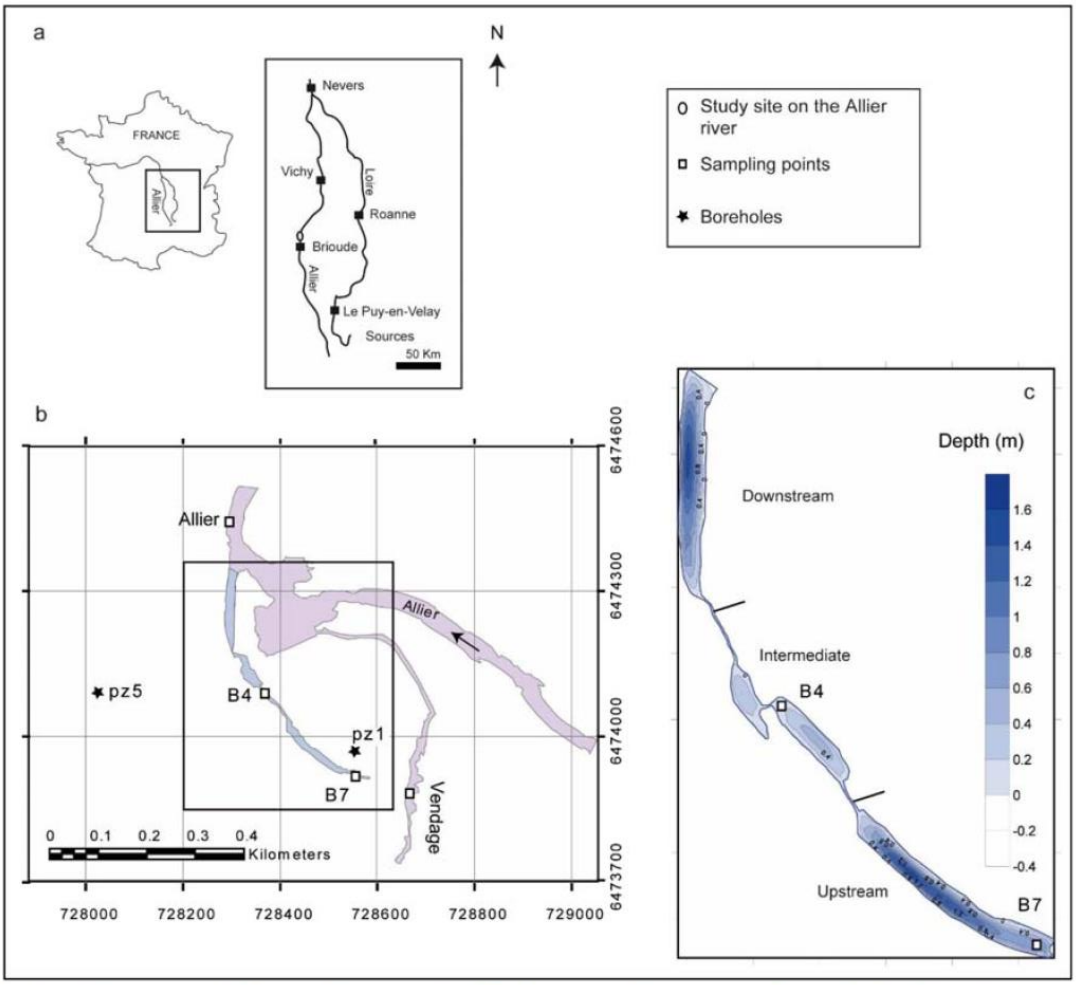

Fig. 1 **a** Location of the Auzon site. **b** Scheme of the Auzon site. **c** The three zones of the Auzon cut-off meander. Sampling points are noted as open squares and boreholes as black stars

Aldrich and used as received. Acetonitrile and methanol for HPLC were from Carlo-Erba and VWR, respectively. All the solutions were prepared in water purified using a reverse osmosis RIOS 5 and Synergy (Millipore) device (resistivity 18 MΩ cm, DOC < 0.1 mg L^{-1}).

Chemical analyses

Dissolved organic carbon (DOC) concentrations were measured using a Shimadzu TOC-L analyzer. Phthalic acid was used for calibration. Analyses were done in triplicate. The reproducibility of measurements was of 2% maximum. Major anions (Cl^-, Br^-, NO_3^-, NO_2^-) were analyzed using a Thermofisher Dionex DX120 HPLC.

Spectral measurements

Absorption spectra were recorded using a Varian Cary 3 spectrophotometer in a 5-cm path length quartz cell. Spectra were scanned from 200 to 800 nm at 1-nm interval and corrected for the ultrapure water reference. A_{280} was obtained by dividing the absorbance at 280 nm by 5. $SUVA_{254}$ was obtained by dividing the decadic absorption coefficient at 254 nm (m^{-1}) by the DOC concentration (mg L^{-1}). It gives the aromatic carbon content of DOM from the relationship proposed by Weisshar et al. (2003):

$$\text{Percent aromaticity} = 6.52 \times SUVA_{254} + 3.63 \quad (1)$$

The ratio E_2/E_3 was obtained by dividing the absorbance at 254 by that at 365 nm (Peuravouri and Pihlaja 1997). It is an indicator of the aromaticity and the average molecular weight (Mw) of DOM. Mw was calculated using the relationship proposed by Lou and Xie (2006) in the case of humic and fulvic acids isolated from a forest soil and from Suwannee River (International Humic Substances Society):

$$Mw = 0.315 \times \exp(4.96/(-1.72 + E_2/E_3)) \quad (2)$$

The spectral slope $S_{275-295}$ was calculated as the slope of the linear regression of $\ln(a_\lambda)$ on λ, between $\lambda = 275$ and 295 nm, where a_λ is the napierian absorption coefficient expressed in m^{-1}. ....

Fluorescence spectra were scanned on a Perkin Elmer LS-55 spectrofluorometer in a 1-cm path length quartz cell. Both slit widths were set to 10 nm, and the scanning speed at 240 nm min^{-1}. When necessary, the solutions were diluted to have an absorbance ≤ 0.10 at 250 nm. Emission spectra were recorded between 250 and 600 nm for different excitation wavelengths (260, 310, and 370 nm). FI that is an indicator of relative contribution of aquatic/microbial and terrestrial DOM sources was obtained by dividing the emission intensity at 450 nm by that at 500 nm with excitation at 370 nm (McKnight et al. 2001). BIX informs on the importance of freshly autochthonous DOM, it was obtained by dividing the ratio of emission intensity at 380 nm to that at 430 nm with excitation at 310 nm (Huguet et al. 2009).

Irradiation experiments

TMP and FFA were used independently as chemical probes to estimate the formation rate of ^{3}DOM* and $^1O_2$ in the water samples, respectively (Rosario-Ortiz and Canonica 2016 and references therein). The processes are the following. ^{3}DOM* produced after reactions 3 and 5 undergoes deactivation through reaction 5, transfers its energy to O_2 through reaction 6, or oxidizes TMP by reaction 7. $^1O_2$ is deactivated by the solvent in reaction 8 and oxidizes FFA through reaction 9. 6-Hydroxypyran-3-one (P) is the main oxidation product of FFA by singet oxygen (chemical yield of 85%) (Haag et al. 1984).

$$\mathrm{DOM} + h\nu \rightarrow {}^1\mathrm{DOM}^* \quad (3)$$

$$^1\mathrm{DOM}^* \rightarrow {}^3\mathrm{DOM}^* \quad (4)$$

$$^3\mathrm{DOM}^* \rightarrow \mathrm{DOM} \quad (5)$$

$$^3\mathrm{DOM}^* + O_2 \rightarrow \mathrm{DOM} + {}^1O_2 \quad (6)$$

$$^3\mathrm{DOM}^* + \mathrm{TMP} \rightarrow \mathrm{DOM}_{+H} + \mathrm{TMP}_{-H}^{\cdot} \quad (7)$$

$$^1O_2 + \mathrm{solvent} \rightarrow O_2 \quad (8)$$

$$^1O_2 + \mathrm{FFA} \rightarrow \mathrm{P} \quad (9)$$

According to these reactions, the rate of TMP consumption, R^{TMP}, is equal to:

$$R^{TMP} = R_a \times \Phi_T \times k_7[TMP]_0 / (k_d + k_7[TMP]_0) \quad (10)$$

where R_a is the rate of light absorption by DOM (Einstein L^{-1} s^{-1}), Φ_T, the quantum yield of ^{3}DOM* formation, k_5, the rate constant of reaction between ^{3}DOM* and TMP (reaction 7), $[TMP]_0$, the initial concentration of TMP and k_d, the first order rate constant decay of ^{3}DOM* by deactivation (reaction 5) and reaction with oxygen (reaction 6), the sum $k_5 + k_6$.

The rate of R^P is equal to:

$$R^P = 0.85 \times R_a \times \Phi_{SO} \times k_9[FFA]_0 / (k_8 + k_9[FFA]_0) \quad (11)$$

where Φ_{SO} is the polychromatic quantum yield of singlet oxygen formation, k', the rate constant of reaction between singlet oxygen and FFA (reaction 9, 1.2×10^8 s^{-1}) (Haag et al. 1984), $[FFA]_0$, the initial concentration of FFA and k_d', the first-order rate constant of deactivation of singlet oxygen (reaction 8, 2.5×10^5 s^{-1} in water) (Wilkinson et al. 1995).

R_a was obtained using the relationship:

$$R_a = \sum_{\lambda_1}^{\lambda_2} I_0^{\lambda} \left(1 - 10^{-A\lambda}\right) \times \Delta\lambda \times 1000 N^{-1} \quad (12)$$

where I_0^{λ} is the amount of photons at λ reaching the solution, averaged between $\lambda-2.5$ nm and $\lambda+2.5$ nm (photons cm^{-3} nm^{-1} s^{-1}); A_λ is the averaged absorbance of the solution at λ calculated between $\lambda-2.5$ nm and $\lambda+2.5$ nm for a path length equal to 1.4 cm; λ_1 and λ_2 are the integration limits, N is the number of Avogadro, and $\Delta\lambda$ is the wavelength interval chosen at 5 nm.

Solutions containing FFA (100 μM) or TMP (50 μM) were put in a cylindrical reactor (1.4 cm, i.d.) made out of Pyrex-glass open to air and irradiated in a device equipped with six polychromatic tubes (Sylvania, F15 W/350BL) emitting within the wavelength range 300–450 nm (maximum emission at 365 nm, Fig. SI-2). A radiometer QE65000 from Ocean optics was used to measure the spectral distribution of the light emitted by the tubes. In addition, the use of metamitron as a chemical actinometer (Kouras et al. 2011) allowed us to get the amount of light received by the solution per nm and second. Fifteen milliliters of solutions were irradiated for each experiment. Aliquots (500 μL) were removed at selected intervals and immediately analyzed by HPLC. Irradiations had a duration of 30 min where FFA and TMP reached a conversion extent comprised between 10 and 20%. TMP and P concentrations were monitored by HPLC using a Waters apparatus equipped with a 2695 separation module, a 2996 photodiode array detector and a reverse phase Nucleodur, Macherey-Nagel C_8 column (5 μm, 150 mm × 4.6 mm). A flow rate of 1 mL min^{-1} was used for all analyses and the eluent was a mixture of 20% methanol and 80% water acidified with orthophosphoric acid (0.1%) for the experiments with FFA while a mobile phase of 50% acetonitrile and 50% acidified water was used for the experiments with TMP. All experiments and HPLC analyses were carried out in duplicate. The initial rates of TMP disappearance (R^{TMP}) and of P formation (R^P) were obtained by plotting the concentration of TMP and P over irradiation time, respectively.

Statistical analyses

Statistical analyses and tests discussed in this work (Pearson correlation, principal component analysis (PCA), and hierarchical clustering) were performed with the R statistical software (R version 3.6.1, R Foundation for Statistical Computing). PCA is a powerful tool used for reducing the dimensionality of a set of variables and for identifying the main axes of variance within a dataset. PCA thus allows for easy data exploration and visualization by transforming it into fewer dimensions that nonetheless retains most of the information and brings out strong trends and patterns (Lever et al. 2017). PCA can also help identify clusters in the data which are grouped using hierarchical clustering. Distinct PCAs were conducted for DOM optical indices with and without sensitizing parameters. Pearson correlation coefficients were reported for all correlations where data were normally distributed. *P* values < 0.01 were considered statistically significant.

Results and discussion

Chemical and spectral properties of DOM

Tables 1 and SI-1 summarize results obtained from chemical and optical analyses of the samples and Fig. SI-3 presents the absorption spectra. The pH varied within a very narrow range around the neutrality. Nitrite, nitrate, and chloride were found as major ions. Nitrite concentration was less than 0.165 mg L^{-1} and nitrate concentration less than 2.7 mg L^{-1} except in the Allier River where it reached 5.3 mg L^{-1} in March and in the Vendage River with values up to 21 mg L^{-1}. These levels are too low to have a significant effect on the photochemical experiments in our irradiation conditions (Vione et al. 2005). DOC ranged between 3.28 and 36.0 mg C L^{-1} with lowest values measured for B4 and B7 in March and October and PZ1 in October and highest values for the Vendage River and PZ5 in July. DOC of Allier River samples varied moderately over the year ranging from 4.74 to 6.39 mg C L^{-1}, while, for the other sites, a strong DOC increase was measured in July with values exceeding those measured in March and October by factors comprised between 2.9 and 5.3. In July 2018, the water surface of the cut-off meander and Vendage River was covered with aquatic plants. The presence of these aquatic plants may explain the high DOC increase in July considering that macrophytes can release organic matter through photosynthetic processes (Reitsema et al. 2018). It was reported that released DOC mostly consists of small (< 1000 Da) molecules that include amino acids and simple sugars (Søndergaard 1981).

The UV-visible absorption spectra were typical of DOM showing a featureless decreasing exponential decay from 200 to 500 nm and a more or less pronounced shoulder between 250 and 300 nm attributable to aromatic moieties (Fig. SI-3). Except in July, the DOM of the two riverine sites, Allier and Vendage, exhibited the highest A_{280} and $SUVA_{254}$ values (0.394–0.629 and 2.82–1.55 mg C L^{-1} m^{-1}) and the highest aromatic content (22–15.2%). These values were however in

Table 1 Chemical and optical characteristics of water samples (see experimental part). *A_{280} was measured in a 5-cm path length cell

Site	Season	pH	DOC (mg C L^{-1})	A_{280}*	SUVA (L m^{-1} mg C^{-1})	Aromaticity (%)	$S_{275–295}$ (nm^{-1})	E_2/E_3	Mw (kDa)	BIX	FI
Allier	March	7.47	5.5	0.516	2.60	21	0.0126	5.22	1.3	0.812	1.35
	July	7.29	6.4	0.629	2.82	22	0.0138	5.24	1.3	0.988	1.46
	Oct.	6.98	4.7	0.394	2.36	19	0.0147	5.38	1.2	0.936	1.38
B4	March	7.30	4.9	0.128	0.78	8.7	0.0156	6.01	1.0	1.10	1.54
	July	7.13	14	0.150	0.30	5.6	0.0148	5.57	1.1	2.25	1.59
	Oct.	7.40	4.9	0.209	1.15	11	0.0127	5.12	1.4	1.06	1.6
B7	March	6.93	3.3	0.139	1.10	11	0.0152	5.43	1.2	1.09	1.58
	July	6.85	15	0.569	0.49	6.8	0.0134	4.6	1.8	1.02	1.55
	Oct.	6.91	4.6	0.224	1.26	12	0.0117	5.52	1.2	1.09	1.6
Vendage	March	7.82	9.6	0.594	1.78	15	0.0139	6.38	0.91	0.956	1.45
	July	7.87	36.0	0.578	0.44	6.50	0.0139	5.75	1.1	0.989	1.49
	Oct.	7.71	10.5	0.581	1.55	13.7	0.0117	4.56	1.8	1.11	1.54
PZ1	March	7.04	6.66	0.234	1.08	10.7	0.0166	9.3	0.61	1.02	1.54
	July	7.11	14.5	0.271	0.55	7.22	0.0146	6.50	0.89	1.25	1.60
	Oct.	7.26	3.36	0.143	1.25	11.8	0.0152	7.06	0.80	1	1.57
PZ5	March	7.15	9.97	0.094	0.30	5.59	0.0177	10.8	0.54	1.22	1.71
	July	7.10	33.8	0.309	0.280	5.46	0.0156	8.12	0.68	1	1.62
	Oct.	7.41	6.4	0.112	0.53	7.09	0.0176	8.19	0.68	1.16	1.66

the low range of those found for other river samples (Weisshar et al. 2003). The lowest aromatic content was measured for PZ5 water samples (5.06–7.09%), and it was comparable to those reported for some oceanic samples (Weisshar et al. 2003). DOM of PZ1 samples exhibited higher values (7.22–11.8%) closer to those of the two cut-off meander samples. $SUVA_{254}$ dropped significantly in July for B4, B7, PZ1, and Vendage River samples, indicating that the organic matter released in summer was less aromatic than in the other seasons. In contrast, for PZ5, $SUVA_{254}$ did not change although a significant DOC increase showing that in this case the nature of DOM was more constant over the year.

Variations of $S_{275–295}$ among samples paralleled those of E_2/E_3 as often reported (Helms et al. 2008). Highest values were measured for PZ5 and PZ1 samples for which we could therefore estimate that calculated Mw were low (0.543–0.889 kDa) compared to those of the other water samples (1.0–1.75 kDa). The low Mw values in PZ1 and PZ5 can be explained by the adsorption of larger macromolecules to the soil constituents during the percolation/transfer processes.

Emission spectra recorded for excitation at 260, 310, and 370 nm were used to calculate indices. All the samples exhibited an intense emission at 340 nm and a humic-like peak (λexc 260 nm/λem 380–460 nm) (Coble 2007) (Fig. SI-4). Values of fluorescence indices $1.35 < FI < 1.7$ and $0.81 \leq BIX \leq 2.2$ showed that all the samples predominantly contained DOM of autochthonous origin with freshly produced organic matter (McKnight et al. 2001; Huguet et al. 2009; Birdwell and Engel 2010). With lowest FI values, the Allier and Vendage River samples had the highest terrestrial organic matter content in accordance with the highest aromaticity and the highest A_{280} values.

To sum up, although DOM was mainly microbially derived whatever the sampling sites, chemical and spectral properties varied among the samples that can be ranked. DOM of riverine sampling sites Allier and Vendage are on the top of the scale for their absorbance, aromaticity, average molecular weight and highest terrestrial organic matter content while DOM from PZ5 is clearly on the bottom of the scale. DOM from B4 and B7 lay in the medium of the scale and PZ1 approaches B4 and B7 for $SUVA_{254}$, and aromaticity but PZ5 for average molecular weight.

Sensitizing properties

The use of TMP and FFA as chemical probes had for objective to compare the ability of the different samples to generate ^{3}DOM* and $^1O_2$ under irradiation and thus to get information on their ability to photodegrade micropollutants.

All the water samples were able to photodegrade TMP and to oxidize FFA into P (Fig. SI-5) in accordance with the photochemical generation of ^{3}DOM* and $^1O_2$, respectively (reactions 3-9). Kinetic data are reported in Table 2. R^{TMP} ranged from 0.2×10^{-8} to 1.43×10^{-8} M s^{-1} for TMP (5×10^{-5} M) and thus varied by a factor of 7 among samples while the rate of P formation (R^P) ranged from 0.73×10^{-9} and 4.09×10^{-9} M s^{-1} for FFA (10^{-4} M) varying by a factor 5.6. According to Eq. 10, R^{TMP} is proportional to the rate of light absorption by the water samples, the quantum yield of ^{3}DOM* formation and the percentage of ^{3}DOM* trapped by TMP at 5×10^{-5} M. If we make the hypothesis that this percentage is quite constant among water samples, then we get, $R^{TMP} = Cte \times R_a \times \Phi_T$. On the other hand, according to Eq. 11, R^P is equal to $Cte' \times R_a \times \Phi_{SO}$. The linear increase of R^{TMP} with R^P ($R = 0.80$, $p < 0.01$, Fig. 2) as already observed (McKay et al. 2017) confirmed that Φ_T variations paralleled those of Φ_{SO} in accordance with the direct involvement of ^{3}DOM* in the formation of $^1O_2$.

R^{TMP} and R^P were the highest for Allier and Vendage Rivers in July and October, and for PZ1 and PZ5 in July and the lowest for B4 and B7 samples in March. As PZ1 and PZ5 did not contain the more highly absorbing DOM, it means that variations of R^{TMP} and R^P did not parallel those of light absorption. Therefore, in a second step, we corrected R^{TMP} and R^P for the rate of light absorbance and got access to the R^{TMP}/R_a ratios that are proportional to Φ_T and to Φ_{SO} according to our mechanistic hypotheses. This gives a better view of the capacity of DOM chromophores to generate reactive species and allows us to rank them in terms of sensitizing capacity. Moreover, our data can be compared with the ones reported in the literature for other DOM sampled in various aquatic systems. Ranging from 0.010 to 0.063, Φ_{SO} fall within the values previously published 0.010–0.039 for Sandvik et al. (2000) and 0.009–0.055 for Peterson et al. (2012).

Correlations among variables

PCA was run with 11 variables: A_{280}, SUVA, E_2/E_3, $S_{275}/_{295}$, BIX, FI, Ra, R^{TMP}, R^P, R^{TMP}/Ra, and Φ_{SO}. This analysis revealed that the first two principal factors (PC1 and PC2) explained 54.19% and 20.62% of the total variance, respectively and thus 74.81% of the total variance (Fig. 3). The score plot of the different samples and the Pearson correlation coefficients are also shown in Fig. 3. Variables E_2/E_3, $S_{275}/_{295}$, R^{TMP}/Ra, Φ_{SO}, and FI occurred in the positive part of PC1 axis and were positively correlated. The correlation coefficient of Φ_{SO} with R^{TMP}/Ra, $S_{275}/_{295}$, E_2/E_3 and FI was equal to 0.93, 0.74, 0.77 and 0.67 respectively with $p < 0.01$. It was often reported in the literature that f_{TMP} ($= \Phi_T \times k_5/k_d$) that is close to our R^{TMP}/Ra ratio as well as Φ_{SO} were positively correlated with E_2/E_3 and thus increased when Mw of DOM decreased (Dalrymple et al. 2010; McKay et al. 2017; Maizel and Remucal 2017). Mw of DOM increases with the abundance in high molecular weight molecules. The big macromolecules are expected to reduce the sensitizing properties (i) through internal deactivation processes or (ii) by

Table 2 Results of the kinetic data processing (see experimental part)

Site	Season	$R_a/10^{-6}$ (Einstein L^{-1} s^{-1})	$R^{TMP}/10^{-8}$ (M s^{-1})	R^{TMP}/R_a	$R^P/10^{-9}$ (M s^{-1})	Φ_{SO}
Allier	March	3.48	0.810	0.0023	2.05	0.010
	July	4.30	1.38	0.0032	3.32	0.013
	October	2.67	1.38	0.0052	1.95	0.012
B4	March	0.77	0.370	0.0048	0.810	0.015
	July	1.03	0.520	0.0050	1.33	0.021
	October	1.48	0.280	0.0019	1.22	0.014
B7	March	0.94	0.200	0.0021	0.730	0.011
	July	2.14	0.850	0.0040	2.42	0.019
	October	1.36	0.270	0.0020	1.41	0.017
Vendage	March	3.43	1.09	0.0032	1.89	0.0078
	July	3.51	1.43	0.0041	4.09	0.019
	October	4.36	0.720	0.0016	3.26	0.012
PZ1	March	1.03	0.810	0.0079	2.20	0.030
	July	1.63	1.28	0.0077	3.12	0.031
	October	0.75	0.600	0.0080	1.85	0.040
PZ5	March	0.34	0.360	0.011	1.21	0.050
	July	1.51	1.43	0.0095	2.67	0.029
	October	0.41	0.580	0.014	1.59	0.063

scavenging of reactive species (Boyle et al. 2009). A_{280}, Ra, and SUVA are three variables connected to DOM absorbance and are logically correlated ($R = 0.63–0.98$, $p < 0.01$). The position of these variables in the negative part of PC1 axis indicated that high DOM absorbance negatively affected the sensitizing properties. This appears reasonable as high DOM absorbance is associated to a high aromatic content and/or great abundance of highly conjugated molecules. It can be also seen that FI was negatively correlated with SUVA, A_{280} and Ra ($R = -0.79, -0.72, -0.72$ with $p < 0.01$) in accordance with the lower absorptivity/molecular weight of fresh autochthonous DOM compared to allochthonous DOM. PC1 seemed thus associated to the relative abundance of low/high molecular weight and low/high absorbing chromophores.

PC2 was positively correlated to R^{TMP} and R^P and negatively to BIX. Riverine DOM samples except Vendage October, and piezometer DOM samples had moderate positive loadings while cut-off meander DOM samples moderate to low negative loadings. PC2 seemed therefore associated to the conjugated character of chromophores. In riverine samples, the conjugated molecules have an allochthonous origin while in piezometer samples they come from soil organic matter and microorganisms. In the cut-off meander, the organic matter is fresh and poorly conjugated in average. The cut-off meander DOM of microbial/macrophytes origin had little better sensitizing properties than Riverine DOM of terrestrial origin either due to the lower concentration of highly absorbing compounds or to better inherent sensitizing properties (Felcyn et al. 2012; Bodhipaksha et al. 2015; Maizel and Remucal 2017; McCabe and Arnold 2017).

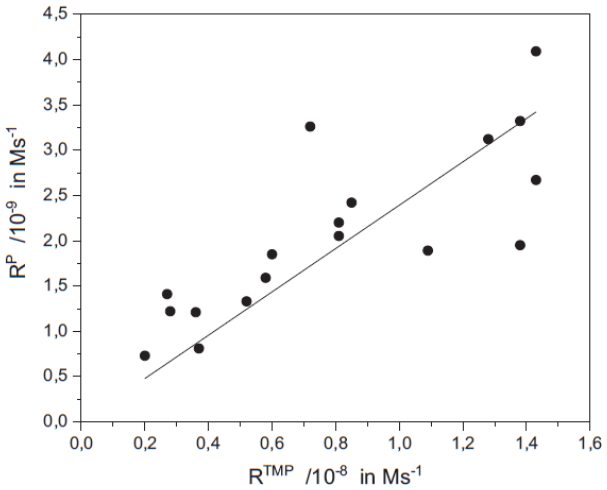

Fig. 2 Plot of the rate of P formation (R^P) vs the rate of TMP consumption (R^{TMP})

Links between DOM properties and hydrological movements

Related to this study, it appeared that B4, B7, and PZ1 showed similarities in terms of chemical, spectral and sensitizing properties of DOM. To better visualize this, we run a PCA based on the 6 spectral variables: A_{280}, SUVA, E_2/E_3, $S_{275}/_{295}$, BIX, and FI. The hierarchical clustering is shown in Fig. 4. A first

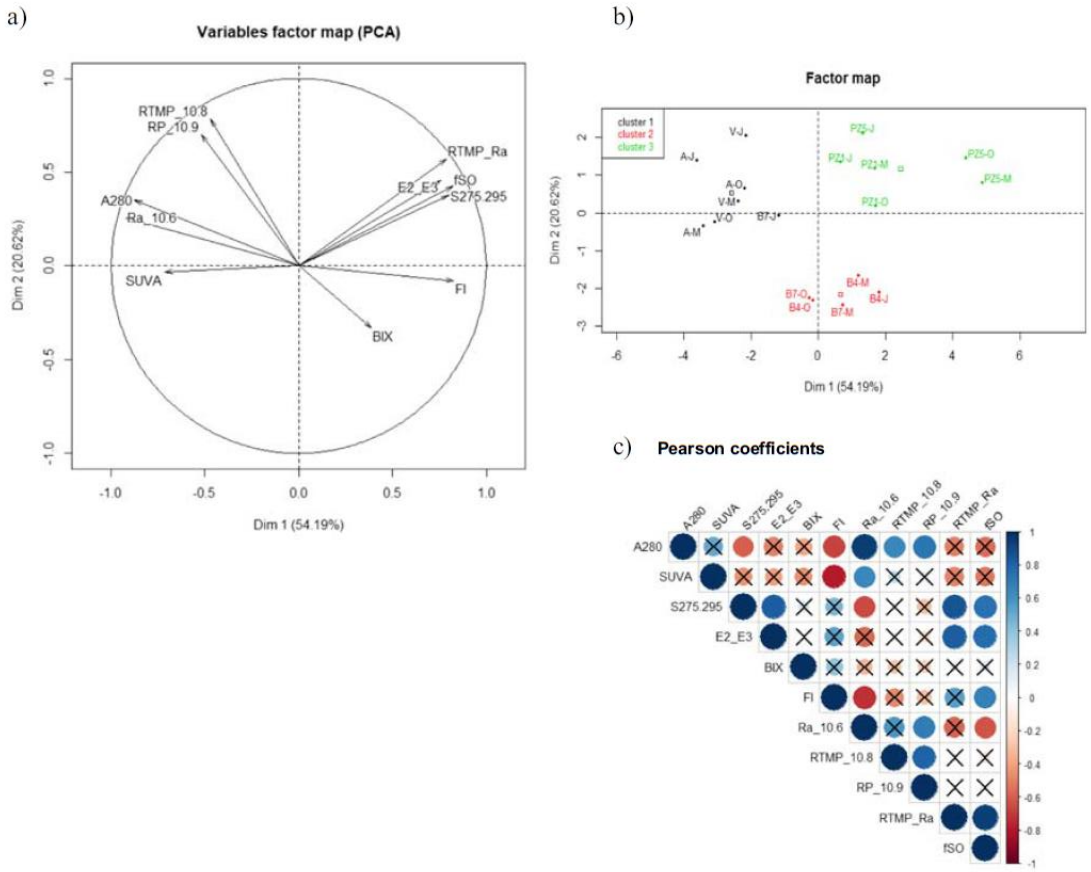

Fig. 3 Variable factor map (**a**) and individual factor map (**b**) and Pearson coefficients (**c**) from PCA obtained from 11 variables: A_{280}, SUVA, E_2/E_3, $S_{275}/_{295}$, BIX, FI, Ra, R^{TMP}, R^{P}, R^{TMP}/Ra, and Φ_{SO}. The symbols not barred with a black cross correspond to p values < 0.01

cluster was composed by DOM of Riverine Allier March, July and October and Vendage March, a second by DOM of B4 and B7 in October, a third by DOM of Vendage in July and October and B7 in July, a fourth by PZ5 March and October and a fifth by PZ1 March, July, and October, B4 and B7 in March, and PZ5 in July. B4 July showed a very singular behavior and was alone. These observations were reinforced by a previous research that had underlined the supplying of cut-off meander by the Allier River. This supply takes place by the surface connection at the downstream confluence and by an underground connection through the upstream paleochannel (Quenet et al. 2019). In this latter case, B7 is the closest location to the paleochannel arrival. B7 is fed by the Allier River with 64% of contribution (Quenet et al. 2019). This supplies lead to more similar physical and chemical conditions between B4, B7 and PZ1 in particular during winter and spring (Quenet et al. 2019).

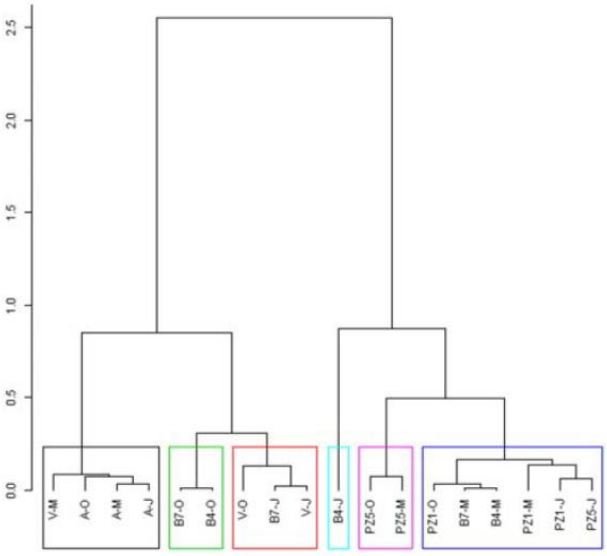

Fig. 4 Hierarchical clustering obtained from PCA obtained from 6 variables: A_{280}, SUVA, E_2/E_3, $S_{275}/_{295}$, BIX, and FI

The sampling site PZ5 that is situated on the left bank is much less affected by the Allier River. Indeed, the alluvial groundwater was identified to supply the cut-off meander during low flow at the left bank. Thus, PZ5, influenced by the alluvial aquifer, is apart considering both the hydrodynamic functioning (Quenet et al. 2019) and the results of this study (DOM and DOC results). Moreover, PZ sampling points

present some differences compared to the surface sampling points as groundwater has a percolation origin. At last, DOM river Allier all over the year and Vendage in March were apart as they are running water crossing forests and fields. They are enriched in organic matter from soil compared to the other DOM and are more aromatic. DOM Vendage in July and October were close to DOM of B4 October and B7 October suggesting connections.

To conclude, this Auzon site presents a diversity of DOMs that were characterized by their chemical and spectral properties and their ability to generate reactive species across the year. Three sub-groups were identified: DOM of running rivers, DOM of standing water cut-off meander and DOM of aquifers. As expected, parameters variations were linked to hydrologic movements, vegetation cover and organic matter inputs. Analysis of the data also informs on the hydrological functioning of this wetland.

Acknowledgments The authors thank Mahaut Sourzac (UMR EPOC) for helping in PCA calculations.

Funding information This paper is part of a project that has received funding from the European Union's Horizon 2020 research and innovation program under the Marie Skłodowska-Curie grant agreement No 765860 (Aquality).

Compliance with ethical standards

Disclaimer The paper reflects only the author's view and that the Agency is not responsible for any use that may be made of the information it contains.

References

Beauger A (2008) Impact de la capture d'un chenal fluviatile par une ancienne gravière sur la distribution des macroinvertébrés benthiques. Rev Sci Eau J Water Sci 21:87–98. https://doi.org/10.7202/017933ar

Beauger A, Delcoigne A, Voldoire O, Serieyssol K, Peiry J-L (2015) Distribution of diatom, Macrophyte and benthic macroinvertebrate communities related to spatial and environmental characteristics: the example of a cut-off meander of the river Allier (France). Cryptogam Algol 36:323–355. https://doi.org/10.7872/crya/v36.iss3.2015.323s

Birdwell JE, Engel AS (2010) Characterization of dissolved organic matter in cave and spring waters using UV-vis absorbance and fluorescence spectroscopy. Org Geochem 41:270–280. https://doi.org/10.1016/j.orggeochem.2009.11.002

Bodhipaksha LC, Sharpless CM, Chin YP, Sander M, Langston WK, Mackay AA (2015) Triplet photochemistry of effluent and natural organic matter in whole water and isolates from effluent receiving rivers. Environ Sci Technol 49:3453–3463. https://doi.org/10.1021/es505081w

Boyle ES, Guerriero N, Thiallet A, Vecchio RD, Blough NV (2009) Optical properties of humic substances and CDOM: relation to structure. Environ Sci Technol 43:2262–2268. https://doi.org/10.1021/es803264g

Coble PG (2007) Marine optical biogeochemistry: the chemistry of ocean color. Chem Rev 107:402–418. https://doi.org/10.1021/cr050350

Coelho C, Guyot G, ter Halle A, Cavani L, Ciavatta C, Richard C (2011) Photoreactivity of humic substances: relationship between fluorescence and singlet oxygen production. Environ Chem Lett 9:447–451. https://doi.org/10.1007/s10311-010-0301-3

Cooper WJ, Zika RG (1983) Photochemical formation of hydrogen peroxide in surface and ground waters exposed to sunlight. Science 220, 711:–712. https://doi.org/10.1126/science.220.4598.711

Dalrymple RM, Carfagno AK, Sharpless CM (2010) Correlations between dissolved organic matter optical properties and quantum yields of singlet oxygen and hydrogen peroxide. Environ Sci Technol 44:5824–5829. https://doi.org/10.1021/es101005u

Davidson N (2014) How much wetland has the world lost? Long-term and recent trends in global wetland area. Mar Freshw Res 65:936–941. https://doi.org/10.1071/MF14173

De Haan H, De Boer T (1987) Applicability of light absorbance and fluorescence as measures of concentration and molecular size of dissolved organic carbon in humic Laken Tjeukemeer. Water Res 21:731–734. https://doi.org/10.1016/0043-1354(87)90086-8

Felcyn JR, Davis JCC, Tran LH, Berude JC, Latch DE (2012) Aquatic photochemistry of Isoflavone phytoestrogens: degradation kinetics and pathways environ. Sci Technol 46:6698–6704. https://doi.org/10.1021/es301205a

Gao H, Sabo JL, Chen X, Liu Z, Yang Z, Ren Z, Liu M (2018) Landscape heterogeneity and hydrological processes: a review of landscape-based hydrological models. Landsc Ecol 33:1461–1480. https://doi.org/10.1007/s10980-018-0690-4

Gleick PH (1998) Water in crisis: paths to sustainable water use. Ecol Appl 8:571–579. https://doi.org/10.2307/2641249

Haag WR, Hoigné JR, Gassman E, Braun AM (1984) Singlet oxygen in surface waters part I: Furfyryl alcohol as a trapping agent. Chemosphere 13:631–640. https://doi.org/10.1016/0045-6535(84)90199-1

Helms JR, Stubbins A, Ritchie JD, Minor EC, Kieber DJ, Mopper K (2008) Absorption spectral slopes and slope ratios as indicators of molecular weight, source, and photobleaching of chromophoric dissolved organic matter. Limnol Oceanogr 53:955–969. https://doi.org/10.2307/40058211

Huguet A, Vacher L, Relexans S, Saubusse S, Froidefond JM, Parlanti E (2009) Properties of fluorescent dissolved organic matter in the Gironde Estuary. Org Geochem 40:706–719. https://doi.org/10.1016/j.orggeochem.2009.03.002

Kouras S, de Sainte-Claire P, ter Halle A, Amine-Khodja A, Richard C (2011) Mechanism of asymmetric triazine-5(4h)-one photodeamination. Evidence for triplet state keto-enol tautomerism. J Phys Chem A 115:14397–14406. https://doi.org/10.1021/jp208907f

Lever J, Krzywinski M, Altman N (2017) Principal component analysis. Nat Methods 14:641–642. https://doi.org/10.1038/nmeth.4346

Lou T, Xie H (2006) Photochemical alteration of the molecular weight of dissolved organic matter. Chemosphere 65:2333–2342. https://doi.org/10.1016/j.chemosphere.2006.05.001

Maizel AC, Remucal CK (2017) Molecular composition and photochemical reactivity of size-fractionated dissolved organic matter. Environ Sci Technol 51:2113–2123. https://doi.org/10.1021/acs.est.6b05140

McCabe AJ, Arnold WA (2016) Seasonal and spatial variabilities in the water chemistry of prarie pothole wetlands influence the photoproduction of reactive intermediates. Chemosphere 155(C): 640–647. https://doi.org/10.1016/j.chemosphere.2016.04.078

McCabe AJ, Arnold WA (2017) Reactivity of triplet excited states of dissolved natural organic matter in stormflow from mixed-use watersheds. Environ Sci Technol 51:9718–9728. https://doi.org/10.1021/acs.est.7b01914

McCullough IM, Cheruvelil KS, Collins SM, Soranno PA (2019) Geographic patterns of the climate sensitivity of lakes. Ecol Appl 29:2019, in press. https://doi.org/10.1002/eap.1836

Mckay G, Huang W, Romera-Castillo C, Crouch JE, Rosario-Ortiz FL, Jaffé R (2017) Predicting reactive intermediate quantum yields from dissolved organic matter photolysis using optical properties and antioxidant capacity. Environ Sci Technol 51:5404–5413. https://doi.org/10.1021/acs.est.6b06372

McKnight DM, Boyer EW, Westerhoff PK, Doran PT, Kulbe T, Andersen DT (2001) Spectrofluorometric characterization of dissolved organic matter for indication of precursor organic material and aromaticity. Limnol Oceanogr 46:38–48. https://doi.org/10.4319/lo.2001.46.1.0038

Peterson BM, McNally AM, Cory RM, Thoemke JD, Cotner JB, McNeill K (2012) Spatial and temporal distribution of singlet oxygen in Lake Superior. Environ Sci Technol 46:7222–7229. https://doi.org/10.1021/es301105e

Peuravouri J, Pihlaja K (1997) Molecular size distribution and spectroscopic properties of aquatic humic substances. Anal Chim Acta 337: 133–149. https://doi.org/10.1016/S0003-2670(96)00412-6

Queimaliños C, Reissig M, Pérez GL, Soto Cárdenas C, Gerea M, Garcia PE, García D, Diéguez MC (2019) Linking landscape heterogeneity with lake dissolved organic matter properties assessed through absorbance and fluorescence spectroscopy: Spatial and seasonal patterns in temperate lakes of Southern Andes (Patagonia, Argentina). Sci Total Environ 686:223–235. https://doi.org/10.1016/j.scitotenv.2019.05.396

Quenet M, Celle-Jeanton H, Voldoire O, Albaric J, Huneau F, Allain E, Garreau A, Peiry J-L, Beauger A (2019) Study of river/oxbow surface water - alluvial groundwater interactions using hydrodynamic, geochemical and isotopic approaches (Auzon oxbow, Allier River, Auvergne, France). J Hydrol 577:123936. https://doi.org/10.1016/j.jhydrol.2019.123936

Reitsema RE, Meire P, Schoelynck J (2018) The future of freshwater macrophytes in a changing world: dissolved organic carbon quantity and quality and its interactions with macrophytes. Front Plant Sci 9: 629. https://doi.org/10.3389/fpls.2018.00629

Rosario-Ortiz FL, Canonica (2016) S probe compounds to assess the photochemical activity of dissolved organic matter. Environ Sci Technol 50:12532–12547. https://doi.org/10.1021/acs.est.6b02776

Sandvik S, Bilski P, Pakulski J, Chignell C, Coffin R (2000) Photogeneration of singlet oxygen and free radicals in dissolved organic matter isolated from the Mississippi and Atchafalaya River plumes. Mar Chem 69:139–152. https://doi.org/10.1016/S0304-4203(99)00101-2

Shang J, Chen J, Shen Z, Xiao X, Yang H, Wang Y, Ruan A (2015) Photochemical degradation of PAHs in estuarine surface water: effects of DOM, salinity, and suspended particulate matter. Environ Sci Pollut Res 22:12374–12383. https://doi.org/10.1007/s11356-015-4543-2

Sobek S, Tranvik LJ, Prairie YT, Kortelainen P, Cole JJ (2007) Patterns and regulation of dissolved organic carbon: an analysis of 7,500 widely distributed lakes. Limnol Oceanogr 52:1208–1219. https://doi.org/10.4319/lo.2007.52.3.1208

Søndergaard M (1981) Kinetics of extracellular release of 14 C-labelled organic carbon by submerged macrophytes. Oikos 36:331–347. https://doi.org/10.2307/3544631

Stedmon CA, Markager S (2005) Resolving the variability in dissolved organic matter fluorescence in a temperate estuary and its catchment using PARAFAC analysis. Limnol Oceanogr 50:686–697. https://doi.org/10.4319/lo.2005.50.2.0686

Sutton MA, Bleeker A, Howard CM, Bekunda M, Grizzetti B, de Vries W, van Grinsven HJM, Abrol YP, Adhya TK, Billen G, Davidson EA, Datta A, Diaz R, Erisman JW, Liu XJ, Oenema O, Palm C, Raghuram N, Reis S, Scholz RW, Sims T, Westhoek H, Zhang FS (2013) Our nutrient world: the challenge to produce more food and energy with less pollution. NERC/Centre for Ecology & Hydrology, Edinburgh

Timko SA, Romera-Castillo C, Jaffé R, Cooper WJ (2014) Photoreactivity of natural dissolved organic matter from fresh to marine waters in the Florida Everglades, USA. Environ Sci 16:866–878. https://doi.org/10.1039/C3EM00591G

Vione D, Maurino V, Minero C, Pelizzetti E (2005) Reactions induced in natural waters by irradiation of nitrate and nitrite ions. Hdb Env Chem Vol 2, Part M, Springer-Verlag Berlin pages 221–253

Weisshar J, Aiken GR, Bergamaschi BA, Fram MS, Fugii R, Mopper K (2003) Evaluation of specific ultraviolet absorbance as an indicator of the chemical composition and reactivity of dissolved organic carbon. Environ Sci Technol 37:4702–4708. https://doi.org/10.1021/es030360x

Wilkinson F, Helman WP, Ross AB (1995) Rate constants for the decay and reactions of the lowest electronically excited singlet state of molecular oxygen in solution. An expanded and revised compilation. J Phys Chem Ref Data 24:663–677. https://doi.org/10.1063/1.555965

Zepp RG, Wolfe NL, Baughman GL, Hollis RC (1977) Singlet oxygen in natural waters. Nature 267:421–423. https://doi.org/10.1038/267421a0

Zsolnay A, Baigar E, Jimenez M, Steinweg B, Saccomandi F, (1999) Differentiating with fluorescence spectroscopy the sources of dissolved organic matter in soils subjected to drying. Chemosphere 38: 45–5010. https://doi.org/10.1016/S0045-6535(98)00166-0

Supporting Information

Study of the dissolved organic matter (DOM) of the Auzon cut-off meander (Allier river, France) by spectral and photoreactivity approaches

Davide Palma[a], Mohamad Sleiman[a], Olivier Voldoire[b], Aude Beauger[b], Edith Parlanti[c], Claire Richard[a*]

[a]Université Clermont Auvergne, CNRS, SIGMA-Clermont, ICCF, F-63000 Clermont-Ferrand, France

[b]Université Clermont Auvergne, CNRS, GEOLAB, F-63000 Clermont-Ferrand, France

[c]Université Bordeaux, CNRS, UMR EPOC, Talence F-33405, France

* Corresponding author: Claire Richard

Claire.richard@uca.fr

Tel: +33 (0)4 73 40 71 42

Fax: +33 (0)4 73 40 77 00

Text 1. Full description of the site

The study area is a cut-off meander of the Allier River, a tributary of the Loire River situated in the Massif central (France) (**Fig. SI-1a & b**) in the southern part of a graben (in the small subsidence basin of Brioude). The area is about 400 m a.s.l and 160 km from the source. The study area presents a temperate continental climate with relatively hot summers (air temperatures up to 24.6°C and 23.9°C in mean respectively in July and August) and cold winters (mean temperatures around -2 and -3°C from December to February; "Météo-France" n.d.). Annual precipitations are moderate (692 mm on average) due to a shelter effect which affects the valley and most of the events occur between May and October (423 mm in cumulative precipitation; "Météo-France" n.d.). Mountainous areas of the upper Allier catchment are more humid with a total precipitation around 2000 mm mainly occurring during winter and late spring and minimums during summer (around 570 mm). The basin is composed of metamorphic and basaltic bedrock and filled with Oligocene sand and clay deposits. The agricultural activities (grazing and cereals production) remain the main anthropogenic pressures. Most of the water resource of the area is located in the modern alluvial formations that constitute the aquifer of the Allier River alluvial groundwater. This resource is intensely exploited for the supply of drinking water but not on the study site. This unconfined aquifer extends over a width of between 0.5 and 2 km and a thickness of 15 m in the most favorable areas, as for the Auzon cut-off meander.

In 1989. the Auzon cut-off meander was formed when the Allier River captured a gravel-pit and modified the course of the stream. The upper part of the channel was rapidly in-filled by sand and gravels; since then, only the downstream end of the cut-off meander remains connected to the main stream conferring it the first stage in oxbow cycle. The cut-off meander analyzed over its approximate 560 m length was divided into three distinct zones (**Fig. SI-1c**): 1) the upstream zone disconnected from the river and similar to a pond. with an important development of macrophytes (197 m length. 13 m width. maximum depth around 1.80 m. slope = 0.01%; 2) the intermediate zone corresponding to a geomorphological riffle characterized by the alternation of lentic and lotic areas with dominant mineral substrates (176 m length, width ranging from 30 cm to 8 m, maximum depth around 0.40 m, slope = 0.39%); 3) the downstream zone characterized by bedload deposits coming from the river and macrophytes (188 m length. 17 m width. maximum depth around 1.60 m. slope = 0.06%). Since the first studies in 2007, the site's monitoring is extending to water quality analyses by sampling surface water within the cut-off meander and the Allier River to complete ecological investigations in 2012. In 2014, SOAHAL Observatory (Système d'Observation d'une Annexe Hydraulique de l'Allier) was set with the implantation of deep observation boreholes to monitor alluvial groundwater and complete the water quality monitoring.

Fig. SI-2. Fluorescent tubes irradiance.

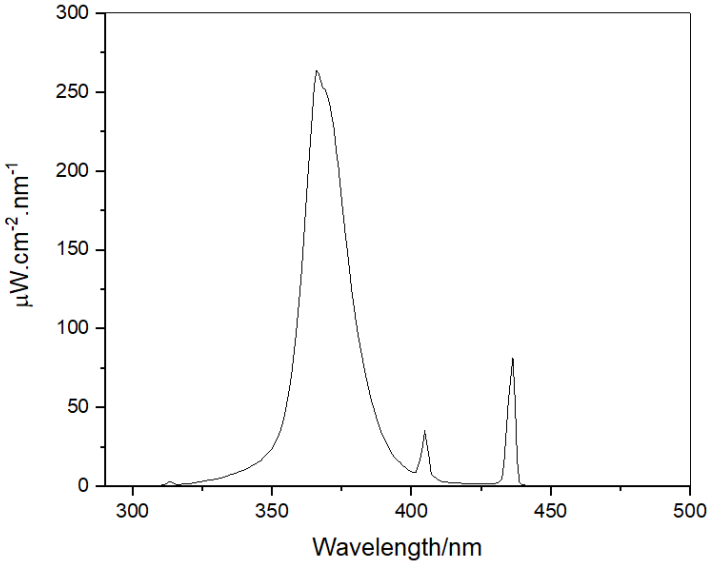

Fig. SI-3. UV-visible spectra of the different samples.

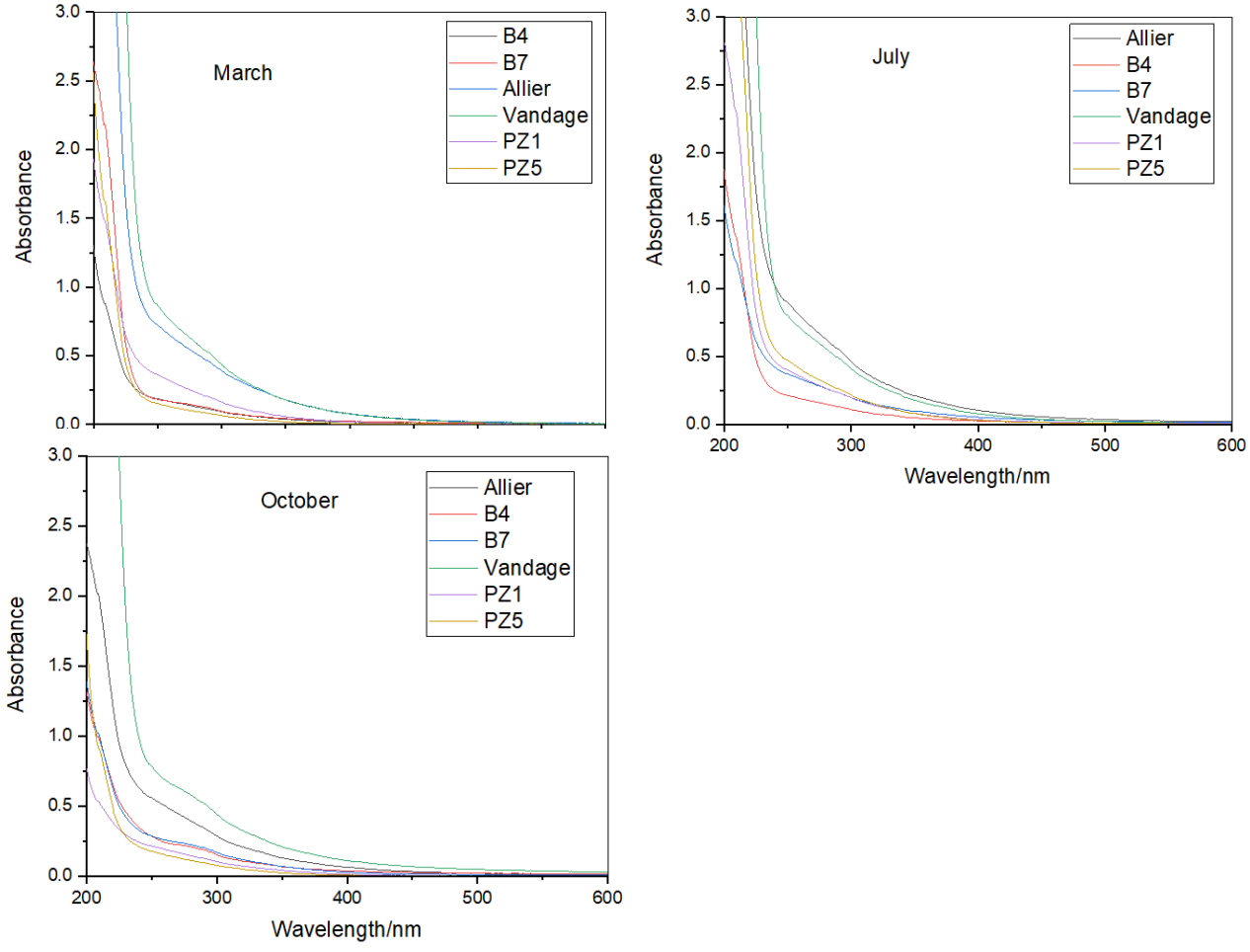

Fig. SI-4. Emission spectra of samples upon excitation at 260 nm. Black line for March. red line for July and blue line for October.

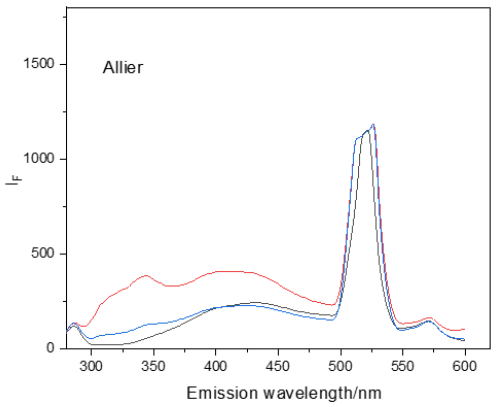

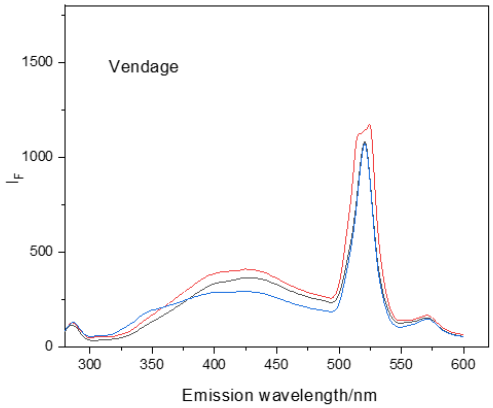

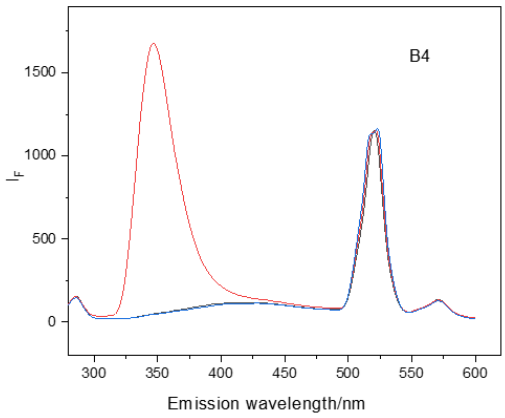

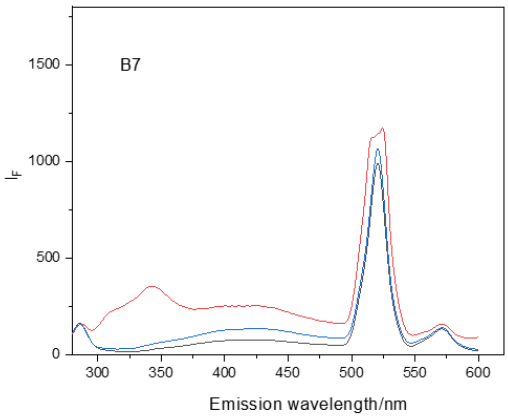

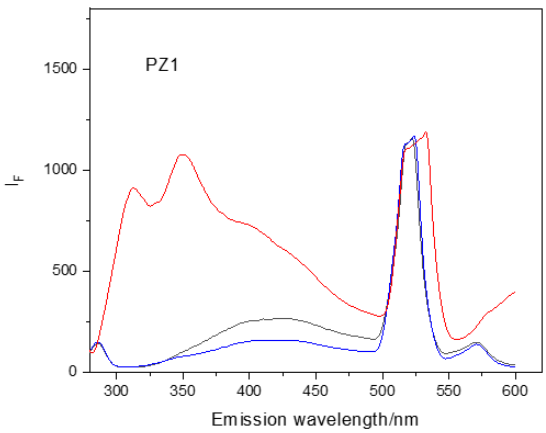

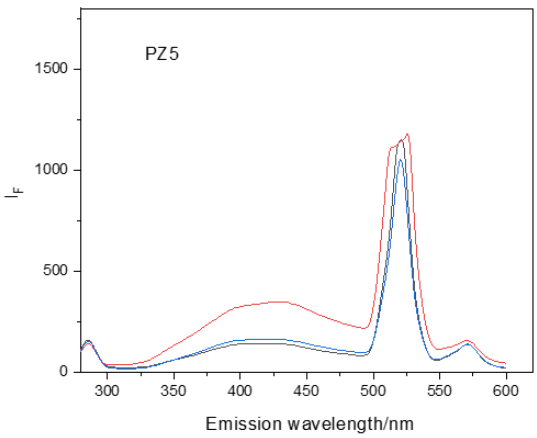

Fig SI-5. A) Typical consumption profile of TMP when irradiated in the presence of cut-off meander DOM and B) formation of photoproduct of FFA.

A)

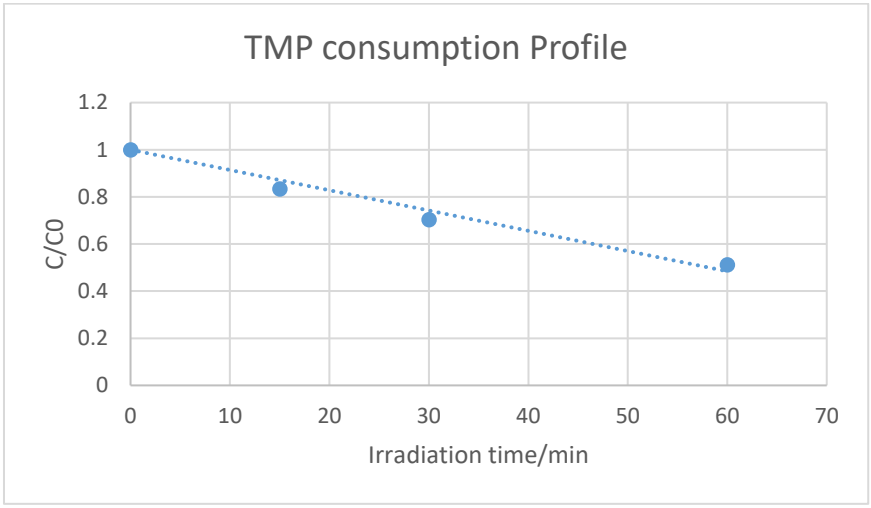

B)

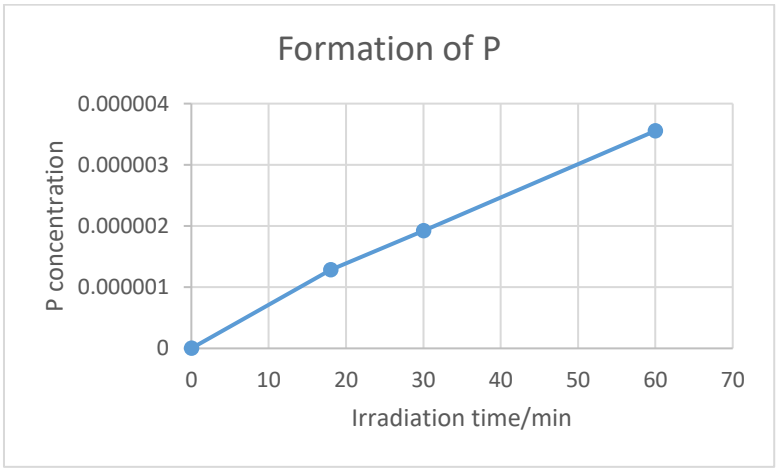

Table SI-1 : Concentration of major ions ($mg.L^{-1}$) in the different samples.

March	Cl^-	Br^-	NO_2^-	NO_3^-
Allier	10.9	0.0	0.014	5.3
B4	31.5	0.0	0.014	0.62
B7	15.9	0.0	0.011	2.7
Vendage	56.5	0.0	0.165	21
PZ1	45.1	0.0	0.010	1.3
PZ5	78.7	0.0	0.011	1.8

July	Cl^-	Br^-	NO_2^-	NO_3^-
Allier	9.2	0.0	0.01	2.5
B4	19.8	0.0	0.01	1.2
B7	11.6	0.0	0.01	3.3
Vendage	52.4	0.0	1.19	16.0
PZ1	10.8	0.0	0.01	2.2
PZ5	35.0	0.0	0.02	3.9

October	Cl^-	Br^-	NO_2^-	NO_3^-
Allier	10.1	0.0	0.01	1.5
B4	19.1	0.0	0.01	0.2
B7	15.2	0.0	0.01	1.9
Vendage	84.5	0.0	1.21	13.8
PZ1	12.5	0.0	0.01	0.1
PZ5	82.3	0.0	0.02	0.4

MANUSCRIPT 2

Fluorescence analysis allows to predict the oxidative capacity of humic quinones in dissolved organic matter: implication for pollutant degradation.

Publishing journal: Environmental Chemistry Letters

Date of acceptance: 6 November 2020

Environmental Chemistry Letters
https://doi.org/10.1007/s10311-020-01137-z

ORIGINAL PAPER

Fluorescence analysis allows to predict the oxidative capacity of humic quinones in dissolved organic matter: implication for pollutant degradation

Davide Palma[1] · Edith Parlanti[2] · Mahaut Sourzac[2] · Olivier Voldoire[3] · Aude Beauger[2] · Mohamad Sleiman[1] · Claire Richard[1]

Received: 15 June 2020 / Accepted: 6 November 2020

Abstract

Dissolved organic matter (DOM) controls the degradation and sequestration of aquatic pollutants and, in turn, water quality. In particular, pollutant degradation is performed by oxidant species that are generated by exposure of DOM to solar light, yet, since DOM is a very complex mixture of poorly known substances, the relationships between potential oxidant precursors in DOM and their oxydative capacity is poorly known. Here, we hypothesized that production of oxidant species could be predicted using fluorescence analysis. We analysed water samples from an alluvial plain by fluorescence spectroscopy; the three-dimensional spectra were then decomposed into seven individual components using a multi-way algorithm. Components include a protein-like fluorophore, e.g. tryptophan-like and tyrosine-like, three humic fluorophores, 2-naphthoxyacetic acid, and a by-product. We compared component levels with the ability of water samples to generate reactive species under solar light. The results show a strong correlation between reactive species production and the intensity of two humic-like fluorophores assigned to reduced quinones. Monitoring these fluorophores should thus allow to predict the ability of DOM degradation of pollutants in surface waters.

Keywords Dissolved organic matter · Cut-off meander · Quinonic-like components · Triplet excited states · Singlet oxygen · Correlation

Introduction

Dissolved organic matter (DOM) encompasses ubiquitous natural components able to generate oxidant species under solar light exposure and thus to degrade aquatic pollutants in surface waters. Previous works have shown that the capacity of DOM to generate reactive species under solar irradiation could be predicted measuring its absorbance properties (Dalrymple et al 2010; Mckay et al. 2017; Peterson et al. 2012; Palma et al. 2020). Previous works also suggested that correlations may exist between DOM photoreactivity and fluorescence parameters (Coelho et al. 2011) or individual fluorescent components identified by deconvolution of the three-dimensional spectra by parallel factor analysis (PARAFAC, Timko et al. 2014; Bai et al. 2018; Batista et al. 2016).

Here, our goal was to investigate the fluorophores linked to the photochemical generation of oxidant species such as DOM triplet excited states (^{3}DOM*) and singlet oxygen (SO) on waters sampled in an experimental site. This site was chosen because it offers a variety of water types: riverine, underground and stagnant. The individual fluorescent components were identified using literature data and the OpenFluor database and their spatial and temporal distribution were determined. Finally, the exploration of correlations between component intensities and rates of oxidant species formation allowed to connect reactive species formation to

Electronic supplementary material The online version of this article (https://doi.org/10.1007/s10311-020-01137-z) contains supplementary material, which is available to authorized users.

✉ Claire Richard
Claire.richard@uca.fr

[1] Université Clermont Auvergne, CNRS, SIGMA-Clermont, ICCF, 63000 Clermont-Ferrand, France

[2] Université Bordeaux, CNRS, EPOC UMR 5805, 33405 Talence, France

[3] Université Clermont Auvergne, CNRS, GEOLAB, 63000 Clermont-Ferrand, France

Published online: 23 November 2020

the presence of reduced quinonic structures identified based on the literature data.

Experimental

Site description and samplings

The experimental site is the SOAHAL Observatory 'Système d'Observation d'une Annexe Hydraulique de l'ALlier' (Peiry et al 2014). This study area, previously described (Palma et al 2020), is a cut-off meander of the Allier River, a tributary of the Loire River situated in the temperate zone (Massif central, France). It includes the Auzon cut-off meander, the Allier River and its tributary Vendage, as well as two aquifers, the alluvial fluvial flow and the watershed ones (Figure SI-1). Water samples were collected in March, July and October 2018 in Allier River, in Vendage River, in the cut-off meander at sampling sites B4 and B7, and in the piezometers PZ1 and PZ5 (Figure SI-1).

Fluorescence spectra recording and deconvolution

The three-dimensional fluorescence spectra recording is described in Supporting Information. All fluorescence signals were normalized using the area under the Raman peak at excitation 350 nm of purified water; reverse osmosis RIOS 5 and Synergy-Millipore device, resistivity 18 MΩ cm, DOC < 0.1 mg L^{-1} (Cory and McKnight 2005). Solutions were diluted before measurement to have an absorbance < 0.1 at 250 nm, and the recorded spectra were multiplied by the dilution coefficient. Parallel factor analysis is classically used to decompose the three-dimensional spectra and facilitate the identification and quantification of independent underlying fluorescent signals, termed "components" (Murphy et al 2013). The multi-way parallel factor analysis model was run for 3 to 8 components with non-negativity constraints using the DOMFluor toolbox (ver. 1.7) for MATLAB (R14-6.5) as described by Stedmon and Bro (2008). Seven components were determined, based on the examination of the residuals from models, split half analysis and visual inspection of spectral shapes of each component, and compared to previously validated components using the OpenFluor fluorescence database (Murphy et al 2014).

Rates of reactive species production

2,4,6-Trimethylphenol (Sigma-Aldrich, certified reference material) was used to scavenge ^{3}DOM* while furfuryl alcohol (Sigma-Aldrich, 98%) to trap SO. The protocol used to measure the consumption of these probes and the processes used to establish the rate laws are described in SI and in Palma et al (2020). Briefly, the rate of 2,4,6-trimethylphenol consumption (R^{TMP}) is equal to

$$R^{TMP} = R^{3DOM*} \times \alpha_{TMP} = R_a \times \Phi_{3DOM*} \times \alpha_{TMP} \quad (1)$$

where R^{3DOM*} is the rate of ^{3}DOM* production and α_{TMP} the fraction of ^{3}DOM* trapped by 2,4,6-trimethylphenol. R_a is the rate of light absorption by DOM between 300 and 450 nm calculated using the Beer–Lambert law $I_a = I_0 \times (1 - 10^{-A})$, the absorption spectrum of DOM and the emission spectrum of the tubes, Φ_{3DOM*}, the quantum yield of ^{3}DOM* production. The rate of 2-hydroxypyranone formation (R^P), the main product of reaction between furfuryl alcohol and SO (chemical yield = 85%) is equal to:

$$R^P = 0.85 \times R^{SO} \times \alpha_{FFA} = 0.85 \times R_a \times \Phi_{SO} \times \alpha_{FFA} \quad (2)$$

where R^{SO} is the rate of SO production, Φ_{SO} is the quantum yield of SO production and α_{FFA} the fraction of SO trapped by furfuryl alcohol.

Statistical analyses

Statistical analyses were performed with the R statistical software (R version 3.6.1, R Foundation for Statistical Computing). To reveal the relationships between the DOM fluorescence characteristics and its capacity to generate reactive species under irradiation, principal component analysis was conducted on scaled and centred data of all samples and 10 variables, i.e. the 7 individual parallel factor analysis components, and the different rates. Pearson correlation coefficients were reported for all correlations where data were normally distributed. P-values < 0.01 were considered statistically significant.

Results and discussion

Assignment of the individual parallel factor analysis components

The contour plots of the 7 individual components determined by parallel factor analysis decomposition are presented in Fig. 1. Components C1 to C5 have been successfully matched in the OpenFluor database with similarity scores higher than 0.95. Component C1 (λ_{exc} = 300 and < 250) nm/λ_{em} = 390 nm) is a widespread component generally found in marine and terrestrial aquatic environments and attributed to low molecular weight substances (Osburn et al. 2011; Coble 2007). Component C2 (λ_{exc} = 280 nm/λ_{em} = 300, 340 nm) seems to gather the protein-like fluorophores with emission at 300 nm for tyrosine-like and the emission at 330–350 nm for tryptophane-like fluorophores (Coble 2007; Parlanti et al. 2000).

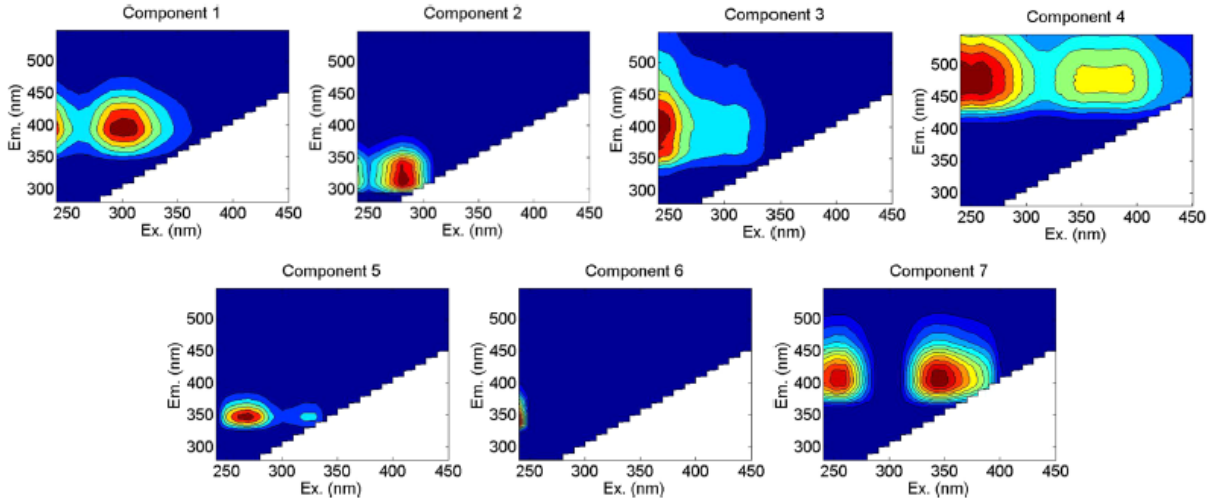

Fig. 1 Fluorescence signatures of the seven components identified by parallel factor analysis decomposition of the three-dimensional spectra. They were assigned by comparison with the literature or to commercial compound spectrum, to widespread low molecular weight component (Component 1—C1), to protein-like fluorophores (Component 2—C2), to (photo)degraded terrestrial component (Component 3—C3), to microbially reduced quinone-like fluorophores (Component 4—C4), to 2-naphthoxy-acetic acid (Component 5—C5), to a non-identified component probably linked to C5 (Component 6—C6), and to reduced quinone-like component (Component 7—C7)

Component C3 (λ_{exc} = 245 and 315 nm/λ_{em} = 400 nm) was already observed (Osburn et al 2012; Romero et al 2017; Stedmon et al 2003) and assigned as fluorophores from terrestrial origin possibly produced by (photo)degradation (Osburn et al 2012). Component C4 (λ_{exc} = 260 and 370 nm/λ_{em} = 480 nm) is also a widespread component that has been described as high molecular weight fluorophores (Kowalczuk et al 2013; Murphy et al 2006; Stedmon et al 2007). It was found to be produced during bacterial processing of DOM (Amaral et al 2016) and could derive from microbial metabolism (Romera-Castillo et al 2011).

Component C4 has also strong analogies with component SQ2 (λ_{exc} = 270 and 380 nm/λ_{em} = 462 nm) assigned by Cory and McKnight 2005 to reduced quinone-like component. Component C5 (λ_{exc} = 270 and 325 nm/λ_{em} = 345 nm) was assigned to 2-naphthoxy-acetic acid by comparison with an authentic sample (SI). 2-Naphthoxy-acetic acid is generally used for controlling of preharvest fruit drop on strawberries and tomatoes. The detection of this highly fluorescent anthropogenic compound in the cut-off meander water samples is explained by the presence of vegetable farming near the site.

Component C6 (λ_{exc} < 245 nm/λ_{em} = 345 nm) did not find matches in OpenFluor-database. At last, C7 had strong analogies with component labelled SQ3 (λ_{exc} = 265 and 345 nm/λ_{em} = 412 nm) assigned once again to a reduced quinone-like component (Cory and McKnight 2005).

Spatial and temporal distribution of the individual parallel factor analysis components

The spatial and temporal variations of the component fluorescence intensities are shown in Fig. 2. The intensity of 2-naphthoxy-acetic (C5) acid and C6 was particularly important in B4-July. Components C5 and C6 appeared together in Allier-July, B7-July, PZ5-July and Vendage-July suggesting that C6 could be a degradation product of 2-naphthoxy-acetic acid. C1 and C2 were detected in high amounts in PZ1-July, Allier River-July and B7-July, while in moderate amounts in Vendage River and Allier-River-October and in minor amounts in the other water samples. As a part of the cut-off meander was covered with aquatic plants in July, these results suggest a microbial or algal origin for C1 and C2. C3 was mainly present in Allier River and Vendage River, both characterized by the highest DOM aromaticity (Palma et al 2020). C4 and C7 were detected in all the samples in quite similar fluorescence intensities, suggesting that they could have common origins and fates. Higher intensities were found in July than in March or October and in River than in cut-off meander samples.

Correlation between individual parallel factor analysis components and photoreactivity of dissolved organic matter

Results on the dissolved organic matter (DOM) photoreactivity of the different samples are shown Fig. 3. The

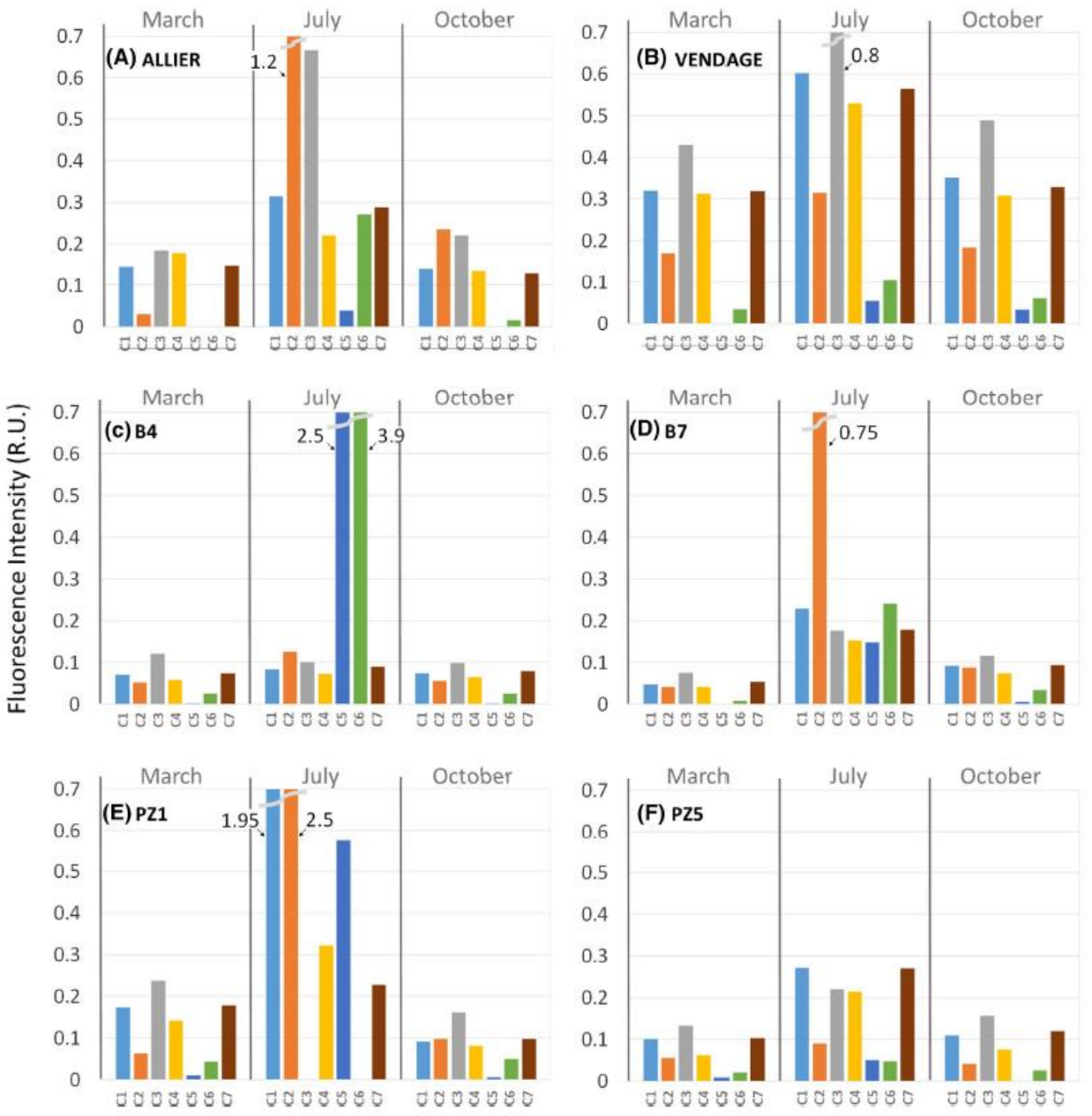

Fig. 2 Temporal variations of the seven components determined by parallel factor analysis decomposition—C1) widespread low molecular weight component; C2) protein-like fluorophores, C3) (photo)degraded terrestrial component; C4) microbially reduced quinone-like fluorophores, C5) 2-naphthoxy-acetic acid, C6) non-identified component probably linked to the component C5 and C7) reduced quinone-like component—for the six studied sites: **A** Allier, **B** Vendage, **C** cut-off meander sites B4, **D** cut-off meander sites B7, **E** piezometer PZ1 and **F** piezometer PZ5. Fluorescence intensities are reported in Raman units (R.U.)

rivers Allier and Vendage logically contained the more absorbing DOM (Fig. 3A) because their waters enrich in soil aromatic organic matter while crossing forests and fields areas. The rates of 2,4,6-trimethylphenol consumption (R^{TMP}, Fig. 3B) and the rates of hydroxypyranone formation (R^{P}, Fig. 3C) shows parallel variations with highest values in July and lowest values in B4 and B7 sampling sites.

As R^{TMP} was proportional to R^{3DOM*} Eq. (1) and R^{P} to R^{SO} Eq. (2) according to our mechanistic hypotheses, the

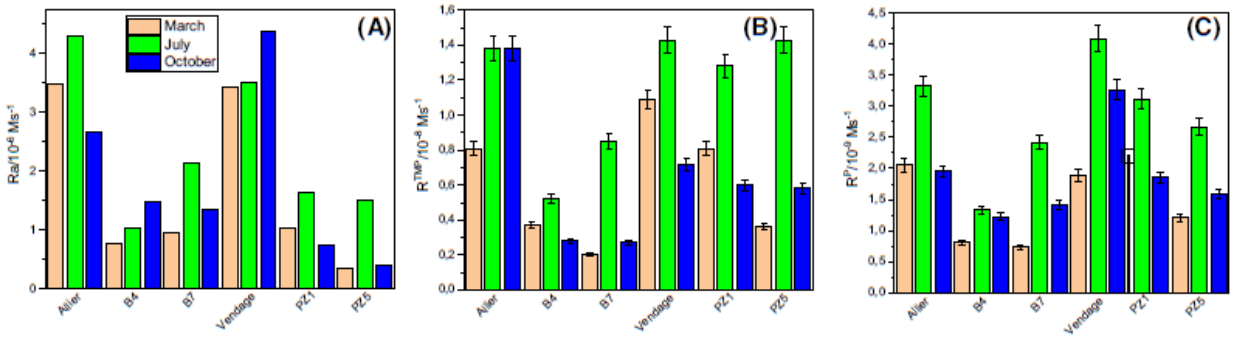

Fig. 3 Variations of dissolved organic matter (DOM) photoreactivity in the six studied sites: Allier, Vendage, cut-off meander sites B4, cut-off meander sites B7, PZ1 and PZ5, in March, July and October. **A** rate of light absorption (R_a), **B** rate of 2,4,6-trimethylphenol consumption (R^{TMP}), **C** rate of hydroxypyranone formation (R^P)

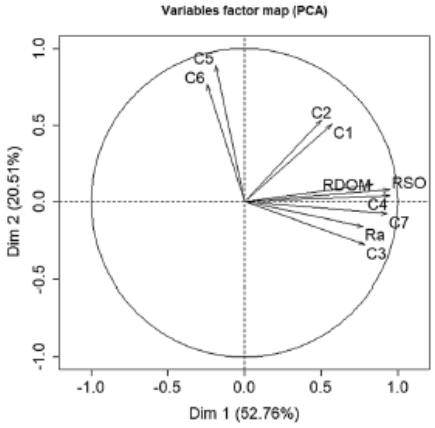

Fig. 4 Variable factor map from principal component analysis (PCA) obtained from 10 variables: the seven components determined by parallel factor analysis decomposition of the three-dimensional spectra (C1—widespread low molecular weight component, C2—protein-like fluorophores, C3—(photo)degraded terrestrial component, C4—microbially reduced quinone-like fluorophores, C5—2-naphthoxy-acetic acid, C6—non-identified component probably linked to the component C5 and C7—reduced quinone-like component, the rate of light absorption (R_a), the rate of triplet excited state formation (R^{3DOM*}) and the rate of singlet oxygen production (R^{SO})

principal component analysis of Fig. 4a is performed with R^{3DOM*} and R^{SO}. R^{3DOM*} and R^{SO} were positively correlated to each other ($R = 0.8$, $p < 0.01$) in accordance with the formation of singlet oxygen from ^{3}DOM*. Moreover, R^{3DOM*} was positively correlated to microbially derived fluorophores C4 and to reduced quinone-like component C7 ($R = 0.74$ and 0.72, $p < 0.01$, respectively), R^{SO} to C4, C7 and degraded terrestrial component C3 ($R = 0.88$, 0.88 and 0.73, with $p < 0.01$, respectively) and Ra to C3, C4 and C7 ($R = 0.75$, 0.7 and 0.69, with $p < 0.01$, respectively) (Fig. 4a and SI-4). The other components did not show any correlation. However, C1 assigned to low molecular weight substances was very near to protein-like fluorophores C2 on the variable factor map and C5, assigned to 2-naphthoxy-acetic acid, to non-identified component C6. It shows that C1 had common features with C2, and C5 with C6.

Previous works reported that the formation rate of singlet oxygen was coupled to the abundance of humic-like components emitting at long wavelength for DOM of both marine (Timko et al. 2014; Bai et al. 2018) and terrestrial origin (Batista et al. 2016; Coelho et al. 2011). Compared to these works, we were able to identify the moieties involved in the correlation, and we propose that C4 and C7 could be attributed to the reduced forms of quinonic humic-like components (Cory and McKnight 2005). This result is in line with the study of Zheng et al (2019) in which a positive correlation between electron accepting capacity of DOM, to which quinones strongly contribute, and the presence of one of the fluorescent parallel factor analysis components proposed to represent oxidized quinoid-like structures was reported.

Conclusion

We found a strong positive correlation between two individual parallel factor analysis components representing DOM quinonic moieties (C4 and C7) and DOM photoreactivity, specifically the generation of oxidant species like DOM triplet excited states and singlet oxygen. This finding confirms the role played by quinonic compounds in the sensitizing properties of natural organic matter and suggests that monitoring these compounds using fluorescence spectroscopy could be a valid approach for a rapid estimation of the sensitizing properties of DOM.

Acknowledgements This paper is part of a project that has received funding from the European Union's Horizon 2020 research and

innovation programme under the Marie Skłodowska-Curie Grant agreement No. 765860 (Aquality).

References

Amaral V, Graeber D, Calliari D, Alonso C (2016) Strong linkages between DOM optical properties and main clades of aquatic bacteria. Limnol Oceanogr 61:906–918. https://doi.org/10.1002/lno.10258

Bai Y, Cui Z, Su R (2018) Influence of DOM components, salinity, pH, nitrate, and bicarbonate on the indirect photodegradation of acetaminophen in simulated coastal waters. Chemosphere 205:108–117. https://doi.org/10.1016/j.chemosphere.2018.04.087

Batista APS, Teixeira ACSC, Cooper WJ, Cottrell BA (2016) Correlating the chemical and spectroscopic characteristics of natural organic matter with the photodegradation of sulfamerazine. Water Res 93:20–29. https://doi.org/10.1016/j.watres.2015.11.036

Coble PG (2007) Marine optical biogeochemistry: the chemistry of ocean color. Chem Rev 107:402–418. https://doi.org/10.1021/cr050350+

Coelho C, Guyot G, ter Halle A, Cavani L, Ciavatta C, Richard C (2011) Photoreactivity of humic substances: relationship between fluorescence and singlet oxygen production. Environ Chem Lett 9:447–451. https://doi.org/10.1007/s10311-010-0301-3

Cory RM, Mcknight DM (2005) Fluorescence spectroscopy reveals ubiquitous presence of oxidized and reduced quinones in DOM. Environ Sci Technol 39:8142–8149. https://doi.org/10.1021/es050696 2

Dalrymple RM, Carfagno AK, Sharpless CM (2010) Correlations between Dissolved Organic Matter Optical Properties and Quantum Yields of Singlet Oxygen and Hydrogen Peroxide. Environ Sci Technol 44(5824):5829. https://doi.org/10.1021/es101005u

Golanoski K, Fang S, Del Vecchio R, Blough NV (2012) Investigating the mechanism of phenol photooxidation by humic substances. Environ Sci Technol 46:3912–3920. https://doi.org/10.1021/es300142y

Kowalczuk P, Tilstone GH, Zabłocka M, Rottgers R, Thomas R (2013) Composition of dissolved organic matter along an atlantic meridional transect from fluorescence spectroscopy and parallel factor analysis. Mar Chem 157:170–184. https://doi.org/10.1016/j.marchem.2013.10.004

Mckay G, Huang W, Romera-Castillo C, Crouch JE, Rosario-Ortiz FL, Jaffé R (2017) Predicting reactive intermediate quantum yields from dissolved organic matter photolysis using optical properties and antioxidant capacity. Environ Sci Technol 51:5404–5413. https://doi.org/10.1021/acs.est.6b06372

Murphy KR, Ruiz G, Dunsmuir W, Waite T (2006) Optimized parameters for fluorescence-based verification of ballast water exchange by ships. Environ Sci Technol 40:2357–2362. https://doi.org/10.1021/es0519381

Murphy KR, Stedmon CA, Graeber D, Bro R (2013) Fluorescence spectroscopy and multi-way techniques. PARAFAC Anal Methods 5:6557–6566. https://doi.org/10.1039/c3ay41160e

Murphy KR, Stedmon CA, Wenig P, Bro R (2014) OpenFluor- an online spectral library of auto-fluorescence by organic compounds in the environment. Anal Methods 6:658–661. https://doi.org/10.1039/c3ay41935e

Osburn CL, Wigdahl CR, Fritz SC, Sarosb JE (2011) Dissolved organic matter composition and photoreactivity in prairie lakes of the U.S. Great Plains Limnol Oceanogr 56:2371–2390. https://doi.org/10.4319/lo.2011.56.6.2371

Osburn C, Osburn L, Handsel LT, Mikan MP, Paerl HW, Montgomery MT (2012) Fluorescence tracking of dissolved and particulate organic matter quality in a river-dominated estuary. Environ Sci Technol 46:8628–8636. https://doi.org/10.1021/es3007723l

Palma D, Sleiman M, Voldoire O, Beauger A, Parlanti E, Richard C (2020) Study of the dissolved organic matter (DOM) of the Auzon cut-off meander (Allier River, France) by spectral and photoreactivity approaches. Environ Sci Poll Res 27:26385–26394. https://doi.org/10.1007/s11356-020-09005-7

Parlanti E, Worz K, Geoffroy L, Lamotte M (2000) Dissolved organic matter fluorescence spectroscopy as a tool to estimate biological activity in a coastal zone submitted to anthropogenic inputs. Org Geochem 31:1765–1781. https://doi.org/10.1016/S0146-6380(00)00124-8

Peiry J-P, Beauger A, Celle-Jeanton H, Voldoire O, Casado A (2014) SOHAL: système d'observation d'une annexe hydraulique de l'Allier. Colloque de restitution du CPER Auvergne, Dec 2014, Clermont Ferrand, France

Peterson BM, McNally AM, Cory RM, Thoemke JD, Cotner JB, McNeill K (2012) Spatial and temporal distribution of singlet oxygen in lake superior. Environ Sci Technol 46:7222–7229. https://doi.org/10.1021/es301105e

Romera-Castillo CH, Sarmento XA, Alvarez-Salgado J, Gasol M, Marras C (2011) Net production and consumption of fluorescent colored dissolved organic matter by natural bacterial assemblages growing on marine phytoplankton exudates. Appl Environ Microbiol 77:7490–7498. https://doi.org/10.1128/AEM.00200-11

Romero CM, Engel RE, D'Andrilli J, Chen C, Zabinski C, Millera PR, Wallander R (2017) Bulk optical characterization of dissolved organic matter from semiarid wheat-based cropping systems. Geoderma 306:40–49. https://doi.org/10.1016/j.geoderma.2017.06.029

Sharpless CM (2012) Lifetimes of triplet dissolved natural organic matter (DOM) and the effect of $NaBH_4$ reduction on singlet oxygen quantum yields: Implications for DOM photophysics. Environ Sci Technol 46:4466–4473. https://doi.org/10.1021/es300217h

Stedmon CA, Markager S, Bro R (2003) Tracing DOM in aquatic environments using a new approach to fluorescence spectroscopy. Mar Chem 82:239–254. https://doi.org/10.1016/S0304-4203(03)00072-0

Stedmon CA, Thomas DN, Granskog M, Kaartokallio H, Papadimitriou S, Kuosa H (2007) Characteristics of dissolved organic matter in Baltic coastal sea ice: Allochthonous or autochthonous origins? Environ Sci Technol 41:7273–7279. https://doi.org/10.1021/es071210f

Stedmon CA, Bro R (2008) Characterizing dissolved organic matter fluorescence with parallel factor analysis: a tutorial. Limnol Oceanogr Meth 6:572–579. https://doi.org/10.4319/lom.2008.6.572

Timko SA, Romera-Castillo C, Jaff R, Cooper WJ (2014) Photo-reactivity of natural dissolved organic matter from fresh to marine waters in the Florida Everglades, USA. Environ Sci Process Impacts 16:866–878. https://doi.org/10.1039/C3EM00591G

Zheng X, Liu Y, Fu H, Qu X, Yan M, Zhang S, Zhu D (2019) Comparing electron donating/accepting capacities (EDC/EAC) between crop residue-derived dissolved black carbon and standard humic

substances. Sci Tot Environ 673:29–35. https://doi.org/10.1016/j.scitotenv.2019.04.022

Zhou H, Lian L, Yan S, Song W (2017) Insights into the photo-induced formation of reactive intermediates from effluent organic matter: The role of chemical constituents. Water Res 112:120–128. https://doi.org/10.1016/j.watres.2017.01.048

Supporting Information

Fluorescence analysis allows to predict the oxydative capacity of humic quinones in dissolved organic matter. Implication for pollutant degradation

Davide Palma[a], Edith Parlanti[b], Mahaut Sourzac[b], Olivier Voldoire[c], Aude Beauger[b], Mohamad Sleiman[a], Claire Richard[a*]

[a]Université Clermont Auvergne, CNRS, SIGMA-Clermont, ICCF, F-63000 Clermont-Ferrand, France

[b]Univ. Bordeaux, CNRS, EPOC UMR 5805, Talence F-33405, France

[c]Université Clermont Auvergne, CNRS, GEOLAB, F-63000 Clermont-Ferrand, France

* Corresponding author: Claire Richard

Claire.richard@uca.fr

Tel: +33 (0)4 73 40 71 42

Fax: +33 (0)4 73 40 77 00

Figure SI-1. a) Location of the Auzon site; b) Scheme of the Auzon site, c) the three zones of the Auzon cut-off meander. Sampling points (Allier River, Vendage River, B4 cut-off meander and B7 cut-off meander) are noted as open squares and boreholes (piezometer PZ1 and piezometer PZ5) as black stars.

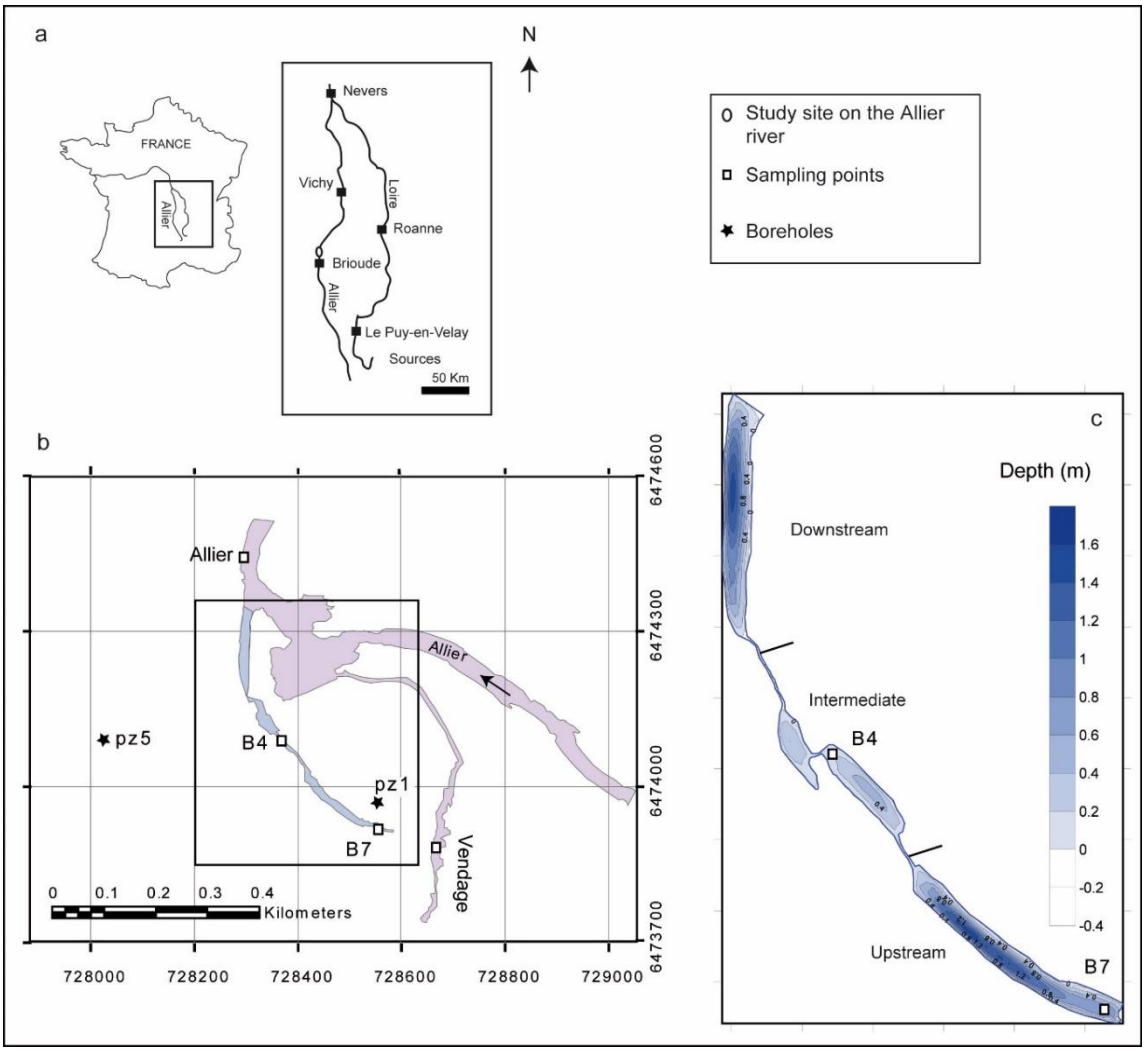

Three dimensional fluorescence spectra recording

UV-visible spectra were recorded on a Cary 3 (Varian). The three dimensional fluorescence spectra were measured using a Perkin-Elmer LS55 spectrofluorometer equipped with a pulsed Xe arc lamp. Slits were set at 10 nm for excitation and 10 nm for emission. Twenty-four emissions scans were recorded at excitation wavelength (λ_{ex}) comprised between 220 and 450 nm with 10 nm steps. The emission wavelengths (λ_{em}) were scanned from *250 to 600 nm.*

Rates of reactive species production

Furfuryl alcohol (Sigma-Aldrich, 98%) was used to trap singlet oxygen and 2,4,6-trimethylphenol (Sigma- Aldrich, certified reference material) to scavenge ^{3}DOM*. Their stock solutions were prepared in water purified using a reverse osmosis RIOS 5 and Synergy (Millipore) device (resistivity 18 MΩ cm, DOC < 0.1 mg L^{-1}) and stored at 4°C until use. Water samples containing either furfuryl alcohol at 100 □M or 2,4,6-trimethylphenol at 50 □M were irradiated with six polychromatic fluorescent tubes (Sylvania, F15 W/350BL) emitting between 300 and 450 nm, with a maximum at 365 nm. The 2,4,6-trimethylphenol (TMP) and furfuryl alcohol (FFA) losses and the formation of 2-hydroxypyranone (P), the main product of reaction between furfuryl alcohol and singlet oxygen were monitored by HPLC analysis as previously described (Palma et al 2020).

We postulated that the following processes took place to establish the rate laws:

$$DOM + h\square \rightarrow {}^1DOM^* \quad (1)$$

$$^1DOM^* \rightarrow {}^3DOM^* \quad (2)$$

$$^3DOM^* \rightarrow DOM \quad (3)$$

$$^3DOM^* + O_2 \rightarrow DOM + {}^1O_2 \quad (4)$$

$$^3DOM^* + TMP \rightarrow DOM_{+H}^{\cdot} + TMP_{-H}^{\cdot} \quad (5)$$

$$^1O_2 + solvent \rightarrow O_2 \quad (6)$$

$$^1O_2 + FFA \rightarrow P \quad (7)$$

According to this scheme, ^{3}DOM* can deactivate, react with oxygen to yield singlet oxygen or be trapped by 2,4,6-trimethylphenol. The rate of 2,4,6-trimethylphenol consumption (R^{TMP}) was thus equal to:

$$R^{TMP} = k_5\times(^3DOM^*)\times(TMP)$$
$$= k_5\times(TMP)\times R_a\times\Phi_{3DOM^*}/(k_3+ k_4\times(O_2)+ k_5\times(TMP))$$
$$= R_a\times\Phi_{3DOM^*}\times\alpha_{TMP}$$

where R_a is the rate of light absorption by DOM between 300 and 450 nm, Φ_{3DOM^*}, the quantum yield of ^{3}DOM* production and α_{TMP} the fraction of ^{3}DOM* trapped by 2,4,6-trimethylphenol.

The rate of formation of 2-hydroxypyranone (R^P), the main photoproduct of reaction between furfuryl alcohol and singlet oxygen (chemical yield =85%) was equal to:

$$= 0.85\times R_a\times\Phi_{SO}\times(FFA)/(k_6+ k_7\times(FFA)) = 0.85\times R_a\times\Phi_{SO}\times\alpha_{FFA}$$

where Φ_{SO} is the quantum yield of singlet oxygen production and α_{FFA} the fraction of singlet oxygen trapped by furfuryl alcohol.

Ra was obtained using the relationship:

$$R_a = \sum_{\lambda_1}^{\lambda_2} I_0^{\lambda} \left(1 - 10^{-A\lambda}\right) \times \Delta\lambda \times 1000 N^{-1} \qquad \text{eq 5}$$

where I_0^{λ} expressed in Photons.cm^{-3}.nm^{-1}.s^{-1}, is the amount of photons reaching the solution averaged between λ-2.5 nm and λ+2.5 nm; A_{λ} is the averaged absorbance of the solution between λ-2.5 nm and λ+2.5 nm for a path length equal to 1.4 cm, λ_1 and λ_2, are the wavelengths chosen for the integration limits, N is the number of Avogadro and $\Delta\lambda$ is the wavelength interval chosen equal here it is equal to 5 nm.

Assignment of individual component C5 to 2-naphthoxy-acetic acid

2-Naphthoxy-acetic acid (98%) was purchased from Sigma-Aldrich. The three dimensional emission spectrum of commercial 2-naphthoxy-acetic acid is very similar to that of the individual component C5 (Figure SI-2).

Figure SI-2: Three dimensional emission spectrum spectrum of 2-naphthoxy-acetic acid (5×10^{-5} M) in water

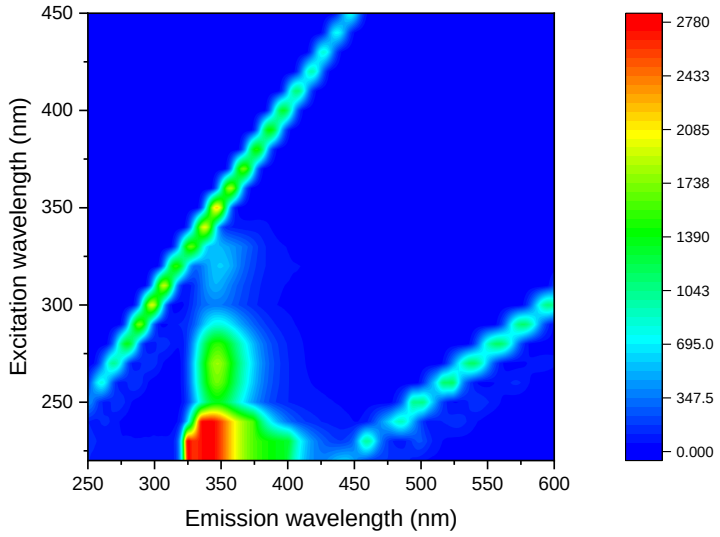

In addition, B4-July was analyzed on a high resolution mass spectrometer Orbitrap Q-Exactive (Thermo Scientific) coupled to an ultra-high performance liquid chromatography system (UHPLC) Ultimate 3000

RSLC (Thermo Scientific) equipped with an Acquity Phenomenex (2.1 mm×100 mm, 1.7 µm particle size) analytical column (Waters, USA). The aqueous solvent (A) consisted of a mixture of 0.1% formic acid and the organic phase (B) was acetonitrile. The separation was achieved with a gradient program consisting of 0-7.5 min 5%, 7.5-8.5 min 99% of the mobile phase B. After 80.5 min the gradients were returned to the initial conditions and analytical column was reconditioned for 3.5 min. The flow rate was set to 0.450 ml/min. The injection volume was 20 µL. The main peak was detected in negative mode at m/z= 201.0552 corresponding to $C_{12}H_9O_3$ with a fragment at m/z=157.0649 corresponding to the loss of CO_2 (Figure SI-3).

These data confirm the assignment of component C5 to 2-naphthoxy-acetic acid.

Its concentration in B4-July was estimated to $(5.0\pm0.5)\times10^{-7}$ M.

Figure SI-3: UPLC-HRMS spectrum of the water sample B4-July in negative mode. The peak eluted at 4.29 min shows the same m/z value than the authentic 2-naphthoxy-acetic acid.

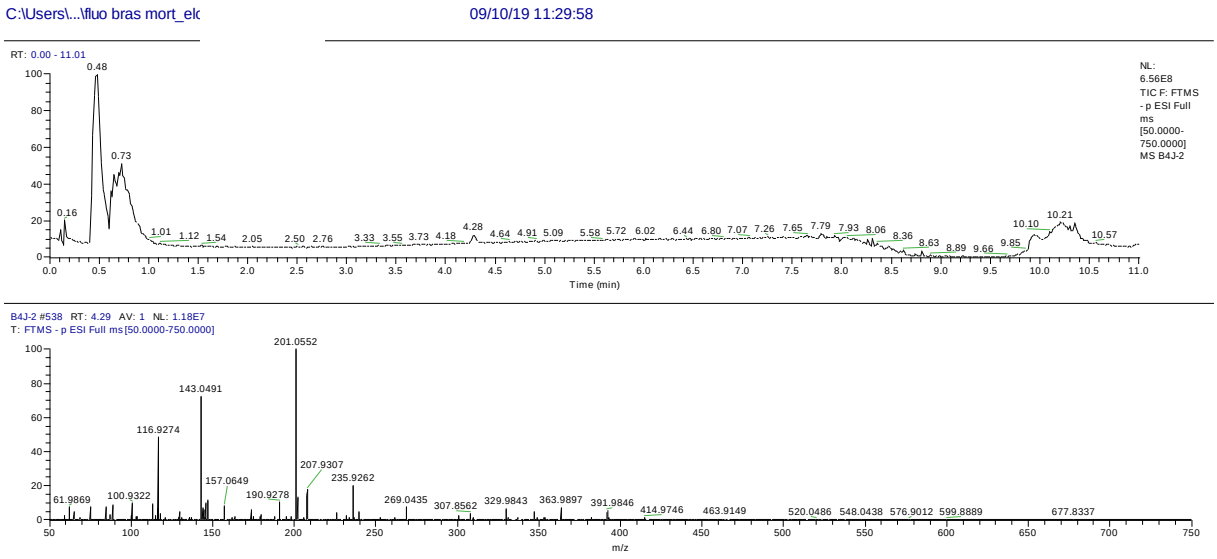

Figure SI-4 : Pearson coefficients from principal component analysis obtained from 10 variables: the seven components determined by parallel factor analysis (PARAFAC) algorithm (C1- widespread low molecular weight component; C2 - protein-like fluorophores; C3 - (photo)degraded terrestrial component; C4 - microbially-reduced quinone-like fluorophores; C5 - 2-naphthoxy-acetic acid; C6 - non-identified component probably linked to the component C5 and C7 - reduced quinone-like component), the rate of light absorption (Ra), the rate of triplet excited state production (R^{3DOM*}) and

the rate of singlet oxygen production (R^{SO}). The symbols not barred with a black cross correspond to p-values < 0.01.

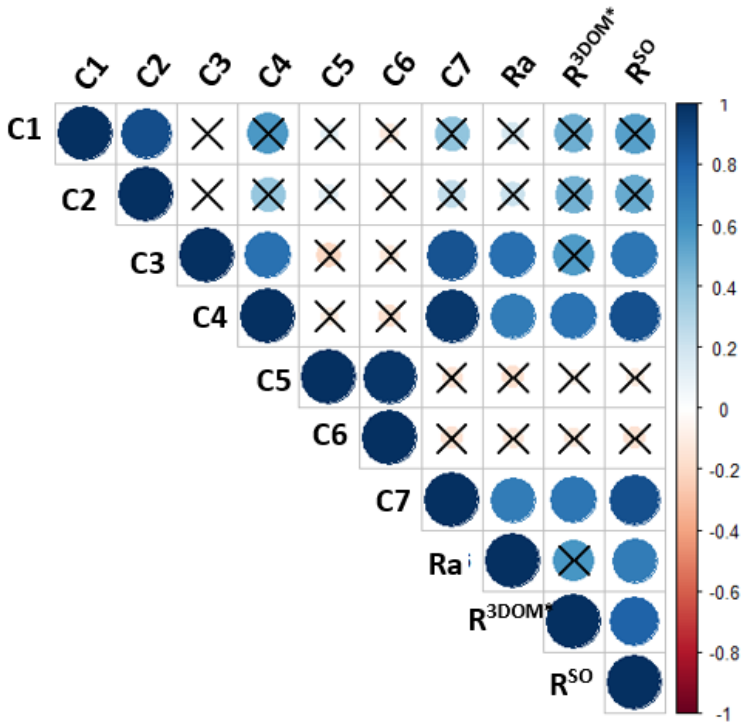

MANUSCRIPT 3

New route to toxic nitro and nitroso products upon irradiation of micropollutant mixtures containing Imidacloprid: role of NOx and effect of Natural Organic Matter.

Publishing journal: Environmental Science & Technology

Date of acceptance: 15 February 2020

Environmental Science & Technology

pubs.acs.org/est

Article

New Route to Toxic Nitro and Nitroso Products upon Irradiation of Micropollutant Mixtures Containing Imidacloprid: Role of NO_x and Effect of Natural Organic Matter

Davide Palma, Yara Arbid, Mohamad Sleiman,* Pascal de Sainte-Claire, and Claire Richard*

Cite This: *Environ. Sci. Technol.* 2020, 54, 3325−3333

Read Online

ACCESS | Metrics & More | Article Recommendations | Supporting Information

ABSTRACT: In this study, we reveal the capacity of imidacloprid (a neonicotinoid insecticide) to photoinduce the nitration and nitrosation of three aromatic probes (phenol, resorcinol, and tryptophan) in water. Using a gas-flow reactor and a NO_x analyzer, the production of gaseous NO/NO_2 was demonstrated during irradiation (300−450 nm) of imidacloprid (10^{-4} M). Quantum calculations showed that the formation of NO_x proceeds via homolytic cleavage of the RN−NO_2 bond in the triplet state. In addition to gaseous NO/NO_2, nitrite and nitrate were also detected in water, with the following mass balance: 40 ± 8% for NO_2, 2 ± 0.5% for NO, 52 ± 5% for NO_3^-, and 16 ± 2% for NO_2^-. The formation of nitro/nitroso probe derivatives was evidenced by high-resolution mass spectrometry, and their yields were found to range between 0.08 and 5.1%. The contribution of NO_3^-/NO_2^- to the nitration and nitrosation processes was found to be minor under our experimental conditions. In contrast, the addition of natural organic matter (NOM) significantly enhanced the yields of nitro/nitroso derivatives, likely via the production of triplet excited states (^{3}NOM*) and HO$^\bullet$. These findings reveal the importance of investigating the photochemical reactivity of water contaminants in a mixture to better understand the cocktail effects on their fate and toxicity.

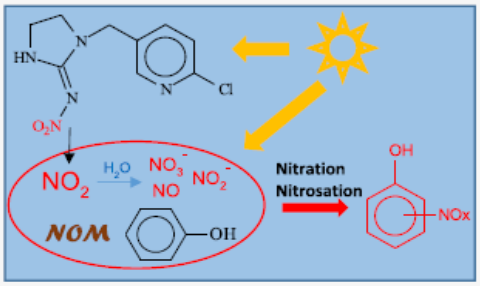

INTRODUCTION

Imidacloprid (1-[(6-chloropyridin-3-yl)methyl]-*N*-nitro-imidazolidin-2-imine, IMD, Scheme 1) is a widely used and effective neonicotinoid insecticide.[1] IMD, like other neonicotenoids, is used in a variety of crops, and its applications have been recently extended to the domestic sector and animal health.[1] Once released into the environment, it can reach the aquatic, atmospheric, and terrestrial compartments and be in contact with a lot of living organisms.[2−4] IMD affects the central nervous system of insects,[5] and there are increasing concerns about its deleterious effects with confirmed toxicity for pollinators, especially bees.[6] Toxicity or adverse effects in other species have also been reported.[7−9]

Scheme 1. Molecular Structure of IMD and Its Main Photoproducts

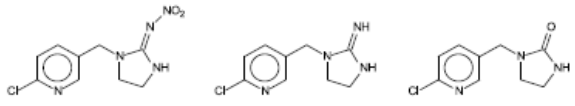

Several studies have been performed to investigate the fate of IMD under solar light, mainly in aqueous solutions,[1,10−13] on plant leaves and cuticles,[14−16] and more recently on solid thin films.[17] Desnitro-IMD (1-[(6-chloropyridin-3-yl)methyl]-imidazolidin-2-imine) was reported to be the main photoproduct and the urea-IMD (1-[(6-chloropyridin-3-yl)methyl]-imidazolidin-2-one) is a minor photoproduct (Scheme 1).[16] The formation of these byproducts seems to imply the cleavage of the N−NO_2 bond; however, the fate of NO_2 is not yet clear. Recently, the formation of gaseous nitrogen oxides during the irradiation of IMD at the surface of a germanium attenuated total reflectance crystal was investigated.[17] The authors detected nitrous oxide (N_2O), which was proposed to be formed by the recombination of detached NO_2 with the IMD fragments, in the electronic ground state.

In previous studies, we showed that the fungicides chlorothalonil and thiophanate-methyl can photoinduce the degradation of other pesticides during irradiation.[18,19] These reactions can take place in surface waters, where fungicides are present together with a wide range of other chemicals, and on solid supports such as the surface of leaves, where pesticides are often applied in combination. However, the effect that a

Received: December 11, 2019
Revised: February 10, 2020
Accepted: February 15, 2020
Published: February 15, 2020

https://dx.doi.org/10.1021/acs.est.9b07304
Environ. Sci. Technol. 2020, 54, 3325−3333

pollutant can have on another pollutant remains largely overlooked in photochemical studies, and little is known about the transformation of photostable pollutants via light-induced reactive intermediates of other co-pollutants. The ability of IMD to release NO_2 upon irradiation makes this compound important to study in this context because nitration of chemicals has been reported in a lot of systems generating NO_2.[20−28]

The goal of this study was thus to explore the formation of reactive NO_x via IMD photolysis and their reactivity toward surrogates of water contaminants and typical moieties of natural organic matter (NOM; phenol, resorcinol, and tryptophan). In particular, we investigated the formation of nitro- and nitroso-derivatives, two potentially toxic categories of compounds, from the three selected probes under polychromatic irradiation (300−450 nm) in the presence of IMD. Experiments were carried out using a flow-tube reactor equipped with a NO_x analyzer, whereas the formation of byproducts was characterized by high-resolution ultrahigh-performance liquid chromatography system−electrospray ionization-mass spectrometry (UHPLC−ESI-MS). Theoretical calculations were also performed to elucidate the mechanisms of NO_x formation. To the best of our knowledge, this is the first study reporting on the measurement of NO_x during irradiation of IMD in water and on their role in nitrosation/nitration of other water pollutants. Environmental implications of this light-induced indirect degradation are discussed.

MATERIALS AND METHODS

Chemicals and Materials. Imidacloprid (PESTANAL, analytical standard), resorcinol (purity 99%), phenol (purity ≥ 99.5%), L-tryptophan (purity ≥ 98%), and 2,4-dinitrophenylhydrazine (DNPH, purity 97%) were purchased from Sigma-Aldrich and used as received. Sodium nitrite (Rectapur 98%), sodium nitrate (Fluka, purity 99%), 2- and 4-nitrophenol (Fluka, purity ≥ 99%), and 4-nitrosophenol (Aldrich-Chemie, purity 60% due to the water content of 40%) were also used without further purification. Suwannee River NOM (2R101N) was purchased from IHSS. Water was purified using a reverse osmosis RiOs 5 and Synergy (Millipore) device (resistivity 18 MΩ cm, DOC < 0.1 mg·L^{-1}). All solvents or other reactants were of the highest grade available.

Irradiation. Two different irradiation devices were used. To monitor NO_x formation in the gas phase, device 1 was designed with a cylindrical Pyrex gas flow reactor (0.65 L, length 27 cm, and diameter 5.7 cm) containing 200 mL of IMD solution (10^{-4} M or 25.6 mg·L^{-1}) and irradiated from the top with two fluorescent tubes (Sylvania F15W/BL 368, 438 mm × 26 mm, 300−450 nm, and λ_{max} at 365 nm, see Figure S1) placed at a distance of 5 cm. The rate of incident light entering the solution was measured using a QE65000 radiometer (Ocean Optics); it was equal to 1.3×10^{16} photon·cm^{-2}·s^{-1}. The gas flow reactor was connected to a NO_x chemiluminescence analyzer (Thermo Scientific i-42 NO_x analyzer), as shown in Figure 1. Experiments were carried out under a continuous flow of clean air to reduce the residence time of NO_x and minimize NO_2 photolysis. The gaseous inlet of the reactor was connected to flow controllers for N_2 and O_2 (model Brooks 4800 Series), allowing the selection of the atmosphere under which irradiation was performed (pure N_2, pure O_2, or a 80/20 O_2/N_2 mixture) and to adjust the flow rate to 0.7 L min^{-1}. Background levels of NO_x in the gas inlet were negligible (<0.4 ppbv). Before irradiation, the levels of NO_x in

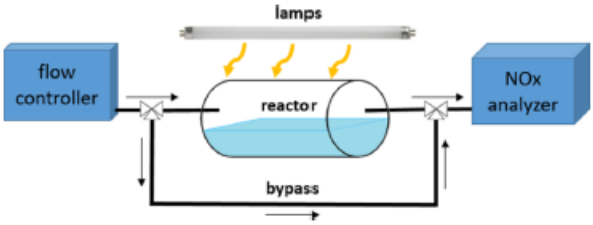

Figure 1. Schematic representation of device 1 used to monitor NO_x formation upon irradiation of IMD solutions.

the gas phase of the reactor were monitored continuously every 10 s until they reached a steady state within a few minutes (Figure S2). Despite the fact that NO_2 concentrations of up to 40 ppbv were detected initially (first 30 s), a background level of NO_x (<5 ppbv) was quickly reached. This production of NO_2 might possibly be due to IMD photolysis under indoor lighting during the preparation and handling of the solutions. During IMD irradiation, we have chosen to monitor NO_x levels in the gas phase of the reactor at selected times and not continuously. After selected irradiation times, the light was turned off, and the outlet of the reactor was connected to the NO_x analyzer. NO_x levels were measured every 10 s for a period of 1−2 min at a flow rate of 0.7 L min^{-1}. The time profile of NO_x concentrations shown in Figure S2 corresponds to the decay of the NO_x level in the reactor due to dilution with clean air. The level of NO_x measured was relatively constant at 1, 2, 4, and 6 h of IMD irradiation, in accordance with a steady-state regime. The levels of NO_x generated were then obtained by integrating the time profiles of NO_x concentrations. For calculating the yields of NO_x, the ratio of NO_x concentrations (ppbv) was converted into molar by taking into account the gas phase volume of the reactor (450 mL). By measuring the converted quantity (in moles) of IMD during the irradiation period, it was possible to calculate the molar yield for NO and NO_2.

A second device, device 2, was used to monitor the formation of nitro- and nitroso-derivatives. Fifteen milliliters of solutions was placed in a cylindrical Pyrex reactor sealed with an air-tight silicon cap and surrounded by six fluorescent tubes (Sylvania F15W/BL 368), installed inside a custom-made cylindrical irradiation device. Solutions were not buffered, but pH was controlled during the reactions. The initial pH was 6.5 ± 0.3, and in the course of the reactions, the pH was set to above 5. In the case of IMD + resorcinol mixtures, aliquots were sampled after several selected irradiation times, and the consumption profiles of IMD and nitro- and nitroso-resorcinol were obtained. For IMD + phenol and IMD + tryptophan mixtures and experiments with nitrate/nitrite and NOM, aliquots were only sampled after 16 h of irradiation. Samples were analyzed by HPLC to monitor the loss of IMD and the probes and by UHPLC−high-resolution mass spectrometry (HRMS) to characterize the photoproducts and estimate their levels. For the experiment with 10^{-5} M IMD and 10^{-4} M resorcinol, 75 mL was irradiated in portions of 25 mL, and water was evaporated up to 6 mL using a rotavapor before further analyses. Experiments were done in duplicate or triplicate.

Analytical methods. Absorption spectra were recorded using a Varian Cary 3 spectrophotometer. IMD, phenol, resorcinol, and L-tryptophan concentrations were monitored by HPLC (Waters Alliance 2695) equipped with a photodiode

https://dx.doi.org/10.1021/acs.est.9b07304
Environ. Sci. Technol. 2020, 54, 3325−3333

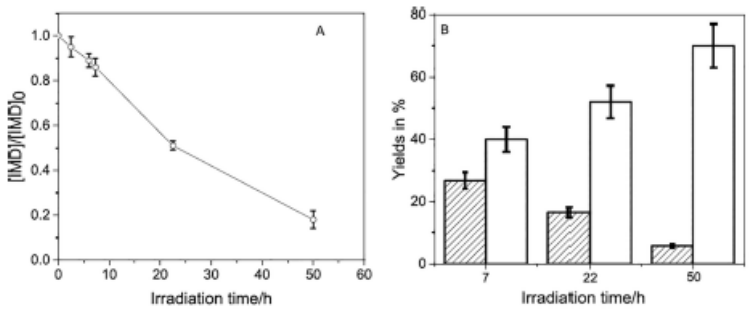

Figure 2. Consumption profile of aqueous IMD (10^{-4} M) irradiated in device 1 (A) and yields of NO_3^- (white bars) and NO_2^- (shaded bars) (B). Error bars are standard deviations.

array detector (Waters 2996) and an EC150/4.6 Nucleodur 100-5 C_8 endcapped column. The HPLC conditions are presented in Table S1. Photoproducts were quantified using the same instrument after derivatization with DNPH.[29] The derivatizing solution (15 mL) was prepared by mixing concentrated HCl, ultrapure water, and acetonitrile at a ratio of 2:5:1. Fifty microliters of this solution was added to 5 mL of sample solution. The derivatization reaction was completed in 5 min, and HPLC analyses were run shortly after. Calibration used derivatized NO_2^- solutions in the concentration range 10^{-6} to 10^{-5} M. All the HPLC analyses were done in triplicate, and the presented data are the mean values obtained.

NO_3^- was measured by ionic chromatography on a Dionex ICS-5000$^+$ using a column model Dionex Ion Pack AS11 2 mm × 250 mm; the flow was 0.25 mL·min^{-1}; and the mobile phase was an aqueous solution of KOH at the concentration of 0.43 mM for the first 4.5 min followed by linear gradient for up to 18 min of runtime by increasing the KOH concentration up to 11.70 mM. The injection volume was 750 μL, and the temperature of the column oven was set to 30 °C. External standards were prepared using $NaNO_3$ in the concentration range 50−200 μg·L^{-1}. Nitro- and nitroso-derivatives of phenol, resorcinol, and L-tryptophan were characterized, and their concentrations were estimated by HRMS performed on an Orbitrap Q-Exactive (Thermo Scientific) coupled to an UHPLC system, Ultimate 3000 RSLC (Thermo Scientific). Because of the lack of available standards, desnitro-IMD and the minor photoproducts were tentatively identified by HRMS, but quantification was not possible. Analyses were carried out in both negative (ESI$^-$) and positive (ESI$^+$) electrospray modes. The column used was the same column used for HPLC-UV. The binary solvent system was composed of acetonitrile and acidified water using formic acid at 40 and 60%, respectively, with a flow rate of 1.0 mL min^{-1}. Nitro- and nitroso-phenols were quantified by the injection of external standards of 4-nitro and 4-nitroso-phenols at concentrations varying from 5×10^{-7} to 4×10^{-6} M (Figure S3). Because of commercial unavailability of nitrated derivatives, the concentrations of nitro- and nitroso-resorcinols were estimated using the calibration curves of 4-nitro- and 4-nitroso-phenols. The concentrations of nitro-tryptophan and nitroso-tryptophan were estimated using L-tryptophan at the concentration of 10^{-6} M as a reference. Yields were obtained by dividing the photoproducts' concentrations by the loss of IMD in concentration and by multiplying these ratios by 100.

Computational Method. Potential energy surfaces (PESs) were investigated with the Gaussian series of programs.[30] Density functional theory (DFT) calculations (optimizations, frequency calculations, identification of transition states, and IRC calculations) were performed at the MN12SX/6-311++G(d,p)//MN12SX/6-31+G(d,p) level of calculation. Among the large set of hybrid range-separated functionals that we tested, MN12SX[31] gave the best agreement between the experimental and theoretical absorption spectra. Finally, the time-dependent-DFT (TD-DFT) method was used to compute singlet excited states. The triplet state was explored with conventional self-consistent field calculations. The solvent was modeled implicitly with the polarizable continuum model (PCM). Electronic energies are reported throughout (Gibbs free energies are not provided here because low vibrational modes may introduce large uncertainties in this calculation).

RESULTS AND DISCUSSION

Photolysis of IMD. The degradation profile of neutral aqueous IMD (10^{-4} M) irradiated in device 1 is shown in Figure 2A. HPLC-UV and UHPLC−HRMS analyses indicated that the main photoproduct was desnitro-IMD (Figure S4). Three minor photoproducts were also found: a compound produced by addition of an oxygen atom on IMD (IMD + O), another one produced by addition of two oxygen atoms on desnitro-IMD (desnitro-IMD + 2O), and the nitroso derivative of IMD (IMD-O) as traces (Table S2).

NO_3^- and NO_2^- were detected in the aqueous phase (Figure S4). The yield of NO_3^- increased constantly to reach 72 ± 5% after 50 h of irradiation (Figure 2B, white bars). In contrast, the yield of NO_2^- decreased from 27% after 7 h of irradiation to 6% after 50 h (Figure 2B, shaded bars). The higher accumulation of NO_3^- compared to that of NO_2^- is consistent with the spectral properties and the known photoreactivity of these ions. NO_3^- (λ_{max} = 300 nm and ε = 8 M^{-1}·cm^{-1}) absorbs much less solar light than NO_2^- (λ_{max} = 355 nm and ε = 22 M^{-1}·cm^{-1}), and its quantum yield of photolysis is also lower (reactions 1−4) leading to a smaller photolysis rate[32]

$$NO_3^- + h\nu \rightarrow NO_2 + O^{\bullet -} \qquad \Phi \approx 0.01 \qquad (1)$$

$$NO_3^- + h\nu \rightarrow NO_2^- + O(^3P) \qquad \Phi \approx 0.001 \qquad (2)$$

$$NO_2^- + h\nu + H^+ \rightarrow NO + HO^{\bullet} \qquad \Phi = 0.025 \qquad (3)$$

$$NO_2^- + h\nu \rightarrow NO_2 + e_{aq}^- \qquad \Phi < 0.0019 \qquad (4)$$

The detection of IMD + O and of desnitro-IMD + 2O appears to be consistent with the formation of hydroxyl radicals through reactions 1 and 3.

https://dx.doi.org/10.1021/acs.est.9b07304
Environ. Sci. Technol. 2020, 54, 3325−3333

Table 1. Formation of NO_x after 2 h of Irradiation of IMD (10^{-4} M) or NO_3^-/NO_2^- Mixtures in Device 1

conditions	quantity of IMD converted	quantity of NO_2 formed (molar yield)	quantity of NO formed (molar yield)
IMD (10^{-4} M)	380 ± 20 μg	24 ± 5 μg (40 ± 8%)	0.88 ± 0.20 μg (2 ± 0.5%)
NO_3^- (1.8×10^{-6} M) + NO_2^- (1.7×10^{-6} M)		1.6 ± 0.3 μg	3.9 ± 0.8 μg
NO_3^- (2×10^{-5} M) + NO_2^- (5×10^{-6} M)		4.8 ± 1.0 μg	11.6 ± 2.3 μg

NO_x Formation upon Irradiation of IMD. We also measured the NO_x formation in the gaseous phase above the solutions. NO and NO_2 were successfully detected upon irradiation of IMD (10^{-4} M) in device 1. Examples of collected data are shown in Figure S2. During the first 2 h of reaction of irradiation, 24 μg of NO_2 and 0.88 μg of NO were produced, whereas the IMD loss was around 380 μg (see Table 1). After integrating the nitrite and nitrate levels produced and considering the volume of gas (200 mL) and of water (450 mL), an overall mass balance of IMD conversion into inorganic *N*-containing products was determined: 40 ± 8% for NO_2, 2 ± 0.5% for NO, 52 ± 5% for nitrate, and 16 ± 2% for nitrite.

As the presence of NO_3^-/NO_2^- in the aqueous solution could potentially generate NO_x,[33] we irradiated these ions independently to estimate their contribution to the pool of NO_x detected upon irradiation of IMD. We chose to perform these comparative experiments with NO_3^- = 1.8×10^{-6} M and NO_2^- = 1.7×10^{-6} M corresponding to the concentrations estimated after 2 h of irradiation in device 1 (Figure S4). The irradiation of this mixture for 2 h yielded 15-fold less NO_2 and 4.4-fold more NO than the irradiation of IMD (10^{-4} M) (Table 1). The amount of NO_x formed above the IMD solution was 4.5-fold higher than that above the NO_3^-/NO_2^- solution, showing that IMD was the main contributor. Moreover, the higher yield of NO in the latter system confirmed that the NO_x precursor in the NO_3^-/NO_2^- mixture was NO_2^-, through reaction 3. At higher concentrations of NO_3^-/NO_2^- (2.0×10^{-5} M and 5×10^{-6} M, respectively), not far from those reached after 16 h of IMD irradiation, NO and NO_2 levels were 3-fold higher than in the previous case, respectively, showing that, in this concentration range, the NO and NO_2 amounts accumulated in proportion to NO_2^- concentration. Again, the amount of NO_x generated from NO_2^- (2.0×10^{-5} M) was still below the one formed upon irradiation of IMD solution.

As previously shown, the bond N–NO_2 was cleaved when IMD was irradiated in the solid phase at 305 and 254 nm.[17] However, some questions remain unanswered: would the proposed mechanism in the solid phase and at short wavelengths be still valid in solution and at longer wavelengths, and thus at lower excitation energies? How is NO formed and how the oxygen atom is eliminated? In an attempt to answer these questions, we performed quantum calculations.

Theoretical Calculations. Several conformers were found for the solvated imidacloprid system. The structure of the global minimum was similar to that found from the recent first-principles[17,34] and crystallographic investigations[34] (see the Supporting Information section for all structures reported in this work). Moreover, the DFT method used here was able to reproduce accurately the experimental absorption spectrum (see Figure 3).

A detailed investigation of the ground state (S_0), the first triplet state (T_1), and the first singlet excited state (S_1) was performed. Some of the key results are shown in Figure 4 and discussed below. The minima and transition state structures are given in the Supporting Information section. The

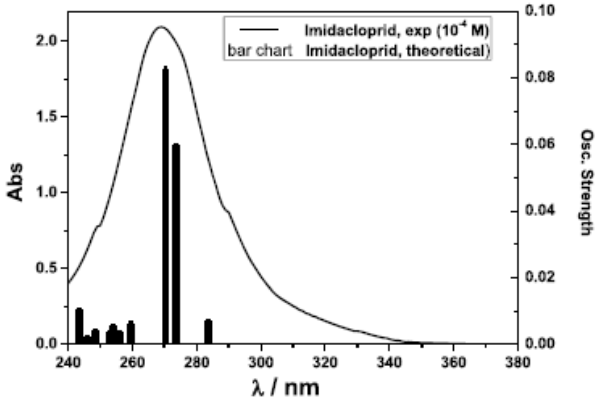

Figure 3. Experimental (Abs, left axis) and theoretical (oscillator strengths, right axis) absorption spectra of imidacloprid (theoretical spectrum for the most stable conformer (Figure S5a)) at the TD-MN12SX/6-311++G(d,p),PCM//MN12SX/6-31+G(d,p),PCM level. The oscillator strength is the probability of absorption. It is related to the dipole strength of the transition and is proportional to the molar absorptivity maximum for this transition. The S_1–S_0 transition is optically active (284 nm). The oscillator strength of this transition is 0.02, which is significant (an ε of about 6000 L·mol^{-1}·cm^{-1} can be estimated from this value, when a UV-vis half-width at half-height of 0.333 eV is used to model the absorption spectrum).

dissociation pathways of interest are depicted in this figure: NO_2 is shown on the left-hand side of Figure 4, and triplet atomic oxygen (a reaction that is precursor to the production of NO) is shown on the right-hand side of Figure 4. The minimum energy path was followed to investigate the formation of NO_2 in S_1 by performing partial optimizations of imidacloprid for fixed RN–NO_2 bond distances. The MEP maximum is indicated by a dashed level in Figure 4.

S_0 and S_1 States. Our results show that the departure of atomic triplet oxygen is not favored in the ground state because the predissociated intermediate ^{1}**RNNO–O** (R(O–O) = 1.523 Å; 56.4 kcal·mol^{-1}) cannot be reached because of very large activation energy (106.1 kcal·mol^{-1}). Similarly, the formation of NO_2 is not expected in the ground state because the respective electronic dissociation energy in S_0 is large (64.4 kcal·mol^{-1}; **RN** + NO_2). A transition state could not be found between imidacloprid (^{1}**RNNO$_2$**) and separated radicals in S_0. This is expected for homolytic dissociations in the ground state. In S_1, the dissociation of the RN–NO_2 bond required 14.0 kcal·mol^{-1} (MEP maximum). In addition, the in-cage dissociation complex ^{1}**RN···NO$_2$** is less stable (85.3 kcal·mol^{-1}) than the respective reactant (79.3 kcal·mol^{-1}). Thus, dissociation in S_1 is less favored than that in the triplet state (an activation energy of 6.1 kcal·mol^{-1} was found in T_1, and the reaction is now exothermic; see Figure 4). Moreover, our results show that the heterolytic dissociation mechanism would lead to **RN**$^+$/NO_2^- species, which are slightly less stable (see also Supporting Information) than the respective separated radicals (**RN**/NO_2). Thus, it seems reasonable to consider that

https://dx.doi.org/10.1021/acs.est.9b07304
Environ. Sci. Technol. 2020, 54, 3325−3333

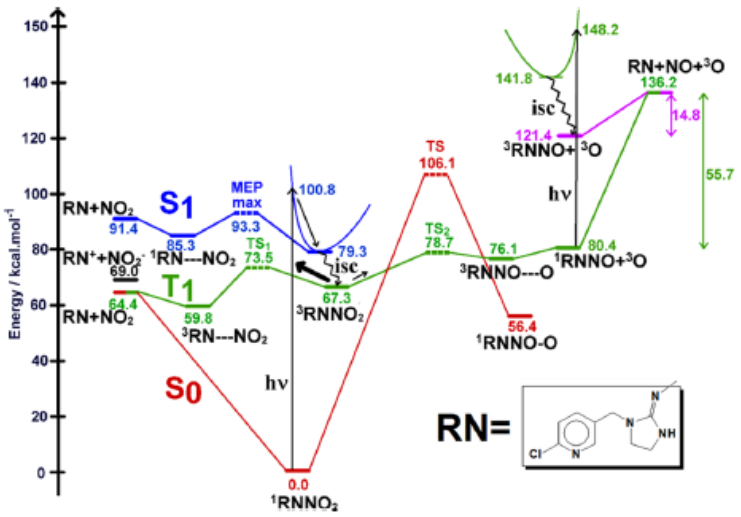

Figure 4. Electronic energies of stationary points in the ground state (S_0, red), first triplet (T_1, green), and first singlet (S_1, blue) excited states of imidacloprid (^{1}**RNNO$_2$**). Calculations were performed by the MN12SX/6-311++G(d,p),PCM//MN12SX/6-31+G(d,p),PCM method. Transition states and the MEP maximum are represented by dashed levels. Dashed bonds represent long-range separations. The energies of separated fragments **RN** + NO_2 and ^{1}**RNNO** + ^{3}**O** are also given in the figure. The energies of the heterolytic dissociation products (left-hand side, black) and the triplet state of **RNNO** (right-hand side, purple) are also indicated. The separated fragments **RN** and NO_2 in S_1 are, respectively, in the first doublet excited state (**RN**) and the doublet ground state (NO_2).

it is these radicals that are eventually obtained in the liquid phase. However, considering the small energy difference between heterolytic and homolytic dissociation energies, a mixture of homolytic and heterolytic dissociation products might not be completely ruled out. Implicit solvation models underestimate the solvation free energy of small ions, the cases of the proton and hydroxide being emblematic of this issue. In order to address this point, we computed $\Delta G^{*m}_{r,calc}$ the dissociation Gibbs free energy for both heterolytic and homolytic NO_2 cleavage. In this calculation, $RT \times \ln(24.46)$ was added to $\Delta G^{*}_{r,calc}$ to account for the free energy change of 1 mol of an ideal gas from 1 atm to 1 M.[35] $\Delta G^{0}_{r,calc} = \Delta G^{*}_{r,calc} + RT \times \ln(24.46)$ was 58.6 and 49.2 kcal·mol^{-1}, respectively, for the heterolytic and homolytic dissociation reactions, thus a difference of 9.4 kcal·mol^{-1} (recall that the respective difference in electronic energies was smaller, i.e., 4.6 kcal·mol^{-1}). Considering the implicit solvation model may underestimate the solvation free energy for NO_2^- by as much as 10 kcal·mol^{-1}, the radical dissociated species are still more stable than the heterolytic dissociation fragments, in agreement with our results.

Triplet State T_1. Second, S_1/T_1 intersystem-crossing (isc) is favored because minimum energy geometries in S_1 and T_1 are very similar for **RNNO$_2$**, and the energy gap is small (less than 0.1 kcal·mol^{-1} at the Franck−Condon geometry). In addition, in the triplet state, the barrier for NO_2 dissociation (6.1 kcal·mol^{-1}) is significantly smaller than that for dissociation into a triplet atomic oxygen and a singlet fragment (^{1}**RNNO** + ^{3}**O**; 11.4 kcal·mol^{-1}), in agreement with our experimental findings. Moreover, the in-cage dissociation complex ^{3}**RNNO···O** is thermodynamically less stable than the respective reactant ^{3}**RNNO$_2$**, and this reaction is displaced toward the reactant. Nevertheless, this pathway is investigated below to see if this reaction could play a role, even minor, in the formation of NO radicals.

NO Formation, A Minor Pathway. The mechanism of production of nitric oxide from ^{1}**RNNO** is also shown in Figure 4. NO bond dissociation energy was 55.7 kcal·mol^{-1} for ^{1}**RNNO** in the ground state, whereas cleavage in the triplet state (reached through S_1 followed by isc) required only 14.8 kcal·mol^{-1} (**RN** is obtained). A transition state could not be found in T_1, and the energy of activation may be identified with the dissociation energy in that case. Thus, the formation of NO as a primary product from RNNO is probably a minor pathway.

Thus, our quantum calculations provide strong evidence that photolysis of IMD mainly leads to NO_2 formation in the overall triplet state's PES, while NO formation is a minor pathway.

Evidence for Nitro-/Nitroso-Derivative Formation. Nitrate and nitrite ions which generate HO$^\bullet$ radicals simultaneously with NO or NO_2 have been reported to photoinduce the nitration and/or the nitrosation of phenolic derivatives.[20−24] Whether the photolysis of IMD could also contribute to the formation of such toxic products was a hypothesis that we aimed to verify in this study. Thus, IMD was irradiated with each of the three probes, shown in Scheme 2, in a small reactor (device 2) for 16 h. Under these conditions, the loss of IMD irradiated alone reached 60% (Figure S7). We first compared the probes' consumption (10^{-4} M) in the absence and in the presence of IMD (10^{-4} M) to quantify the photoinductive effect (Table S4). The disappearance of phenol and resorcinol was drastically faster in the presence of IMD, evidencing a strong effect. Only in the case

Scheme 2. Selected Probes

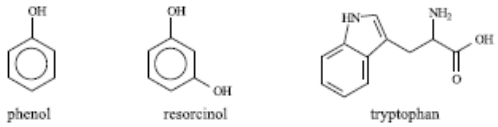

https://dx.doi.org/10.1021/acs.est9b07304
Environ. Sci. Technol. 2020, 54, 3325−3333

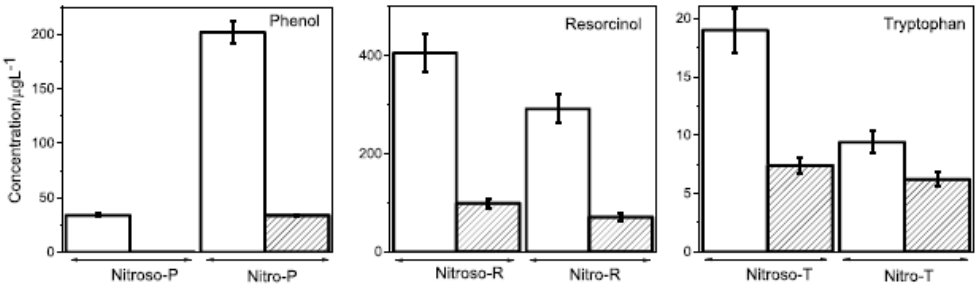

Figure 5. Concentrations of nitro- and nitroso-derivatives of phenol, resorcinol, and tryptophan detected after 16 h of irradiation of the probes (10^{-4} M) in device 2 in the presence of IMD (10^{-4} M) (white bars) and in the presence of the mixture of NO_3^- (2×10^{-5} M) and NO_2^- (5×10^{-6} M) (shaded bars). Error bars are standard deviations.

Table 2. Effect of NOM (11 mg·L^{-1}) on the Photo-Nitration/Photo-Nitrosation of Resorcinol (10^{-4} M) after 2 h of Irradiation in Device 2 in the Presence of IMD (10^{-4} M) or NO_2^- (5×10^{-6} M)[a]

conditions	% resorcinol converted	nitroso-derivatives formed (μg·L^{-1})	nitro-derivatives formed (μg·L^{-1})
IMD + resorcinol	7.0 ± 0.3	83 ± 8	44 ± 4
IMD + resorcinol + NOM	18 ± 1	110 ± 10	88 ± 9
NO_2^- + resorcinol	<1	20 ± 2	1 ± 0.1
NO_2^- + resorcinol + NOM	<1	55 ± 5	35 ± 3

[a]The light screening effect of NOM (10%) is taken into account.

of tryptophan, the acceleration effect was small because of the fast photolysis of the probe under the studied conditions.

Then, we monitored the formation of nitro-/nitroso-derivatives by UHPLC−HRMS analyses. Figure S8 shows the formation profile of nitroso- and nitro-resorcinols upon irradiation of IMD (10^{-4} M) and resorcinol (10^{-4} M). The concentration of the two photoproducts increased linearly up to 7 h of irradiation before reaching a plateau value after 16 h. Nitro- and nitroso-derivatives were also detected with phenol and tryptophan. The detected levels after 16 h of irradiation are given in Figure 5 (white bars) and Table S4. The estimated yields of nitro-resorcinols reached 3.3% of converted IMD and those of nitroso-resorcinols 5.1%. The yield of nitro-phenols (ortho + para derivatives)[21] was equal to 2.6%, but that of nitroso-phenols (ortho + para derivatives) was smaller (0.5%). For tryptophan, both yields were very small, reaching only 0.08% (nitro-derivatives) and 0.14% (nitroso-derivatives) of tryptophan converted because of the fast-direct photolysis of tryptophan.

Experiments were also performed at lower reactant concentrations to determine the impact of this parameter on the rates. A 10-fold decrease of the concentration of IMD for a concentration of resorcinol kept constant at 10^{-4} M reduced the amount of nitro-resorcinols by 18-fold and that of nitroso-resorcinols by 9-fold, while the sum of the two photoproducts was reduced by about 10-fold (Table S4). A 10-fold decrease of the concentration of resorcinol for a concentration of IMD kept constant at 10^{-4} M decreased 3-fold the amount of nitro-resorcinols and 100-fold that of nitroso-resorcinols, and their sum (nitro + nitroso) was reduced by about 5-fold (Table S4). These results indicate that the reaction rate was proportional to the concentrations of reactants. The decay rate of resorcinol followed a first-order kinetic with a rate constant k that can be expressed as: $k = 5.9 \times 10^{-3}$ [IMD] s^{-1}.

We also studied the nitro/nitrosation capacity of the NO_3^-/NO_2^- mixture to quantify their contributions in these reactions (shaded bars in Figure 5 and Table S4). For these comparisons, we fixed NO_3^-/NO_2^- concentrations to those measured in the IMD solution after 16 h of irradiation in device 2 (2×10^{-5} and 5×10^{-6} M, respectively), and the mixtures of NO_3^-/NO_2^- and probes were irradiated for 16 h in device 2. Nitrosation was 121-fold lower in the case of phenol, 4.1-fold in the case of resorcinol, and 2.6-fold in the case of tryptophan than in the presence of IMD, while nitration was 5.9-fold lower for phenol, 4.1-fold for resorcinol, and 1.5-fold for tryptophan. One concludes that the contributions of NO_3^-/NO_2^- to the nitration/nitrosation processes observed in irradiated IMD solutions were minor, especially for phenol and resorcinol, even though we acknowledge that the conditions chosen for the comparative experiments (fixed NO_3^-/NO_2^- concentrations) cannot perfectly reproduce the dynamic and complex evolution of NO_3^-/NO_2^- during IMD irradiation.

Effect of NOM on Nitration/Nitrosation of Probes. Another important aspect we attempted to explore is the effect of NOM on these photochemical nitration/nitrosation reactions. The experimental conditions and results are reported in Table 2. NOM (11 mg·L^{-1}) increased the percentage of resorcinol loss in the presence of IMD by a factor of 2.6, after correction for the light screening effects (10%). The formation of nitroso- and nitro-resorcinols in IMD solutions was increased by a factor of 1.3 and 2.0, respectively, and the formation of nitro- and nitroso-resorcinols in NO_2^- solutions by factors of 35 and 2.8, respectively. The very low formation of nitro-resorcinols in the system NO_2^- + resorcinol was already shown.[20] These data highlight the significant effect of NOM on the nitro-/nitroso-derivative formation.

Reaction Mechanism. Many reactions are expected to take place in this complex system. The main ones are summarized below. The photolysis of IMD in water generates NO_2 in the liquid phase ($NO_{2(l)}$) together with the radical RN, as shown by the quantum calculations, and the latter mainly gives rise to desnitro-IMD (reaction 5). The radicals O(^{3}P) and RNNO are also produced, but in much lower amounts (reaction 6). The reactivity of NO_2 in water is very high. It is reported in the literature that NO_3^- and NO_2^- are generated according to reactions 7a and 7b through the intermediary

https://dx.doi.org/10.1021/acs.est.9b07304
Environ. Sci. Technol. 2020, 54, 3325−3333

dimerization of $NO_{2(l)}$.[36,37] NO_3^- and $NO_{(l)}$ can also be produced through reaction 8.[37,38] In our experiments, $N_2O_{4(g)}$ cannot be distinguished from $NO_{2(g)}$. Reaction 8 is probably the major NO formation pathway, but the photolysis of RNNO (reaction 11), of $NO_{2(g)}$ (reaction 12), and of NO_2^- (reaction 3) is the alternative pathway for NO formation. NO is stable in water and volatilizes in the gaseous phase (reaction 9).[37] It generates $NO_{2(g)}$ by reacting with oxygen (reaction 10).

In this scheme, we did not take into account the oxidation of IMD by $HO^\bullet$ formed in reaction 3 because the formation of oxidation products (IMD + O) was small. NO_2^- and NO_3^- could also be oxidized by $HO^\bullet$.[39] However, because of the high concentration of IMD compared to those of NO_2^- and NO_3^- in the first half of the reaction, IMD and its main photoproduct desnitro-IMD are expected to be the main sinks of $HO^\bullet$.

$$\text{IMD} + h\nu \rightarrow \text{NO}_{2(l)} + \text{RN} \quad (5)$$

$$\text{IMD} + h\nu \rightarrow \text{O}(^3\text{P}) + \text{RNNO} \quad (6)$$

$$2\text{NO}_{2(l)} \leftrightarrow \text{N}_2\text{O}_{4(l)} \quad (7a)$$

$$\text{N}_2\text{O}_{4(l)} + \text{H}_2\text{O} \rightarrow \text{NO}_3^- + 2\text{H}^+ + \text{NO}_2^- \quad (7b)$$

$$3\text{NO}_{2(l)} + \text{H}_2\text{O} \leftrightarrow 2\text{NO}_3^- + 2\text{H}^+ + \text{NO}_{(l)} \quad (8)$$

$$\text{NO}_{(l)} \leftrightarrow \text{NO}_{(g)} \quad (9)$$

$$2\text{NO}_{(g)} + \text{O}_2 \rightarrow 2\text{NO}_{2(g)} \quad (10)$$

$$\text{RNNO} + h\nu \rightarrow \text{NO}_{(l)} + \text{radical} \quad (11)$$

$$\text{NO}_{2(g)} + h\nu \rightarrow \text{NO}_{(g)} + \text{O}(^3\text{P}) \quad (12)$$

The nitration/nitrosation of phenolic/aromatic compounds in the presence of NO_2^- or NO_3^- has already been studied.[20−25,39−41] NO_2 is recognized as having a key role in these reactions, even though the mechanisms are not fully understood. Several studies attributed the formation of phenoxyl radicals to the reaction of phenols with NO_2,[20,25,39,41] while others to their reaction with $HO^\bullet$.[40] Once formed, the phenoxyl radicals further react with NO_2 to yield the ortho- and para-derivatives of nitro-phenols. Similarly, the reaction of phenoxyl radicals with NO is expected to generate nitroso-phenols. The effect of NOM on these reactions is difficult to predict because of the existence of opposite reactions. Indeed, on the first hand, NOM can potentially favor the nitro/nitrosation reactions by generating photooxidants, such as the triplet excited states (^{3}NOM*), singlet oxygen, or $HO^\bullet$, that are expected to induce the formation of phenoxyl radicals, as shown in the literature.[39] In addition, ^{3}NOM* or $HO^\bullet$ could be able to oxidize NO_2^- and NO_3^- into NO_x[39] (see process 13 related to NO_2^-)

$$\text{NO}_2^- + {}^3\text{NOM}^*/\text{HO}^\bullet \rightarrow \text{NO}_2 + \text{NOM}^{\bullet-}/\text{OH}^- \quad (13)$$

On the other hand, NOM could also be a sink for NO_x because of the presence of aromatic moieties in its structure and therefore could inhibit the nitration/nitrosation reaction to some extent.[26,42] The overall effect of NOM will thus depend on the experimental conditions, and in particular on the relative concentrations of reactants. In our set-up, the presence of NOM (11 mg·L^{-1}) in IMD or NO_2^- solutions containing resorcinol (10^{-4} M) increased the amounts of nitro- and nitroso-resorcinols, showing that in this case, NOM favors the formation of the phenoxyl radical and of NO_2. Because Suwannee River NOM contains 68% of fulvic acids and fulvic acids contain ~3 mmol oxidizable phenol per g of carbon,[43] there are about 20 μM of oxidizable phenols originating from NOM in a solution containing 11 mg/L. Under these conditions, where the quenching molecule is in large excess over phenolic moieties in NOM, it can be expected that the majority of NOM-derived photooxidants will be quenched by the probe compounds to form phenoxyl radicals, which can then further react with NO_x to produce nitro-/nitroso-phenol/resorcinol, enhancing the yields of these products as it is observed.

Environmental Significance. Our study showed that NO_x (NO and NO_2) could be generated by irradiation of IMD, and that these NO_x were capable of reacting with phenolic probes to produce nitro- and nitroso-derivatives. This suggests that in surface water, IMD could induce the formation of nitro and nitroso derivatives of other contaminants that could be toxicants in the aquatic environment. The importance of the phenomenon will depend on the level of IMD present in surface waters. The frequency of IMD detection in surface waters is high, and the concentration of IMD varies in a large range reaching 1 μg·L^{-1} in agricultural areas.[3,4] Based on this work and on the light absorption capacities of IMD and NO_2^-, one can calculate that at 1 μg·L^{-1}, IMD could generate as much as nitroso-/nitro-derivatives as NO_2^- at 0.1 μg·L^{-1}. The relative contributions of NO_2^- and IMD to nitroso-/nitro-derivative formation depend therefore on their levels in water. NO_2^- is present in surface waters at a maximal concentration of 0.1 mg·L^{-1}.[44] In many cases, the NO_2^- concentration will be high enough to make negligible the contribution of IMD in nitro/nitrosation reactions. However, in waters containing very low levels of NO_2^- and high levels of IMD, IMD might play a role in the nitro/nitrosation reactions.

On the other hand, we observed that NOM (11 mg·L^{-1}) enhanced the nitro and nitrosation reactions of phenols (10^{-4} M). The yield of nitro-resorcinol was multiplied by 2, whereas that of nitroso-resorcinol by 1.3, and when NO_2^- was used instead of IMD, the yields of nitro-resorcinol and of nitroso-resorcinol were increased by 35-fold and 2.8-fold, respectively. This can be explained by the enhanced formation of phenoxyl radicals in the quenching of NOM deriving photooxidants by phenols. However, this effect might be concentration-dependent. The level of NOM used in this study falls in the range of typical NOM levels found in rivers and eutrophic lakes,[45] but those of probes are high. At environmentally relevant concentrations of the probe compounds (<1 μM), phenolic moieties in NOM are in excess, and it might be possible that the NOM-bound phenoxyl radicals, at higher concentrations than the probe-derived phenoxyl radicals, might outcompete the latter for reaction with NO_x. In other words, under environmentally relevant conditions, a shift toward nitration/nitrosation of NOM seems possible, and the yield of nitro-/nitroso-derivatives of probes could then be lower compared to the ones in the absence of NOM. The incorporation of N inorganic nitrogen (N) into NOM via photolysis of nitrate/nitrite and/or in advanced oxidation process treatments was already reported and were also shown to generate potentially toxic compounds.[26−28] Therefore, such reactions might also have environmentally negative consequences. We could not detect any significant structural changes in NOM using HRMS analyses. Nevertheless, further experiments using N-labeled

https://dx.doi.org/10.1021/acs.est.9b07304
Environ. Sci. Technol. 2020, 54, 3325−3333

IMD or nitrite/nitrate and other hyphenated techniques may provide evidence for NOM nitration/nitrosation. Therefore, consistent monitoring of nitro/nitroso byproducts is highly recommended to verify their potential formation.

Our study confirms the capacity of water contaminants to interact with each other under irradiation and to induce mutual degradation. Mutual effects can involve reactions between excited- and ground-state contaminants or the intermediary formation of reactive species like NO_x in the case of IMD. Up to now, they have been poorly investigated in photochemical studies and would deserve more attention. Thus, future studies should further consider the investigation of the "cocktail effect" on the environmental fate of contaminants and more specifically the reactivity of intermediates in order to enable a more reliable monitoring of nontarget pollutants and assessment of potential risks.

■ ASSOCIATED CONTENT

Supporting Information

The Supporting Information is available free of charge at https://pubs.acs.org/doi/10.1021/acs.est.9b07304.

Spectrum of light received by the solutions in devices 1 and 2, NO_x formation in device 1 upon photolysis of IMD (10^{-4} M), calibration curve for nitroso-phenol and nitro-phenol, profiles of NO_x, NO_3^-, NO_2^-, nitroso-resorcinol, and nitro-resorcinol formation and of IMD consumption, structure and Cartesian coordinates of the minimum energy structures of IMD in S_0 (a), S_1 (b), and T_1 (c), of TS (d), of intermediate RNNO−O (e) in S_0, of TS_1 in T_1 (f), of TS_2 in T_1 (g), of ^{3}RN−NO_2 (h) and ^{3}RN−NO_2 in T_1 (i), of ^{1}RNNO (j) and ^{3}RNNO (k) at the B3LYP/6-311++G(d,p)//B3LYP/6-31+G-(d,p) level, minima and transition state structures with Cartesian coordinates, photo-nitration and photo-nitrosation of the probes after 16 h of irradiation in the presence of IMD (10^{-5} or 10^{-4} M) or a mixture of NO_3^- (2×10^{-5} M) and NO_2^- (5×10^{-6} M), and the effect of NOM (11 mg L^{-1}) on the photo-nitration/photo-nitrosation of resorcinol (10^{-4} M) after 2 h of irradiation in device 2 in the presence of IMD (10^{-4} M) or NO_2^- (5×10^{-6} M) (PDF)

■ AUTHOR INFORMATION

Corresponding Authors

Mohamad Sleiman − *Université Clermont Auvergne, CNRS, SIGMA Clermont, Institut de Chimie de Clermont-Ferrand F-63000 Clermont-Ferrand, France;* orcid.org/0000-0002-2273-1053; Email: Mohamad.sleiman@sigma-clermont.fr

Claire Richard − *Université Clermont Auvergne, CNRS, SIGMA Clermont, Institut de Chimie de Clermont-Ferrand F-63000 Clermont-Ferrand, France;* orcid.org/0000-0001-6520-5494; Phone: +33 (0)4 73 40 71 42; Email: Claire.richard@uca.fr; Fax: +33 (0)4 73 40 77 00

Authors

Davide Palma − *Université Clermont Auvergne, CNRS, SIGMA Clermont, Institut de Chimie de Clermont-Ferrand F-63000 Clermont-Ferrand, France*

Yara Arbid − *Université Clermont Auvergne, CNRS, SIGMA Clermont, Institut de Chimie de Clermont-Ferrand F-63000 Clermont-Ferrand, France*

Pascal de Sainte-Claire − *Université Clermont Auvergne, CNRS, SIGMA Clermont, Institut de Chimie de Clermont-Ferrand F-63000 Clermont-Ferrand, France*

Complete contact information is available at: https://pubs.acs.org/10.1021/acs.est.9b07304

Notes

The authors declare no competing financial interest.

The paper reflects only the author's view, and the Agency is not responsible for any use that may be made from the information it contains.

■ ACKNOWLEDGMENTS

This paper is part of a project that received funding from the European Union's Horizon 2020 research and innovation programme under the Marie Skłodowska-Curie grant agreement no. 765860 (Aquality). The authors also thank the European Regional Development Fund of the European Union and the Région Auvergne-Rhône-Alpes for financial support under the Program "Nouveau Chercheur" (no. AV0004494), which allowed the acquisition of the NO_x analyzer. We thank Martin Leremboure and Guillaume Voyard (CNRS engineers), for assistance with chromatographic and mass spectrometry analyses, and the anonymous reviewers who helped to improve the manuscript.

■ REFERENCES

(1) Jeschke, P.; Nauen, R.; Schindler, M.; Elbert, A. Overview of the status and global strategy for neonicotinoids. *J. Agric. Food Chem.* **2011**, *59*, 2897−2908.

(2) Désert, M.; Ravier, S.; Gille, G.; Quinapallo, A.; Armengaud, A.; Pochet, G.; Savelli, J.-L.; Wortham, H.; Quivet, E. Spatial and temporal distribution of current-use pesticides in ambient air of Provence-Alpes-Côte-d'Azur Region and Corsica, France. *Atmos. Environ.* **2018**, *192*, 241−256.

(3) Struger, J.; Grabuski, J.; Cagampan, S.; Sverko, E.; Mcgoldrick, D.; Marvin, C. H. Factors influencing the occurrence and distribution of neonicotinoid insecticides in surface waters of southern Ontario, Canada. *Chemosphere* **2017**, *169*, 516−523.

(4) Hladik, M. L.; Kolpin, D. W.; Kuivila, K. M. Widespread occurrence of neonicotinoid insecticides in streams in a high corn and soybean producing region, USA. *Environ. Pollut.* **2014**, *193*, 189−196.

(5) Abou-Donia, M. B.; Goldstein, L. B.; Bullman, S.; Tu, T.; Khan, W. A.; Dechkovskaia, A. M.; Abdel-Rahman, A. A. Imidacloprid induces neurobehavioral deficits and increases expression of glial fibrillary acidic protein in the motor cortex and hippocampus in offspring rats following in utero exposure. *J. Toxicol. Environ. Health. A* **2008**, *71*, 119−130.

(6) Laycock, I.; Lenthall, K. M.; Barratt, A. T.; Cresswell, J. E. Effects of imidacloprid, a neonicotinoid pesticide, on reproduction in worker bumble bees (Bombus terrestris). *Ecotoxicology* **2012**, *21*, 1937−1945.

(7) Woodcock, B. A.; Isaac, N. J. B.; Bullock, J. M.; Roy, D. B.; Garthwaite, D. G.; Crowe, A.; Pywell, R. F. Impacts of neonicotinoid use on long-term population changes in wild bees in England. *Nat. Commun.* **2016**, *7*, 12459.

(8) Berheim, E. H.; Jenks, J. A.; Lundgren, J. G.; Michel, E. S.; Grove, D.; Jensen, W. F. Effects of Neonicotinoid Insecticides on Physiology and Reproductive Characteristics of Captive Female and Fawn White-tailed Deer. *Sci. Rep.* **2019**, *9*, 1−10.

(9) Duzguner, D.; Erdogan, E. Acute oxidant and inflammatory effects of imidacloprid on the mammalian central nervous system. *Pestic. Biochem. Physiol.* **2010**, *97*, 13−18.

(10) Moza, P. N.; Hustert, K.; Feicht, E.; Kettrup, A. Photolysis of imidacloprid in aqueous solution. *Chemosphere* **1998**, *36*, 497−502.

https://dx.doi.org/10.1021/acs.est.9b07304
Environ. Sci. Technol. 2020, 54, 3325−3333

(11) Redlich, D.; Shahin, N.; Ekici, P.; Friess, A.; Parlar, H. Kinetical study of the photoinduced degradation of imidacloprid in aquatic media. *Clean: Soil, Air, Water* **2007**, *35*, 452−458.
(12) Wamhoff, H.; Schneider, V. Photodegradation of imidacloprid. *J. Agric. Food Chem.* **1999**, *47*, 1730−1734.
(13) Zheng, W.; Liu, W. P.; Wen, Y. Z.; Lee, S.-J. Photochemistry of insecticide imidacloprid: direct and sensitized photolysis in aqueous medium. *J. Environ. Sci.* **2004**, *16*, 539−542.
(14) Schippers, N.; Schwack, W. Photochemistry of imidacloprid in model systems. *J. Agric. Food Chem.* **2008**, *56*, 8023−8029.
(15) Scholz, K.; Reinhard, F. Photolysis of imidacloprid (NTN 33893) on the leaf surface of tomato plants. *Pestic. Sci.* **1999**, *55*, 652−654.
(16) Schippers, N.; Schwack, W. Phototransformation of imidacloprid on isolated tomato fruit cuticles and on tomato fruits. *J.Photochem. Photobiol. B* **2010**, *98*, 57−60.
(17) Aregahegn, K. Z.; Shemesh, D.; Gerber, R. B.; Finlayson-Pitts, B. J. Photochemistry of thin solid films of the neonicotinoid imidacloprid on surfaces. *Environ. Sci. Technol.* **2017**, *51*, 2660−2668.
(18) Monadjemi, S.; ter Halle, A.; Richard, C. Accelerated dissipation of the herbicide cycloxydim on wax films in the presence of the fungicide chlorothalonil and under the action of solar light. *J. Agric. Food Chem.* **2014**, *62*, 4846−4851.
(19) Kouras-Hadef, S.; Hamdache, S.; de Sainte-Claire, P.; Sleiman, M.; Jaber, F.; Richard, C. Light induced degradation of the fungicide Thiophanate-methyl in water: Formation of a sensitizing photoproduct. *J.Photochem. Photobiol. A* **2018**, *360*, 262−269.
(20) Machado, F.; Boule, P. Photonitration and photonitrosation of phenolic derivatives induced in aqueous solution by excitation of nitrite and nitrate ions. *J. Photochem. Photobiol. A: Chem.* **1995**, *86*, 73−80.
(21) Vione, D.; Maurino, V.; Pelizzetti, E.; Minero, C. Phenol Photonitration and Photonitrosation upon Nitrite Photolysis in basic solution. *Int. J. Environ. Anal. Chem.* **2004**, *84*, 493−504.
(22) Suzuki, J.; Yagi, N.; Suzuki, S. Photochemical nitrosation of phenol in aqueous nitrite solution. *Chem. Pharm. Bull.* **1984**, *32*, 2803−2808.
(23) De Laurentiis, E.; Minella, M.; Berto, S.; Maurino, V.; Minero, C.; Vione, D. The fate of nitrogen upon nitrite irradiation: Formation of dissolved vs. gas-phase species. *J. Photochem. Photobiol. A: Chem.* **2015**, *307*−*308*, 30−34.
(24) Scholes, R. C.; Prasse, C.; Sedlak, D. L. The Role of Reactive Nitrogen Species in Sensitized Photolysis of Wastewater-Derived Trace Organic Contaminants. *Environ. Sci. Technol.* **2019**, *53*, 6483−6491.
(25) Vione, D.; Maurino, V.; Minero, C.; Pelizzetti, E. New processes in the environmental chemistry of nitrite: nitration of phenol upon nitrite photoinduced oxidation. *Environ. Sci. Technol.* **2002**, *36*, 669−676.
(26) Thorn, K. A.; Cox, L. G. Ultraviolet irradiation effects incorporation of nitrate and nitrite nitrogen into aquatic natural organic matter. *J. Environ. Qual.* **2012**, *41*, 865−881.
(27) Yang, P.; Ji, Y.; Lu, J.; Huang, Q. Formation of nitrophenolic byproducts during heat-activated peroxydisulfate oxidation in the presence of natural organic matter and nitrite. *Environ. Sci. Technol.* **2019**, *53*, 4255−4264.
(28) Ji, Y.; Wang, L.; Jiang, M.; Lu, J.; Ferronato, C.; Chovelon, J.-M. The role of nitrite in sulfate radical-based degradation of phenolic compounds: An unexpected nitration process relevant to groundwater remediation by in-situ chemical oxidation (ISCO). *Water Res.* **2017**, *123*, 249−257.
(29) Kieber, R. J.; Seaton, P. J. Determination of Subnanomolar Concentrations of Nitrite in Natural Waters. *Anal. Chem.* **1995**, *67*, 3261−3264.
(30) Frisch, M. J.; Trucks, G. W.; Schlegel, H. B.; Scuseria, G. E.; Robb, M. A.; Cheeseman, J. R.; Scalmani, G.; Barone, V.; Mennucci, B.; Petersson, G. A.; Nakatsuji, H.; Caricato, M.; Li, X.; Hratchian, H. P.; Izmaylov, A. F.; Bloino, J.; Zheng, G.; Sonnenberg, J. L.; Hada, M.; Ehara, M.; Toyota, K.; Fukuda, R.; Hasegawa, J.; Ishida, M.; Nakajima, T.; Honda, Y.; Kitao, O.; Nakai, H.; Vreven, T.; Montgomery, J. A., Jr.; Peralta, J. E.; Ogliaro, F.; Bearpark, M.; Heyd, J. J.; Brothers, E.; Kudin, K. N.; Staroverov, V. N.; Keith, T.; Kobayashi, R.; Normand, J.; Raghavachari, K.; Rendell, A.; Burant, J. C.; Iyengar, S. S.; Tomasi, J.; Cossi, M.; Rega, N.; Millam, J. M.; Klene, M.; Knox, J. E.; Cross, J. B.; Bakken, V.; Adamo, C.; Jaramillo, J.; Gomperts, R.; Stratmann, R. E.; Yazyev, O.; Austin, A. J.; Cammi, R.; Pomelli, C.; Ochterski, J. W.; Martin, R. L.; Morokuma, K.; Zakrzewski, V. G.; Voth, G. A.; Salvador, P.; Dannenberg, J. J.; Dapprich, S.; Daniels, A. D.; Farkas, O.; Foresman, J. B.; Ortiz, J. V.; Cioslowski, J.; Fox, D. J. *Gaussian 09*, Revision C.01; Gaussian, Inc.: Wallingford CT, 2010.
(31) Peverati, R.; Truhlar, D. G. Screened-exchange density functionals with broad accuracy for chemistry and solid-state physics. *Phys. Chem. Chem. Phys.* **2012**, *14*, 16187−16191.
(32) Vione, D.; Maurino, V.; Minero, C.; Pelizzetti, E. Reactions induced in natural waters by irradiation of nitrate and nitrite ions. *Environmental Photochemistry*; Springer-Verlag Berlin, 2005; Vol. 2, Part M, pp 221−253.
(33) Richards-Henderson, N. K.; Anderson, C.; Anastasio, C.; Finlayson-Pitts, B. J. The effect of cations on NO_2 production from the photolysis of aqueous thin water films of nitrate salts. *Phys. Chem. Chem. Phys.* **2015**, *17*, 32211−32218.
(34) Le Questel, J.-Y.; Graton, J.; Cerón-Carrasco, J. P.; Jacquemin, D.; Planchat, A.; Thany, S. H. New insights on the molecular features and electrophysiological properties of dinotefuran, imidacloprid and acetamiprid neonicotinoid insecticides. *Bioorg. Med. Chem.* **2011**, *19*, 7623−7634.
(35) Bryantsev, V. S.; Diallo, M. S.; Goddard, W. A., III Calculation of Solvation Free Energies of Charged Solutes Using Mixed Cluster/Continuum Models. *J. Phys. Chem. B* **2008**, *112*, 9709−9719.
(36) Grätzel, M.; Henglein, A.; Lilie, J.; Beck, G. Pulsradiolytische untersuchung einiger elementarprozesse der oxydation und reduktion des nitritions. *Ber. Bunsenges. Phys. Chem.* **1969**, *73*, 646−653.
(37) Tan, S. P.; Piri, M. Modeling the Solubility of Nitrogen Dioxide in Water Using Perturbed-Chain Statistical Associating Fluid Theory. *Ind. Eng. Chem. Res.* **2013**, *52*, 16032−16043.
(38) Burdick, C. L.; Freed, E. S. The equilibrium between nitric oxide, nitrogen peroxide and aqueous solution of nitric acid. *J. Am. Chem. Soc.* **1921**, *43*, 518−530.
(39) Vione, D.; Minella, M.; Maurino, V.; Minero, C. Indirect Photochemistry in Sunlit Surface Waters: Photoinduced Production of Reactive Transient Species. *Chem.—Eur. J.* **2014**, *20*, 10590−10606.
(40) Barzaghi, P.; Herrmann, H. A mechanistic study of the oxidation of phenol by $OH/NO_2/NO_3$ in aqueous solution. *Phys. Chem. Chem. Phys.* **2002**, *4*, 3669−3675.
(41) Alfassi, Z. B.; Huie, R. E.; Neta, P. Substituent effects on rates of one-electron oxidation of phenols by the radicals ClO_2, NO_2, SO_3^-. *J. Phys. Chem.* **1986**, *90*, 4156−4158.
(42) Semitsoglou-Tsiapou, S.; Templeton, M. R.; Graham, N. J. D.; Mandal, S.; Hernández Leal, L.; Kruithof, J. C. Potential formation of mutagenicity by low pressure-UV/H2O2 during the treatment of nitrate-rich source waters. *Environ. Sci.: Wat. Res . Technol.* **2018**, *4*, 1252−1261.
(43) Ma, H.; Allen, H.; Yin, Y. Characterization of isolated fractions of dissolved organic matter from natural waters and a wastewater effluent. *Wat. Res.* **2001**, *35*, 985−996.
(44) Keeney, D.; Olson, R. A. Sources of nitrate to ground water. *Crit. Rev. Environ. Control.* **1986**, *16*, 257−304.
(45) Perdue, E. M. Natural Organic Matter. In *Biogeochemistry of Inland Waters*; Likens, G. E., Ed.; Academic Press, 2009; pp 503−516.

https://dx.doi.org/10.1021/acs.est.9b07304
Environ. Sci. Technol. 2020, 54, 3325−3333

Supporting Information

New evidence of a "cocktail effect" through formation of nitro/nitroso products during irradiation of imidacloprid: influence of NOx, and natural organic matter

Davide Palma, Yara Arbid, Mohamad Sleiman*, Pascal de Sainte-Claire, Claire Richard*

Université Clermont Auvergne, CNRS, SIGMA Clermont, Institut de Chimie de Clermont-Ferrand, F-63000 Clermont-Ferrand, France

Mohamad.sleiman@sigma-clermont.fr

Claire.richard@uca.fr

Tel : +33 (0)4 73 40 71 42

Fax : +33 (0)4 73 40 77 00

Figure SI-1 . Irradiance of the fluorescent tubes Sylvania F15W/BL 368S used in devices 1 and 2.

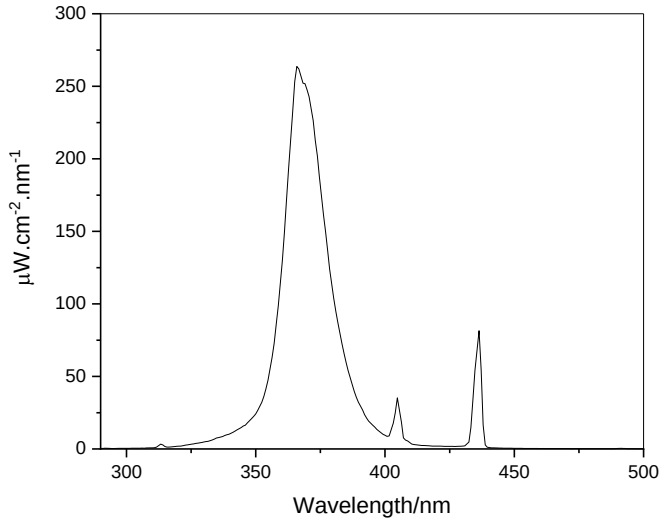

Figure SI-2. Background level of NOx formation (A) and NOx formation upon irradiation of IMD (10^{-4} M) for 1 h in device 1 (B). After selected irradiation times, the light was turned off and the outlet of the reactor connected to the NOx analyzer. NOx were measured every 10 seconds for a period of 1-2 min at a flow rate of 0.7 L min^{-1}. The time profile of NOx concentrations corresponds to the decay of NOx level in the reactor due to the dilution with clean air.

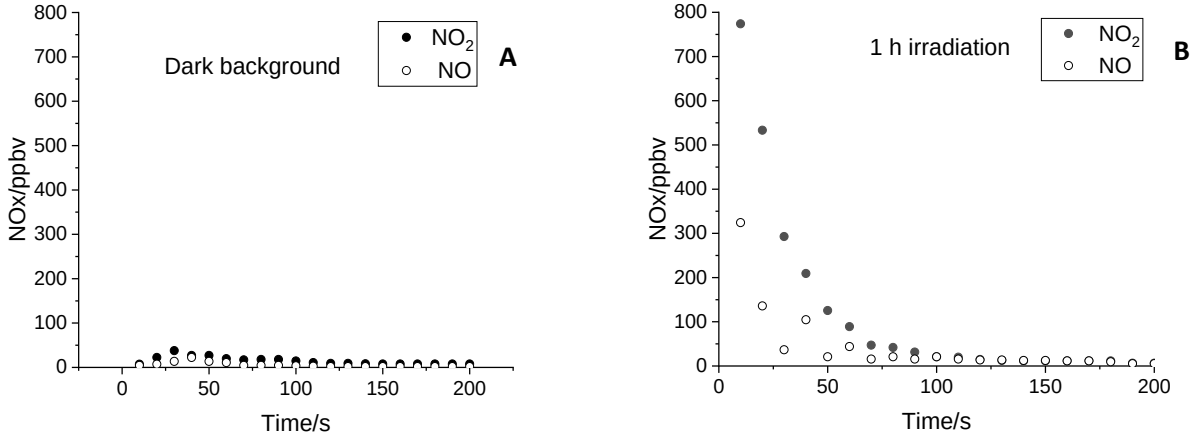

Table SI-7. HPLC conditions used for separation and analysis of the different compounds.

Compound	H_2O (%)	ACN	Detection wavelength/nm
IMD	60	40	270
Phenol	60	40	270
L-tryptophan	85	15	280
Resorcinol	70	30	274
NO_2^- (derivatized)	60	40	307

Figure SI-3. Calibration curve for nitroso-phenol (open circles) and for nitro-phenol (black circles). Area were obtained by UPLC-HR-MS analyses in electrospray negative mode. For nitrosophenol m/z= 122.0237 (5 ppm) and for nitrophenol m/z=138.0186 (5 ppm).

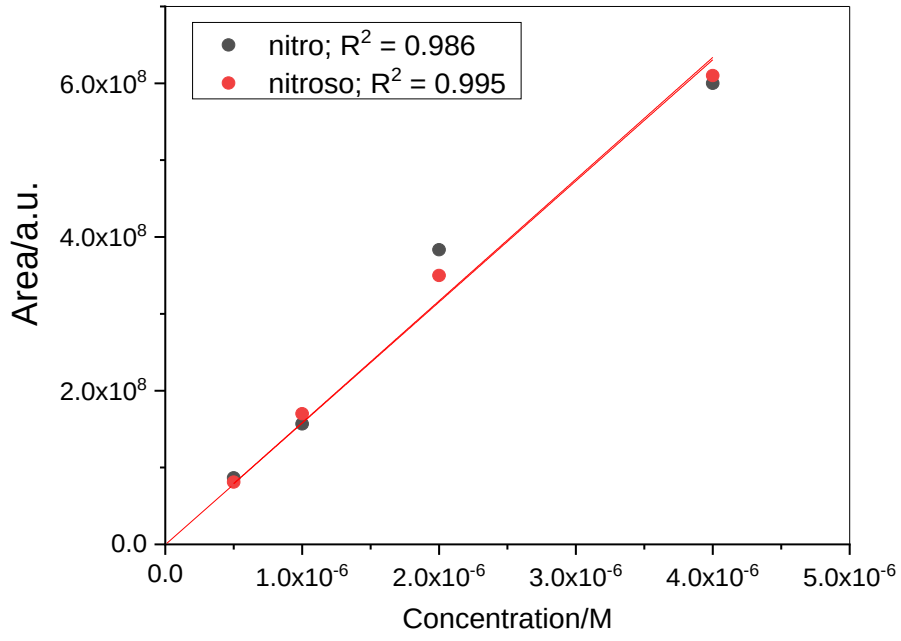

Figure SI-4. Consumption profile of aqueous IMD (10^{-4} M) irradiated in device 1, formation of NO_3^- and NO_2^- (A) and area UPLC-HRMS of desnitro-IMD (B). IMD was analyzed by HPLC-UV, NO_3^- by ionic chromatography, NO_2^- by HPLC-UV after derivatization by DNPH. Desnitro-IMD was identified by UPLC-HRMS (m/z = 22.0740/213.0709, Δ = 2.2 ppm).

A)

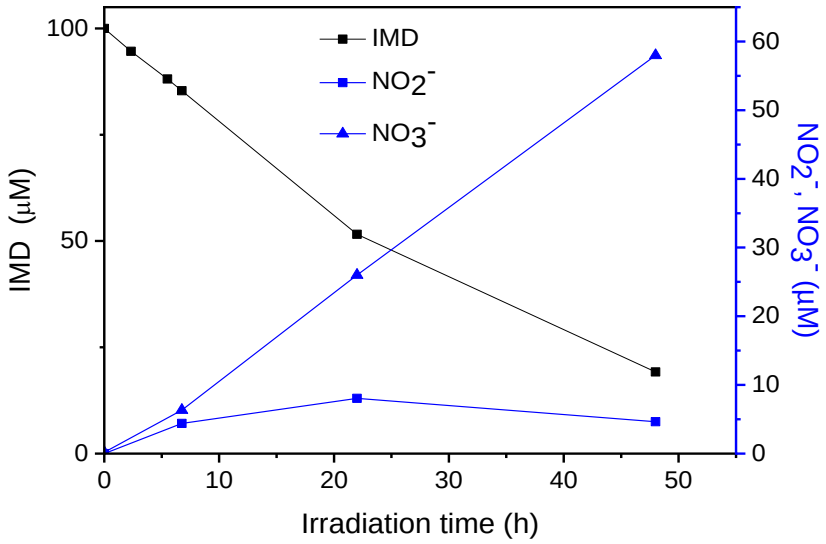

B)

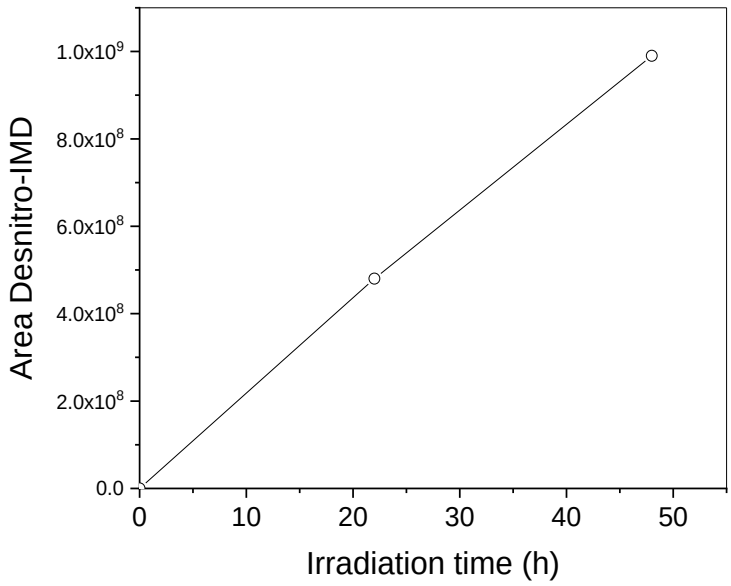

Table SI-2: UPLC-HMRS of IMD and photoproducts.

Name	m/z exp. in ES^+	m/z theor. in ES^+	Δppm	Formula of the neutral molecule
IMD	256.0603/ 258.0571	256.0596/ 258.0566	2.82	$C_9H_{10}ClN_5O_2$
IMD+O	272.0549/ 274.0517	272.0545/ 274.0515	1.38	$C_9H_{10}ClN_5O_3$
IMD-O	240.0650/ 242.0620	240.0647/ 242.0617	1.52	$C_9H_{10}ClN_5O$
Desnitro-IMD	211.0746/ 213.0717	211.0745/ 213.0716	0.33	$C_9H_{11}ClN_4$
Desnitro-IMD+2O	243.0650/ 245.0619	243.0643/ 245.0614	2.84	$C_9H_{11}ClN_4O_2$

Figure SI-5. Structures (a)-(k) of the minimum energy structures and TSs at the MN12SX/6-311++G(d,p),PCM//MN12SX/6-31+G(d,p),PCM level. Energies are given relatively to the global minimum (see Figure 4). Specific bond distances (Å) are also indicated.

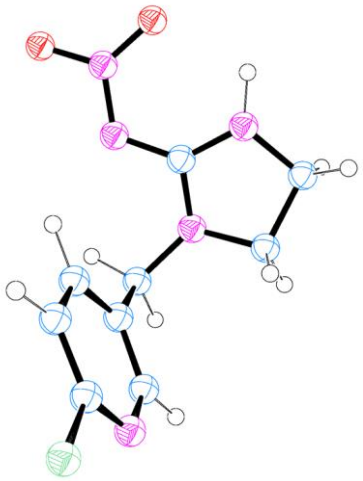

Global min in S_0, $^1RNNO_2$ (a)
0.0 kcal mol^{-1}

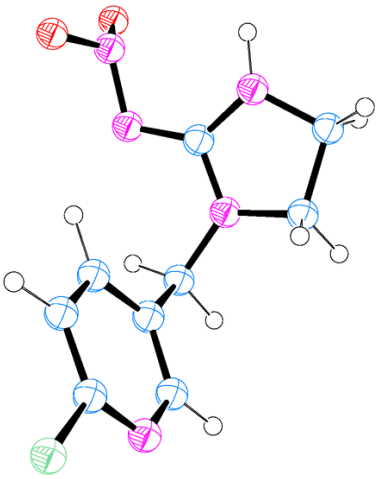

Min in S_1 (b)
79.3 kcal mol^{-1}

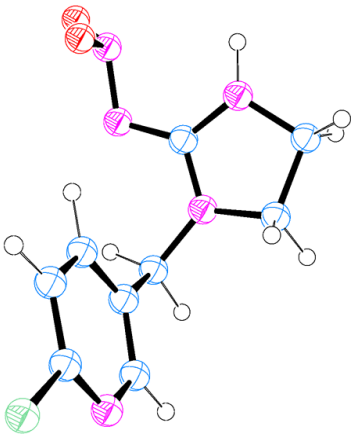

Min in T_1, $^3RNNO_2$ (c)
67.3 kcal mol^{-1}

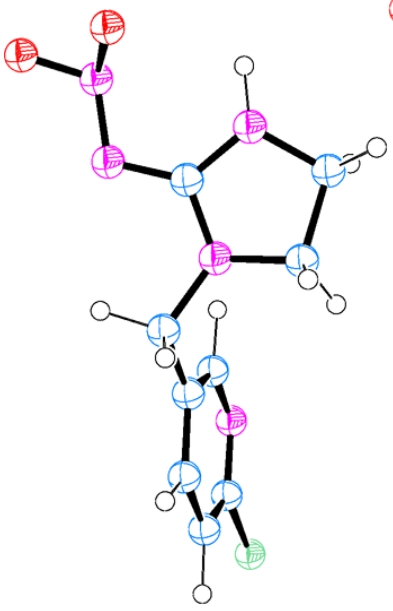

TS in S_0 (d)
106.1 kcal mol^{-1}

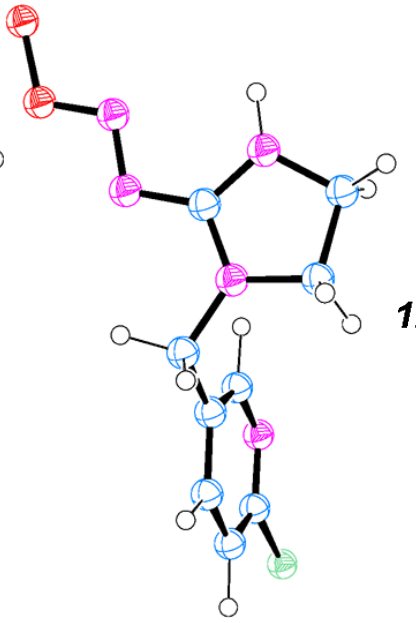

^1RNNO-O (e)
56.4 kcal mol^{-1}

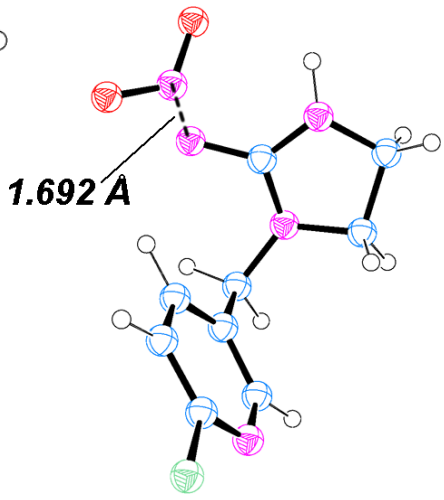

TS_1 in T_1 (f)
73.4 kcal mol^{-1}

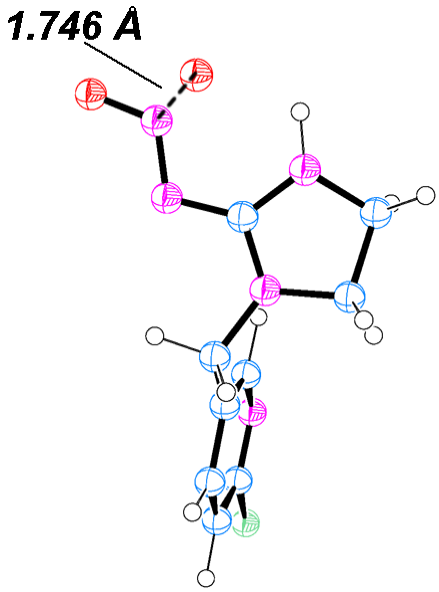

TS_2 in T_1 (g)

78.7 kcal mol^{-1}

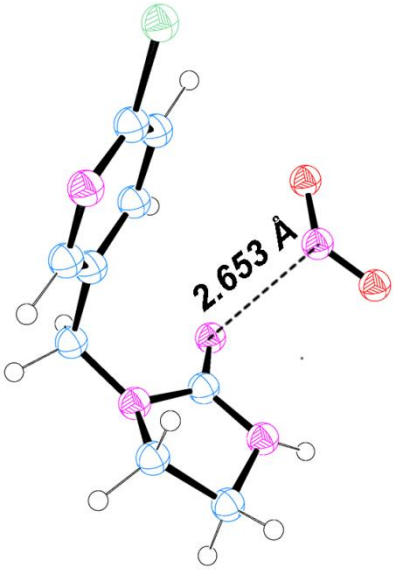

$^3RN{-}{-}{-}NO_2$ (h)

59.8 kcal mol^{-1}

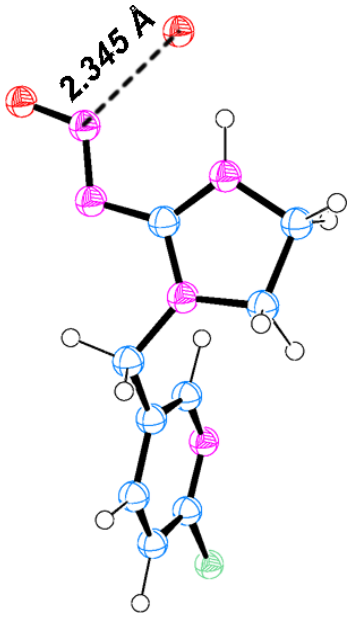

^3RNNO-O in T_1 (i)

76.1 kcal mol^{-1}

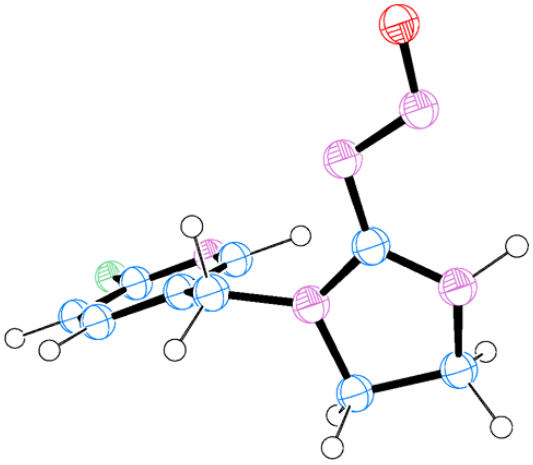

^1RNNO (j)

80.4 kcal/mol

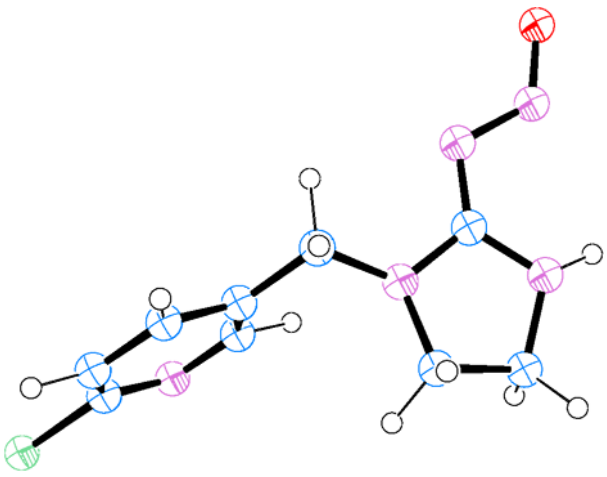

^3RNNO (k)

121.4 kcal/mol

Table SI-3:

Min S_0, $^1RNNO_2$ (a)			Min S_1 (b)			Min T_1, $^3RNNO_2$ (c)			TS S_0 (d)			^1RNNO-O (e)		
C -3.904635	0.765039	0.032387	C -3.398081	0.341802	0.079196	C -3.362675	-0.347631	-0.074888	C -0.203027	-0.349078	1.121773	C -0.154117	0.191187	1.381299
C -2.651975	1.265986	-0.317873	C -2.294923	1.176317	0.255215	C -2.232460	-1.117072	-0.347477	H -0.281192	-0.106962	2.195510	H -0.106941	0.737387	2.336454
C -1.771163	0.388254	-0.933223	C -1.082502	0.731770	-0.248795	C -1.023506	-0.662472	0.156625	C -0.927867	1.995016	0.518132	C -0.739471	2.341866	0.147460
C -2.166764	-0.931261	-1.177332	C -1.017011	-0.505420	-0.896764	C -0.987178	0.524124	0.897419	C -2.038247	2.499264	-0.402607	C -1.809222	2.629975	-0.911387
C -3.448748	-1.301054	-0.779059	C -2.191008	-1.246366	-0.998624	C -2.187175	1.202458	1.087676	H 0.065289	2.357516	0.229170	H 0.281189	2.492397	-0.221553
N -4.312703	-0.469965	-0.181967	N -3.370853	-0.830912	-0.522588	N -3.364975	0.775416	0.614761	H -1.113855	2.266057	1.571397	H -0.881746	2.940803	1.060570
H -0.776932	0.727778	-1.229275	H -0.190402	1.353466	-0.141601	H -0.110339	-1.235334	-0.023647	H -1.666108	2.679980	-1.422076	H -1.412985	2.518630	-1.930749
H -2.387350	2.301614	-0.116328	H -2.391683	2.132733	0.763368	H -2.306763	-2.033495	-0.928024	H -2.521117	3.407213	-0.029650	H -2.254452	3.623066	-0.803036
H -3.809069	-2.319038	-0.948182	H -2.192201	-2.220737	-1.492300	H -2.212382	2.137059	1.652683	N -1.031695	0.548155	0.348818	N -0.982752	0.931296	0.453497
Cl -5.046843	1.828429	0.817110	Cl -4.947854	0.860345	0.690667	Cl -4.909736	-0.885948	-0.680589	N -2.954805	1.363624	-0.384090	N -2.783146	1.578648	-0.630835
C -1.232405	-1.933964	-1.814625	C 0.284558	-1.025771	-1.465310	C 0.307430	1.054822	1.468931	H -3.762834	1.318289	-0.997301	H -3.601560	1.412056	-1.206440
H -1.798679	-2.809084	-2.160279	H 0.121930	-1.973713	-1.994034	H 0.132063	1.999553	1.999723	C -2.283558	0.237601	-0.063034	C -2.199555	0.582978	0.040735
H -0.725483	-1.498193	-2.682400	H 0.717191	-0.308883	-2.173030	H 0.737372	0.344379	2.185474	N -2.734621	-1.004600	-0.084846	N -2.702912	-0.649266	0.324821
C -0.574092	-3.204168	0.277229	C 1.131843	-2.341972	0.556493	C 1.135361	2.343184	-0.572120	N -3.959398	-1.067285	-0.660242	N -3.874881	-0.779031	-0.195123
C 0.789058	-3.429027	0.931785	C 2.423456	-2.204268	1.370553	C 2.415193	2.194510	-1.400977	O -4.611643	-2.141095	-0.408242	O -4.346713	-1.939414	0.072304
H -1.068425	-4.135321	-0.020573	H 1.028070	-3.311187	0.056855	H 1.036222	3.327626	-0.102311	O -5.110203	-0.465414	0.134532	O -5.621750	-2.141845	-0.462369
H -1.253750	-2.632790	0.931988	H 0.232750	-2.158848	1.167751	H 0.230410	2.138675	-1.167309	H -0.594941	-1.366250	0.989337	H -0.644501	-0.770714	1.576793
H 1.249157	-4.371466	0.600354	H 3.217372	-2.862363	0.989606	H 3.203420	2.879828	-1.057836	C 1.242504	-0.290799	0.691388	C 1.240908	-0.022062	0.843308
H 0.746251	-3.415572	2.024795	H 2.272044	-2.399108	2.435751	H 2.245955	2.346043	-2.470799	C 1.593661	-0.164240	-0.652341	C 1.469772	-0.258065	-0.511323
N -0.214848	-2.410322	-0.893377	N 1.268626	-1.268798	-0.425800	N 1.301086	1.300108	0.439606	C 2.279394	-0.394872	1.619394	C 2.348739	-0.015140	1.691979
N 1.544992	-2.291783	0.421331	N 2.767602	-0.804712	1.131045	N 2.786811	0.811780	-1.113668	H 0.821427	-0.066346	-1.418580	H 0.640957	-0.266019	-1.222977
H 2.526684	-2.126330	0.609672	H 3.643477	-0.393806	1.439213	H 3.658194	0.398663	-1.430265	C 3.598640	-0.382619	1.185131	C 3.615398	-0.245686	1.172933
C 0.977749	-1.810901	-0.690410	C 2.172605	-0.379626	0.008438	C 2.210014	0.409620	0.025425	H 2.059851	-0.483432	2.684555	H 2.226772	0.173523	2.759720
N 1.360434	-0.869752	-1.568602	N 2.361218	0.770849	-0.659494	N 2.440532	-0.712142	0.738625	C 3.810872	-0.256142	-0.184742	C 3.706360	-0.466007	-0.198603
N 2.579242	-0.334902	-1.426154	N 3.279295	1.593014	0.010847	N 3.347063	-1.548856	0.067730	H 4.433881	-0.460282	1.877288	H 4.503037	-0.245919	1.801116
O 2.875910	0.546229	-2.242636	O 4.420065	1.561650	-0.596315	O 4.205043	-2.174075	0.755423	Cl 5.450699	-0.230562	-0.787984	Cl 5.279412	-0.743932	-0.906833
O 3.377159	-0.691010	-0.533892	O 2.747453	2.691061	0.409641	O 2.498420	-2.230334	-0.725516	N 2.857413	-0.145456	-1.090040	N 2.682984	-0.474873	-1.031162

Cartesian coordinates of the minimum energy structures and TSs at the MN12SX/6-311++G(d,p),PCM//MN12SX/6-31+G(d,p),PCM level.

TS_1, T_1 (f)			TS_2, T_1 (g)			^3RN---NO_2 (h)			^3RNNO-O in T_1 (i)		
C 3.187194	0.227055	-0.124355	C -0.205293	-0.060599	1.314892	C 2.814838	-0.330504	-0.104796	C -0.119348	0.059714	1.469669
C 2.151026	1.138337	0.074237	H -0.225749	0.396895	2.317390	C 2.114040	0.556284	0.708377	H -0.069546	0.605839	2.425420
C 0.975015	0.646553	0.621106	C -1.037432	2.128770	0.331767	C 0.901175	0.115662	1.220359	C -1.011961	2.155277	0.347300
C 0.879107	-0.711259	0.943283	C -2.129584	2.411617	-0.703288	C 0.436348	-1.163967	0.903215	C -2.178567	2.355329	-0.625482
C 1.988973	-1.514046	0.692219	H -0.045765	2.465962	0.008335	C 1.243134	-1.952450	0.083372	H -0.044390	2.445562	-0.078388
N 3.132100	-1.057506	0.166573	H -1.264221	2.578975	1.311582	N 2.416805	-1.548618	-0.417693	H -1.158771	2.696668	1.295427
H 0.138042	1.327863	0.800686	H -1.716339	2.479670	-1.720069	H 0.313353	0.770053	1.867321	H -1.840656	2.350273	-1.672011
H 2.270553	2.187294	-0.186483	H -2.695331	3.321754	-0.483212	H 2.507230	1.545953	0.930126	H -2.733398	3.278748	-0.434443
H 1.966680	-2.580645	0.929145	N -1.088372	0.671828	0.437138	H 0.939235	-2.968736	-0.181882	N -1.065274	0.715845	0.595987
Cl 4.689901	0.800493	-0.804530	N -2.966371	1.222997	-0.571628	Cl 4.350410	0.173373	-0.772346	N -2.997235	1.179441	-0.350447
C -0.389542	-1.299857	1.516466	H -3.745817	1.032188	-1.193510	C -0.908128	-1.653261	1.387958	H -3.826097	0.923517	-0.890056
H -0.200563	-2.300278	1.925345	C -2.262716	0.219044	-0.023736	H -0.902819	-2.744665	1.506130	C -2.262662	0.235823	0.242243
H -0.778435	-0.671310	2.328589	N -2.607783	-1.069180	0.109505	H -1.139081	-1.213097	2.368362	N -2.592191	-1.049179	0.519810
C -1.356164	-2.374792	-0.593330	N -3.779593	-1.321407	-0.472256	C -2.131166	-1.961989	-0.816481	N -3.771921	-1.362575	0.037006
C -2.639341	-2.062339	-1.370850	O -4.195045	-2.471112	-0.504790	C -3.316312	-1.199517	-1.397255	O -4.181012	-2.488907	0.271856
H -1.313314	-3.403713	-0.220838	O -5.077016	-0.351132	0.178466	H -2.317457	-3.035770	-0.700481	O -5.042584	-0.382344	-1.673348
H -0.452574	-2.169155	-1.190489	H -0.599483	-1.080291	1.416376	H -1.226612	-1.815491	-1.433860	H -0.503267	-0.945154	1.687434
H -3.477316	-2.694880	-1.044078	C 1.214956	-0.100755	0.803031	H -4.270264	-1.631624	-1.055222	C 1.260847	-0.028331	0.862984
H -2.515145	-2.155929	-2.453515	C 1.507667	-0.062886	-0.559029	H -3.306916	-1.162074	-2.491041	C 1.450728	-0.180374	-0.509285
N -1.441694	-1.426608	0.518570	C 2.288934	-0.215521	1.688497	N -1.997941	-1.317254	0.485603	C 2.399265	0.002449	1.670371
N -2.871707	-0.672843	-0.985360	H 0.708298	0.036117	-1.296650	N -3.085288	0.122779	-0.824530	H 0.597108	-0.199956	-1.190479
H -3.677759	-0.121158	-1.268011	C 3.583197	-0.300980	1.195184	H -3.789700	0.848562	-0.910140	C 3.655784	-0.128373	1.096183
C -2.250335	-0.412582	0.167004	H 2.116853	-0.238813	2.765821	C -2.443143	-0.018085	0.379887	H 2.307632	0.129040	2.750445
N -2.366870	0.699289	0.925083	C 3.736657	-0.256583	-0.188209	N -2.271254	0.910898	1.266655	C 3.706095	-0.278963	-0.287035
N -2.480190	2.017349	-0.129050	H 4.444850	-0.392440	1.852223	N -0.783212	2.567466	-0.175823	H 4.565384	-0.108351	1.691679
O -3.713558	2.017662	-0.435706	Cl 5.345353	-0.362644	-0.862800	O -1.580424	2.968442	-0.977686	Cl 5.264756	-0.448675	-1.059718
O -1.882135	3.011505	0.314613	N 2.749246	-0.137062	-1.053440	O -0.042379	3.151509	0.565595	N 2.654169	-0.302675	-1.082295

Figure SI-6. Structures of **RN^+** (a), **RN^+,H_2O** (b) and **RN,H_2O** (c) obtained at the MN12SX/6-31+G(d,p),PCM level and calculation of RN^+ energy:

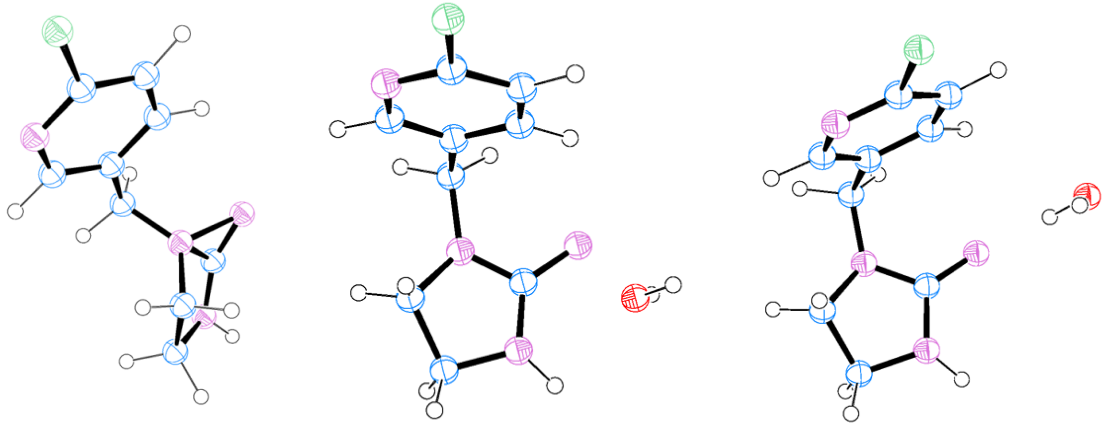

(a) **(b)** **(c)**

Calculation of RN^+ energy:

Optimization of RN^+ at the MN12SX/6-31+G(d,p),PCM level gave rise to the high energy cyclized species in Fig SI-6a. This structure is similar to that found in the gas phase (MN12SX/6-31+G(d,p)) and it became clear that the PCM model was not sufficient to account for solvent effects here. It was thus decided to optimize RN^+ at the MN12SX/6-31+G(d,p),PCM level in the presence of one water molecule (implicit + explicit solvation model). The obtained geometry is shown below in Figure SI-6b (no spurious cyclization). Thus, the more accurate energy of RN^+ (RN^+/NO_2^- at 69.0 kcal/mol in Figure 4) was that of RN^+ obtained at the MN12SX/6-31+G(d,p),PCM level and corrected with the energy difference below, i.e:

$$E_{text}(RN^+) = E(RN^+) + [E(RN^+,H_2O) - E(RN,H_2O)] - [E(RN^+) - E(RN)]$$

These species computed at the MN12SX/6-311++G(d,p),PCM // MN12SX/6-31+G(d,p),PCM level

i.e: $E_{text}(RN^+) = E(RN) + [E(RN^+,H_2O) - E(RN,H_2O)]$

Figure SI-7. Consumption profile of IMD (10^{-4} M) upon irradiation in device 2. The concentrations of IMD were determined by HPLC-UV.

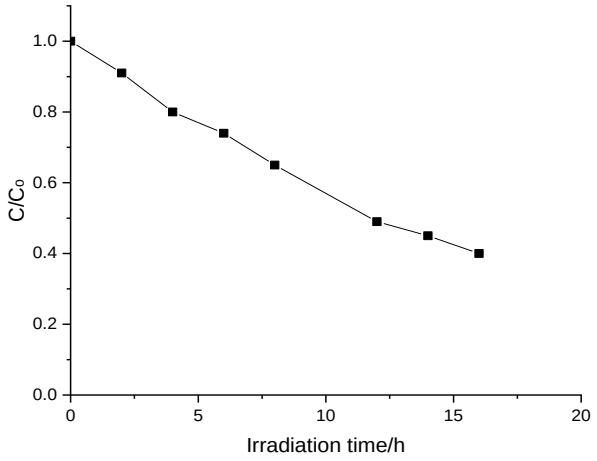

Figure SI-8: Formation of nitroso-resorcinol (open circles) and nitro-resorcinol (full circles) upon irradiation in device 2 of IMD (10^{-4} M) and resorcinol (10^{-4} M). The concentrations of nitroso and nitro-resorcinols were estimated using calibration curves of Figure SI-3.

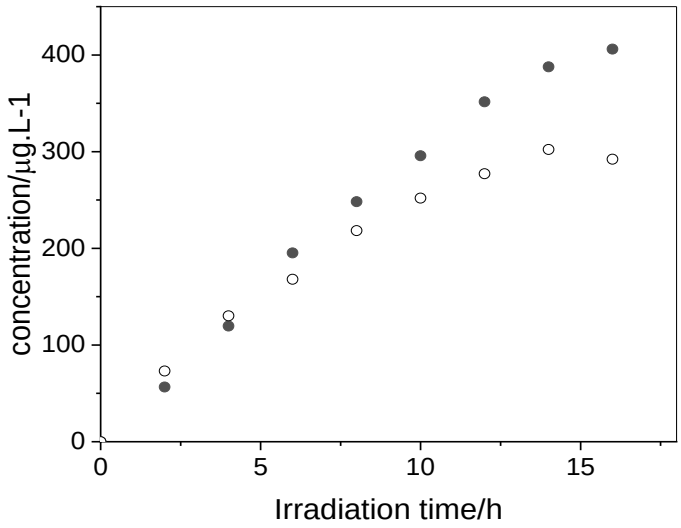

Table SI-4: Photonitration and photonitrosation of the probes after 16 h of irradiation in device 2 in presence of IMD (10^{-5} or 10^{-4} M) or a mixture of NO_3^- (2×10^{-5} M) and NO_2^- (5×10^{-6} M). The concentrations of IMD and of the probes were obtained by HPLC-UV while the amunts of nitro and nitro-derivatives by UPLC-HRMS.

Conditions	**% of converted IMD**	**% of converted probe**	**Nitroso derivative formed ($\mu g.L^{-1}$)**	**Nitro derivative formed ($\mu g.L^{-1}$)**	**Sum ($\mu g.L^{-1}$)**
Phenol (10^{-4} M)	-	< 0.5	-	-	-
Phenol (10^{-4} M)+ IMD (10^{-4} M)	56±3	14±1	34±2	202±10	236±12
Phenol (10^{-4} M)+ NO_2^-/NO_3^-	-	3.4±0.1	0.28±0.02	34±2	34±2
Resorcinol (10^{-4} M)	-	< 0.5	-	-	-
Resorcinol (10^{-4} M)+IMD (10^{-4} M)	58±3	29±1	406±40	292±29	498±69
Resorcinol (10^{-4} M)+IMD (10^{-5} M)	61±3	46±5	43±4	16±2	59±6
Resorcinol (10^{-5} M)+IMD (10^{-4} M)	62±3	58±5	3.6±0.8	100±20	104±21
Resorcinol (10^{-4} M)+ NO_2^-/NO_3^-		6.2±0.3	99±9	70.8±7	170±16
Tryptophan (10^{-4} M)	-	91±5	-	-	-
Tryptophan (10^{-4} M)+IMD (10^{-4} M)	60±3	95±5	19±2	9.4±0.9	28±3
Tryptophan (10^{-4} M)+ NO_2^-/NO_3^-	-	96±5	7.4±0.7	6.2±0.6	14±2

MANUSCRIPT 4

PFAS Degradation in Ultrapure and Groundwater Using Non-Thermal Plasma

Publishing journal: Molecules

Date of acceptance: 5 February 2021

molecules

MDPI

Article

PFAS Degradation in Ultrapure and Groundwater Using Non-Thermal Plasma

Davide Palma [1], Dimitra Papagiannaki [2], Manuel Lai [3], Rita Binetti [2], Mohamad Sleiman [1], Marco Minella [4,*] and Claire Richard [1,*]

[1] Université Clermont Auvergne, CNRS, Sigma Clermont, ICCF, 63178 Aubière, France; davide.palma@etu.uca.fr (D.P.); mohamad.sleiman@sigma-clermont.fr (M.S.)
[2] SMAT S.p.A., Research Centre, C.so Unità d'Italia 235/3, 10127 Torino, Italy; dimitra.papagiannaki@smatorino.it (D.P.); rita.binetti@smatorino.it (R.B.)
[3] IRIS s.r.l., Via Papa Giovanni Paolo Secondo 26, 10043 Orbassano, Italy; manuel.lai@irissrl.org
[4] Department of Chemistry and Interdepartmental Centre Nanostructured Interfaces and Surfaces (NIS), University of Torino, Via Pietro Giuria 5, 10125 Torino, Italy
* Correspondence: marco.minella@unito.it (M.M.); claire.richard@uca.fr (C.R.)

Abstract: Perfluoroalkyl substances (PFAS) represent one of the most recalcitrant class of compounds of emerging concern and their removal from water is a challenging goal. In this study, we investigated the removal efficiency of three selected PFAS from water, namely, perfluorooctanoic acid (PFOA), perfluorohexanoic acid (PFHxA) and pefluorooctanesulfonic acid (PFOS) using a custom-built non-thermal plasma generator. A modified full factorial design (with 2 levels, 3 variables and the central point in which both quadratic terms and interactions between couple of variables were considered) was used to investigate the effect of plasma discharge frequency, distance between the electrodes and water conductivity on treatment efficiency. Then, the plasma treatment running on optimized conditions was used to degrade PFAS at ppb level both individually and in mixture, in ultrapure and groundwater matrices. PFOS 1 ppb exhibited the best degradation reaching complete removal after 30 min of treatment in both water matrices (first order rate constant 0.107 min^{-1} in ultrapure water and 0.0633 min^{-1} in groundwater), while the degradation rate of PFOA and PFHxA was slower of around 65% and 83%, respectively. During plasma treatment, the production of reactive species in the liquid phase (hydroxyl radical, hydrogen peroxide) and in the gas phase (ozone, NO_x) was investigated. Particular attention was dedicated to the nitrogen balance in solution where, following to NO_x hydrolysis, total nitrogen (TN) was accumulated at the rate of up to 40 $mg^N\ L^{-1}\ h^{-1}$.

Keywords: non-thermal plasma; PFAS; NO_x; water treatment; advanced oxidation processes

Citation: Palma, D.; Papagiannaki, D.; Lai, M.; Binetti, R.; Sleiman, M.; Minella, M.; Richard, C. PFAS Degradation in Ultrapure and Groundwater Using Non-Thermal Plasma. *Molecules* **2021**, *26*, 924. https://doi.org/10.3390/molecules26040924

Academic Editor: Giorgio Vilardi
Received: 14 January 2021
Accepted: 5 February 2021
Published: 9 February 2021

1. Introduction

The availability of clean water sources is worldwide rapidly diminishing, so the availability of effective technologies capable to ensure water reuse has become a primary necessity. This is not only a challenge for those countries having scarce freshwater resources but also for densely populated regions like Europe where over 64% of freshwater is collected from rivers [1]. Most operating wastewater treatment plants (WWTPs) rely on traditional treatments (e.g., biological treatment, sedimentation and active carbon filtration) unable to totally remove a large number of bio-recalcitrant anthropogenic compounds often referred to as CECs (Contaminants of Emerging Concern) that are returned to the environment [2–4]. For most CECs typical surface water concentration ranges from few ppt to tens of ppb but removal efficiency can drastically change depending on pollutant's initial concentration, wastewater characteristics and the type of adopted technology [5,6]. The presence of CECs in water bodies not only limits water reuse but it is also deleterious for the aquatic fauna as many CECs are toxic

compounds and often endocrine disruptors [7,8]. Among CECs, perfluoroalkyl compounds (PFAS) represent one of the most problematic class of compounds due to their resistance to conventional water treatments and persistence in the environment [9–11].

Advanced Oxidation Processes (AOPs) have been proposed to be implemented together with the conventional biological treatments to efficiently address the removal of CECs from wastewater [12–15]. These processes rely on chemical and/or physical processes generating highly reactive radical species (such as $HO^{\bullet}$ and $SO_4^{\bullet-}$) able to react non selectively with the most organic compounds in solution, including, bio-recalcitrant compounds [16,17]. Among the most conventional AOPs are the Fenton and photo-Fenton processes, ozonation, UV photolysis, H_2O_2 and heterogeneous photocatalysis [18,19]. While ozonation and UV photolysis are relatively simple processes that have also been proven effective in degrading CECs, their large-scale application has been strongly limited by high operational costs.

Water plasma is attracting today the attention of a growing number of researchers due to its promising performances in water treatment applications [20]. Non-thermal plasmas in particular have been intensively studied due to a series of practical advantages like low energy consumption and simple operative equipment [21,22]. From a chemical standpoint, the main advantage in using such technology is the ability to activate different processes at the same time such as the formation of highly reactive species like $H^{\bullet}$, O, $HO^{\bullet}$ radicals, free electrons and ozone, as well as oxidants (e.g., hydrogen peroxide), the generation of ultraviolet light due to the plasma discharge light emission and the generation of shockwaves and high-density electric fields. The degradation mechanism of pollutants is therefore complex. Different electrodes configuration has been explored but the most used geometry for water plasma application is the so called point-to-plane or needle-to-plane geometry where positive or negative polarity is applied to a needle-like electrodes while a larger plate-shaped electrode is grounded [22–24]. According to the polarity applied to the electrode, important differences in terms of treatment efficiency can be observed [21,25]. Due to the chemical stability of the C-F bond in PFAS, these compounds are extremely refractory to degradation resulting in insufficient abatement when using traditional water treatment technologies. Recently, the use of non-thermal plasma for PFAS removal has been investigated by several research groups. Despite the promising results obtained so far, an exhaustive comprehension of the degradation mechanism and the study of simultaneous treatment of different PFAS in real water matrices is poorly documented in the literature [26,27].

The aim of this work was to optimize the performances of a custom-made high voltage discharge generator (European Patent n EP 3 023 392 B1) for water treatment applications and then, to test the removal efficiency of the optimized plasma system on three perfluoroalkyl compounds (PFAS). In the first part of the work, a modified full factorial design (with 2 levels, 3 variables and the central point in which both quadratic terms and interactions between couple of variables were considered) was used to maximize water pollutants removal and the discoloration of methylene blue solution was used as response. Then, the generation of reactive species like hydrogen peroxide, ozone and NO_x has been evaluated during plasma treatment. Attention was dedicated to the nitrogen balance in the solution. Last, the removal efficiency of the plasma treatment on three recalcitrant PFAS (perfluorooctanoic acid (PFOA), perfluorohexanoic acid (PFHxA) and pefluorooctanesulfonic acid (PFOS)) was investigated individually and in mixture, both in ultrapure water and in a real groundwater matrix. Compared to other systems, this discharge generator is capable of delivering high voltage pulses that rise from zero to 120 kV in five nanoseconds. This fast-rising potential is a crucial feature capable of ensuring the generation of the streamer even when working with highly conductive water matrices. Each pulse consists of multiple peaks of 10 nanoseconds reaching 90 to 120 kV. The total duration of the pulse is approximately 250 nanoseconds, considerably shorter than standard Pulsed Electric Field (PEF) systems.

2. Materials and Methods

2.1. Chemicals

PFOA (Perfluorooctanoic acid, analytical standard), PFOS (Perfluorooctanesulfonic acid, solution 40% *w*/*w*), PFHxA (perfluorohexanoic acid, analytical standard), methylene blue (MB, purity > 95%), methyl orange (MO, purity 85%), furfuryl alcohol (FFA, purity 98%), sodium nitrite (purity ≥ 97%), sodium nitrate (purity ≥ 99%), ammonium chloride (purity ≥ 99.5%), potassium hydrogen phthalate (purity ≥ 99.5%), sodium hydroxide (purity ≥ 98.0%), ammonium heptamolybdate tetrahydrate (purity ≥ 99.0%), potassium iodide (purity ≥ 99.0%) and hydrogen peroxide (solution 30% *w*/*w*) were purchased from Sigma-Aldrich and used without further purification. Dry natural organic matter was purchased from International Humic Substances Society (product code 2R101N). 2-Propanol and chromatographic UHPLC-grade methanol were purchased from Carlo Erba Reagents. All aqueous solutions, if not differently specified, were prepared using ultrapure water Millipore Milli-Q™ (TOC < 2 ppb, 18.2 MΩ cm).

2.2. Plasma Generator

The high voltage discharges were generated with a custom-built Marx generator powered with 220 V AC equipped with a pulse-width modulation circuit, a high-voltage transformer and four 990 pF capacitors. A small continuous flow of compressed air with relative humidity around 14% was fed to the spark-gaps' chamber to stabilize the generator's internal atmosphere. The discharge's peak voltage was typically 100–130 kV with peak current values of 20–40 A. The pulse duration was approximately 250 ns and the frequency of discharge could be manually adjusted between 5 and 17 Hz. Electrical measures have been performed using a BK Precision 2190D oscilloscope. Total absorbed power of the generator laid between 299 and 322 W. Water was treated using two different reactors: a 20 mL cylindrical polypropylene (PP) reactor was used in the first part of the work aimed to the optimization of working parameters while a 50 mL Pyrex glass (PG) reactor was used for all other experiments. The PP reactor on one site limited the risk of damage of the reactor wall as a consequence of the generated shock waves, whilst on the other side caused Total Organic Carbon (TOC) and Total Nitrogen (TN) potential contamination from plastics and rubber parts. For both reactors, the same electrodes have been used consisting in one stainless steel bar having 10 mm diameter and a tungsten sintered electrode with a diameter of 3 mm on the other side. In the PG reactor the distance between the electrodes determined whether the discharge was forming underwater (distance < 2 mm) or at the water surface (distance > 2 mm). For both reactors, the headspace was in connection with the room air. Schematic representation of the experimental setup is shown in Figure 1. Both the plasma generator and the reactors were positioned inside a Faraday cage.

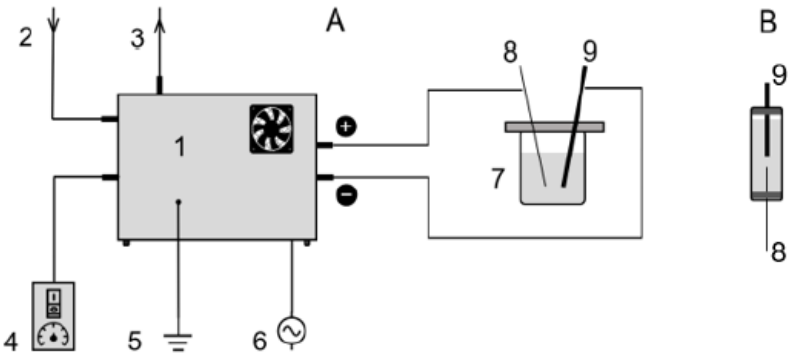

Figure 1. Schematic representation of the plasma generator connected to the Pyrex glass (PG) reactor (A): (1) plasma generator, (2) air inlet, (3) air outlet, (4) plasma switch and frequency control, (5) ground, (6) 220 V power supply, (7) PG reactor, (8) sintered tungsten electrode, (9) stainless steel electrode. polypropylene (PP) reactor (B).

2.3. Analytical Methods

PFAS analyses were carried out using a SCIEX X500R QTOF system coupled to a Shimadzu ExionLC UHPLC system equipped with a Luna® Omega Polar C18 100 LC Column (3 µm particle size, 100 × 2.1 mm) heated at 40 °C. Injection volume was 50 µL and the mobile phase was a mixture of 5 mM Ammonium Acetate in H_2O (A) and 5 mM Ammonium Acetate in MeOH (B) at a 0.350 mL/min flow. The gradient elution started with 95% A and 5% B, which was held up to 1 min and then gradually changed up to 100% B within 10 min. This ratio was kept for 2 min and then gradually reversed into the initial conditions until 15 min of elution. MS analysis was performed with the X500R QTOF mass spectrometer, which operated in negative Electrospray Ionization mode (ESI). The source conditions were set as the following: gas temperature 500 °C, Curtain gas pressure 30 psi, ion spray voltage −4500 V. The acquisition was done using the SWATH (Sequential Window Acquisition of All Theoretical Fragment Ions) mode, which is a Data Independent Acquisition (DIA) method where all the precursor ions within the determined *m*/*z* range are fragmented in a methodical and unbiased way. The SWATH mode consisted of a TOF MS full scan, followed by MS/MS experiments with fixed quadrupole (Q1) isolation windows. The full scan covered a mass range of *m*/*z* 100–1500 with an accumulation time of 0.05 s. The Q1 precursor ions' isolation strategy (MS/MS scans) covered a mass range of *m*/*z* 50–1500 with window width of 25 Da and each SWATH window had an accumulation time of 0.03 s. A collision energy (CE) of 35 eV with a CE spread of 15 eV was applied. The chromatograms and mass spectra were processed with the SCIEX OS 1.7 software. PFAS quantification was based on six-points calibration curves (10, 50, 100, 500, 1000 and 5000 ppt) having $R^2 > 0.99$ for all compounds.

The concentration of NO, NO_2, NO_x and O_3 produced during plasma treatment was determined using the Horiba APOA-360 Ambient Ozone Monitor and the Horiba APNA-370 Ambient NO_x Monitor. Air was sampled 2 cm above treated water surface using a polytetrafluoroethylene (PTFE) gas sampling tube and the air flow was then split in two and sent to the NO_x and ozone analyzers simultaneously. Total sampling flow was 1.5 L/min.

Total nitrogen was measured using a Shimadzu TOC-VCSH Total Organic Carbon Analyzer, equipped with an ASI-V autosampler and fed with zerograde air. Main nitrogen inorganic ions (NO_3^-, NO_2^- and NH_4^+) were determined with a Dionex DX 500 ion chromatograph equipped with a gradient pump GP40, an electrochemical suppression unit (ASRS 300 for anions and CERS 500 for cations), an ED40 detector and a Rheodyne injector (100 µL injection loop). The separation columns used were Dionex Ion Pac AS9-HC with an AG9-HC guard column for the anions and Dionex CS12A with a CG12A guard column for the cations. The used eluents were 9 mM K_2CO_3 (anions) and 20 mM methanesulfonic acid (cations). In both cases, the total flow rate was 1 mL/min.

The formation of H_2O_2 along plasma treatment was determined spectrophotometrically at 350 nm in presence of iodide (method is reported in Supplementary Materials).

All spectrophotometric analyses were performed using a Varian CARY 100 Scan double-beam UV–Vis spectrophotometer, using quartz cuvettes with 10 mm path length.

3. Results and Discussion

3.1. Plasma Parameters Optimization

As the plasma generator used in this work had never been tested for organic pollutants degradation, the first part of the experimental work was dedicated to the optimization of the following operational parameters: applied polarity, frequency of

discharge, water conductivity, distance between the electrodes and reactor material. This first experimental part was carried out using the polypropylene (PP) reactor.

3.1.1. Applied Polarity

To understand the effect of polarity in our system, the degradation of Methyl Orange (MO) was performed using both positive and negative polarity applied to the pointy tungsten electrode. The test was performed on 15 mL of MO solutions at two different concentrations, 3×10^{-5} M and 5.5×10^{-5} M. Degradation tests of 15 min were performed with both polarities and in both cases the degradation profiles for MO were faster with positive polarity (at the two MO concentrations the slope was higher by 1.8 and 3.9-fold) (Figure S1).This behavior has been previously reported for similar setups and can be explained in terms of volume of solution covered by the discharge [21]. Higher rate of formation of HO• for positive discharges have been reported as well [25].

3.1.2. Water Conductivity, Frequency of Discharge and Distance between Electrodes

The development of the DOE was carried out to investigate the role of three factors on the degradation of methylene blue (MB) (full list of the experiments is reported in Table S1). The investigated variables and explored ranges are:

a. frequency of the electrical discharge (5–17 Hz)
b. distance between the electrodes (1–10 mm)
c. water conductivity (20–300 µS/cm)

MB was selected because exhibited faster degradation rates compared to MO and gave a more reliable and faster feedback. The initial absorbance of the solution at 665 nm was fixed to 0.7 and discoloration was monitored measuring the absorbance at this wavelength (Abs_{665nm}). All solutions were prepared in ultrapure water and conductivity was adjusted using sodium chloride. The DOE consisted of a series of 13 duplicated experiments performed in randomized order. The obtained regression equation (R^2 for the model 95.6%) avoiding the not statistically relevant terms is:

$$k = 0.1883 + 0.03144 \times a - 0.07976 \times b + 0.001587 \times c + 9.763 \times 10^{-4} \times a \times b - 8.206 \times 10^{-5} \times a \times c + 6.383 \times 10^{-3} \times b^2 - 3.847 \times 10^{-6} \times c^2,$$

where k is the exponential term of the fitting equation used for the degradation profiles of MB ($Abs_{665} = y_0 + A \times 10\text{^}(-k\ t)$), a is the frequency of discharge (Hz), b is the electrodes distance (mm) and c is water conductivity (µS/cm).

The frequency of discharge showed a positive correlation with the rate of discoloration of the MB solution (Table S2). This is intuitively explainable in term of higher production rate of reactive species. The water conductivity was negatively correlated with the rate of discoloration. This can be explained considering that as water conductivity increased, plasma discharge formation was limited by the competitive phenomenon of charge transport by ions in solution. Furthermore, at higher conductivities the length of the discharge shortened and the efficiency of reactive species production might decreased [28]. Considering the results of DOE, all following experiments have been performed in the Pyrex glass (PG) reactor in the optimized conditions, that is, with a frequency of discharge of 17 Hz, distance between electrodes of 5 mm and without addition of sodium chloride.

3.2. Identification of Reactive Species

3.2.1. Role of HO•

To estimate the contribution of HO• in the degradation process during plasma treatment, a solution of MB 10^{-5} M, was treated in the PG reactor, in the presence of increasing concentration of 2-propanol (0–2 mM). Figure 2 shows the degradation profile for MB in the presence of different concentration of 2-propanol and the transformation rate of the substrate with the increase of the concentration of the scavenger. The initial

degradation rate of MB (computed as the product between the first order kinetic constant obtained from the exponential fit of the MB degradation profiles and the initial substrate concentration) was inhibited by 2-propanol up to a plateau value of ≈1.5 × 10^{-8} M s^{-1}. The high inhibition of the MB transformation rate with the increase of 2-propanol suggested (i) a high production of hydroxyl radicals; (ii) an active role of this species during the degradation of MB in the explored experimental conditions and (iii) the presence of other processes concurring in the degradation of MB alternative to its reaction with HO• (e.g., oxidation/reduction of the substrate at the electrodes, UV/Vis photolysis…).

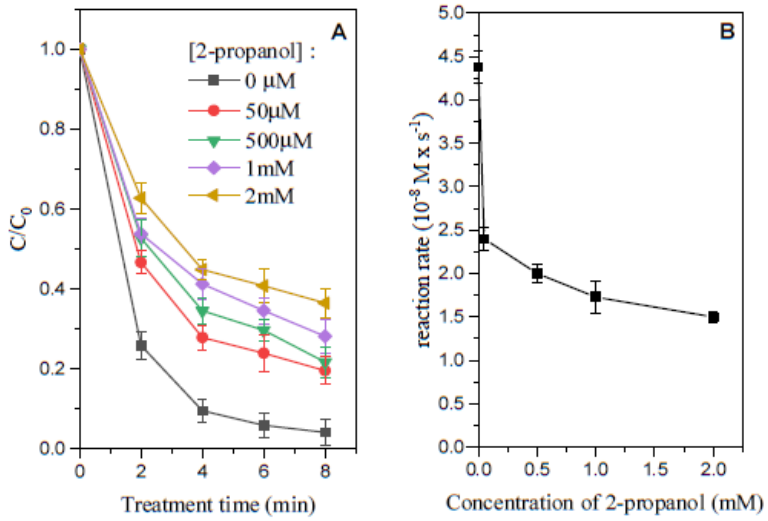

Figure 2. Degradation profiles of methylene blue (MB) (initial concentration 10^{-5} M) in the presence of increasing concentrations of 2-propanol, treated in the PG reactor (A). Evolution of the reaction rate for MB degradation in presence of increasing concentration of 2-propanol (0–2 mM range) (B).

3.2.2. H_2O_2 Production

The formation of H_2O_2 is commonly observed in plasma treated solutions [28,29] through the reactions reported below (Equations (1)–(7)). The formation of H_2O_2 is initiated by the formation during the high energetic discharge of high-energy electrons (*e^-) able to react both with dissolved oxygen (Equation (1)) and water (Equation (2))[30].

$$O_2 + {}^*e^- \rightarrow 2\,O + {}^*e^- \quad (1)$$

$$H_2O + {}^*e^- \rightarrow HO^\bullet + H^\bullet + {}^*e^- \quad (2)$$

$$O_2 + O \rightarrow O_3 \quad (3)$$

$$H_2O + O \rightarrow 2\,HO^\bullet \quad (4)$$

$$2\,HO^\bullet \rightarrow H_2O_2 \quad (5)$$

$$HO^\bullet + O_3 \rightarrow HOO^\bullet + O_2 \quad (6)$$

$$2\,HOO^\bullet \rightarrow H_2O_2 + O_2 \quad (7)$$

We quantified the formation of H_2O_2 and determined how the position of the discharge in the PG reactor could affect this production rate. 50 mL of MilliQ water were

exposed to the two types of discharge for 10 min and the concentration of H_2O_2 was determined along treatment. Figure 3 shows the concentration of H_2O_2 as a function of the treatment time in the case of surface and underwater discharge. The results not only confirmed that H_2O_2 was formed along plasma treatment but also showed that the rate of formation is strongly dependent by the type of plasma discharge. Surface discharge led to a production rate 18-fold higher than underwater discharge (21.9 μM/min against 1.2 μM/min, respectively). This difference could be explained considering that, in the case of surface discharge, reactions (1–6) could take place at the liquid-air interface where the concentration of dissolved oxygen reach its maximum [31].

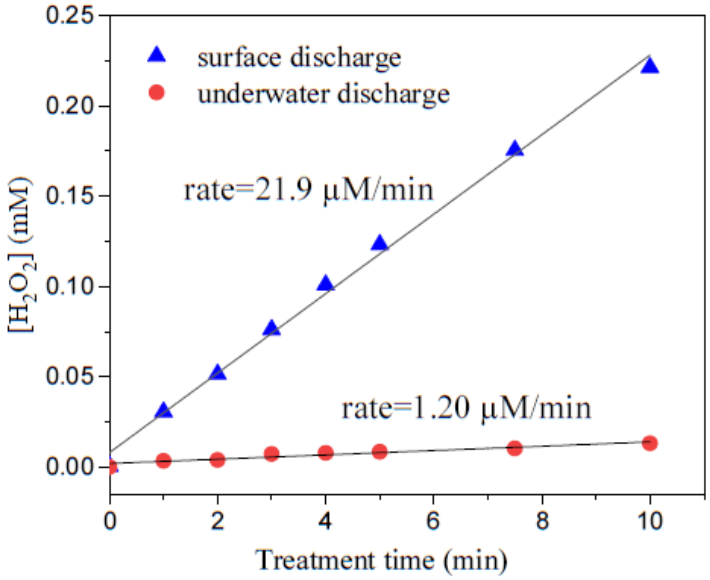

Figure 3. Concentration of hydrogen peroxide produced during plasma treatment of 50 mL of ultrapure water in PG reactor with surface and underwater discharge.

3.2.3. Ozone and NO_x Production

The formation of ozone and NO_x in plasma discharges is commonly reported in the literature [31–34]. Significant concentration of O_3 in the gas phase was measured when working with surface discharge. Data was registered for a total duration of 10 min divided in 1 min of background acquisition, 6 min of plasma discharge and 3 min of post-discharge analysis. NO, NO_2, NO_x and O_3 concentration profiles are shown in Figure 4. Background concentration of ozone in the room air was 1 ppb with negligible fluctuation over time. After plasma discharge was turned on, ozone concentration rapidly reached a stationary concentration of around 45 ppb and then dropped back to the pre-discharge values in around 4 min after interruption of the discharge. NO and NO_2 concentrations on the other hand linearly increased throughout sampling period even after the discharge was turned off without reaching a stationary value. In particular, NO concentration increased at a slightly higher rate starting immediately after the plasma discharged was turned on and according to the literature it was the main NO_x specie formed inside the plasma: NO was oxidized by the ozone produced during the plasma treatment to give NO_2 and some authors even reported this reaction to be quantitative [34]. The increase of the concentration of NO_2 was concomitant with the change in the accumulation rate of ozone, as predicted by the reaction between NO and O_3 that give NO_2 and limited the

accumulation of ozone. According to this theory, the production rate of both NO and O_3 could be significantly higher than the measured ones.

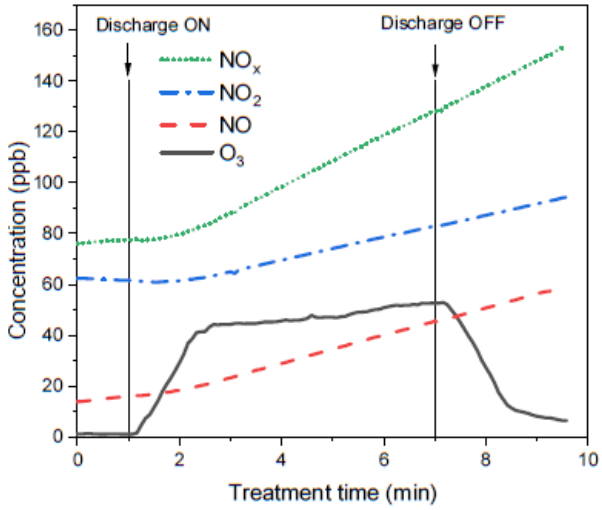

Figure 4. NO, NO_2, NO_x and O_3 concentration profiles measured before, during and after plasma treatment of 50 mL of ultrapure water in the PG reactor using superficial discharge.

3.3. Total Nitrogen and Nitrogen Speciation in Solution

As the formation of NO_x was observed in the gas phase, TN concentration with superficial and surface discharge was measured during experiments carried out in ultrapure water. In both cases the treatment duration was set to 8 min and TN was measured with intervals of 2 min. The nitrogen fixation appeared to be strongly dependent on the type of discharge adopted with TN increasing around 8 times faster with surface discharge with respect to underwater discharge due to the hydrolysis of the NO_x produced when the plasma discharge takes place in contact with air [35,36]. To investigate TN evolution in a more complex mixture, the same experiment was repeated replacing ultrapure water with a solution of Natural Organic Matter (NOM) 10 mg/L. Treatment time was extended to 30 min. The presence of NOM did not significantly modify the evidences observed in ultrapure water and confirmed that nitrogen fixation was more efficient with surface discharge. The TN concentration increased linearly (i.e., rate of production constant) with the treatment time both in ultrapure water and in NOM solution and both with underwater and surface discharge. The TN accumulation rates for the two samples are reported in Figure 5A (measured concentrations are reported in Figure S2). The zero order kinetic for the fixation of nitrogen (d[TN]/dt = constant) is in agreement with the hypothesis that this was directly related to the production of NO_x at the liquid/air interface as a consequence of the high energetic discharges, the frequency of discharge was constant during the treatments.

Furthermore, for the sample of NOM treated with surface discharge, nitrite, nitrate and ammonium concentrations were measured, in addition to TN, using ionic chromatography. These results showed that most part of nitrogen (~90% *w*/*w* of nitrogen) was fixed in solution in the form of nitrate ions with little formation of nitrite ions (<10% *w*/*w* of nitrogen) and negligible production of ammonium.

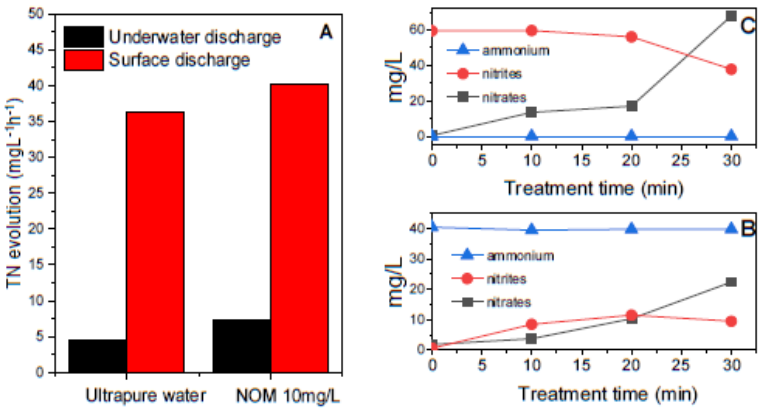

Figure 5. Comparison between the TN accumulation rate during treatment with surface and underwater discharge for a solution of ultrapure water and for a solution of NOM 10 mg/L (A); Concentration of ammonium, nitrite and nitrate ions over 30 min treatment with surface discharge in a solution on ammonium 40 mg/L (B) and in a solution of nitrite 60 mg/L (C).

To better understand if the observed nitrate ions were formed directly in the plasma discharge or if they derived from the oxidation of other inorganic nitrogen species, two experiments were carried out. The first with ammonium (40 mg/L), the second with nitrites (60 mg/L) in ultrapure water with superficial discharge. The concentration of nitrites, nitrates and ammonium was monitored along treatment. When ammonium was spiked in the treated solution its concentration did not change along treatment meaning that ammonium was not produced in the first place and that the plasma discharge was not capable of oxidizing it at a significant rate. When nitrites were spiked in solution on the other hand, their concentration at the end of the treatment was reduced to around 40% of the initial value. At the same time the increase of nitrates' concentration was considerably higher than before confirming that the plasma was able to oxidize a significant portion of nitrite to nitrate ions. Nitrates formation in the system under study takes therefore place both in a direct (especially in the first 20 min of treatment) and indirect way via the oxidation of previously formed nitrite ions (significant after 20 min of treatment).

3.4. Metals Release from the Electrodes

Since the electrodes were visibly consuming with use, the concentrations of Fe, Cr, Ni, W and Hg was measured in sample of ultrapure water treated with surface discharge for 15 min. Iron and tungsten release was found to be significant being these two metals the main components of the electrodes used in this work (stainless steel and sintered tungsten). The release of chromium and nickel in treated solutions was limited while no mercury was detected (Table 1). The metal release in solution due to electrodes consumption is a potential drawback of this technology very little mentioned in the literature. These data highlight how an appropriate choice of electrodes material is crucial when designing water plasma applications. As an example, in the tested experimental conditions the release of iron was not a problem being its concentration lower than the common limit of law for the discharge of treated water in surface waters (e.g., for the Italian legislation 2 mg/L [37]) furthermore iron species in solution could trigger additional processes (e.g., Fenton and photo-Fenton ones) able to produce further reactive species. On the contrary the concentration of tungsten should be a significant problem, being its measured concentration >1 mg/L after 15 min of treatment.

Table 1. Concentration in µg/L of Fe, Cr, Ni, W and Hg measured in a sample of ultrapure water treated with surface plasma discharge for 15 min. LOD = Limit of Detection.

min	Fe	Cr	Ni	W	Hg
0	4.8	0.0	3.5	142	<LOD
1	6.2	0.0	4.5	217	<LOD
3	5.3	0.0	4.6	285	<LOD
5	10.8	0.1	4.3	418	<LOD
10	25.2	1.7	5.3	787	<LOD
15	52.1	4.5	6.9	1118	<LOD

3.5. Degradation of PFAS

Individual solutions of PFOA, PFOS and PFHxA were prepared in MilliQ and in groundwater matrices (chemical parameters of groundwater are reported in Table S3) at a concentration of 1 ppb. 50 mL of each sample solution were treated with surface plasma discharge in the PG reactor for 30 min and samples were taken at different time intervals during treatment in order to evaluate the degradation profiles. A mixture solution of these three compounds was prepared as well, in the same matrices with a final concentration of 1 ppb for each compound. Treatment time was extended to 1 h. All experiments were performed in triplicates.

In all the cases an exponential decay of the concentration of the substrates with the treatment time was observed (i.e., the degradation process had always a pseudo first order kinetics).

When compounds were treated individually, the best results were obtained for PFOS whose degradation was complete in ultrapure water and reached 85% in groundwater (Figure 6A). Removal efficiency of PFHxA on the other hand was slightly better in groundwater than in ultrapure water with degradation after 30 min of 40% and 35%, respectively (Figure 6B). PFOA was degraded of around 50% of initial concentration regardless the matrix (Figure 6C).

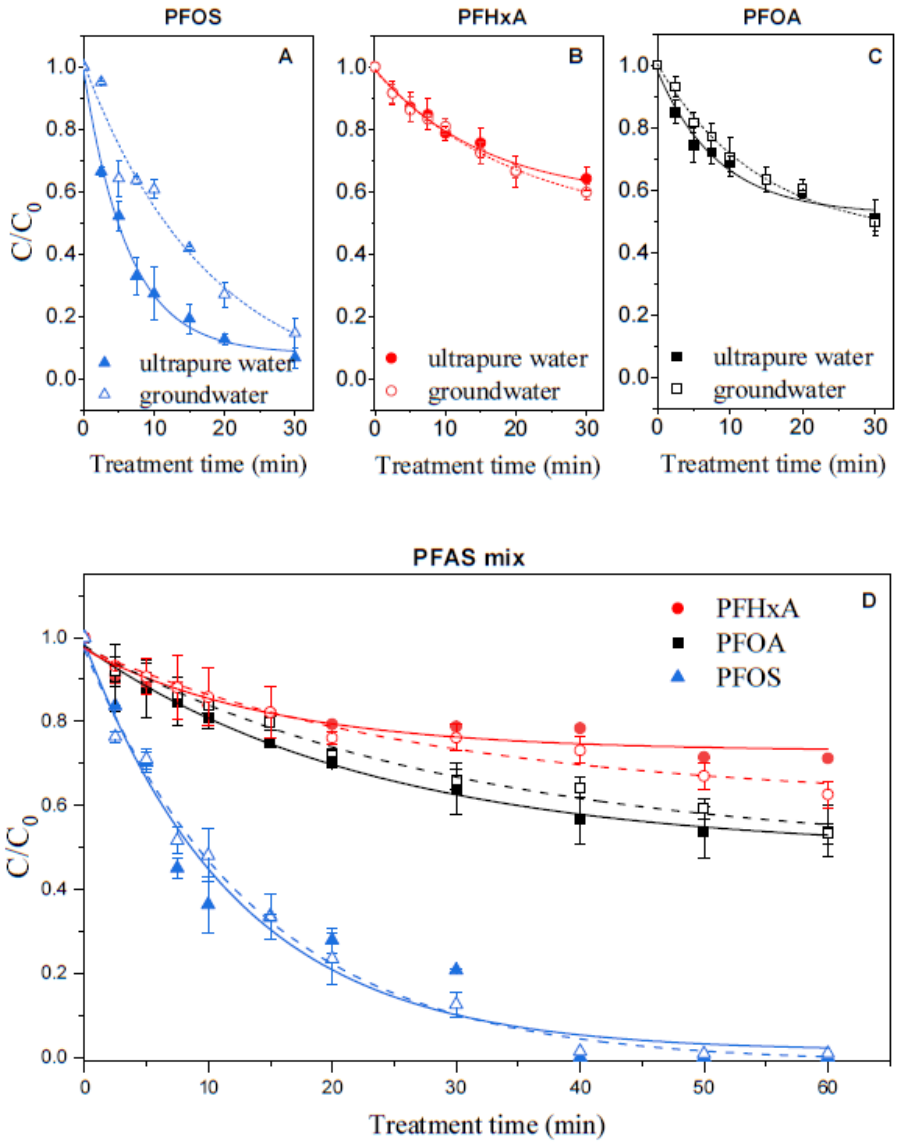

Figure 6. Degradation of pefluorooctanesulfonic acid (PFOS) (A), perfluorohexanoic acid (PFHxA) (B) and perfluorooctanoic acid (PFOA) (C) treated individually in ultrapure and groundwater matrices. Degradation of perfluoroalkyl substances (PFAS) treated in mixture (D) in ultrapure (solid symbols, solid lines) and groundwater (open symbols, dashed lines).

When treated in mixture the degradation profiles obtained for the three compounds showed that degradation is generally slower due to the competition among substrates for the produced reactive species. In mixture the data largely confirmed the results obtained for individual solutions with PFOS no longer detected after 30 min, PFOA removed for around 46% after 1 h in both matrices and PFHxA being the most recalcitrant compound with 29% removal in ultrapure water and 38% removal obtained in groundwater (Figure 6D). The first order degradation rate constants for the three investigated substrates both individually and in mixtures are reported in the Figure S3.

4. Conclusions

In this work, the operational parameters of a custom-built non-thermal plasma generator have been optimized using an experimental design. The analysis of the reactor gas phase revealed that significant production of ozone and NO_x takes place during water treatment. In solution NO_x hydrolysis led to an increase of total nitrogen (up to 40 mgL^{-1} h^{-1}) mainly under the form of nitrate ions. A significant release of iron and tungsten in solution was observed as a consequence of the gradual oxidation of the electrodes material.

Secondly, the plasma generator running on optimized conditions has been used for the degradation of three perfluoroalkyl compounds PFOA, PFOS and PFHxA in solution. The compounds were treated both individually and in mixture using two different water matrices, ultrapure water and groundwater. In both cases PFOS removal was found to be the most efficient with the parent compound no longer detected after 30 min of treatment. The promising degradation results obtained for tested compounds and in particular for PFAS, suggest that this technology could be efficiently used for the treatment of contaminated groundwater, especially when water conductivity is low; environmental concentrations of PFAS in contaminated groundwater where the illicit discharge was done, typically fall within the concentration range explored in this work [9,38–42]. Being the PFAS probably the most recalcitrant compounds among the contaminants of emerging concern, the promising results with PFAS makes us confident that the plasma technology here investigated is also able to degrade less inert compounds.

Preliminary investigations regarding the nature of the transformation products obtained during the plasma treatment of the tested perfluorinated compounds highlighted the formation of shorter-chain PFAS compounds in both ultrapure and groundwater. The identification and quantification of the transformation products of PFOA, PFOS and PFHxA produced during plasma treatment is currently under investigation.

Supplementary Materials: Method for the determination of H_2O_2 is reported at p.1 of Supplementary Material, Figure S1: effect of applied polarity on the degradation of methyl orange, Figure S2: TN values measured in samples of ultrapure water (A) and for a solution of NOM 10 mg/L (B) treated with surface and underground discharge, Figure S3: First order kinetic constant of PFAS degradation (min^{-1}) for individual treatment and in mixture in both ultrapure and underground water, Table S1: Experiments list of the DOE including the variables values used for each experiment and the observed experimental result (k), Table S2: Regression equation and p values obtained for the three parameters (frequency of discharge, electrodes distance and water conductivity) explored in the DOE, Table S3: Chemical parameters of underground water sampled in the city of Volpiano (Turin, Italy) used for the preparation of PFAS solutions.

Author Contributions: Data curation, D.P. (Davide Palma); Funding acquisition, M.L., R.B. and C.R.; Methodology, D.P. (Davide Palma), D.P. (D.P. (Dimitra Papagiannaki)) and M.M.; Project administration, C.R.; Supervision, M.L., M.M. and C.R.; Writing—original draft, D.P. (Davide Palma); Writing—review & editing, D.P. (Davide Palma), D.P. (Dimitra Papagiannaki), M.S. and M.M.. All authors have read and agreed to the published version of the manuscript.

Funding: This paper is part of a project that received funding from the European Union's Horizon 2020 research and innovation programme under the Marie Skłodowska-Curie grant agreement no. 765860 (Aquality).

Acknowledgments: The authors would like to thank Mery Malandrino for the technical support provided for ICP analysis.

Conflicts of Interest: The authors declare no conflict of interest.

References

1. European Environment Agency. Available online: https://www.eea.europa.eu/ (accessed on 7 February 2021).
2. Čelić, M.; Jaén-Gil, A.; Briceño-Guevara, S.; Rodriguez-Mozaz, S.; Gros, M.; Petrović, M. Extended suspect screening to identify contaminants of emerging concern in riverine and coastal ecosystems and assessment of environmental risks. *J. Hazard. Mater.* **2021**, *404*, 124102, doi:10.1016/j.jhazmat.2020.124102.
3. Agüera, A.; Bueno, M.J.M.; Fernández-Alba, A.R. New trends in the analytical determination of emerging contaminants and their transformation products in environmental waters. *Environ. Sci. Pollut. Res.* **2013**, *20*, 3496–3515, doi:10.1007/s11356-013-1586-0.
4. Mostofa, K.M.; Liu, C.-Q.; Vione, D.; Gao, K.; Ogawa, H. Sources, factors, mechanisms and possible solutions to pollutants in marine ecosystems. *Environ. Pollut.* **2013**, *182*, 461–478, doi:10.1016/j.envpol.2013.08.005.
5. Watkinson, A.; Murby, E.; Costanzo, S. Removal of antibiotics in conventional and advanced wastewater treatment: Implications for environmental discharge and wastewater recycling. *Water Res.* **2007**, *41*, 4164–4176, doi:10.1016/j.watres.2007.04.005.
6. Clara, M.; Strenn, B.; Gans, O.; Martinez, E.; Kreuzinger, N.; Kroiss, H. Removal of selected pharmaceuticals, fragrances and endocrine disrupting compounds in a membrane bioreactor and conventional wastewater treatment plants. *Water Res.* **2005**, *39*, 4797–4807, doi:10.1016/j.watres.2005.09.015.
7. Hutchinson, T.H.; Brown, R.; Brugger, K.E.; Campbell, P.M.; Holt, M.; Länge, R.; McCahon, P.; Tattersfield, L.J.; Van Egmond, R. Ecological risk assessment of endocrine disruptors. *Environ. Heal. Perspect.* **2000**, *108*, 1007–1014, doi:10.1289/ehp.001081007.
8. Krzeminski, P.; Tomei, M.C.; Karaolia, P.; Langenhoff, A.; Almeida, M.; Felis, E.; Gritten, F.; Andersen, H.R.; Fernandes, T.; Manaia, C.M.; et al. Performance of secondary wastewater treatment methods for the removal of contaminants of emerging concern implicated in crop uptake and antibiotic resistance spread: A review. *Sci. Total. Environ.* **2019**, *648*, 1052–1081, doi:10.1016/j.scitotenv.2018.08.130.
9. Valsecchi, S.; Rusconi, M.; Mazzoni, M.; Viviano, G.; Pagnotta, R.; Zaghi, C.; Serrini, G.; Polesello, S. Occurrence and sources of perfluoroalkyl acids in Italian river basins. *Chemosphere* **2015**, *129*, 126–134, doi:10.1016/j.chemosphere.2014.07.044.
10. Dauchy, X.; Boiteux, V.; Colin, A.; Hémard, J.; Bach, C.; Rosin, C.; Munoz, J.-F. Deep seepage of per- and polyfluoroalkyl substances through the soil of a firefighter training site and subsequent groundwater contamination. *Chemosphere* **2019**, *214*, 729–737, doi:10.1016/j.chemosphere.2018.10.003.
11. Mussabek, D.; Ahrens, L.; Persson, K.M.; Berndtsson, R. Temporal trends and sediment–water partitioning of per- and polyfluoroalkyl substances (PFAS) in lake sediment. *Chemosphere* **2019**, *227*, 624–629, doi:10.1016/j.chemosphere.2019.04.074.
12. Trojanowicz, M.; Bojanowska-Czajka, A.; Bartosiewicz, I.; Kulisa, K. Advanced Oxidation/Reduction Processes treatment for aqueous perfluorooctanoate (PFOA) and perfluorooctanesulfonate (PFOS)—A review of recent advances. *Chem. Eng. J.* **2018**, *336*, 170–199, doi:10.1016/j.cej.2017.10.153.
13. Giannakis, S.; Lin, K.-Y.A.; Ghanbari, F. A review of the recent advances on the treatment of industrial wastewaters by sulfate radical-based Advanced Oxidation Processes (SR-AOPs). *Chem. Eng. J.* **2021**, *406*, 127083, doi:10.1016/j.cej.2020.127083.
14. Tian, F.-X.; Ye, W.-K.; Xu, B.; Hu, X.-J.; Ma, S.-X.; Lai, F.; Gao, Y.-Q.; Xing, H.-B.; Xia, W.-H.; Wang, B. Comparison of UV-induced AOPs (UV/Cl, UV/NHCl, UV/ClO and UV/HO) in the degradation of iopamidol: Kinetics, energy requirements and DBPs-related toxicity in sequential disinfection processes. *Chem. Eng. J.* **2020**, *398*, 125570, doi:10.1016/j.cej.2020.125570.
15. Palma, D.; Prevot, A.B.; Brigante, M.; Fabbri, D.; Magnacca, G.; Richard, C.; Mailhot, G.; Nisticò, R. New Insights on the Photodegradation of Caffeine in the Presence of Bio-Based Substances-Magnetic Iron Oxide Hybrid Nanomaterials. *Materials* **2018**, *11*, 1084, doi:10.3390/ma11071084.
16. Zhou, K.; Wang, Z.; Wang, X.; Jiao, G.; Li, Y.; Sun, S.-P.; Chen, X.D. Degradation of emerging pharmaceutical micropollutants in municipal secondary effluents by low-pressure UVC-activated HSO_5^- and $S_2O_8^{2-}$ AOPs. *Chem. Eng. J.* **2020**, *393*, 124712, doi:10.1016/j.cej.2020.124712.
17. Zhou, Z.; Liu, X.; Sun, K.; Lin, C.; Ma, J.; He, M.; Ouyang, W. Persulfate-based advanced oxidation processes (AOPs) for organic-contaminated soil remediation: A review. *Chem. Eng. J.* **2019**, *372*, 836–851, doi:10.1016/j.cej.2019.04.213.
18. Pal, P.; Sardar, M.; Pal, M.; Chakrabortty, S.; Nayak, J. Modelling forward osmosis-nanofiltration integrated process for treatment and recirculation of leather industry wastewater. *Comput. Chem. Eng.* **2019**, *127*, 99–110, doi:10.1016/j.compchemeng.2019.05.018.
19. Cao, Y.; Qiu, W.; Zhao, Y.; Li, J.; Jiang, J.; Yang, Y.; Pang, S.-Y.; Liu, G. The degradation of chloramphenicol by O3/PMS and the impact of O3-based AOPs pre-oxidation on dichloroacetamide generation in post-chlorination. *Chem. Eng. J.* **2020**, *401*, 126146, doi:10.1016/j.cej.2020.126146.
20. Sj, L.; Sh, M.; Yc, H.; Mc, C. Effects of pulsed and continuous wave discharges of underwater plasma on Escherichia coli. *Sep. Purif. Technol.* **2018**, *193*, 351–357.
21. Joshi, A.; Locke, B.; Arce, P.; Finney, W. Formation of hydroxyl radicals, hydrogen peroxide and aqueous electrons by pulsed streamer corona discharge in aqueous solution. *J. Hazard. Mater.* **1995**, *41*, 3–30, doi:10.1016/0304-3894(94)00099-3.
22. Tezuka, M.; Iwasaki, M. Plasma induced degradation of chlorophenols in an aqueous solution. *Thin Solid Films* **1998**, *316*, 123–127, doi:10.1016/s0040-6090(98)00401-5.
23. Locke, B.R.; Sato, M.; Sunka, P.; Hoffmann, M.R.; Chang, J.-S. Electrohydraulic Discharge and Nonthermal Plasma for Water Treatment. *Ind. Eng. Chem. Res.* **2006**, *45*, 882–905, doi:10.1021/ie050981u.

24. Yamatake, A.; Angeloni, D.M.; Dickson, S.E.; Emelko, M.B.; Yasuoka, K.; Chang, J.-S. Characteristics of Pulsed Arc Electrohydraulic Discharge for Eccentric Electrode Cylindrical Reactor using Phosphate-Buffered Saline Water. *Jpn. J. Appl. Phys.* **2006**, *45*, 8298–8301, doi:10.1143/jjap.45.8298.
25. Sunka, P.; Babický, V.; Clupek, M.; Lukes, P.; Simek, M.; Schmidt, J.; Cernák, M. Generation of chemically active species by electrical discharges in water. *Plasma Sources Sci. Technol.* **1999**, *8*, 258–265, doi:10.1088/0963-0252/8/2/006.
26. Stratton, G.R.; Dai, F.; Bellona, C.L.; Holsen, T.M.; Dickenson, E.R.V.; Thagard, S.M. Plasma-Based Water Treatment: Efficient Transformation of Perfluoroalkyl Substances in Prepared Solutions and Contaminated Groundwater. *Environ. Sci. Technol.* **2017**, *51*, 1643–1648, doi:10.1021/acs.est.6b04215.
27. Saleem, M.; Biondo, O.; Sretenović, G.; Tomei, G.; Magarotto, M.; Pavarin, D.; Marotta, E.; Paradisi, C. Comparative performance assessment of plasma reactors for the treatment of PFOA; reactor design, kinetics, mineralization and energy yield. *Chem. Eng. J.* **2020**, *382*, 123031, doi:10.1016/j.cej.2019.123031.
28. Kirkpatrick, M.J.; Locke, B.R. Hydrogen, Oxygen, and Hydrogen Peroxide Formation in Aqueous Phase Pulsed Corona Electrical Discharge. *Ind. Eng. Chem. Res.* **2005**, *44*, 4243–4248, doi:10.1021/ie048807d.
29. Sun, B.; Sato, M.; Clements, J.S. Oxidative Processes Occurring When Pulsed High Voltage Discharges Degrade Phenol in Aqueous Solution. *Environ. Sci. Technol.* **2000**, *34*, 509–513, doi:10.1021/es990024+.
30. Guo, H.; Jiang, N.; Wang, H.; Shang, K.; Lu, N.; Li, J.; Wu, Y. Pulsed discharge plasma induced WO3 catalysis for synergetic degradation of ciprofloxacin in water: Synergetic mechanism and degradation pathway. *Chemosphere* **2019**, *230*, 190–200, doi:10.1016/j.chemosphere.2019.05.011.
31. Reddy, P.M.K.; Raju, B.R.; Karuppiah, J.; Reddy, E.L.; Subrahmanyam, C. Degradation and mineralization of methylene blue by dielectric barrier discharge non-thermal plasma reactor. *Chem. Eng. J.* **2013**, *217*, 41–47, doi:10.1016/j.cej.2012.11.116.
32. Li, J.; Yao, S.; Wu, Z. NOx production in plasma reactors by pulsed spark discharges. *J. Phys. D: Appl. Phys.* **2020**, *53*, 385201, doi:10.1088/1361-6463/ab946a.
33. Rahman, M.; Cooray, V.; Montano, R.; Liyanage, P.; Becerra, M. NOX production by impulse sparks in air. *J. Electrost.* **2011**, *69*, 494–500, doi:10.1016/j.elstat.2011.06.008.
34. Lesage, O.; Falk, L.; Tatoulian, M.; Mantovani, D.; Ognier, S. Treatment of 4-chlorobenzoic acid by plasma-based advanced oxidation processes. *Chem. Eng. Process. Process. Intensif.* **2013**, *72*, 82–89, doi:10.1016/j.cep.2013.06.008.
35. Schnabel, U.; Handorf, O.; Yarova, K.; Zessin, B.; Zechlin, S.; Sydow, D.; Zellmer, E.; Stachowiak, J.; Andrasch, M.; Below, H.; et al. Plasma-Treated Air and Water—Assessment of Synergistic Antimicrobial Effects for Sanitation of Food Processing Surfaces and Environment. *Foods* **2019**, *8*, 55, doi:10.3390/foods8020055.
36. Sarangapani, C.; Lu, P.; Behan, P.; Bourke, P.; Cullen, P.J. Humic acid and trihalomethane breakdown with potential by-product formations for atmospheric air plasma water treatment. *J. Ind. Eng. Chem.* **2018**, *59*, 350–361, doi:10.1016/j.jiec.2017.10.042.
37. Decreto Legislativo 3 Aprile 2006, n. 152, Norme in Materia Ambientale. Available online: https://www.camera.it/parlam/leggi/deleghe/06152dl.htm (accessed on 23 November 2020).
38. Bertanza, G.; Capoferri, G.U.; Carmagnani, M.; Icarelli, F.; Sorlini, S.; Pedrazzani, R. Long-term investigation on the removal of perfluoroalkyl substances in a full-scale drinking water treatment plant in the Veneto Region, Italy. *Sci. Total. Environ.* **2020**, *734*, 139154, doi:10.1016/j.scitotenv.2020.139154.
39. Pitter, G.; Da Re, F.; Canova, C.; Barbieri, G.; Jeddi, M.Z.; Daprà, F.; Manea, F.; Zolin, R.; Bettega, A.M.; Stopazzolo, G.; et al. Serum Levels of Perfluoroalkyl Substances (PFAS) in Adolescents and Young Adults Exposed to Contaminated Drinking Water in the Veneto Region, Italy: A Cross-Sectional Study Based on a Health Surveillance Program. *Environ. Heal. Perspect.* **2020**, *128*, 027007, doi:10.1289/ehp5337.
40. Mastrantonio, M.; Bai, E.; Uccelli, R.; Cordiano, V.; Screpanti, A.; Crosignani, P. Drinking water contamination from perfluoroalkyl substances (PFAS): An ecological mortality study in the Veneto Region, Italy. *Eur. J. Public Heal.* **2018**, *28*, 180–185, doi:10.1093/eurpub/ckx066.
41. Manea, S.; Salmaso, L.; Lorenzoni, G.; Mazzucato, M.; Russo, F.; Mantoan, D.; Martuzzi, M.; Fletcher, T.; Facchin, P. Exposure to PFAS and small for gestational age new-borns: A birth records study in Veneto Region (Italy). *Environ. Res.* **2020**, *184*, 109282, doi:10.1016/j.envres.2020.109282.
42. Yong, Z.Y.; Kim, K.Y.; Oh, J.-E. The occurrence and distributions of per- and polyfluoroalkyl substances (PFAS) in groundwater after a PFAS leakage incident in 2018. *Environ. Pollut.* **2021**, *268*, 115395, doi:10.1016/j.envpol.2020.115395.

Supporting information

PFAS degradation in ultrapure and groundwater using non-thermal plasma

Davide Palma [a], Dimitra Papagiannaki [b], Manuel Lai [c], Rita Binetti [b], Mohamad Sleiman [a], Marco Minella [d,*], Claire Richard [a,*]

[a] Université Clermont Auvergne, CNRS, Sigma Clermont, ICCF, 63178, Aubière, France

[b] SMAT S.p.A., Research Centre, C.so Unità d'Italia 235/3, Torino, Italy

[c] IRIS s.r.l., Via Papa Giovanni Paolo Secondo 26, 10043 Orbassano, Italy.

[d] Department of Chemistry and Interdepartmental Centre Nanostructured Interfaces and Surfaces (NIS), University of Torino, Via Pietro Giuria 5, 10125 Torino, Italy.

* Corresponding authors. E-mail addresses: marco.minella@unito.it, claire.richard@uca.fr

Measurement of hydrogen peroxide

The formation of H_2O_2 along plasma treatment was determined using two reagent solutions prepared as follows in two 250 mL flasks: solution A contained 16.5 g of potassium iodide, 0.5 g of sodium hydroxide and 0.05 g of ammonium heptamolybdate tetrahydrate, and solution B contained 10 g of potassium hydrogen phthalate. Both flasks were brought to volume using ultrapure water and the solutions were maintained under stirring until complete solubilisation. Determination of H_2O_2 was performed by mixing 3 mL of sample with 1 mL of solution A and 1 mL of solution B that were let to react for 1 min before measuring the absorbance at 350 nm. H_2O_2 concentrations were determined using a calibration curve.

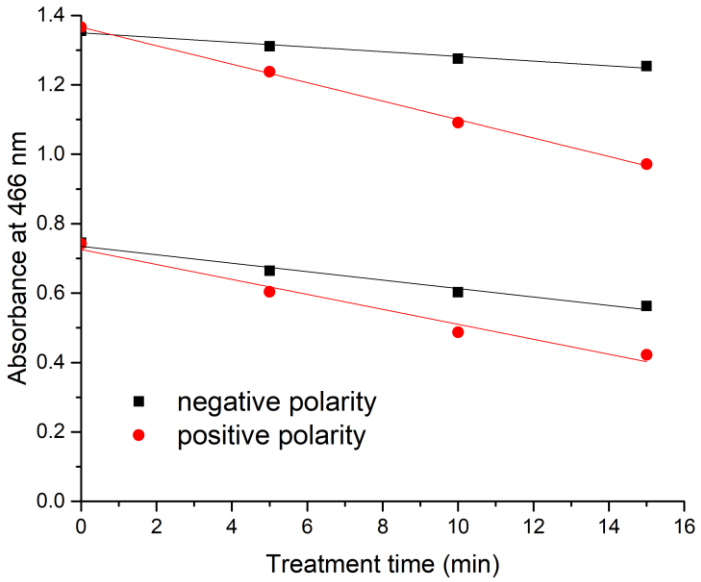

Figure S1. *Degradation profile of MO 3×10^{-5} M (initial absorbance at 466 nm = 0.75) and 5.5×10^{-5} M (initial absorbance at 466 nm = 1.4) solutions treated using negative and positive polarity.*

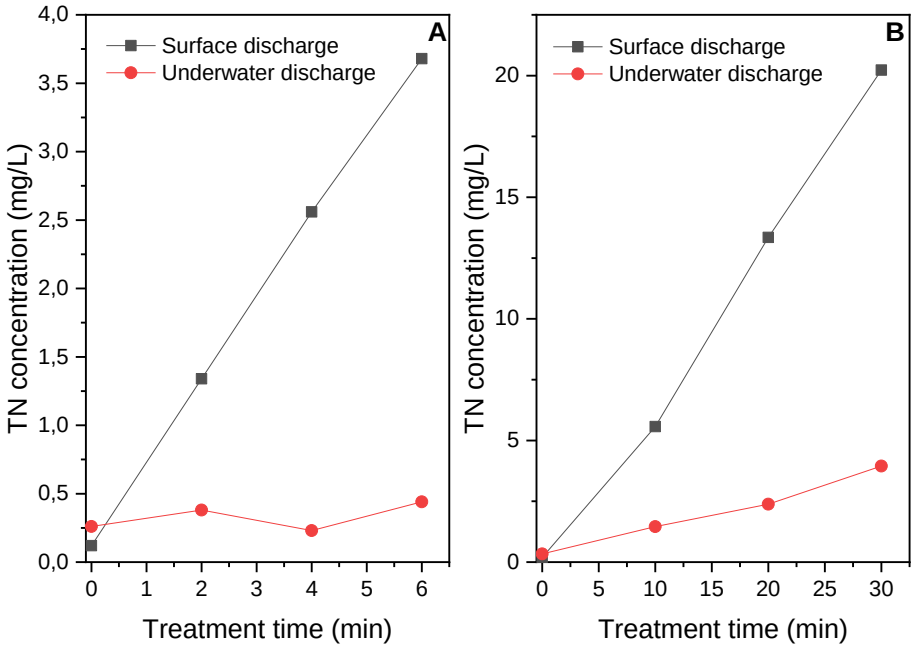

Figure S2. *TN values measured in samples of ultrapure water (A) and for a solution of NOM 10 mg/L (B) treated with surface and underground discharge.*

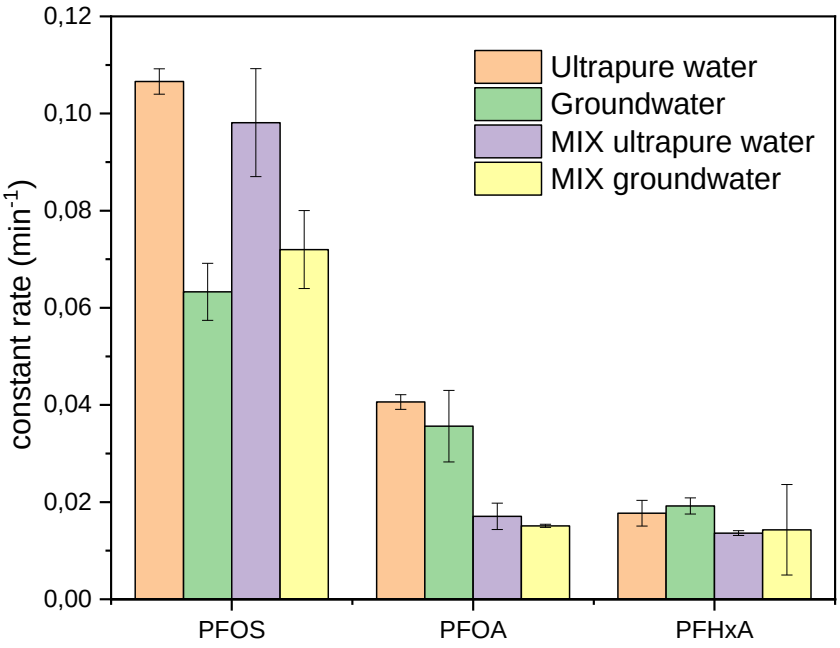

Figure S3. *First order kinetic constant of PFAS degradation (min^{-1}) for individual treatment and in mixture in both ultrapure and underground water.*

Table S8. *Experiments list of the DOE including the variables values used for each experiment and the observed experimental result (k). Reported k values are average values of two repetitions.*

Experiments number	Frequency (Hz)	Electr. Distance (mm)	H_2O conductivity (µS/cm)	*k*
1	5	1	20	0,2950
2	5	1	300	0,2937
3	5	10	20	0,2631
4	5	10	300	0,2297
5	17	1	20	0,6597
6	17	1	300	0,4042
7	17	10	20	0,7473
8	17	10	300	0,4448
9	5	5,5	160	0,1976
10	11	1	160	0,4415
11	11	5,5	20	0,3511
12	17	5,5	300	0,2900
13	11	5,5	160	0,3729

Table S9. *Regression equation and p values obtained for the three parameters (frequency of discharge, electrodes distance and water conductivity) explored in the DOE.*

Parameter	Coeff.	Sigma	t	*p* value	Signif.
Constant	0,23055	0,08196	2,813	0,02	Yes
Frequency (Hz)	0,0224286	0,005373	4,175	0,002	Very
Electr. Distance (mm)	-0,0006329	0,007545	-0,084	0,935	No
H_2O conductivity (µS/cm)	-0,0005632	0,0002303	-2,446	0,037	Yes

Table S10. *Chemical parameters of underground water sampled in the city of Volpiano (Turin, Italy) used for the preparation of PFAS solutions.*

pH		8,1
Conductivity	µS/cm	195,45
TOC	µg/L	270
nitrites	mg/L	n.d.
nitrates	mg/L	8
Chlorides	mg/L	3
Sulphates	mg/L	8
Sodium	mg/L	4
Potassium	mg/L	1,0
Calcium	mg/L	22,8
Magnesium	mg/L	11,6

MANUSCRIPT 5

Evolution of SRNOM photo-oxidant properties under UV-C irradiation: role of carbonyls in the production of OH radicals

Accepted for publication on June 24th 2021
Journal: Water Research

Evolution of SRNOM photo-oxidant properties under UV-C irradiation: role of carbonyls in the production of OH radicals

Davide Palma[1], Amina Khaled[1], Mohamad Sleiman[1], Guillaume Voyard[1], Claire Richard[1]*

[1] Université Clermont Auvergne, CNRS, SIGMA-Clermont, ICCF, F-63000 Clermont-Ferrand, France

* : corresponding author

Email : claire.richard@uca.fr

Tel : +33 (0)4 73 40 71 42

Fax : +33 (0)4 73 40 77 00

Abstract

The present study aimed to investigate the changes in the chemical composition, and in the optical and photooxidant properties of Suwannee River Natural Organic Matter (SRNOM) induced by UVC (254 nm) treatment. The extent of the photodegradation was first assessed by UV-visible/fluorescence spectroscopies and organic carbon analysis. An in-depth investigation of the chemical changes was also conducted using liquid chromatography-mass spectrometry and gas chromatography-mass spectrometry after derivatizations. A series of mono, di and tricarbonyls and mono and dicarboxylic acids in C_1-C_6 were identified in samples irradiated from 1 to 4 h. After 3 h of irradiation, carbonyls accounted for 46% of the organic carbon remaining in solution whereas carboxylic acids represented about 2%. Then, we investigated the modifications of the photooxidant properties of SRNOM induced by these chemical changes. At 254 nm, UVC pre-irradiated SRNOM photodegraded glyphosate 29 times faster than original SRNOM and the reaction was fully inhibited by 2-propanol (5×10^{-3} M). This enhanced photooxidant properties at 254 nm toward glyphosate was therefore reasonably due to •OH radicals formation, as confirmed by additional ESR measurements. A mechanism involving a chain reaction was proposed based on independent experiments conducted on carbonyl compounds, particularly pyruvic acid and acetone. The findings of this study show that UVC pre-treatment of NOM can enhance the removal of water pollutants and suggests a possible integration of a NOM pre-activation step in engineered water treatment sytems.

Key-words: Natural organic matter, carbonyls, hydroperoxides, chain reaction, glyphosate, •OH radicals

1. Introduction

Natural organic matter (NOM) is a complex mixture of organic compounds formed in soils, sediments and natural waters as a result of microbial and chemical transformation of plant tissues and microbial remains and it is an ubiquitous constituent of surface waters and drinking water supplies. NOM needs to be removed in the process of drinking water production because it can affect the color and organoleptic parameters of water and it can act as a carrier of toxic organic compounds [Zoschke et al , 2012 ; Tang et al , 2014]. Under UVC radiations (200-280 nm), typically used to remove bacterial and chemical contamination [Sillanpää et al., 2018], NOM undergoes extensive degradation even though complete mineralization is not usually achieved; the generation of potentially harmful by-products originating from NOM degradation is a crucial aspect of drinking water production [Buchanan et al, 2006]. Even though great efforts were put toward a better understanding of the fate of NOM in

UVC treaments [Ike et al, 2019 ; Paul et al, 2012 ; Varanasi et al, 2018 ; Sarathy et al, 2011 ; Kulovaara et al, 1996; Schmitt-Kopplin et al, 1996 ; Corin et al, 1996 ; Polewski et al, 2005 ; Lamsal et al, 2011; Rougé et al, 2020], many questions related to the nature of intermediary photoproducts formed and their photoreactivity remain unanswered and need to be further investigated.

Due to its heterogeneity and chemical complexity, NOM transformation was often studied by monitoring global parameters using techniques such as absorption or fluorescence spectroscopy, total organic carbon analysis, ^{13}C NMR, pyrolysis and gel permeation chromatography [Ike et al, 2019 ; Paul et al, 2012 ; Hao et al, 2020 ; Sarathy and Mohseni, 2007 ; Fukushima et al, 2001 ; Schmitt-Kopplin et al, 1996 ; Polewski et al, 2005]. These analytical techniques allowed to assess an overall decrease of NOM UV-visible absorbance, of aromaticity and of molecular weight during oxidation processes. Several studies focused on the identification of small molecules, generated from NOM breakdown, by coupling derivatization techniques with liquid chromatography-mass spectrometry (LC-MS) or gas chromatography-mass spectrometry (GC-MS). Formation of C_1-C_4 carbonyl compounds and C_2-C_5 carboxylic acids, amino acids and alcohols in UVC treatments was reported [Thomson et al, 2004 ; Agbaba et al, 2016 ; Zhong et al, 2017 ; Corin et al, 1996]. Some of these photoproducts were also found upon irradiation of NOM with natural or simulated solar-light (> 290 nm) [Brinkmann et al, 2003 ; de Bryun et al, 2011 ; Goldstone at al, 2002 ; Kieber et al, 1990].

The presence of NOM in UVC treatments has been generally reported to lower treatment efficiency due to its ability to scavenge the reactive species generated under irradiation and/or to absorb photons competitively, therefore decreasing the degradation rate of target compounds [Wang et al, 2016]. However, NOM is able to generate oxidant species such as hydroxyl radicals (•OH), singlet oxygen ($^1O_2$) and triplet excited states (^{3}NOM*) under irradiation [Vione et al, 2014] and can also promote the degradation of contaminants during UVC treatment [Lester et al, 2013]. The photosensitizing properties of NOM may evolve during the UVC treatment because NOM itself undergoes chemical changes. Yet, to the best of our knowledge, very few studies investigated the effect of such modifications on the ability of NOM to generate photooxidants in the course of engineered water treatments. Treatments of NOM with hypochlorous acid and ozone were reported to increase its capacity to generate $^1O_2$ in simulated solar light due to the possible formation of quinone-like molecules [Mostafa and Rosario-Ortiz, 2013 ; Leresche et al, 2019] but also to decrease its capacity to generate ^{3}NOM* due to photosensitizers destruction [Wenk et al, 2015]. On the other hand, UV/chlorine treatment of NOM at high chlorine dosage was found to increase its ability to generate ^{3}NOM*, $^1O_2$, and •OH, upon irradiation within the range 290-400 nm [Zhou et al, 2021]. Again, these effects were proposed to be due to the formation of quinone and ketone functional groups.

The goal of this work was to study the chemical changes of SRNOM under UVC irradiation and to determine how these changes affect its photodegrading properties. In the first part, spectral

changes of irradiated SRNOM solutions were monitored by UV-visible and fluorescence spectroscopies while photoproducts were analyzed by derivatization of SRNOM followed by liquid chromatography coupled to high resolution mass spectrometry (UHPLC-HRMS) or gas chromatography coupled to mass spectrometry (GC-MS). In the second part, we studied the effect of the UVC pre-irradiation on the photosensitizing properties of SRNOM. For the experiments at 254 nm, we chose glyphosate, as a probe molecule, for two reasons. It is non-absorbant at 254 nm and thus poorly subject to photolysis. Moreover, its aliphatic and saturated structure makes it difficult to oxidize except by very oxidant species such as •OH. The photooxidant properties of carbonyls at 254 nm was also studied for comparison. For the experiments at λ > 300 nm, we used recommanded probe molecules to compare the formation of •OH, ^{3}SRNOM* and singlet oxygen before and after UVC pre-irradiation [Rosario-Ortiz and Canonica, 2016].

2. Material and methods

2.1. Chemicals

SRNOM (2R101N) was purchased from the International Humic Substances Society (IHSS). Glyphosate (99.7%) and H_2O_2 (> 30%) were obtained from Fluka. Methylglyoxal (40% in weight), pyruvic acid (98%), glycolic acid (98%), acetone (> 99.5%), 2,4,6-trimethyphenol (TMP, certified reference material), furfuryl alcohol (FFA, analytical grade), terephtalic acid (98%), hydroxyl-terephtalic acid (97%), 2,4-dinitrophenylhydrazine (DNPH, 97%), bis(trimethylsilyl)trifluoro-acetamide containing 1% trimethylchlorosilane (BSTFA + 1% TMCS, 98.5% exluding TMCS), NaH_2PO_4 (≥ 99.5%), Na_2HPO_4 (≥ 99%), horseradish peroxidase (52 units per mg of solid), 4-hydroxyphenylacetic acid (98%), 5,5-dimethyl-1-pyrroline-N-oxide (DMPO, > 98%) and catalase (2000-5000 units per mg of protein were purchased from and Sigma Aldrich. Water was purified by reverse osmosis RIOS 5 and Synergy, Millipore device, with resistivity 18 MΩ cm and DOC < 0.1 mg L^{-1}. All chemicals were used as received.

2.2. UVC pre-irradiation of SRNOM

Briefly, 10 mg of SRNOM were dissolved in 250 ml of purified water to reach a concentration of 40 mg L^{-1}. SRNOM solutions were buffered at pH 7 using phosphate buffers (10^{-3} M) except for experiments conducted to monitor the pH evolution during irradiation or designed to the detection of carboxylic and hydroxylic intermediates. In these cases, SRNOM solutions were neutralized to pH = 7 ± 0.2 using freshly prepared NaOH (0.1 M). All the solutions were stored at 4°C. SRNOM solutions (30 mL) were poured in a quartz glass cylindrical vessel (2 cm i.d. × 19 cm) and were irradiated in a device equipped with 4 germicidal tubes (253.7 nm, General Electric, 15 W). The photon flux entering the solution, corresponding to 2.9×10^{-6} Einstein$L^{-1}s^{-1}$, was calculated by measuring the rate of glyphosate loss in

the presence of H_2O_2 (SI-Text 1, Fig SI-1). SRNOM solutions were irradiated for 1 h, 2 h, 3 h and 4 h in separate experiments and labelled $SRNOM_{1h}$, $SRNOM_{2h}$, $SRNOM_{3h}$, and $SRNOM_{4h}$, respectively. Irradiated solutions were used for analyses or sensitizing investigations within the 24 h following irradiation.

2.3. Analysis of original and UVC pre-irradiated SRNOM

UV-visible spectra were recorded on a Varian Cary 3 UV-Vis spectrophotometer. Fluorescence spectra were recorded using a Perkin Elmer LS 55 Luminescence Spectrometer. The excitation wavelength was set at 255 nm and the absorbance of solutions was adjusted at 0.10 ± 0.01 at 255 nm by dilution with purified water. The emission spectra were corrected for the dilution coefficient. Dissolved organic carbon (DOC) was measured using a Shimadzu 5050 TOC analyser. Carbonyls contained in SRNOM and irradiated SRNOM were analyzed by DNPH derivatization [Soman et al, 2008] (SI Text 2). Analyses were performed by ultra-high performance liquid chromatography (UHPLC) coupled to high resolution mass spectrometry (HRMS). HRMS was performed on an Orbitrap Q-Exactive (Thermoscientific) coupled to Ultimate 3000 RSLC (Thermoscientific) UHPLC. Analyses were run in negative (ESI^-) electrospray modes. The column was a Kinetec EVO C_{18} 100 mm / 2.1 mm, 1.7 µm (Phenomenex). Details of separation conditions are given in (SI Text 3). Molecular formulas were obtained setting the difference between experimental and accurate masses to ≤ 5 ppm while structures are proposed based on the number of DNPH molecules linked to carbonyls and on the number of double bonds in the carbonyl (NDB). In several cases, several isomers are possible and given structures are thus only indicative. Pyruvic acid and methylglyoxal were used as references to estimate the concentration of the other carbonyls (SI Text 3 and Fig. SI-2).

Carboxylic and hydroxylic intermediates were detected by a method using BSTFA derivatization (SI Text 4) followed by analysis with gas chromatography/electron impact MS (GC/EI-MS) [Yu et al, 1998]. Solutions were analyzed on an Agilent 6890N Network gas chromatograph coupled to a 5973 Network mass selective detector and Agilent 7683B series injector. Data acquisition and processing and instrument control were performed by Agilent MSD ChemStation software. Separation conditions are described in (SI Text 4). Mass spectra were scanned between m/z 50 and m/z 500 with the source temperature set at 230°C. Identification was based on matching query spectra to spectra present in the reference library (NIST17), with a minimum spectral similarity measure of 95%. Glycolic acid was derivatized by BSTFA as for SRNOM samples and used as a reference for the quantification of other compounds. SRNOM and $SRNOM_{3h}$ were also analyzed by ionic Chromagraphy-Mass spectrometry (IC-MS). Details are given in SI-text 5.

2.4. Sensitizing properties of original and UVC pre-irradiated SRNOM

Glyphosate was used to probe the formation of very oxidant species such as •OH from original and pre-irradiated SRNOM solutions at 254 nm. The solutions containing glyphosate (10^{-5} M) and SRNOM were prepared by adding 25 µL of the stock solution of glyphosate (10^{-2} M) to 10.2 mL of SRNOM (40 mg L^{-1}) and by adding purified water to reach the final volume of 25 mL. For $SRNOM_{3h}$ solutions, the same spike of glyphosate was added to 25 mL of non diluted solution. This way, the two solutions showed the same absorbance of 0.34 at 254 nm. Then, 15 mL of each solution were irradiated in the above-described device. 2-Propanol was used as a quencher of •OH. Glyphosate (10^{-5} M) was also irradiated in the presence of acetone (10^{-4} M), pyruvic acid (10^{-4} M), H_2O_2 (10^{-5} M), acetone (10^{-4} M) + H_2O_2 (10^{-5} M). Furthermore, acetone (10^{-4} M) was irradiated alone and in mixture with H_2O_2 (10^{-5} and 10^{-3} M). All these experiments were conducted in air-saturated solutions. The effect of oxygen on the rate of glyphosate photodegradation in the presence of $SRNOM_{3h}$ was studied by saturating the solution with N_2. Glyphosate concentration was monitored by UHPLC-HRMS by integrating peak area at m/z = 168.0056 (± 5 ppm). AMPA (aminomethylphosphonic acid) with m/z = 110.0002 (± 5 ppm) was the only glyphosate photoproduct detected. Acetone loss and photoproducts formation were monitored by derivatization with DNPH followed by UHPLC-HRMS analysis. Photodegrading properties of SRNOM and $SRNOM_{3h}$ solutions were also investigated under irradiation between 300 and 400 nm. Both solutions were diluted by a half during preparation of mixtures. Terephthalic acid (2×10^{-5} M) was used to probe •OH radicals, 2,4,6-trimethyphenol (2×10^{-5} M) to probe $^3SRNOM^*$ and $^3SRNOM_{3h}^*$ and furfuryl alcohol (5.8×10^{-5} M) to trap $^1O_2$. Solutions buffered at pH 7 were irradiated in a device equipped with 6 fluorescent tubes emitting between 300 and 400 nm [Palma et al, 2020]. Pseudo-first-order rate constants of probes phototransformation were determined by plotting $\ln(C_t/C_0) = k \times t$, where C_t and C_0 are the probe concentration at time t and before irradiation. All the experiments were duplicated.

2.5. Peroxides titration

Peroxides concentration was measured by the spectrofluorimetric quantification method previously described by Miller and Kester, 1988. Details of the experiments are given in SI-text 6.

2.6. ESR experiments

ESR experiments were carried out using a Bruker EMX, 9.8 GHz equipped with a cavity ER4105DR and a xenon lamp (Xenovia 200 - 900 nm). The ESR spectra were obtained at room temperature under

irradiation inside the cell of the following mixtures : DMPO (25 mM) in the presence of SRNOM (20 mg L^{-1}), $SRNOM_{3h}$ or H_2O_2 (5×10^{-3} or 10^{-5} M).

3. Results and discussion

3.1. Spectral changes of SRNOM upon 254-nm irradiation

Fig. 1A shows that the SRNOM solution progressively photobleached. The absorbance at 254 nm declined by 59% and 77% after 3 and 4 h of irradiation, respectively (Table 1). The reduction of DOC as a function of irradiation time revealed that SRNOM also underwent substantial mineralization (35% after 4 h) while the specific ultraviolet absorbance (SUVA) decreased by 42% and 64% after 3 and 4 h of irradiation, respectively, indicating a loss of unsaturated/aromatic moieties [Weisshar et al, 2003] (Table1). Yet, the spectrum shape (Fig. 1B) and the E_2 / E_3 ratio (Table 1) did not change much indicating that photoproducts negligibly contributed to the absorption and were poorly absorbing compounds.

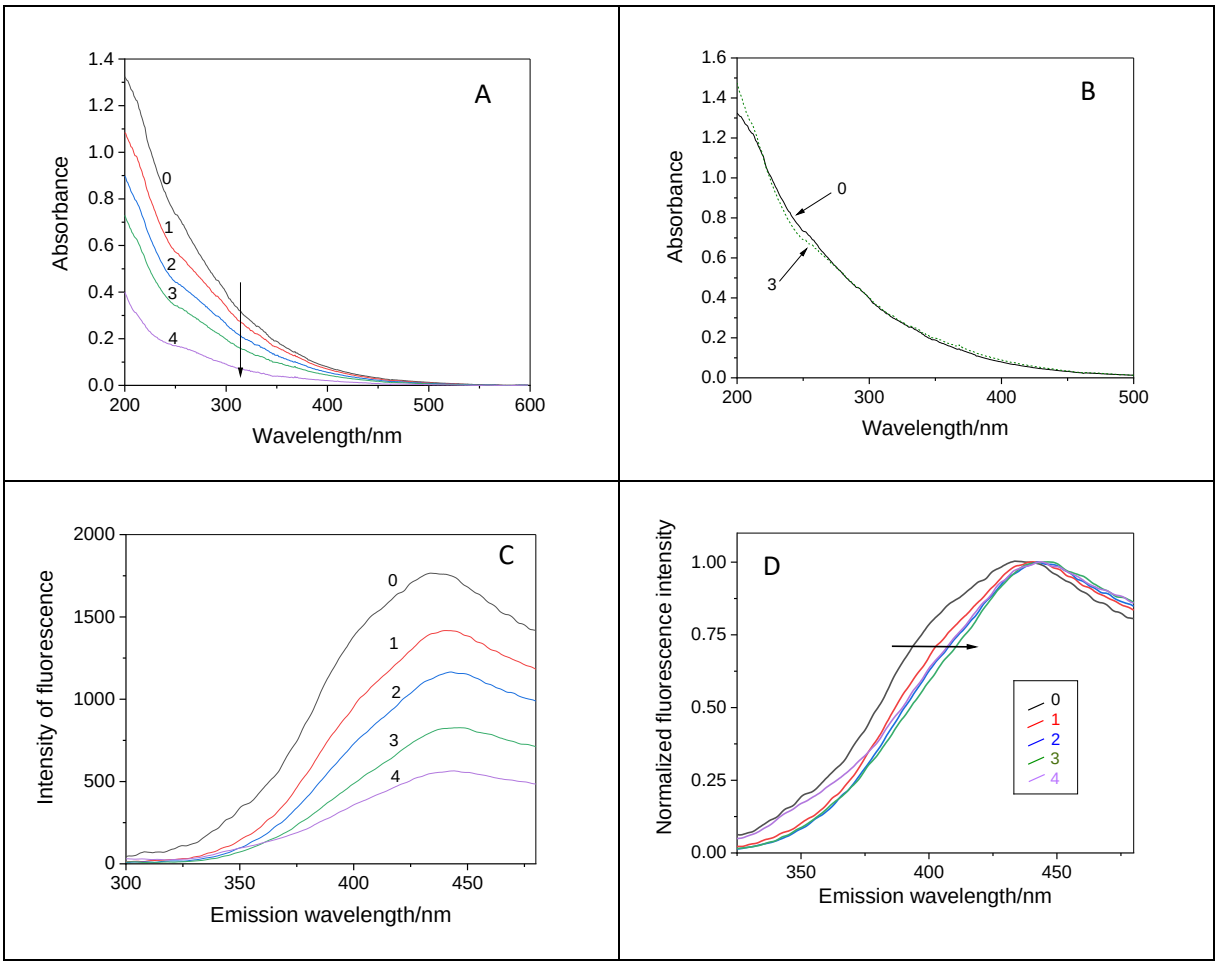

Figure 1. Spectral changes of SRNOM solution (40 mg L^{-1}, phosphate buffers pH 7) upon irradiation at 254 nm. Curve 0 : t = 0 ; curve 1 : t = 1h ; curve 2 : t = 2h ; curve 3 : t = 3h ; curve 4 : t = 4h. A and B : UV-

visible spectra. In B, curve 3 is rescaled to have the same absorbance at 300 nm as curve 0. C and D : Fluorescence spectra recorded at an excitation wavelength of 255 nm, and an absorbance adjusted at 0.10 ± 0.01 at 255 nm. In C, spectra are corrected for the dilution coefficient. In D, spectra are normalized by their respective maximum fluorescence intensity.

Irradiation also led to a breakdown of fluorescent species in accordance with previous studies [Patel-Sorrentino et al, 2004]. The fluorescence intensity at the emission maximum declined by 53% after 3 h of irradiation, and by 68% after 4 h (Fig 1 C). Fig 1D also shows that the blue part of the fluorescence emission spectra disappeared the fastest leading to emission spectra red-shifted by 10 - 15 nm or to a band contraction. On the contrary, treatment of NOM with radicals such as $SO_4^{\bullet -}$ [Zhang et al, 2019] or •OH [Varanasi et al, 2018] was reported to induce a blue-shift of fluorescence emission spectra attributed to preferential degradation of high molecular weight moieties into smaller entities. In these treatments, radicals are expected to react preferentially with biggest macromolecules offering the largest number of attack sites while in photolytic treatment the reactivity of generated excited states is the critical factor. Our results suggest that smaller fluorescent entities initially present in SRNOM or produced during treatment were more subject to photodegradation than larger ones. The reasons could be that they were more light absorbing because more oxidized and/or underwent less deactivation processes than bigger constituents being less embedded in large structures than these latter.

Table 1. Spectral parameters of original and pre-irradiated SRNOM

NOM	A_{254}	DOC mg L^{-1}	SUVA L mgC^{-1} m^{-1}	E_2/E_3
SRNOM	0.83	15.6	5.34	4.88
$SRNOM_{1h}$	0.58	13.7	4.24	3.79
$SRNOM_{2h}$	0.42	13.3	3.16	3.36
$SRNOM_{3h}$	0.34	10.9	3.12	3.69
$SRNOM_{4h}$	0.19	10.1	1.92	4.70

3.2. Carbonyls and carboxylic acids formation upon 254-nm irradiation of SRNOM

Table 2 summarizes the chemicals detected by DNPH or BSTFA derivatization and by CI/MS in SRNOM before irradiation and after irradiation. Detailed MS data are given in Figure SI-3, Tables SI-1 to SI-3 and the structures of photoproducts observed in irradiated samples are shown in Figure 2. In starting SRNOM, we detected 5 carbohydrates in C_5 and C_6 (xylose, rhamnose, fucose, glucose and galactose) mentionned in the IHSS web page, along with 2 monocarboxylated alkanes in C_3 and C_{18} (glyceric and

oleic acids) and 3 dicarboxylated alkanes in C_6, C_9 and C_{12} (hexanedioic, nonanedioic and dodecanedioic acids) (Tables 2 and SI-1). Several carbonyls were found, but only as traces.

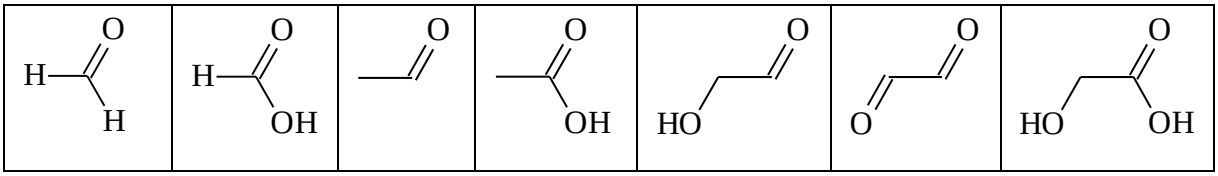

1 2 3 4 5 6 7

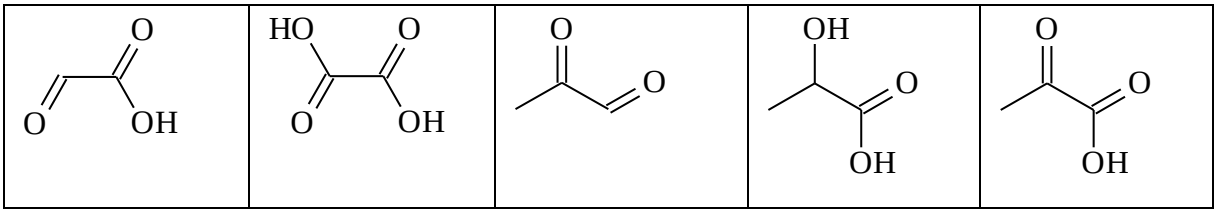

8 9 10 11 12

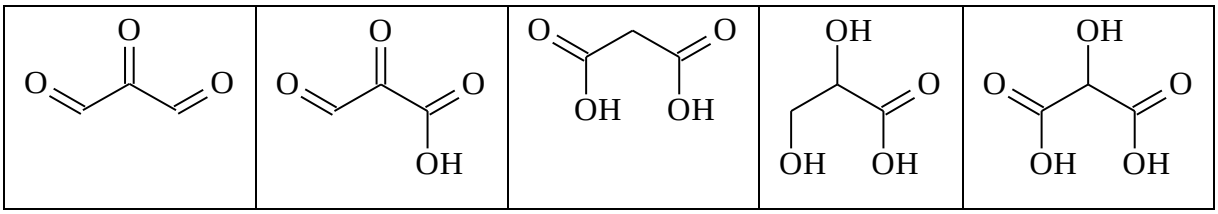

13 14 15 16 17

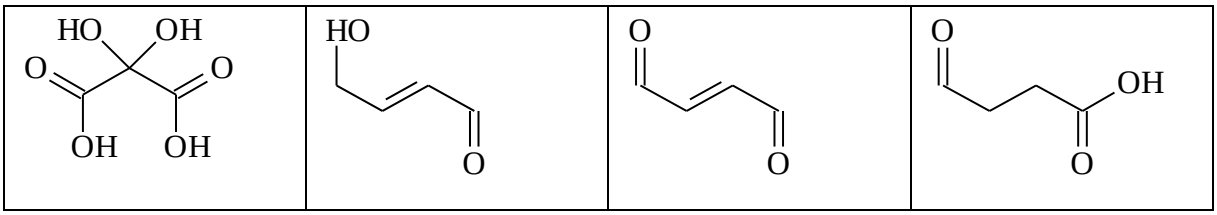

18 19 20 21

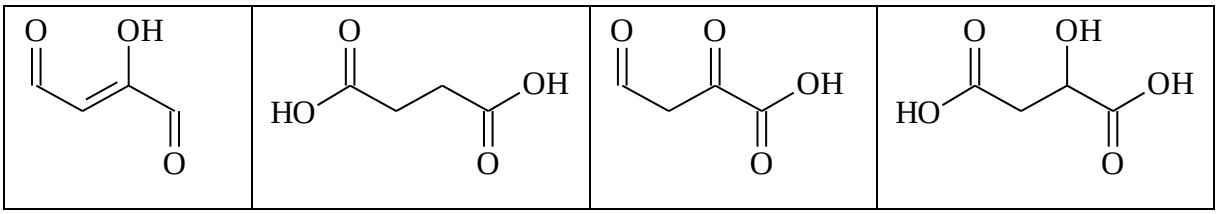

22 23 24 25

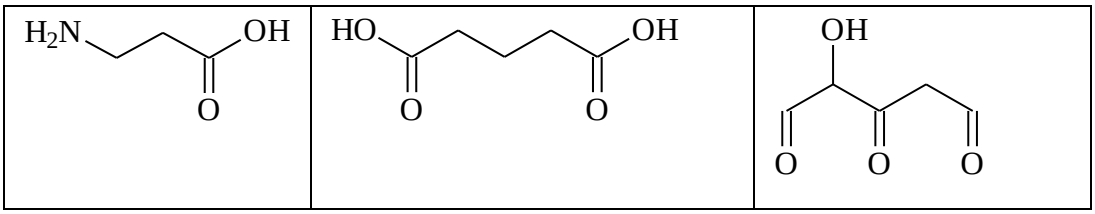

26 27 28

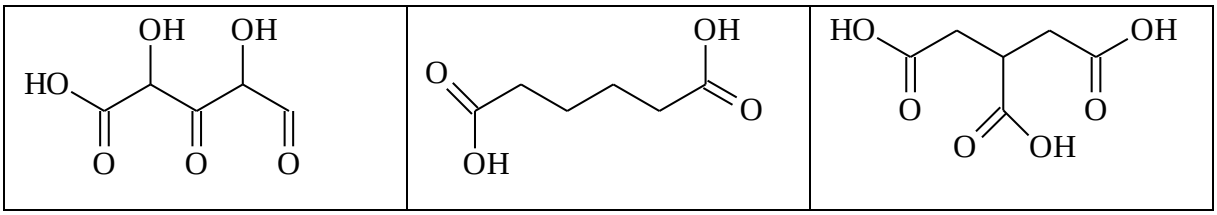

30 31 32

Figure 2. Carbonyls detected in irradiated SRNOM.

In $SRNOM_{3h}$, none of the carbohydrates observed in SRNOM were found while 11 carboxylated alkanes were detected: 5 monocarboxylated in C_1 (formic acid), C_2 (acetic and glycolic acid), C_3 (lactic acid) and C_4 (4-aminobutanoic acid), 7 dicarboxylated alkanes in C_2 (oxalic acid), C_3 (malonic, tartronic, dihydroxymalonic acids), C_4 (butanedioic and malic acids), C_5 (glutaric acid) and C_6 (tricarballylic acid) (Tables 3 and SI-2). In all the irradiated samples, 16 carbonyls in C_1-C_5 were detected among them 7 monocarbonyls (formaldehyde, acetaldehyde, glycoladehyde, glyoxylic acid), 7 dicarbonyls (glyoxal, methylglyoxal, butenedial) and 2 tricarbonyls. Some of these compounds were already reported to be produced by irradiation of natural surface waters or synthetic waters containing NOM with natural or simulated solar-light, by ozone treatment or by UV-based AOPs of solutions of humic substances. This is the case for formic, acetic and oxalic acids [Brinkmann et al, 2003 ; Goldstone et al , 2002], formaldehyde, acetaldehyde, glyoxal and methylglyoxal [Thomson et al, 2004 ; Agbaba et al, 2016 ; Zhong et al, 2017 ; de Bryun et al, 2011 ; Kieber et al, 1990], malonic and butanedioic acids [Corin et al, 1996], and pyruvic acid [Thomson et al, 2004].

The concentration of the different carbonyls after 1, 2, 3 and 4 h of irradiation were estimated using derivatized methylglyoxal and pyruvic acid (Table SI-4). Figure 3A shows the concentration profile of the most concentrated ones, i.e. formaldehyde, glyoxylic acid, pyruvic acid, glyoxal and glycolaldehyde, as a function of irradiation time. The concentration of formaldehyde and glyoxylic acid was maximum after 2 h of irradiation and then declined while that of pyruvic acid, glyoxal and glycolaldehyde increased throughout the 4 h of irradiation. It shows that SRNOM photodegradation still proceeds beyond 4 h although a significant absorbance decrease at 254 nm.

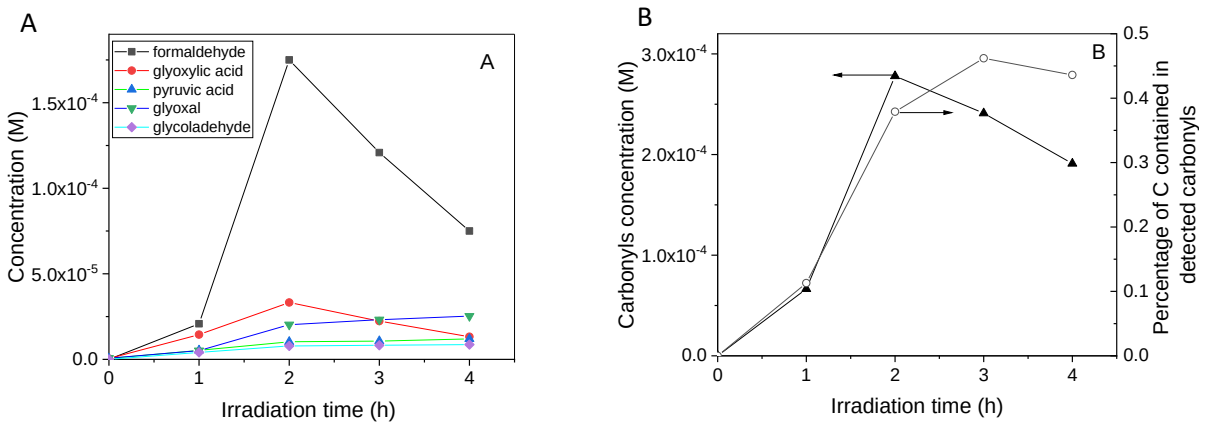

Figure 3: Evolution of carbonyls detected in irradiated SRNOM by DNPH derivatization. A) Concentration of the main carbonyls vs irradiation time and B) Sum of carbonyls concentration (○, left y-axis) and mass percentage of carbon contained in detected carbonyls (◢, right y-axis) vs irradiation time.

The total pool of C_1-C_5 carbonyls was estimated by summing the individual concentrations. Figure 3B shows that their cumulative concentration increased during the first 2 h of irradiation to reach the value of 2.8×10^{-4} M. Based on these concentrations and on the DOC measurements, the mass percentage of carbon atoms contained in the detected carbonyls could be calculated using Eq 1. This percentage was maximum after 3 h of irradiation where it reached 46% (Figure 3B). This high value demonstrates the very important contribution of C_1-C_5 carbonyls to the pool of photoproducts. As most of these compounds poorly absorbed below 300 nm, their high concentration explains the unchanged spectrum shape following irradiation.

$$Mass\ percentage_t = \frac{\sum_{i=1}^{i=n}[c_i]_t \times M_i}{DOC_t} \qquad \text{Eq 1}$$

where $[c_i]_t$ and M_i are the concentration at time t and the molecular mass of carbonyl i, and DOC_t is the organic carbon content in the solution at time t.

The concentration of carboxylic acids detected in $SRNOM_{3h}$ are shown in Table SI-5. In general, BSTFA-GC-MS and CI-MS analyses gave consistent results regarding the concentration estimations. BSTFA-GC-MS was however less performant than CI-MS in the analysis of compounds containing 2 or 3 CO_2H or OH functions such as tartronic, dihydroxymalonic acid, oxalic acid and tricarballylic acids. The difficulty to solubilize lyophilized $SRNOM_{3h}$ in acetonitrile to conduct the BSTFA derivatization or a partial derivatization of these compounds probably explain these discrepancies. Malic, oxalic, butanedioic, glycolic, and malonic acids were the most concentrated acids. However, their concentration in $SRNOM_{3h}$ that laid below 2.8×10^{-6} M, were much lower than those of carbonyls. Eq

1 allowed to determine that the detected carboxylic acids contained only 2% in mass of the $SRNOM_{3H}$ carbon atoms.

Nitrate ions were also detected by CI-MS in SRNOM at a level of 2.9×10^{-6} M, but not in $SRNOM_{3h}$.

The detection of all these compounds suggests that the photodegradation of SRNOM under UVC resulted from a complex set of reactions involving the direct photolysis of SRNOM constituents as well as their oxidation by the radicals generated in the course of the irradiation. Many radicals such as R•, RO•, RO_2•, HO_2•/O_2•$^-$ and •OH can be formed by C-C, C-O, and O-O bond cleavage, phenyl-O^- and RCO_2^- photoionization, addition of oxygen on radicals and various radicalar attacks. Once formed, these radicals could contribute to further degradation of SRNOM constituents and of their by-products. Among them, •OH radical is likely to play a significant role for several reasons. It is the most oxidant species able to react with a wide variety of chemicals by addition on double bonds or by H atom abstraction [Buxton et al, 1988]. NOM was shown to generate •OH radicals [Vaughan and Blough, 1998 ; Page et al, 2011; McKay et al, 2015 ; Gan et al, 2008 ; Sun et al, 2015 ; Dong et al, 2012 ; Aguer and Richard, 1999] under irradiation. In reactions where •OH radicals are purposely produced [Varanasi et al, 2018] the oxidation degree of photoproducts, given by the O/C ratio, is generally high (1-2), as observed here. Last, the photolysis of chlorosalicylic acid, that was proposed to occur via the intermediary formation of •OH radicals [Tafer et al, 2016], yielded glycolic, lactic, and butanedioic acids, acetaldehyde, glycoaldehyde, methylglyoxal, $C_4H_4O_3$, and $C_3O_3H_2$ that were also detected in the present work.

Table 2. Chemicals detected in SRNOM and photoproducts detected in irradiated SRNOM.

Compound	N°	Name	Method of detection	Samples in which the compound was detected
CH_2O	1	formaldehyde	DNPH	$SRNOM_{1h,2h,3h,4h}$
CH_2O_2	2	formic acid	CI/MS	$SRNOM_{3h}$
C_2H_4O	3	acetaldehyde	DNPH	$SRNOM_{1h,2h,3h,4h}$
$C_2H_4O_2$	4	acetic acid	CI/MS	$SRNOM_{3h}$
$C_2H_4O_2$	5	glycolaldehyde	DNPH	$SRNOM_{1h,2h,3h,4h}$
$C_2H_2O_2$	6	glyoxal	DNPH	$SRNOM_{1h,2h,3h,4h}$
$C_2H_4O_3$	7	glycolic acid	BSTFA	$SRNOM_{3h}$
$C_2H_2O_3$	8	glyoxylic acid	DNPH	$SRNOM_{1h,2h,3h,4h}$
$C_2H_2O_4$	9	oxalic acid	CI/MS	$SRNOM_{3h}$
$C_3H_4O_2$	10	methylglyoxal	DNPH	$SRNOM_{1h,2h,3h,4h}$
$C_3H_6O_3$	11	lactic acid	BSTFA	$SRNOM_{3h}$
$C_3H_4O_3$	12	pyruvic acid	DNPH	$SRNOM_{1h,2h,3h,4h}$
$C_3H_2O_3$	13		DNPH	$SRNOM_{1h,2h,3h,4h}$
$C_3H_2O_4$	14		DNPH	$SRNOM_{1h,2h,3h,4h}$

$C_3H_4O_4$	15	malonic acid	BSTFA	$SRNOM_{3h}$
$C_3H_6O_4$	16	glyceric acid	BSTFA	SRNOM
$C_3H_4O_5$	17	tartronic acid	BSTFA	$SRNOM_{3h}$
$C_3H_4O_6$	18	dihydroxy malonic acid	BSTFA	$SRNOM_{3h}$
$C_4H_6O_2$	19		DNPH	$SRNOM_{1h,2h,3h,4h}$
$C_4H_4O_2$	20	butenedial	DNPH	$SRNOM_{1h,2h,3h,4h}$
$C_4H_6O_3$	21		DNPH	$SRNOM_{1h,2h,3h,4h}$
$C_4H_4O_3$	22		DNPH	$SRNOM_{1h,2h,3h,4h}$
$C_4H_6O_4$	23	butanedioic acid	BSTFA	$SRNOM_{3h}$
$C_4H_4O_4$	24		DNPH	$SRNOM_{1h,2h,3h,4h}$
$C_4H_6O_5$	25	malic acid	BSTFA	$SRNOM_{3h}$
$C_4H_9NO_2$	26	4-aminobutanoic acid	BSTFA	$SRNOM_{3h}$
$C_5H_8O_4$	27	glutaric acid	BSTFA	$SRNOM_{3h}$
$C_5H_6O_4$	28		DNPH	$SRNOM_{1h,2h,3h,4h}$
$C_5H_{10}O_5$	29	xylose	BSTFA	SRNOM
$C_5H_6O_6$	30		DNPH	$SRNOM_{1h,2h,3h,4h}$
$C_6H_{10}O_4$	31	hexanedioic acid	BSTFA	SRNOM
$C_6H_{12}O_5$	32	L-rhamnose	BSTFA	SRNOM
$C_6H_{12}O_5$	33	fucose	BSTFA	SRNOM
$C_6H_{12}O_6$	34	glucose	BSTFA	SRNOM
$C_6H_{12}O_6$	35	galactose	BSTFA	SRNOM
$C_6H_8O_6$	36		BSTFA	$SRNOM_{3h}$
$C_6H_8O_6$	37	tricarballylic acid	BSTFA	$SRNOM_{3h}$
$C_9H_{16}O_4$	38	azelaic acid	BSTFA	SRNOM
$C_{12}H_{22}O_4$	39	dodecane-dioic acid	BSTFA	SRNOM
$C_{18}H_{34}O_2$	40	oleic acid	BSTFA	SRNOM
$C_{18}H_{36}O_2$	41	stearic acid	BSTFA	$SRNOM_{3h}$

3.3. Effect of SRNOM pre-irradiation on the oxidant properties at 254 nm

In order to explore the photooxidant properties of pre-irradiated SRNOM, we chose glyphosate as a chemical probe. We first checked that it is photostable when irradiated in our device ($k < 2 \times 10^{-4}$ min^{-1}, Table 3). For these experiments, we selected $SRNOM_{3h}$ that showed the highest concentration of intermediary carbonyl compounds (2.4×10^{-4} M) and SRNOM and $SRNOM_{3h}$ were tested at the same absorbance at 254 nm (0.34). In the presence of SRNOM, glyphosate (10^{-5} M) disappeared with a rate constant k of 0.0013 ± 0.0002 min^{-1} in air-saturated solution (Figure 4A and Table 3).constant k of 0.0013 ± 0.0002 min^{-1} in air-saturated solution (Figure 4A and Table 3).

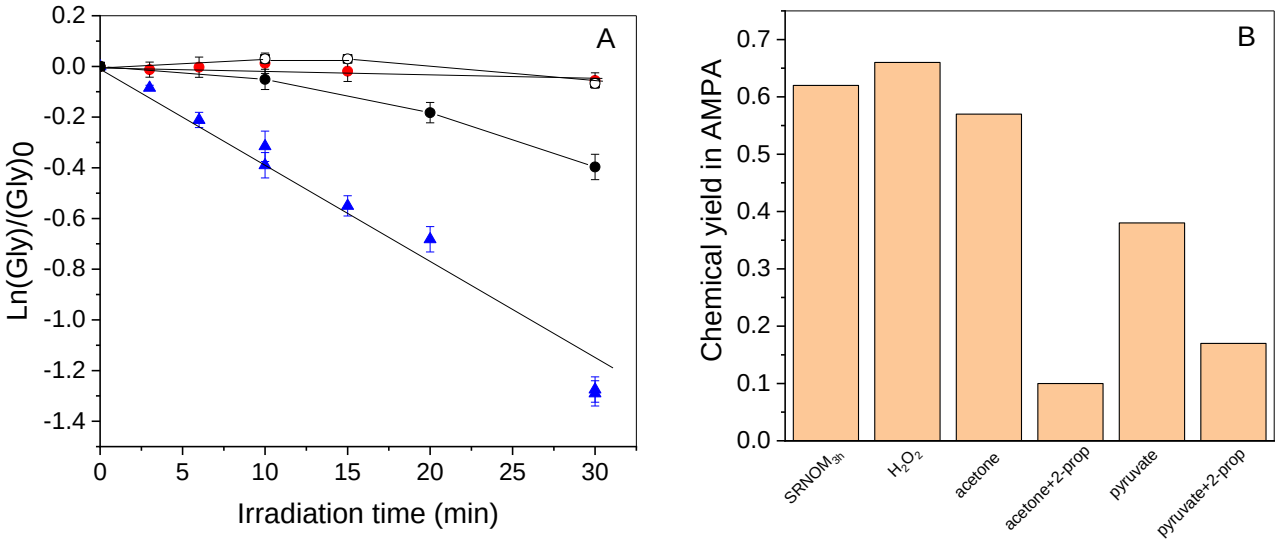

Figure 4. Loss of glyphosate (10^{-5} M) (A) and formation of AMPA (B) under irradiation at 254 nm in presence of SRNOM (●), $SRNOM_{3h}$ (▲), $SRNOM_{3h}$ + 2-propanol (5×10^{-3} M) (○), and $SRNOM_{3h}$ in N_2-saturated medium (●). A_{254} of SRNOM and $SRNOM_{3h}$ is equal to 0.34 in a cuvette and 0.68 in the reactor.

Making the hypothesis that the reaction was due to the reaction of glyphosate with •OH radicals, we used this rate constant to estimate the quantum yield of •OH radicals formation by SRNOM (Φ_{OH}^{SRNOM}) in the first stages of the reaction. Once formed by process 1, •OH radicals react with glyphosate (k_{gly} = $(3.37 \pm 0.10) \times 10^7$ M^{-1} s^{-1}, Vidal et al, 2015) (process 2) and with SRNOM (process 3). We took for k_{SRNOM} the value of 1.6×10^8 M_C^{-1} s^{-1} reported in the literature for Suwannee river fulvic acid [Westoffer et al, 2007].

SRNOM + hν → SRNOM* → •OH	I_a, Φ_{OH}^{SRNOM}	(1)
•OH + Glyphosate →	k_{Gly}	(2)
•OH + SRNOM →	k_{SRNOM}	(3)

The rate of glyphosate photodegradation (R_{Gly}) can be written (SI-Text 7):

$$R_{Gly} = I_0 (1 - 10^{-A_{SRNOM}}) \Phi_{OH}^{SRNOM} \frac{k_{gly}[Gly]}{k_{gly}[Gly] + k_{SRNOM}[SRNOM]} \qquad EQ1$$

where $I_0\ (1 - 10^{-A_{SRNOM}})$ is the rate of light absorption by SRNOM. As SRNOM was diluted 2.44 fold to reach the same absorbance at 254 nm as $SRNOM_{3h}$, [SRNOM] was equal to 6.35 mgC L^{-1} or 0.529 mM_C^{-1}, taking 12 for the molar mass of carbon. In these conditions, one gets that glyphosate trapped 0.38% of •OH radicals and that ϕ_{OH}^{SRNOM} was equal to 0.024; this value is in the range of that reported by Lester et al (2013) at 254 nm (0.047).

Table 3. First-order rate constants of glyphosate loss, and rates of glyphosate, acetone and pyruvate photodegradation at 254 nm under different conditions.

Conditions	k (min^{-1})	R_{Gly} M s^{-1}	$R_{acetone}$ M s^{-1}	$R_{pyruvate}$ M s^{-1}
Glyphosate alone (10^{-5} M)	$< 2 \times 10^{-4}$	$< 3 \times 10^{-11}$		
+ SRNOM	0.0013 ± 0.0002	2.2×10^{-10}		
+ $SRNOM_{3h}$	0.038 ± 0.004	6.3×10^{-9}		
+ $SRNOM_{3h}$ + 2-propanol (5×10^{-3} M)	0.0036 ± 0.0004	6.0×10^{-10}		
+ $SRNOM_{3h}$ N_2 purged	0.002 ± 0.002	3.3×10^{-10}		
+ H_2O_2 (10^{-5} M)	0.0093 ± 0.001	1.5×10^{-9}		
+ acetone (10^{-4} M)	0.0020 ± 0.001 (0-10 min) 0.024 ± 0.003 (10-30 min)	3.3×10^{-10} (0-10 min) 4.0×10^{-9} (10-30 min)	$< 0.9 \times 10^{-8}$ (0-10 min) 2.4×10^{-8} (10-30 min)	
+ pyruvate (10^{-4} M)	0.021 ± 0.002	3.5×10^{-9}		0.5×10^{-9} (0-6 min) 2.1×10^{-8} (6-30 min)
+ acetone (10^{-4} M) + 2-propanol (10^{-4} M)	0.0050 ± 0.0007	8.3×10^{-10}		
+ pyruvate(10^{-4} M) + 2-propanol (10^{-4} M)	0.0057 ± 0.0008	9.5×10^{-10}		
+ acetone (10^{-4} M)	0.016 ± 0.0002	2.7×10^{-9}	1.7×10^{-8}	

+ H_2O_2 (10^{-5} M)				
acetone alone (2.4×10^{-4} M)			$< 0.9 \times 10^{-8}$ (0-10 min) 3.9×10^{-8} (10-30 min)	
+ H_2O_2 (10^{-5} M)			3.5×10^{-8}	
+ H_2O_2 (10^{-3} M)			1.8×10^{-7}	

In the presence of $SRNOM_{3h}$ and in air-saturated solution, glyphosate disappeared much faster than in the presence of SRNOM (Figure 4A) with k= 0.038 ± 0.004 min^{-1} (Table 3). In N_2-purged $SRNOM_{3h}$ solution, the glyphosate photodegradation rate was significantly reduced compared to the one conducted in air-saturated medium (k = 0.002 ± 0.002 min^{-1} in the first 10 min of the reaction, Figure 4A, Table 3) demonstrating the important role played by oxygen in the reaction. Moreover, we irradiated glyphosate and $SRNOM_{3h}$ in the presence of 2-propanol to determine whether •OH radicals were involved in the loss of glyphosate. Using $k_{2\text{-propanol}} = 1.9 \times 10^9$ M^{-1} s^{-1} [Buxton et al, 1998] for the bimolecular rate constant of reaction between •OH and 2-propanol :

$$\text{•OH} + \text{2-propanol} \rightarrow \qquad k_{2\text{-propanol}} \qquad (4)$$

we added 5×10^{-3} M of 2-propanol expecting an inhibition of the reaction > 90% based on $k_{SRNOM3h}[SRNOM_{3h}] \sim 9 \times 10^4$ s^{-1}, as for SRNOM. The inhibition was of 90% (Figure 4A, Table 3) in accordance with a significant contribution of •OH.

Spin trap experiments using DMPO as the spin-trapping reagent were also conducted to confirm the formation of •OH radicals. Figure 5 shows that the four-line signal with an intensity ratio 1:2:2:1 characteristic of the DMPO-OH• adduct was not detected when DMPO was irradiated in the presence of SRNOM (plot a) or H_2O_2 (10^{-5}) (plot c) while it was observed with $SRNOM_{3h}$ (plot b) and H_2O_2 (5×10^{-3} M) (plot d). Again, this result is in line with the production of •OH radicals upon irradiation of $SRNOM_{3h}$ in UVC.

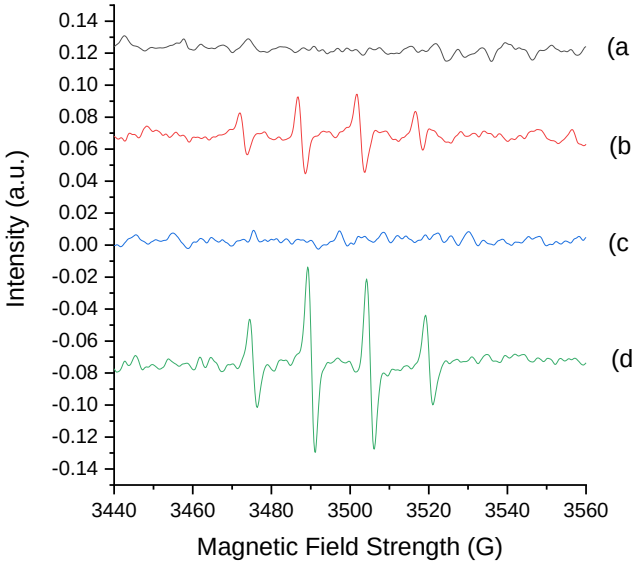

Figure 5 : ESR spectra obtained upon irradiation of DMPO (25 mM) in the presence of SRNOM (20 mg L^{-1}) (a), $SRNOM_{3h}$ (b), H_2O_2 (10^{-5} M) (c) and H_2O_2 (5×10^{-3} M) (d).

Postulating that the disappearance of glyphosate was only due to the reaction with •OH, we made the same calculation for $SRNOM_{3h}$ as for SRNOM, after having replaced processes 1 and 2 by processes 1' and 3' respectively:

$$SRNOM_{3H} + h\nu \rightarrow SRNOM_{3H}^* \rightarrow {}^{\bullet}OH \qquad I_a, \phi_{OH}^{SRNOM3h} \qquad (1')$$

$$^{\bullet}OH + SRNOM_{3H} \rightarrow \qquad k_{SRNOM3h} \qquad (3')$$

and substituting SRNOM by $SRNOM_{3h}$ in EQ1. The TOC analyses showed that $SRNOM_{3h}$ had a DOC content of 10.9 mgC L^{-1} or 0.907 mM_C^{-1} (Table 1). To estimate the percentage of •OH radicals reacting with glyphosate in $SRNOM_{3h}$ solution, we also need to know the value of $k_{SRNOM3h}$. Since $SRNOM_{3h}$ is much less aromatic than SRNOM, and •OH radicals react more easily with aromatic or conjugated structures than with saturated ones, $k_{SRNOM3h}$ is possibly smaller than k_{SRNOM}. Postulating that the rate constant decrease may parallel the absorbance decrease at 254 nm, we opted for $k_{SRNOM3h} = (0.7 \pm 0.3) \times 10^8$ M_C^{-1} s^{-1}. From this value, the percentage of •OH radicals trapped by glyphosate in $SRNOM_{3h}$ solution would lay between 0.3 and 0.8 % and $\phi_{OH}^{SRNOM3h}$ would be comprised between 0.21 and 0.55, a value between 10 and 20 times higher than that found for ϕ_{OH}^{SRNOM}. This value must be considered

as a maximal value and would be lower if radicals other than •OH also contributed to the degradation of glyphosate. To better understand the enhancing effect of the pre-irradiation on the photooxidant properties of SRNOM, we conducted additional experiments and tested potential candidates for their ability to photodegrade glyphosate.

3.4. Peroxides formation and role of H_2O_2 in the oxidant properties at 254 nm

Peroxides are sources of •OH radicals through direct photolysis (process 5) or photo-Fenton reaction and we quantified their formation in our system. Measurements of H_2O_2 and RO_2H + RO_2R were performed on SRNOM and $SRNOM_{3h}$ irradiated for 30 min (Figure 6). In SRNOM, H_2O_2 and RO_2H + RO_2R accumulated linearly. After 30 min of irradiation, the total concentration of H_2O_2 + RO_2H + RO_2R was equal to 16 µM; H_2O_2 was by far the most abundant species (14.2 µM) while RO_2H + RO_2R contributed to the pool of peroxides in a minor way (1.8 µM). In $SRNOM_{3h}$, the peroxides formation was auto-inhibited, slowing down after 10 min. The total concentration reached 15.8 µM after 30 min ; H_2O_2 and RO_2H + RO_2R were in equivalent amounts of ~ 8.0 µM. The formation of H_2O_2 in the photolysis of NOM is well documented in the literature [Garg et al., 2011]. It is formed by dimutation of $O_2^{\cdot-}$ that arises from reduction of dissolved O_2. Peroxides and hydroperoxides are generated after the reaction of $R^{\cdot}$ radicals with dissolved O_2 to yield $RO_2^{\cdot}$ and the reaction of these peroxyl radicals with $O_2^{\cdot-}/HO_2^{\cdot}$ [Sun et al., 2021].

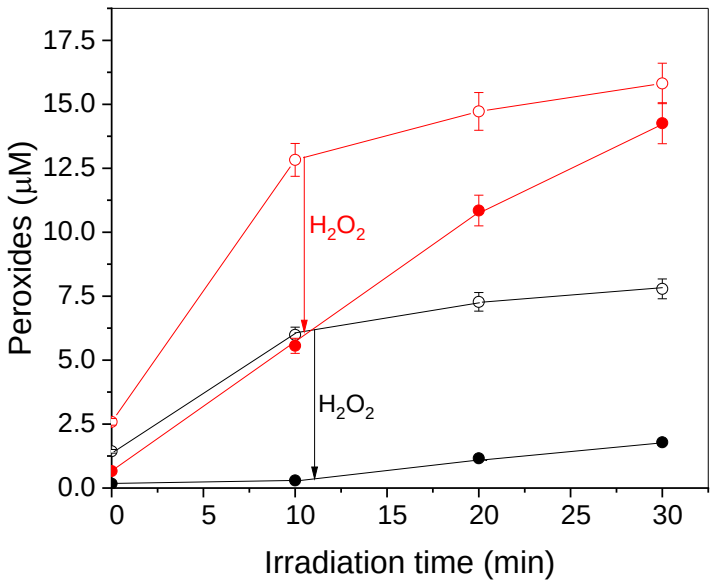

Figure 6 : Formation of peroxides upon irradiation of SRNOM at 254 nm. H_2O_2 + ROOR + ROOH in SRNOM (●) and in $SRNOM_{3h}$ (○); ROOR + ROOH in SRNOM (●) and in $SRNOM_{3h}$ (○).

To determine the contribution of H_2O_2 to the formation of •OH via process (5), we proceeded as follows. We first measured R_{Gly} in the presence of H_2O_2 (10^{-5} M) alone. The value of 1.5×10^{-9} M^{-1} s^{-1} allowed us to check that glyphosate reacted with •OH and to measure the photon flux I_0 in the irradiation device (SI-Text 1). Then, we calculated R_{Gly}^{H2O2} in SRNOM solution using Eq 2, supposing that the photolysis of H_2O_2 produced during the irradiation of SRNOM was the only source of •OH through process 5 (SI-Text 5).

$$H_2O_2 \rightarrow \bullet OH \qquad \emptyset_{OH}^{H2O2} \qquad (5)$$

$$R_{Gly}^{H2O2} = I_{a,H2O2}^{SRNOM}\, \emptyset_{OH}^{H2O2} \frac{k_{gly}\,[Gly]}{k_{gly}[Gly] + k_{SRNOM}\,[SRNOM] + k_{H2O2}\,[H2O2]} \quad EQ2$$

Taking $[H_2O_2]$ = 14 µM (corresponding to the highest value reached for SRNOM), ε_{H2O2} = 19.6 M^{-1} cm^{-1} at 254 nm, A_{254} =0.34 for SRNOM and ℓ = 2, we calculated $I_{a,H2O2}^{SRNOM}$ using the Beer-Lamber law for a mixture (SI-Text 8). Then, taking $k_{H2O2} = 2.7 \times 10^7$ $M^{-1}.s^{-1}$ [Stephan et al, 1996], we got that glyphosate trapped 0.38% of •OH and using ϕ_{OH}^{H2O2} = 1 [Yu and Barker, 2003], we finally obtained $R_{Gly}^{H2O2} = 7.0 \times 10^{-12}$ M s^{-1}. In the case of $SRNOM_{3h}$, we took $[H_2O_2]$ = 8 µM and the same calculation led to R_{Gly}^{H2O2} = (3.0-9.0) × 10^{-12} M s^{-1}. Both values are very small compared to the experimental values 2.2×10^{-10} M s^{-1} and 6.5×10^{-9} M s^{-1} respectively measured for SRNOM and $SRNOM_{3h}$ and it can be concluded that the photochemical decomposition of titrated hydroperoxides negligibly contributed to the oxidation of glyphosate. Spontaneous decomposition of unstable hydroperoxides into RO• and •OH might be an alternative source of •OH radicals. This was considered by Badiali et al (2015) and Krapf et al (2016) in their studies on secondary organic aerosols.

3.5. Role of carbonyls in the photooxidant properties at 254 nm

Given the high concentration of carbonyls detected in $SRNOM_{3h}$ and the known potential of these chemicals as sensitizers, we tested if they could induce the transformation of glyphosate at 254 nm. We first tested pyruvic acid since this compound had been previously detected in our irradiated SRNOM samples. In the presence of this ketoacid (10^{-4} M), in pH 7 buffered solutions, glyphosate (10^{-5} M) disappeared with an apparent first order rate constant equal to 0.021 ± 0.002 min^{-1} (Figure 7A, Table 3). Pyruvate was also photodegraded and the reaction auto-accelerated. During the first 6 min of irradiation, only 1.8×10^{-6} M of pyruvate were transformed against 3.1×10^{-5} M between 6 and 30 min (Figure 7B). The rate of pyruvate loss, $R_{pyruvate}$, in the second part of the curve was equal to 2.1 ×

10^{-8} M s^{-1}, and R_{Gly} to 3.5×10^{-9} M s^{-1}. The experiment was repeated in the presence of 2-propanol added to trap •OH radicals. The concentration 10^{-4} M was chosen for 2-propanol for a theoritical trapping of more than 95% based on $k_{pyruvate\ acid} = 3 \times 10^{8}$ M^{-1} s^{-1} (process 6) [Buxton et al, 1998]. After 30 min, the rate of glyphosate loss was reduced by 75% confirming a significant contribution of •OH in the reaction.

$$\bullet OH + \text{pyruvate} \rightarrow \text{products} \qquad k_{pyruvate} \qquad (6)$$

Although it was not detected in irradiated SRNOM samples, acetone was chosen to represent monocarbonyls because it is a simple molecule, it can be purchased in high purity, it was already studied and its quantum yield of photolysis is known ($\phi_{acetone}$ = 0.061 at 270 nm, Anpo and Kubokawa, 1977). At 10^{-4} M, a concentration falling within the range of that found for intermediary carbonyls, acetone increased the rate of glyphosate photodegradation and the reaction was also auto-accelerated (Figure 7A, Table 3). During the first 10 min of reaction, an averaged k = 0.002 ± 0.001 min^{-1} was obtained while, between 10 and 30 min, we measured k = 0.024 ± 0.003 min^{-1}. In parallel, the decay of acetone was monitored by UHPLC-HRMS after DNPH derivatization. Acetone also disapppeared by an autoaccelerated reaction (Figure 7B). Between 0 and 10 min, the loss of acetone was lower than 5% corresponding to a rate of acetone photodegradation ($R_{acetone}$) < 0.9×10^{-8} M s^{-1} while, between 10 and 40 min, acetone disappeared by 43% and $R_{acetone}$ was equal to 2.4×10^{-8} M s^{-1} (Table 3). During this reaction H_2O_2 was formed (Figure 7B). The H_2O_2 production was of 2 µM between 0 and 10 min and 10 µM between 10 and 30 min which mirrored the autoaccelerated decrease of glyphosate and acetone. In the presence of 2-propanol (10^{-4} M) and acetone (10^{-4} M), glyphosate disappeared by 10% instead of 42% in the absence of 2-propanol after 30 min of irradiation (Figure 7A, Table 3) confirming again a significant contribution of •OH in the reaction (75%).

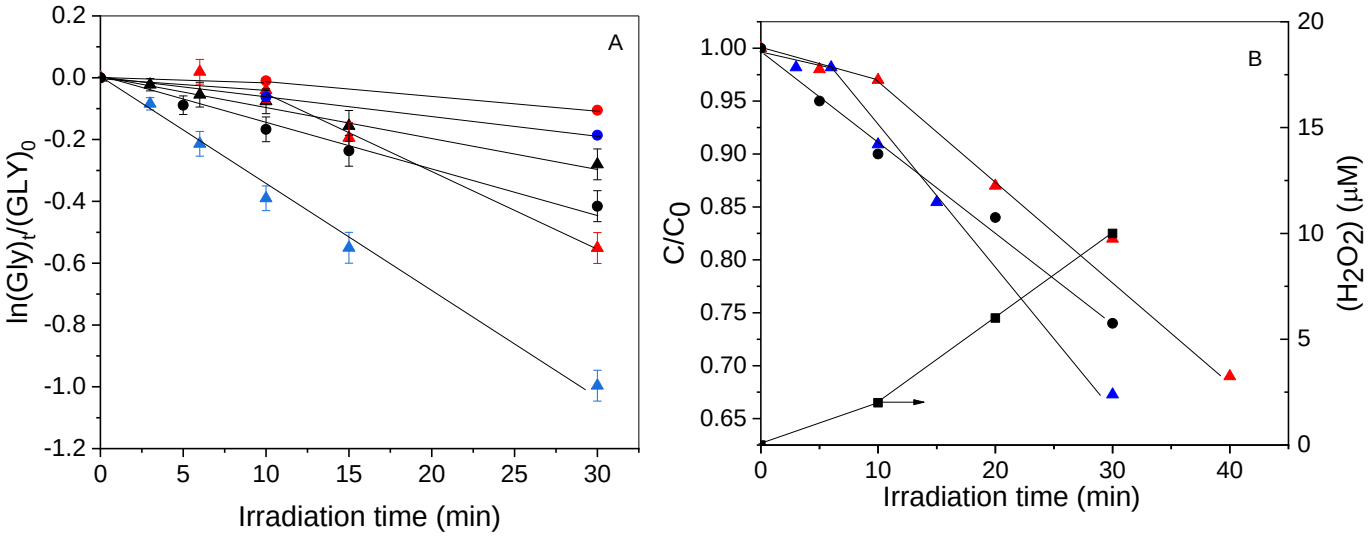

Figure 7: Photolysis of glyphosate (10^{-5} M) (A) in the presence of H_2O_2 (10^{-5} M) (▲), acetone (10^{-4} M) (▲), acetone (10^{-4} M) + H_2O_2 (10^{-5} M) (●), pyruvate (10^{-4} M) (▲), acetone (10^{-4} M) + 2-propanol (10^{-4} M) (●) and pyruvate (10^{-4} M) + 2-propanol (10^{-4} M) (●). B: loss of acetone (▲, ●), of pyruvate (▲), and formation of H_2O_2 (■). Solutions buffered at pH 7.

Acetone was also irradiated alone to check that the observed auto-acceleration was not due to the presence of glyphosate. At 2.4×10^{-4} M, acetone also disappeared in an auto-accelerated reaction with $R_{acetone} < 0.9 \times 10^{-8}$ M^{-1} s^{-1} between 0-10 min and $R_{acetone} = 3.9 \times 10^{-8}$ M^{-} s^{-1} between 10-30 min (Table 3). The photoproducts were pyruvic acid, methyl glyoxal, hydroxyacetone, formadehyde as described by Stephan and Bolton (1999) when they studied the photolysis of acetone in the presence of H_2O_2 at 254 nm. Using the quantum yield of acetone photodegradation in diluted solutions (0.061), and $\varepsilon_{acetone}$ = 16 M^{-1} cm^{-1} at 254 nm, it is possible to calculate the rate of acetone photodegradation by direct photolysis $R_{acetone}^{dp}$ using EQ3:

$$R_{acetone}^{dp} = I_0 \left(1 - 10^{-A_{acetone}}\right) \emptyset_{acetone} \quad EQ3$$

For [acetone]= 10^{-4} M, one gets $R_{acetone}^{dp} = 1.3 \times 10^{-9}$ M s^{-1} and for [acetone]= 2.4×10^{-4} M $R_{acetone}^{dp} = 3.1 \times 10^{-9}$ s^{-1}. These values are consistent with the ones obtained between 0 and 10 min (< 9×10^{-9} M s^{-}

[1]), and one can conclude that $R_{acetone}^{dp}$ being negligible behind $R_{acetone}$ measured in the second part of the curves, other reactions should take place.

An autoaccelerated reaction is generally due to the accumulation of key intermediates. Here, the intermediary chemicals were the acetone photoproducts and peroxides, among which, H_2O_2. We therefore studied the effect of H_2O_2, used a hydroperoxide model, at the concentration of 10^{-5} and 10^{-3} M on the photodegradation of acetone (2.4×10^{-4} M). The photodegradation of acetone was fast till the very beginning of the irradiation ($R_{acetone} = 3.5 \times 10^{-8}$ and 1.8×10^{-7} M s^{-1}, respectively, Table 3) and no auto-accelerating effect was observed. In this mixture, acetone can disappear by reaction with •OH produced from H_2O_2 photolysis (process 7, $k_{acetone} = 1.1 \times 10^8$ M^{-1} s^{-1}, Buxton et al, 1998). Process 8 is a potential competiting pathway of •OH disappearance ($k_{H2O2} = 2.7 \times 10^7$ M^{-1} s^{-1} Buxton et al, 1998).

•OH + acetone	→	products	$k_{acetone}$	(7)
•OH + H_2O_2	→	products	k_{H2O2}	(8)

For $[H_2O_2] = 10^{-3}$ M and [acetone] = 2.4×10^{-4} M, process 8 was expected to significantly reduce the percentage of •OH radicals trapped by acetone. Taking into account that acetone should trap about 50% of •OH, one obtains $R_{acetone} = 1.3 \times 10^{-7}$ M.s^{-1} against 1.8×10^{-7} M s^{-1} measured experimentally. For $[H_2O_2] = 10^{-5}$ M and [acetone] = 2.4×10^{-4} M, process 8 was negligible, and acetone was expected to trap all the •OH radicals produced by H_2O_2 photolysis. Its rate of decay through process 7 ($R^{OH}_{acetone}$) was equal to 2.6×10^{-9} M s^{-1} according to EQ 4.:

$$R_{acetone}^{OH} = I_0 \left(1 - 10^{-A_{H2O2}}\right) \emptyset_{OH}^{H2O2} \qquad EQ4$$

This calculated rate accounted for only 6.6% of the measured rate indicating that an additional radical source was responsible for acetone degradation. Then, we simultaneously irradiated glyphosate (10^{-5} M), H_2O_2 (10^{-5} M) and acetone (10^{-4} M). In this case, the glyphosate photodegradation was fast till the beginning of the irradiation (k = 0.016 min^{-1}) (Figure 7A, Table 3) showing that H_2O_2 or other hydroperoxides are important intermediaries in the reaction.

The results obtained for acetone can be tentatively explained by the chain-reaction mechanism shown in Scheme 1. In the classical chain oxidation of a chemical RH bearing a labile H atom, the initiator produces the primary radicals that start the chain through a transfer reaction by generating the radical R• (process 7). Then R• produces RO_2• by adding O_2 (process 10) and RO_2• regenerates R•

along with RO_2H by abstracting of a H from RH (process 11). The longer the chain length the faster the reaction;in fact, when the chain is long enough, the rate of the propagation reactions becames much higher than the rates of initiation and of transfer. In our case, the calculated rate of acetone photolysis $R_{acetone}^{dp}$ was lower than the experimental rate of acetone photodegradation consistently with the involvement of a chain reaction.

Scheme 1. Mechanism of photodegradation of acetone at 254 nm. In red, in the presence of glyphosate.

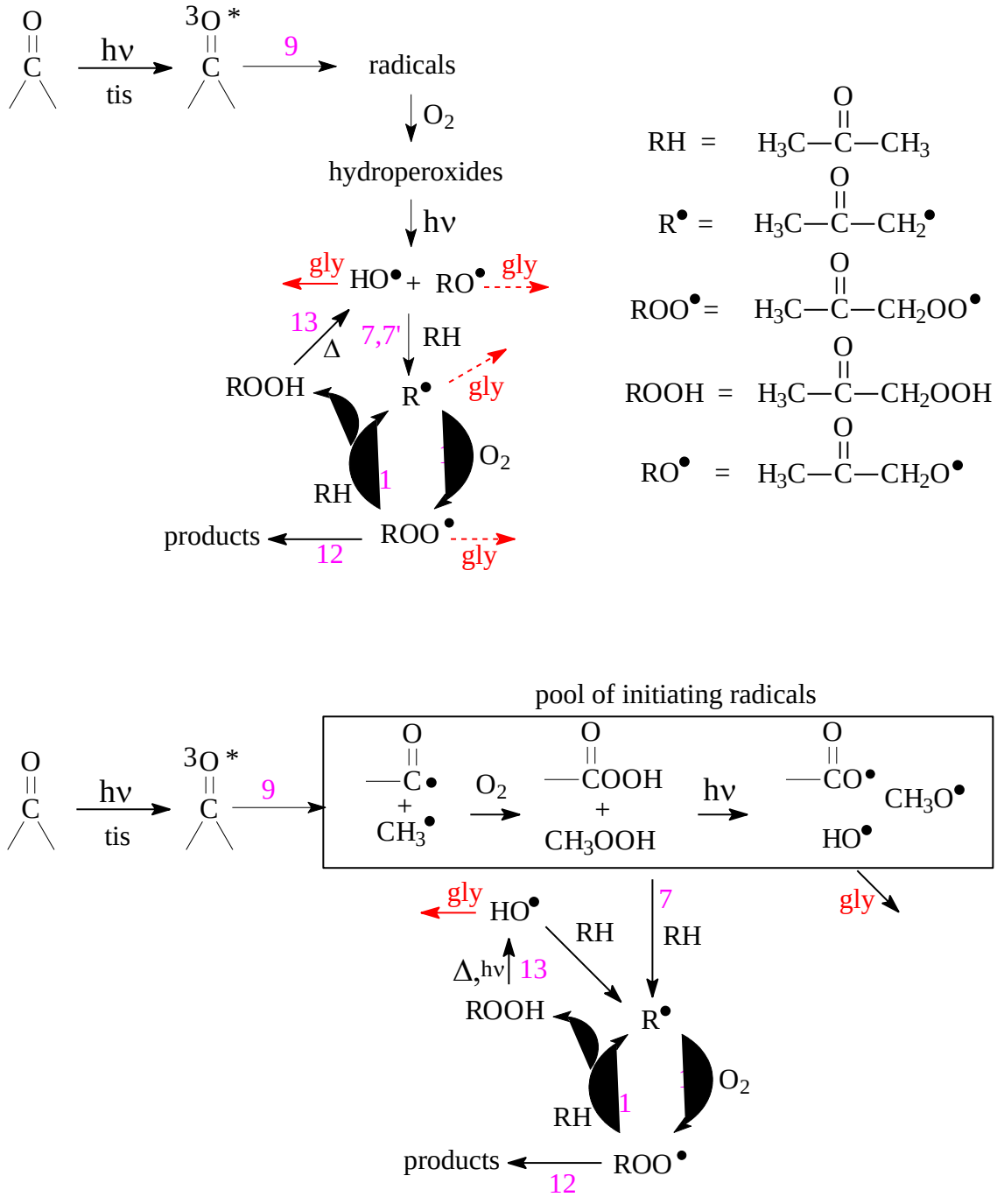

The irradiation of acetone was expected to yield radicals by α-cleavage of the triplet excited state (process 9) [Pearson, 1963]. The triplet could also abstract a H-atom from methyl groups of acetone, however, neither acetone itself nor glyphosate were concentrated enough to compete significantly with cleavage [Anpo and Kubokawa, 1977]. Due to the oxidation of these radicals and to the photolysis of the formed hydroperoxides, there should be a pool of initiating radicals in the system. The acetonyl radical, R•, formed by process 7 [Stephan et al, 1996], should easily react with oxygen (process 10) to yield the peroxyl radical ROO• [Stephan et al, 1996]. This peroxyl radical likely abstracts an H-atom from acetone (process 11) to regenerate the acetonyl radical and produce the hydroperoxide ROOH. The recombination of two peroxide radicals (process 12) terminates this chain reaction.

In this chain reaction, glyphosate might be oxidized by several of the radicals formed in this complex mixture. However, while the reaction with •OH was evidenced, the oxidation with the other radicals remains to be demonstrated. If we make the hypothesis that •OH contributed significantly to the glyphosate degradation, the source of •OH needs to be explained. Indeed, calculations showed that the photolysis of the different hydroperoxides did not yield enough radicals to explain the high rate of glyphosate degradation. An alternative formation of •OH could be the spontaneous decomposition at room temperature of unstable hydroperoxides, here CH_3-CO-CH_2OOH (process 13). According to the works of Badiali et al (2015) and Krapf et al (2016), the formation of very unstable hydroperoxides is plausible. Therefore, despite processes 7, 10 and 11 still taking place, the key process becomes process 13 since it introduced a continuous source of •OH and RO• radicals; consequently, glyphosate degradation reached a significant rate reaction when RO_2H was sufficiently accumulated.

CH_3-CO-$CH_2OOH \rightarrow CH_3$-CO-CH_2O• + •OH (13)

In the case of $SRNOM_{3h}$, carbonyls were present at 2.4×10^{-4} M and hydroperoxides were potentially generated at a fast rate, therefore making it possible the mechanism already proposed in the case of acetone to occur. In accordance, ROOH + ROOR were formed along with H_2O_2. In $SRNOM_{3h}$ solution, R_{gly} was equal to 6.3×10^{-9} M s^{-1}. Considering that glyphosate trapped between 0.3 and 0.8 % of •OH radicals in competition with $SRNOM_{3H}$ constituents, the rate of •OH formation should be comprised between $\sim 8 \times 10^{-7}$ and 2×10^{-6} M s^{-1}. In the model solution containing glyphosate (10^{-5} M), H_2O_2 (10^{-5} M) and acetone (10^{-4} M), Rgly was equal to 2.7×10^{-9} M s^{-1}. Considering that •OH contributed to the reaction at 75% and that glyphosate trapped 3% of •OH in competition with acetone, then the rate of •OH formation should be equal to $\sim 7 \times 10^{-8}$ M s^{-1}. For acetone (2.4×10^{-4} M), it might be $\sim 1.7 \times 10^{-7}$ M s^{-1}. This value is smaller than that estimated for the $SRNOM_{3h}$ solution, and several explanations of this difference can be proposed: (i) $SRNOM_{3h}$ was a much more complex system than H_2O_2 + acetone and quantitative results cannot be directly transferable; furthermore, calculation lays on an

approximate value of the bimolecular reaction rate constant of $SRNOM_{3h}$ with •OH; (ii) Acetone was chosen as a model compound but among the carbonyls formed in $SRNOM_{3h}$, some may absorb more than acetone, especially those bearing double bonds, and/or photodissociate much more easily [Anpo and Kubokawa, 1977]; (iii) $SRNOM_{3h}$ also contained chemicals acting probably as better H-donors than acetone and glyphosate, which should favour process 11 and thus the formation of unstable hydroperoxides; (iv) Oxidant species other than •OH might contribute to the photodegradation of glyphosate.

In the case of SRNOM, R_{Gly} was much higher than R_{Gly}^{H2O2} as for $SRNOM_{3h}$ suggesting that chain reactions might take place as for $SRNOM_{3H}$, although leading to a much slower production of •OH. Accordingly, the 6-times less formation of ROOR+ROOH from SRNOM than from $SRNOM_{3h}$ suggests that unstable hydroperoxides should be produced in smaller amounts by SRNOM than by $SRNOM_{3h}$. Spectral measurements showed that SRNOM is much more aromatic than $SRNOM_{3h}$ which constitutes an important difference in terms of •OH reactions. The •OH radicals are known to add on phenols [Lundquist and Eriksson, 2000] to finally produce unreactive phenoxyl radicals while they generate radicals oxidable into hydroperoxides when they abstract hydrogen atoms from aliphatic compounds. Hence, the presence of carbonyls in $SRNOM_{3h}$ could not only favour the formation of radicals through their photolysis but also constitutes a pool of aliphatic compounds oxidable into hydroperoxides.

AMPA was the main glyphosate photoproduct detected by UHPLC-HRMS (Figure 4B). In the literature, other oxidation products were also detected such as sarcosine [Chen et al, 2007], not detected in this work. After 30 min of irradiation, the highest yield of AMPA was measured with H_2O_2 (66%), followed by $SRNOM_{3h}$ (62%), acetone (57%) and pyruvic acid (38%). Interestingly, when 2-propanol was added to acetone and pyruvate solutions, the yield of AMPA dropped to 10% and 17%, respectively. The formation of AMPA may be thus an indirect evidence of the involvement of •OH radicals in the photodegradation.

3.5. Effect of SRNOM pre-irradiation on •OH, $^1O_2$ and ^{3}SRNOM* formation under simulated solar light

We also compared the ability of SRNOM and $SRNOM_{3h}$ to photoproduce photooxidants $^3SRNOM^*$, $^1O_2$ and •OH in simulated solar light. After normalization for light absorption, the rate of 2,4,6-trimethyphenol was found to be 1.5 times higher in SRNOM than in $SRNOM_{3H}$, in accordance with lower rate of ^{3}SRNOM* formation. Therefore, chromophores yielding ^{3}SRNOM* were partly degraded under UVC irradiation. In the case of $^1O_2$ titrated using furfuryl alcohol, we found rates of formation varying by less than 10% between SRNOM and $SRNOM_{3h}$. At last, results on terephthalic acid used to estimate

the rate of •OH formation showed a higher rate of •OH formation in $SRNOM_{3h}$ solution than in SRNOM solution. Taking $k_{SRNOM} = 1.6 \times 10^8\ M_C^{-1}\ s^{-1}$ and $k_{SRNOM3h} = 0.7 \times 10^8\ M_C^{-1}\ s^{-1}$ for the bimolecular rate constants of reaction with •OH, we got a rate of •OH formation higher by 40% for $SRNOM_{3h}$ solution than for SRNOM solution. This enhancement was much lower than the one observed at 254 nm with glyphosate. The dependence of the •OH formation enhancement on the irradiation wavelength supports the hypothesis of the involvement of poorly conjugated and light absorbing carbonyl compounds in the photochemical production of •OH.

4. Conclusion

This work aimed to investigate the effect of UVC irradiation on the ability of SRNOM to generate oxidant species, in particular •OH radicals under UVC. Through in-depth analytical and kinetic studies, we demonstrated that SRNOM irradiation drastically increased the pool of aliphatic carbonyls together with its capacity of photoinducing the degradation of glyphosate at 254 nm. Several experimental results suggest that •OH radicals contributed to this degradation. To better understand the role of carbonyls in the reaction, we studied the photodegradation of glyphosate in the presence of acetone and pyruvate. Experimental data were explained by a mechanism involving a chain reaction in which •OH radicals may be formed through the spontaneous decomposition of unstable hydroperoxides. The same mechanism might prevail in pre-irradiated SRNOM and explain its high efficiency to photodegrade glyphosate upon irradiation at 254 nm. These results show that in UVC treatments NOM could favour the degradation of micropollutants through its high capacity to generate very oxidant radicals. Such a pretreatment of NOM would deserve to be further studied in combination with other engineered water treatment sytems.

Acknowledgments:

This paper is part of a project that received funding from the European Union's Horizon 2020 research and innovation programme under the Marie Skłodowska-Curie grant agreement no. 765860 (Aquality). The authors would like to thank Martin Leremboure (Engineer CNRS) and Frédéric Emmenegger (Tech CNRS) for UHPLC-MS analyses and Lawrence Frezet (Engineer CNRS) for ESR experiments.

References

Agbaba, J., Jazic, J.M., Tubic, A., M., Maletić S., Kragulj Isakovski M., Dalmacija B. (2016) Oxidation of natural organic matter with processes involving O3, H2O2 and UV light: formation of oxidation and disinfection by-products. RSC Adv. 6, 86212-86219. DOI: 10.1039/C6RA18072H

Aguer, J. P., Richard, C. (1999) Influence of the excitation wavelength on the photoinductive properties of humic substances. Chemosphere 38, 2293-2301. DOI: 10.1016/S0045-6535(98)00447-0

Anpo, M., Kubokawa, Y. (1977) Reactivity of excited triplet alkyl ketones in solution. I. Quenching and hydrogen abstraction of triplet acetone. Bull. Chem. Soc. Jpn. 1977, 50, 1913. DOI: 10.1246/bcsj.50.1913

Badali, K. M., Zhou, S., Aljawhary, D., Antiñolo, M., Chen, W. J., Lok, A., Mungall, E.,

Wong, J. P. S., Zhao, R., Abbatt, J. P. D. (2015) Formation of hydroxyl radicals from photolysis of secondary organic aerosol material. Atmos. Chem. Phys. 15, 7831–7840.

DOI : 10.5194/acp-15-7831-2015

Brinkmann, T., Horsch, P., Sartorius, D., Frimmel, F. H. (2003) Photoformation of low molecular weight organic acids from brown water dissolved organic matter. Environ. Sci. Technol. 37, 4190-4198. DOI: 10.1021/es0263339

Buchanan, W., Roddick, F., Porter, N. (2016) Formation of Hazardous By-Products Resulting from the Irradiation of Natural Organic Matter: Comparison between UV and VUV Irradiation. Chemosphere 63 (7), 1130–1141. DOI: 10.1016/j.chemosphere.2005.09.040.

Buxton, G. V. , Greenstock, C.L. , Helman, W. P. , Ross, A. B. (1988) Critical review of rate constants fro reactions of hydrated electrons, hydrogen atoms and hydroxyl radicas in aqueous solution. J. Phys. Chem. Ref. Data 17, 513-886. DOI: 10.1063/1.555805

Chen, Y., Wu, F., Lin, Y., Deng, N., Bazhin, N., Glebov, E. (2007) Photodegradation of glyphosate in the ferrioxalate system. J. Hazard. Mat. 148, 360–365.

DOI : 10.1016/j.jhazmat.2007.02.044

Corin, N., Backlund, P., Kulovaara, M. (1996) Degradation products formed during UV-irradiation of humic waters. Chemosphere 33, 245-255. DOI: 10.1016/0045-6535(96)00167-1

de Bryun, W.J., Clark, C.D., Pagel, L., Takehara, C. (2011) Photochemical production of formaldehyde, acetaldehyde and acetone from chromophoric dissolved organic matter in coastal waters. J Photochem Photobiol A, 226, 16-22. DOI: 10.1016/j.jphotochem.2011.10.002

Dong, M. M., Rosario-Ortiz, F. L. (2012) Photochemical formation of hydroxyl radical from effluent organic matter. Environ. Sci. Technol. 46, 3788-3794. DOI : 10.1021/es2043454

Fukushima, M., Tatsumi, K. (2001) Degradation characteristics of humic acid during photo-fenton processes. Environ. Sci. Technol. 35, 3683-3690. DOI: 10.1021/es0018825

Gan, D., Jia, M., Vaughan, P. P., Falvey, D. E., Blough, N. V. (2008) Aqueous Photochemistry of Methyl-Benzoquinone J. Phys. Chem. A 112, 2803– 2812. DOI: 10.1021/jp710724e

Garg, S., Rose, A. L., Waite, T. D. (2011) Photochemical production of superoxide and hydrogen peroxide from natural organic matter Geochim. Cosmochim. Acta 75, 4310-4320.

DOI : 10.1016/j.gca.2011.05.014

Goldstone, J.V., Pullin, M.J., Bertilsson, S., Voelker, B.M. (2002) Reactions of hydroxyl radicals with humic substances : bleaching, mineralization and production of bioavailable carbon substrates. Environ. Sci. Technol. 36, 364-372. DOI: 10.1021/es0109646

Hao, W., Zhanghao, C., Feng, S., Jingyi, L., Xin, J., Chao, W., Cheng G. (2020) Characterization for the transformation of dissolved organic matters during ultraviolet disinfection by differential absorbance spectroscopy. Chemosphere 243, 125374. DOI: 10.1016/j.chemosphere.2019.125374

Ike, I. A., Karanfil, T., Cho, J., Hur J. (2019) Oxidation byproducts from the degradation of dissolved organic matter by advanced oxidation processes -A critical review. Water Res. 164 114929. DOI: 10.1016/j.watres.2019.114929

Kieber, R.J., Zhou, X., Mopper, K. (1990) Formation of carbonyl compounds from UV-induced photodegradation of humic substances in natural waters : fate of riverine carbon in the sea. Limnol. Oceanogr. 35, 1503-1515. DOI: 10.4319/lo.1990.35.7.1503

Krapf, M., Haddad, I. E., Bruns, E. A., Molteni, U., Daellenbach, K. R., Prevot, A. S. H., Baltensperger, U., Dommen, J. (2016) Labile Peroxides in Secondary Organic Aerosol.

Chem 1, 603–616. DOI: 10.1016/j.chempr.2016.09.007

Kulovaara, M., Corin, N., Backlund, P., Tervo J. (1996) Impact of UV_{254}-irradiation on aquatic humic substances. Chemosphere 33, 783-790. DOI: 10.1016/0045-6535(96)00233-0

Lamsal, R., Walsh, M. E., Gagnon, G. A. (2011) Comparison of advanced oxidation processes for the removal of natural organic matter. Water Res. 45, 3263-3269. DOI: 10.1016/j.watres.2011.03.038

Lester, Y., Sharpless, C. M., Mamane, H., Linden, K. G. (2013) Production of Photo-oxidants by Dissolved Organic Matter During UV Water Treatment. Environ. Sci. Technol. 47, 11726−11733. DOI : 10.1021/es402879x

Leresche, F., McKay, G., Kurtz, T., von Gunten, U., Canonica, S., Rosario-Ortiz, F. L. (2019)

Effects of Ozone on the Photochemical and Photophysical Properties of Dissolved Organic Matter. Environ. Sci. Technol. 53, 5622−5632. DOI: 10.1021/acs.est.8b06410

Lester, Y., Sharpless, C. M., Mamane, H., Linden, K. G. (2013) Production of Photo-oxidants by Dissolved Organic Matter During UV Water Treatment Environ. Sci. Technol. 47, 11726−11733. DOI: 10.1021/es402879x

Lundqvist, M. J., Eriksson, L. A. (2000) Hydroxyl Radical Reactions with Phenol as a Model for Generation of Biologically Reactive Tyrosyl Radicals. J. Phys. Chem. B 104, 848-855. DOI : 10.1021/jp993011r

McKay, G., Rosario-Ortiz, F. L. (2015) Temperature Dependence of the Photochemical Formation of Hydroxyl Radical from Dissolved Organic Matter Environ. Sci. Technol. 49, 4147– 4154. DOI: 10.1021/acs.est.5b00102

Miller, W.L., Kester, *D.R.* (1988) Hydrogen peroxide measurement in seawater by (p-hydroxyphenyl) acetic acid dimerization. Anal. Chem. 60, 2711-2715. DOI: 10.1021/ac00175a014

Mostafa, S., Rosario-Ortiz, F. L. (2013) Singlet Oxygen Formation from Wastewater Organic Matter. Environ. Sci. Technol. 47, 8179−8186. DOI: 10.1021/es401814s

Page, S. E., Arnold, W. A., McNeill, K. (2011) Assessing the Contribution of Free Hydroxyl Radical in Organic Matter-Sensitized Photohydroxylation Reactions Environ. Sci. Technol. 45, 2818– 2825. DOI: 10.1021/es2000694

Palma, D., Sleiman, M., Voldoire, O. et al. Study of the dissolved organic matter (DOM) of the Auzon cut-off meander (Allier River, France) by spectral and photoreactivity approaches. Environ Sci Pollut Res 27, 26385–26394 (2020). DOI: 10.1007/s11356-020-09005-7

Patel-Sorrentino, N., Mounier, S., Lucas, Y., Benaim, J.Y. (2004) Effects of UV–visible irradiation on natural organic matter from the Amazon basin. Sci. Tot. Environ. 321, 231-239

DOI: 10.1016/j.scitotenv.2003.08.017

Paul, A., Dziallas, C., Zwirnmann, E., Gjessing, E.T., Grossart, H.P. (2012) UV irradiation of natural organic matter (NOM): impact on organic carbon and bacteria. Aquatic Sciences 74, 443–454. DOI: 10.1007/s00027-011-0239-y

Pearson, G. S. (1963) The photoxidation of acetone. J. Chem. Phys. 67, 1686-1692. DOI: 10.1021/j100802a026

Polewski, K., Slawinska, D., Slawinski, J , Pawlak, A. (2005) The effect of UV and visible light radiation on natural humic acid and EPR spectral and kinetic studies. Geoderma 126, 291-299. DOI: 10.1016/j.geoderma.2004.10.001

Rosario-Ortiz, F.L., Canonica, S. (2016) Probe Compounds to Assess the Photochemical Activity of Dissolved Organic Matter. Environ Sci Technol 50, 12532−12547. DOI: 10.1021/acs.est.6b02776

Rougé, V., von Gunten, U., Lafont de Sentenac, M., Massi, M., Wright, P. J., Croué, J. P., Allard, S. (2021). Comparison of the impact of ozone, chlorine dioxide, ferrate and permanganate pre-oxidation on organic disinfection byproduct formation during post-chlorination **Environ. Sci.: Water Res. Technol.** (in press). DOI : 10.1039/D0EW00411A

Sarathy, S. R., Stefan, M. I., Royce, A., Mohseni, M. (2011) Pilot-scale UV/H2O2 advanced oxidation process for surface water treatment and downstream biological treatment: effects on natural organic matter characteristics and DBP formation potential.

Environ. Technol. 32, 1709-1718. DOI: 10.1080/09593330.2011.553843

Sarathy, S. R., Mohseni M. (2007) The Impact of UV/H_2O_2 Advanced Oxidation on Molecular Size Distribution of Chromophoric Natural Organic Matter.

Environ. Sci. Technol. **41**, 8315-8320. DOI: 10.1021/es071602m

Sarathy, S. R., Stefan, M. I., Royce, A., Mohseni, M. (2011) Pilot-scale UV/H2O2 advanced oxidation process for surface water treatment and downstream biological treatment: effects on natural organic

matter characteristics and DBP formation potential. Environ. Technol. 32, 1709-1718. DOI: 10.1080/09593330.2011.553843

Schmitt-Kopplin, P., Hertkorn, N., Schulten, H. R., Kettrup, A. (1998) Structural Changes in a Dissolved Soil Humic Acid during Photochemical Degradation Processes under O2 and N2

Atmosphere. Environ. Sci. Technol. 32, 2531-2541. DOI: 10.1021/es970636z

Sillanpää, M., ChakerNcibi, M., Matilainen, A. (2018) Advanced oxidation processes for the removal of natural organic matter from drinking water sources: A comprehensive review. J Environ. Manag. 208 56-76. DOI: 10.1016/j.jenvman.2017.12.009

Soman, A., Qiu, Y., Chan Li, Q. (2008) HPLC-UV Method Development and Validation for the Determination of Low Level Formaldehyde in a drug Substance. J. Chromatog. Sci. 46 461-465. DOI: 0.1093/chromsci/46.6.461

Stefan, M. , Hoy, A., Bolton, J.R. (1996) Kinetics and Mechanism of the Degradation and Mineralization of Acetone in Dilute Aqueous Solution Sensitized by the UV Photolysis of Hydrogen Peroxide. Environ. Sci. Technol. 30, 2382-2390. DOI : 10.1021/es950866i

Stefan, M. I., Bolton, J. R. (1999) Reinvestigation of the Acetone Degradation Mechanism in Dilute Aqueous Solution by the UV/H_2O_2 Process. Environ. Sci. Technol. 33, 6, 870–873

DOI : 10.1021/es9808548

Sun, L., Qian, J., Blough, N. V., Mopper, K. Insights into the Photoproduction Sites of Hydroxyl Radicals by Dissolved Organic Matter in Natural Waters Environ. Sci. Technol. Lett. 2015, 2 (12) 352–356. DOI: 10.1021/acs.estlett.5b00294

Sun, Q., Ma, J., Yan, S., Song, W. (2021). Photochemical formation of methylhydroperoxide in dissolved organic matter solutions. Env. Sci. Technol. 52, 1076-1087. DOI: 10.1021/acs.est0c07717

Tafer, R., Sleiman, M., Boulkamh, A., Richard, C. (2016) Photomineralization of aqueous salicylic acids. Photoproducts characterization and formation of light induced secondary OH precursors (LIS-OH). Water Res. 106, 496-506. DOI : 10.1016/j.watres.2016.10.038

Tang, W.W., Zeng, G.M., Gong, J.-L., Liang, J., Xu, P., Zhang, C., Huang, B.-B. (2014) Impact of Humic/Fulvic Acid on the Removal of Heavy Metals from Aqueous Solutions Using Nanomaterials: A Review. Sci. Total Environ. 468–469, 1014–1027. DOI: 10.1016/j.scitotenv.2013.09.044.

Thomson, J., Roddick, F.A., Drikas, M. (2004) Vacuum ultraviolet irradiation for natural organic matter removal. J. Water Supply Res. Technol. - Aqua 53 193-206. DOI: 10.2166/aqua.2004.0017

Varanasi, L., Coscarelli, E., Khaksari, M., Mazzoleni, L. R., Minakata, D. (2018) Transformations of dissolved organic matter induced by UV photolysis, Hydroxyl radicals, chlorine radicals, and sulfate radicals in aqueous-phase UV-Based advanced oxidation processes. Water Res. 135, 22-30. DOI: 10.1016/j.watres.2018.02.015

Vaughan, P. P., Blough, N. V. (1998) Photochemical formation of hydroxyl radical by constituents of natural waters. Environ. Sci. Technol. 32, 2947-2953. DOI: 10.1021/es9710417

Vidal, E., Negro, A., Cassano, A., Zalazar, C. (2015) Simplified reaction kinetics, models and

experiments for glyphosate degradation in water by the UV/H2O2 process.

Photochem Photobiol Sci 14, 366-377. DOI: 10.1039/C4PP00248B

Vione, D., Minella, M., Maurino, W., Minero, C. 2014. Indirect Photochemistry in Sunlit Surface Waters: Photoinduced Production of Reactive Transient Species. .Chem. Eur. J. 20, 10590 – 10606. DOI: 10.1002/chem.201400413

Wang, D., Duan, X., He, X., Dionysiou, D. D. (2016) Degradation of dibutyl phthalate (DBP) by UV-254 nm/H2O2 photochemical oxidation: kinetics and influence of various process parameters. Environ Sci Pollut Res Int. 23, 23772-23780. DOI: 10.1007/s11356-016-7569-1

Weisshar, J., Aiken, G. R., Bergamaschi, B. A., Fram, M. S., Fugii, R., Mopper, K. (2003) Evaluation of specific ultraviolet absorbance as an indicator of the chemical composition and reactivity of dissolved organic carbon. Environ Sci Technol 37, 4702–4708. DOI: 10.1021/es030360x

Wenk, J., Aeschbacher, M., Sander, M., von Gunten, U., Canonica, S. (2015) Photosensitizing and inhibitory effects of ozonated dissolved organic matter on triplet-induced contaminant transformation. Environ. Sci. Technol. 49, 8541−8549. DOI: 10.1021/acs.est.5b02221

Westerhoff, P., Mezyk, S. P., Cooper, W. J., Minakata, D. (2007) Electron Pulse Radiolysis Determination of Hydroxyl Radical Rate Constants with Suwannee River Fulvic Acid and Other Dissolved Organic Matter Isolates. Env. Sci Technol 41, 4640-4640. DOI : 10.1021/es062529n

Yu, J., Flagan, R., Seinfeld, J. (1998) Identification of Products Containing -COOH, -OH, and –C=O in atmospheric oxidation of hydrocarbons. Environ. Sci. Technol 32, 2357-2370. DOI: 10.1021/es980129x

Yu, X. Y., Barker, J. R. (2003) Hydrogen peroxide photolysis in acidic aqueous solutions containing chloride ions. I. Chemical mechanism. J. Phys. Chem. A, 107, 9, 1313–1324

DOI : 10.1021/jp0266648

Zhang, S., Rougé, V., Gutierrez, L., Croué, J. P. (2019) Reactivity of chromophoric dissolved organic matter (CDOM) to sulfate radicals: Reaction kinetics and structural transformation

Water Res. 163, 114846. DOI: 10.1016/j.watres.2019.07.013

Zhong, X., Cui, C., Yu, S. (2017) Identifying oxidation intermediates formed during ozone-UV of fulvic acid. Desalination and Water Treatment 74, 258-268. doi.org/10.5004/dwt.2017.20587

Zhou, Y., Cheng, F. , He, D., Zhang, Y., Qua,J. , Yang, X., Chenc, J., Peijnenburg, W. J. G. M. (2021) Effect of UV/chlorine treatment on photophysical and photochemical properties of dissolved organic matter. Water Res. 192, 116857. DOI : 10.1016/j.watres.2021.116857

Zoschke, K., Dietrich, N., Bornick, H., Worch, E. (2012). UV-based advanced oxidation processes for the treatment of odour compounds: efficiency and by-product formation.

Water Res. 46 5365-5373. doi.org/10.1016/j.watres.2012.07.012

Supporting information

Evolution of SRNOM photo-oxidant properties under UV-C irradiation: role of carbonyls in the production of OH radicals

Davide Palma[1], Amina Khaled[1], Mohamad Sleiman[1], Guillaume Voyard[1], Claire Richard[1]*

[1] Université Clermont Auvergne, CNRS, SIGMA-Clermont, ICCF, F-63000 Clermont-Ferrand, France

Text 1: Measurement of I_0, the photon flux entering into the solution from the UV-C source

I_0 was evaluated by chemical actinometry from the rate of glyphosate consumption in the presence of H_2O_2 in the device. Irradiation of H_2O_2 yields •OH radicals that react with glyphosate according to:

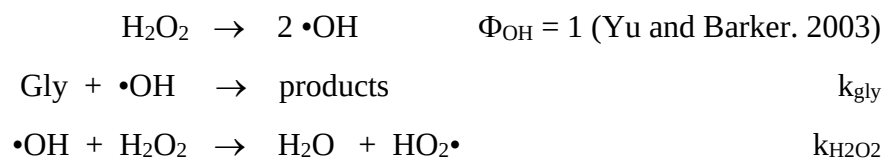

Based on $k_{gly} = 3.7\times10^7$ $M^{-1}.s^{-1}$ [Vidal et al. 2015] and $k_{H2O2} = 2.7\times10^7$ $M^{-1}.s^{-1}$ [Stephan et al. 1996], one gets that glyphosate (10^{-5} M) in presence of H_2O_2 (10^{-5} M) traps 58% of •OH radicals. The rate of glyphosate loss (R_{gly}) is thus equal to :

$$R_{Gly} = I_a^{H2O2}\times\Phi_{OH}\times0.58 = I_0\times(1-10^{-AH2O2})\times\Phi_{OH}\times0.58$$

where I_a^{H2O2} is the rate of light absorption by H_2O_2, A^{H2O2} is the absorbance of the solution at 254 nm. As only H_2O_2 absorbs 254 nm radiations, one gets :

$$A^{H2O2} = \varepsilon_{H2O2} \times [H_2O_2] \times \ell$$

with $\varepsilon_{H2O2} = 19.6\ M^{-1}.cm^{-1}$, $[H_2O_2] = 10^{-5}$ M and $\ell = 2$ cm.

From $R_{gly} = (9.3 \pm 0.5) \times 10^{-8}\ min^{-1}$ (Fig SI-1), we get $I_0 = 2.9 \times 10^{-6}$ Einstein.$L^{-1}.s^{-1}$

Fig SI-1. Loss of glyphosate (10^{-5} M) upon irradiation in the presence of H_2O_2 (10^{-5} M) in the UV-C device equipped with 4 germicidal tubes (General Electric, 15W).

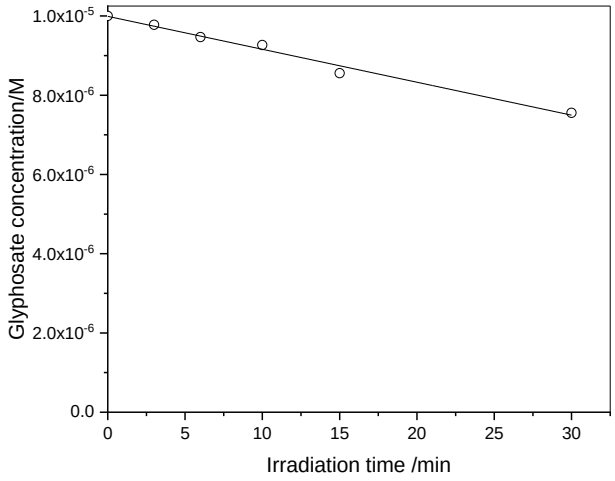

Text 2. Analysis of carbonyls by DNPH derivatization.

In the presence of DNPH carbonyls yield imines and water according to:

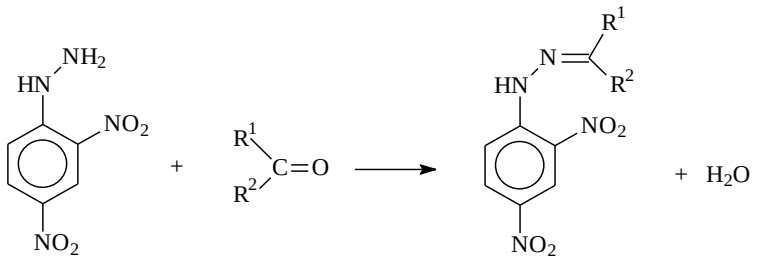

The m/z value of the imine is used to determine the chemical formula of the carbonyl. Pyruvic acid ($C_3H_4O_3$) gives an adduct detected at m/z = 267.0374 in negative mode corresponding to $C_9H_7O_6N_4$.

Methyl glyoxal ($C_3H_4O_2$) that contains 2 carbonyls is derivatized 2 times and gives an adduct detected at m/z = 431.0709 corresponding to $C_{15}H_{11}O_8N_8$.

Pyruvic acid and methylglyoxal were used as references for peak quantification for mono and dicarbonyls, respectively.

Fig SI-2: Calibration curve of pyruvic acid and methylglyoxal.

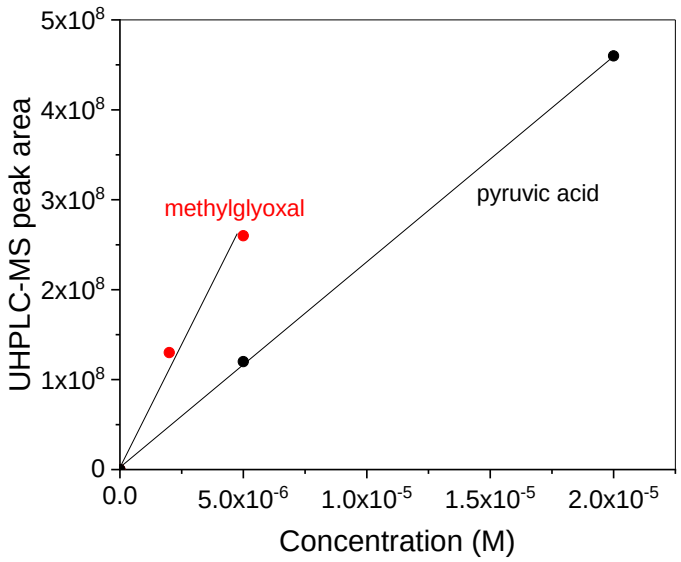

Text 3. UHPLC conditions in UHPLC-MS analyses.

UHPLC separation conditions were the following: The aqueous solvent (A) consisted of a mixture of 0.1% formic acid, and the organic phase (B) was acetonitrile. Separation was achieved with a gradient program consisting of 0–7.5 min 5% and 7.5–8.5 min 99% of mobile phase B. After 8.5 min, the gradient was returned to the initial conditions and the analytical column was reconditioned for 3.5 min. The flow rate was set to 0.450 $ml.min^{-1}$. The spectrometer operated in negative and positive modes. The formulas are proposed based on ppm < 5.

Text 4. Analysis of carboxylic and hydroxylic intermediates by BSTFA derivatization.

The reaction between compounds containing OH (alcohols or carboxylic acids) yields the following silylated derivative that is volatile and detectable by GC-MS:

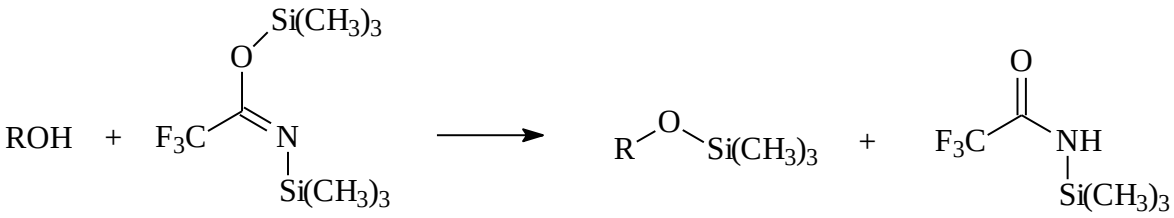

Compound separation was achieved by an HP-5MS (5% phenyl methyl siloxane) capillary column with 30 m length, 0.25 mm internal diameter, and 0.25 mm film thickness. The injector temperature was set at 250 °C and the injection volume was 1.0 µL (split ratio of 20:1). The GC oven temperature program was: 50 °C for 1 min followed by a gradient of 10 °C min^{-1} to 250 °C and held for 5 min. Mass spectra were scanned between m/z 50 and m/z 500 with the source temperature set at 230 °C. Identification was based on matching query spectra to spectra present in the reference library (NIST17). with a minimum spectral similarity measure of 95%.

Glycolic acid was used as a reference compound for the quantification of the other photoproducts.

Text 5. Determination of the rate of glyphosate consumption in SRNOM solutions.

Based on the following processes:

$$SRNOM + h\nu \rightarrow SRNOM^* \rightarrow {}^{\bullet}OH \qquad I_a\Phi_{OH}^{SRNOM} \quad (1)$$

$$^{\bullet}OH + Glyphosate \rightarrow \qquad k_{Gly} \quad (2)$$

$$^{\bullet}OH + SRNOM \rightarrow \qquad k_{SRNOM} \quad (3)$$

the rate of glyphosate (R_{Gly}) loss is equal to :

$$R_{Gly} = k_{Gly}[{}^{\bullet}OH][Gly]$$

Using that the rate of •OH formation is equal to its rate of loss once the quasi stationary state is reached, one can write that:

$$I_a\Phi_{OH}^{SRNOM} = k_{Gly}[{}^{\bullet}OH]_{qss}[Gly] + k_{SRNOM}[{}^{\bullet}OH]_{qss}[SRNOM]$$

This gives:

$$[{}^{\bullet}OH]_{qss} = I_a\Phi_{OH}^{SRNOM} / k_{Gly}[Gly] + k_{SRNOM}[SRNOM]$$

This finally gives:

$$R_{Gly} = I_0 (1 - 10^{-A_{SRNOM}}) \emptyset_{OH}^{SRNOM} \frac{k_{gly}\,[Gly]}{k_{gly}[Gly] + k_{SRNOM}\,[SRNOM]}$$

Text 6. Rate of light absorption of a compound in a mixture.

The rate of light absorption of I alone is equal to:

$Ia_I = I_0 (1\text{-}10^{-(AI)})$

while the rate of light absorption of I in mixture with II, $(Ia_I)^{II}$, is equal to:

$(Ia_I)^{II} = I_0 A_I/(A_I + A_{II}) (1\text{-}10^{-(AI + AII)})$

Where A_I and A_{II} are the absorbance of I and II respectively.

Figure SI-3. Spectrofluorometric quantification of peroxides. The calibration curve measures the concentration of the dimer of 4-hydroxyphenylacetic acid. The excitation wavelength was set at 320 nm.

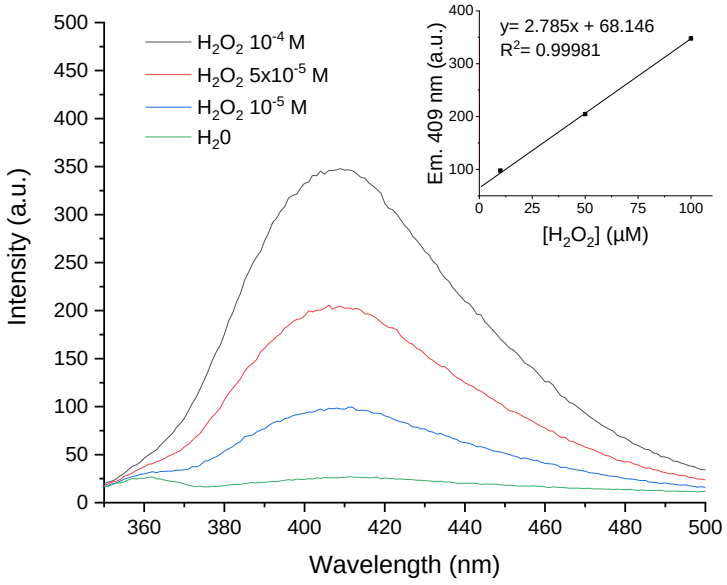

Table SI-1: Carboxylic acids and carbohydrates detected in non-irradiated SRNOM by BSTFA derivatization coupled to GC-MS. The number of OH functions correspond to the number of TMS linked to the compound. NDB is the number of double bond.

	Compounds	Number of OH functions	NDB	Name	N°	m/z adduct and fragments
Acids	$C_3H_6O_4$	3	1	Glyceric acid	16	322, 307, 292, 189, 147, 103, 73
	$C_6H_{10}O_4$	2	2	Hexanedioic acid	31	290, 275, 172, 147, 111, 73
	$C_9H_{16}O_4$	2	2	Azelaic acid	38	332, 317, 217, 147, 73
	$C_{12}H_{22}O_4$	2	2	Dodecane-dioic acid	39	374, 357, 217, 147, 73
	$C_{18}H_{34}O_2$	1	2	Oleic acid	40	396, 339, 183, 129, 73
Carbohy-drates	$C_5H_{10}O_5$	4	1	Xylose	29	438, 217, 204, 147, 73
	$C_6H_{12}O_5$	4	1	L-Rhamnose	32	452, 204, 147, 73
	$C_6H_{12}O_5$	4	1	Fucose	33	452, 217, 204, 147, 73
	$C_6H_{12}O_6$	5	1	Glucose	34	540, 217, 204, 147, 73
	$C_6H_{12}O_6$	5	1	Galactose	35	540, 217, 204, 147, 73

Table SI-2: Carboxylic compounds detected in $SRNOM_{3H}$ by BSTFA derivatization coupled to GC-MS and/or by CI coupled to MS. The number of OH functions corresponds to the number of TMS linked to the compound.

Compound	Number of OH functions	NDB	Name	N°	m/z adduct and fragments
CH_2O_2	1	1	Formic acid	2	
$C_2H_4O_2$	1	1	Acetic acid	4	
$C_2H_2O_4$	2	2	Oxalic acid	9	
$C_2H_4O_3$	2	1	Glycolic acid	7	220, 205, 177, 147, 73
$C_3H_6O_3$	2	1	Lactic acid	11	234, 219, 191, 147, 117, 73
$C_3H_4O_4$	2	2	malonic acid	15	248, 233, 147, 73
$C_3H_4O_5$	3	2	Tartronic acid	17	336, 321, 292, 221, 147, 102, 73
$C_3H_4O_6$	4	2	Dihydroxy malonic acid	18	424, 409, 381, 307, 221, 147, 73
$C_4H_6O_4$	2	2	Butanedioic acid	23	262, 247, 147, 73
$C_4H_6O_5$	3	2	Malic acid	25	350, 335, 307, 245, 233, 175, 147, 73
	2	1	4-amino butanoic acid	26	274, 260, 184, 147, 73
$C_5H_8O_4$	2	2	glutaric acid	27	276, 261, 204, 147, 129, 73
$C_6H_8O_6$	3	3	Tricarballylic acid	37	392, 377, 302, 259, 217, 185, 107, 73
$C_{18}H_{36}O_2$	1	1	Stearic acid	41	356, 341, 145, 117, 73

Table SI-3: Carbonyls compounds detected by DNPH derivatization and UHPLC-HRMS in irradiated in SRNOM solutions. The number of CO functions corresponds to the number of DNPH linked to the compound.

Compound	Number of CO functions	NDB	Name	N°	Δ ppm	m/z adduct in ES^-
CH_2O	1	1	formaldehyde	1	1.9	209.0309
C_2H_4O	1	1	acetaldehyde	3	2.8	223.0469
$C_2H_4O_2$	1	1	glycoaldehyde	5	3.5	239.042
$C_2H_2O_2$	2	2	glyoxal	6	3.1	417.0554
$C_2H_2O_3$	1	2	glyoxylic acid	8	4.5	253.0213
$C_3H_4O_2$	2	2	methylglyoxal	10	2.7	431.0709
$C_3H_4O_3$	1	2	pyruvic acid	12	4.7	267.0374
$C_3H_2O_3$	3	3		13	3.0	625.0793
$C_3H_2O_4$	2	3		14	3.9	461.0454
$C_4H_6O_2$	1	2		19	5.0	265.0581
$C_4H_4O_2$	2	3	butenedial	20	2.1	443.0706
$C_4H_6O_3$	1	2		21	4.6	281.053
$C_4H_4O_3$	2	3		22	2.1	459.0662
$C_4H_4O_4$	2	3		24	3.2	475.0615
$C_5H_6O_4$	3	3		28	4.0	489.0767
$C_5H_6O_6$	2	3		30	3.7	505.0720

Table SI-4. Concentration of carbonyls (M) in original and irradiated SRNOM.

Compound	N°	SRNOM	$SRNOM_{1H}$	$SRNOM_{2H}$	$SRNOM_{3H}$	$SRNOM_{4H}$
formaldehyde	1	4.6E-06	2.1E-05	1.7E-04	1.2E-04	7.5E-05
glycoaldehyde	5	8.3E-09	4.1E-06	7.8E-06	8.2E-06	8.7E-06
glyoxylic acid	8	5.4E-08	1.4E-05	3.3E-05	2.2E-05	1.3E-05
pyruvic acid	12	5.4E-08	5.3E-06	1.0E-05	1.1E-05	1.2E-05
$C_4H_6O_2$	19	1.2E-08	8.3E-07	1.2E-06	1.0E-06	7.9E-07
glyoxal	6	0.00E+00	5.1E-06	2.0E-05	2.3E-05	2.5E-05
methylglyoxal	10	1.4E-07	2.5E-06	5.1E-06	7.6E-06	8.9E-06
$C_3H_2O_3$	13	1.1E-07	1.7E-06	1.1E-05	1.6E-05	2.0E-05
$C_3H_2O_4$	14	0.00E+00	8.0E-07	2.8E-06	2.5E-06	5.8E-07
butenedial	20	0.00E+00	0.00E+00	8.3E-08	1.8E-07	7.1E-08
$C_4H_4O_3$	22	0.00E+00	7.5E-07	7.1E-07	3.1E-06	1.2E-06
$C_4H_4O_4$	24	0.00E+00	2.9E-07	3.1E-07	9.6E-07	3.9E-07
$C_5H_6O_4$	28	0.00E+00	0.00E+00	4.2E-07	6.2E-07	5.0E-07
$C_5H_6O_6$	30	0.00E+00	3.6E-08	1.1E-07	2.6E-07	1.7E-07
$C_3H_2O_3$	13	0.00E+00	0.00E+00	7.5E-07	3.4E-06	5.0E-06

Table SI-5. Concentration of carboxylic acids in SRNOM and $SRNOM_{3H}$.

Compound	N°	SRNOM		$SRNOM_{3H}$	
		CI	BSTFA	CI	BSTFA
Formic acid	2	traces	nd	traces	nd
Acetic acid	4	1.57E-7	nd	1.12E-6	nd
Glycolic acid	7	3.85E-7	nd	1.39E-6	9.11E-7
Oxalic acid	9	3.07E-6	nd	6.42E-6	nd
Lactic acid	11		nd	nd	4.80E-7
Malonic acid	15	1.65E-7	nd	1.66E-6	1.12E-6
Tartronic acid	17	traces	nd	4.49E-7	1.57E-7
Dihydroxymalonic acid	18	6.70E-8	nd	1.05E-6	1.10E-7
Butanedioic acid	23	7.08E-7	nd	1.77E-6	1.32E-6
Malic acid	25	4.07E-7	nd	2.09E-6	2.80E-6
Glutaric acid	27	traces	nd	1.17E-7	5.36E-8
Tricarballylic acid	37	traces	nd	1.80E-6	2.23E-7

Cited literature

[1] J. González-Pérez, F.J. González-Vila, G. Almendros, H. Knicker, The effect of fire on soil organic matter—a review, Environ. Int. 30 (2004) 855–70. https://doi.org/10.1016/j.envint.2004.02.003.

[2] I. Sutzkover-Gutman, D. Hasson, R. Semiat, Humic substances fouling in ultrafiltration processes, Desalination. 261 (2010) 218–231. https://doi.org/10.1016/j.desal.2010.05.008.

[3] H.-R. Schulten, M. Schnitzer, A state of the art structural concept for humic substances, Naturwissenschaften. 80 (1993) 29–30. https://doi.org/10.1007/BF01139754.

[4] The uniqueness of humic substances in each of soil, stream and marine environments, Anal. Chim. Acta. 232 (1990) 19–30. https://doi.org/10.1016/S0003-2670(00)81222-2.

[5] The isolation and characterization of fulvic acid and humic acid from river water, Water Res. 9 (1975) 1079–1084. https://doi.org/10.1016/0043-1354(75)90105-0.

[6] E.M. Thurman, R.L. Wershaw, R.L. Malcolm, D.J. Pinckney, Molecular size of aquatic humic substances, Org. Geochem. 4 (1982) 27–35. https://doi.org/10.1016/0146-6380(82)90005-5.

[7] A.T. Chow, F. Guo, S. Gao, R.S. Breuer, Trihalomethane Reactivity of Water- and Sodium Hydroxide–Extractable Organic Carbon Fractions from Peat Soils, J. Environ. Qual. 35 (2006) 114–121. https://doi.org/10.2134/jeq2004.0394.

[8] K. Mostofa, C.-Q. Liu, M.A. Mottaleb, G. Wan, H. Ogawa, D. Vione, T. Yoshioka, F. Wu, Dissolved Organic Matter in Natural Waters, in: Environ. Sci. Eng. Subser. Environ. Sci., 2013: pp. 1–137. https://doi.org/10.1007/978-3-642-32223-5_1.

[9] V.C. Kennedy, G.W. Zellweger, B.F. Jones, Filter pore-size effects on the analysis of Al, Fe, Mn, and Ti in water, Water Resour. Res. 10 (1974) 785–790. https://doi.org/10.1029/WR010i004p00785.

[10] L.G. Danielsson, On the use of filters for distinguishing between dissolved and particulate fractions in natural waters, Water Res. 16 (1982) 179–182. https://doi.org/10.1016/0043-1354(82)90108-7.

[11] E.M. Thurman, Organic geochemistry of natural waters, Nijhoff / Junk, Dordrecht; Lancaster, 1985.

[12] P.S. Huovinen, H. Penttilä, M.R. Soimasuo, Spectral attenuation of solar ultraviolet radiation in humic lakes in Central Finland, Chemosphere. 51 (2003) 205–214. https://doi.org/10.1016/S0045-6535(02)00634-3.

[13] J.J. Hudson, P.J. Dillon, K.M. Somers, Long-term patterns in dissolved organic carbon in boreal lakes: the role of incident radiation, precipitation, air temperature, southern oscillation and acid deposition, Hydrol. Earth Syst. Sci. 7 (2003) 390–398. https://doi.org/10.5194/hess-7-390-2003.

[14] I. Laurion, M. Ventura, J. Catalan, R. Sommaruga, Attenuation of ultraviolet radiation in mountain lakes: Factors controlling the among- and within-lake variability, Limnol Ocean. (2000) 1274–1288.

[15] D.A. Siegel, A.F. Michaels, Quantification of non-algal light attenuation in the Sargasso Sea: Implications for biogeochemistry and remote sensing, Deep Sea Res. Part II Top. Stud. Oceanogr. 43 (1996) 321–345. https://doi.org/10.1016/0967-0645(96)00088-4.

[16] J.T.O. Kirk, Yellow substance (gelbstoff) and its contribution to the attenuation of photosynthetically active radiation in some inland and coastal south-eastern Australian waters, Mar. Freshw. Res. 27 (1976) 61–71. https://doi.org/10.1071/mf9760061.

[17] S.C. Remke, U. von Gunten, S. Canonica, Enhanced transformation of aquatic organic compounds by long-lived photooxidants (LLPO) produced from dissolved organic matter, Water Res. 190 (2021) 116707. https://doi.org/10.1016/j.watres.2020.116707.

[18] D. Vione, G. Falletti, V. Maurino, C. Minero, E. Pelizzetti, M. Malandrino, R. Ajassa, R.-I. Olariu, C. Arsene, Sources and sinks of hydroxyl radicals upon irradiation of natural water samples, Environ. Sci. Technol. 40 (2006) 3775–3781. https://doi.org/10.1021/es052206b.
[19] R.M. Dalrymple, A.K. Carfagno, C.M. Sharpless, Correlations between Dissolved Organic Matter Optical Properties and Quantum Yields of Singlet Oxygen and Hydrogen Peroxide, Environ. Sci. Technol. 44 (2010) 5824–5829. https://doi.org/10.1021/es101005u.
[20] A.P.S. Batista, A.C.S.C. Teixeira, W.J. Cooper, B.A. Cottrell, Correlating the chemical and spectroscopic characteristics of natural organic matter with the photodegradation of sulfamerazine, Water Res. 93 (2016) 20–29. https://doi.org/10.1016/j.watres.2015.11.036.
[21] K.M. Cawley, J.A. Korak, F.L. Rosario-Ortiz, Quantum Yields for the Formation of Reactive Intermediates from Dissolved Organic Matter Samples from the Suwannee River, Environ. Eng. Sci. 32 (2014) 31–37. https://doi.org/10.1089/ees.2014.0280.
[22] D.R. Lovley, F.H. Chapelle, Deep subsurface microbial processes, Rev. Geophys. 33 (1995) 365–381. https://doi.org/10.1029/95RG01305.
[23] C. Lønborg, M. Søndergaard, Microbial availability and degradation of dissolved organic carbon and nitrogen in two coastal areas, Estuar. Coast. Shelf Sci. (2009). https://doi.org/10.1016/j.ecss.2008.12.009.
[24] R.I. Jones, The influence of humic substances on lacustrine planktonic food chains, Hydrobiologia. 229 (1992) 73–91. https://doi.org/10.1007/BF00006992.
[25] B. Rosenstock, W. Zwisler, M. Simon, Bacterial Consumption of Humic and Non-Humic Low and High Molecular Weight DOM and the Effect of Solar Irradiation on the Turnover of Labile DOM in the Southern Ocean, Microb. Ecol. 50 (2005) 90–101. https://doi.org/10.1007/s00248-004-0116-5.
[26] T.A. Jackson, R.E. Hecky, Depression of Primary Productivity by Humic Matter in Lake and Reservoir Waters of the Boreal Forest Zone, Can. J. Fish. Aquat. Sci. (2011). https://doi.org/10.1139/f80-277.
[27] M.A. Anderson, F.M.M. Morel, The influence of aqueous iron chemistry on the uptake of iron by the coastal diatom Thalassiosira weissflogii1, Limnol. Oceanogr. 27 (1982) 789–813. https://doi.org/10.4319/lo.1982.27.5.0789.
[28] R.E. Sipler, D.A. Bronk, Chapter 4 - Dynamics of Dissolved Organic Nitrogen, in: D.A. Hansell, C.A. Carlson (Eds.), Biogeochem. Mar. Dissolved Org. Matter Second Ed., Second Edition, Academic Press, Boston, 2015: pp. 127–232. https://doi.org/10.1016/B978-0-12-405940-5.00004-2.
[29] Y. Zhang, L. Zhu, X. Zeng, Y. Lin, The biogeochemical cycling of phosphorus in the upper ocean of the East China Sea, Estuar. Coast. Shelf Sci. 60 (2004) 369–379. https://doi.org/10.1016/j.ecss.2004.02.001.
[30] C. Kim, Y. Nishimura, T. Nagata, Role of dissolved organic matter in hypolimnetic mineralization of carbon and nitrogen in a large, monomictic lake, Limnol. Oceanogr. 51 (2006) 70–78. https://doi.org/10.4319/lo.2006.51.1.0070.
[31] M.F. Lehmann, S.M. Bernasconi, J.A. McKenzie, A. Barbieri, M. Simona, M. Veronesi, Seasonal variation of the δC and δN of particulate and dissolved carbon and nitrogen in Lake Lugano: Constraints on biogeochemical cycling in a eutrophic lake, Limnol. Oceanogr. 49 (2004) 415–429. https://doi.org/10.4319/lo.2004.49.2.0415.
[32] Y. Zhang, M.A. van Dijk, M. Liu, G. Zhu, B. Qin, The contribution of phytoplankton degradation to chromophoric dissolved organic matter (CDOM) in eutrophic shallow lakes: field and experimental evidence, Water Res. 43 (2009) 4685–4697. https://doi.org/10.1016/j.watres.2009.07.024.
[33] L. Zhang, W. Fang, X. Li, W. Lu, J. Li, Strong linkages between dissolved organic matter and the aquatic bacterial community in an urban river, Water Res. 184 (2020). https://doi.org/10.1016/j.watres.2020.116089.
[34] P. Fu, K.M.G. Mostofa, F. Wu, C.-Q. Liu, W. Li, H. Liao, L. Wang, J. Wang, Y. Mei, Excitation-emission matrix characterization of dissolved organic matter sources in two eutrophic lakes (Southwestern China Plateau), Geochem. J. 44 (2010) 99–112. https://doi.org/10.2343/geochemj.1.0047.

[35] S.J. Guildford, R.E. Hecky, Total nitrogen, total phosphorus, and nutrient limitation in lakes and oceans: Is there a common relationship?, Limnol. Oceanogr. 45 (2000) 1213–1223. https://doi.org/10.4319/lo.2000.45.6.1213.
[36] Y. Satoh, T. Katano, T. Satoh, O. Mitamura, K. Anbutsu, S. Nakano, H. Ueno, M. Kihira, V. Drucker, Y. Tanaka, T. Mimura, Y. Watanabe, M. Sugiyama, Nutrient limitation of the primary production of phytoplankton in Lake Baikal, Limnology. 7 (2006) 225–229. https://doi.org/10.1007/s10201-006-0187-8.
[37] F. Wu, D. Evans, P. Dillon, S. Schiff, Molecular size distribution characteristics of the metal–DOM complexes in stream waters by high-performance size-exclusion chromatography (HPSEC) and high-resolution inductively coupled plasma mass spectrometry (ICP-MS), J. Anal. At. Spectrom. 19 (2004) 979–983. https://doi.org/10.1039/B402819H.
[38] F.C. Wu, R.B. Mills, R.D. Evans, P.J. Dillon, Kinetics of Metal−Fulvic Acid Complexation Using a Stopped-Flow Technique and Three-Dimensional Excitation Emission Fluorescence Spectrophotometer, Anal. Chem. 76 (2004) 110–113. https://doi.org/10.1021/ac030005p.
[39] P. Boguta, Z. Sokołowska, Zinc Binding to Fulvic acids: Assessing the Impact of pH, Metal Concentrations and Chemical Properties of Fulvic Acids on the Mechanism and Stability of Formed Soluble Complexes, Molecules. 25 (2020). https://doi.org/10.3390/molecules25061297.
[40] F. Song, F. Wu, W. Feng, Z. Tang, J.P. Giesy, F. Guo, D. Shi, X. Liu, N. Qin, B. Xing, Y. Bai, Fluorescence regional integration and differential fluorescence spectroscopy for analysis of structural characteristics and proton binding properties of fulvic acid sub-fractions, J. Environ. Sci. 74 (2018) 116–125. https://doi.org/10.1016/j.jes.2018.02.015.
[41] R.A. Saar, J.H. Weber, Comparison of spectrofluorometry and ion-selective electrode potentiometry for determination of complexes between fulvic acid and heavy-metal ions, Anal. Chem. 52 (1980) 2095–2100. https://doi.org/10.1021/ac50063a025.
[42] J. Wang, C. Lü, J. He, B. Zhao, Binding characteristics of Pb2+ to natural fulvic acid extracted from the sediments in Lake Wuliangsuhai, Inner Mongolia plateau, P. R. China, Environ. Earth Sci. 75 (2016) 768. https://doi.org/10.1007/s12665-016-5608-3.
[43] S. Mounier, R. Redon, Copper complexing properties of dissolved organic matter: PARAFAC treatment of fluorescence quenching, Biogeochemistry. (2011). https://www.academia.edu/18760921/Copper_complexing_properties_of_dissolved_organic_matter_PARAFAC_treatment_of_fluorescence_quenching (accessed November 10, 2020).
[44] K.C. Christoforidis, S. Un, Y. Deligiannakis, Effect of metal ions on the indigenous radicals of humic acids: high field electron paramagnetic resonance study, Environ. Sci. Technol. 44 (2010) 7011–7016. https://doi.org/10.1021/es101708f.
[45] K. Mostofa, C.-Q. Liu, X. Feng, T. Yoshioka, D. Vione, X. Pan, F. Wu, Complexation of Dissolved Organic Matter with Trace Metal Ions in Natural Waters, in: Photobiogeochemistry Org. Matter Princ. Pract. Water Environ., 2013: pp. 769–849. https://doi.org/10.1007/978-3-642-32223-5_9.
[46] N. Senesi, Molecular and quantitative aspects of the chemistry of fulvic acid and its interactions with metal ions and organic chemicals : Part II. The fluorescence spectroscopy approach, Anal. Chim. Acta. 232 (1990) 77–106. https://doi.org/10.1016/S0003-2670(00)81226-X.
[47] B.A. Poulin, J.N. Ryan, G.R. Aiken, Effects of Iron on Optical Properties of Dissolved Organic Matter, Environ. Sci. Technol. 48 (2014) 10098–10106. https://doi.org/10.1021/es502670r.
[48] T.D. Waite, F.M.M. Morel, Ligand exchange and fluorescence quenching studies of the fulvic acid-iron interaction: Effects of ph and light, Anal. Chim. Acta. 162 (1984) 263–274. https://doi.org/10.1016/S0003-2670(00)84247-6.
[49] S. Wagner, F. Schubotz, K. Kaiser, C. Hallmann, H. Waska, P.E. Rossel, R. Hansman, M. Elvert, J.J. Middelburg, A. Engel, T.M. Blattmann, T.S. Catalá, S.T. Lennartz, G.V. Gomez-Saez, S. Pantoja-Gutiérrez, R. Bao, V. Galy, Soothsaying DOM: A Current Perspective on the Future of Oceanic Dissolved Organic Carbon, Front. Mar. Sci. 7 (2020). https://doi.org/10.3389/fmars.2020.00341.
[50] J.I. Hedges, Global biogeochemical cycles: progress and problems, Mar. Chem. 39 (1992) 67–93. https://doi.org/10.1016/0304-4203(92)90096-S.

[51] M.A. Moran, W.M. Sheldon, R.G. Zepp, Carbon loss and optical property changes during long-term photochemical and biological degradation of estuarine dissolved organic matter, Limnol. Oceanogr. 45 (2000) 1254–1264. https://doi.org/10.4319/lo.2000.45.6.1254.
[52] H. Canada, Guidance on Natural Organic Matter in Drinking Water, Aem. (2020). https://www.canada.ca/en/health-canada/programs/consultation-organic-matter-drinking-water/document.html (accessed November 30, 2020).
[53] F. Worrall, T.P. Burt, Trends in DOC concentration in Great Britain, J. Hydrol. 346 (2007) 81–92. https://doi.org/10.1016/j.jhydrol.2007.08.021.
[54] B. Eikebrokk, R. Vogt, H. Liltved, NOM increase in Northern European source waters: Discussion of possible causes and impacts on coagulation/contact filtration processes, Water Sci. Technol. Water Supply. 4 (2004). https://doi.org/10.2166/ws.2004.0060.
[55] E. Lipczynska-Kochany, Effect of climate change on humic substances and associated impacts on the quality of surface water and groundwater: A review, Sci. Total Environ. 640–641 (2018) 1548–1565. https://doi.org/10.1016/j.scitotenv.2018.05.376.
[56] E. Hood, M.N. Gooseff, S.L. Johnson, Changes in the character of stream water dissolved organic carbon during flushing in three small watersheds, Oregon, J. Geophys. Res. Biogeosciences. 111 (2006). https://doi.org/10.1029/2005JG000082.
[57] L. Yang, S.-W. Chang, H.-S. Shin, J. Hur, Tracking the evolution of stream DOM source during storm events using end member mixing analysis based on DOM quality, J. Hydrol. 523 (2015) 333–341. https://doi.org/10.1016/j.jhydrol.2015.01.074.
[58] S. Chen, R. Cao, S. Yoshitake, T. Ohtsuka, Stemflow hydrology and DOM flux in relation to tree size and rainfall event characteristics, Agric. For. Meteorol. 279 (2019) 107753. https://doi.org/10.1016/j.agrformet.2019.107753.
[59] D. Palma, M. Sleiman, O. Voldoire, A. Beauger, E. Parlanti, C. Richard, Study of the dissolved organic matter (DOM) of the Auzon cut-off meander (Allier River, France) by spectral and photoreactivity approaches, Environ. Sci. Pollut. Res. Int. 27 (2020) 26385–26394. https://doi.org/10.1007/s11356-020-09005-7.
[60] C.M. Villanueva, S. Cordier, L. Font-Ribera, L.A. Salas, P. Levallois, Overview of disinfection by-products and associated health effects, Curr. Environ. Health Rep. 2 (2015) 107–115.
[61] L. Yang, D. Kim, H. Uzun, T. Karanfil, J. Hur, Assessing trihalomethanes (THMs) and N-nitrosodimethylamine (NDMA) formation potentials in drinking water treatment plants using fluorescence spectroscopy and parallel factor analysis, Chemosphere. 121 (2015) 84–91.
[62] A.D. Pifer, S.L. Cousins, J.L. Fairey, Assessing UV- and fluorescence-based metrics as disinfection byproduct precursor surrogate parameters in a water body influenced by a heavy rainfall event, J. Water Supply Res. Technol.-Aqua. 63 (2014) 200–211. https://doi.org/10.2166/aqua.2013.122.
[63] J.M. Symons, T.A. Bellar, J.K. Carswell, J. DeMarco, K.L. Kropp, G.G. Robeck, D.R. Seeger, C.J. Slocum, B.L. Smith, A.A. Stevens, National Organics Reconnaissance Survey for Halogenated Organics, J. AWWA. 67 (1975) 634–647. https://doi.org/10.1002/j.1551-8833.1975.tb02318.x.
[64] P.C. Singer, Control of Disinfection By-Products in Drinking Water, J. Environ. Eng. 120 (1994) 727–744. https://doi.org/10.1061/(ASCE)0733-9372(1994)120:4(727).
[65] Evlampidou Iro, Font-Ribera Laia, Rojas-Rueda David, Gracia-Lavedan Esther, Costet Nathalie, Pearce Neil, Vineis Paolo, Jaakkola Jouni J.K., Delloye Francis, Makris Konstantinos C., Stephanou Euripides G., Kargaki Sophia, Kozisek Frantisek, Sigsgaard Torben, Hansen Birgitte, Schullehner Jörg, Nahkur Ramon, Galey Catherine, Zwiener Christian, Vargha Marta, Righi Elena, Aggazzotti Gabriella, Kalnina Gunda, Grazuleviciene Regina, Polanska Kinga, Gubkova Dasa, Bitenc Katarina, Goslan Emma H., Kogevinas Manolis, Villanueva Cristina M., Trihalomethanes in Drinking Water and Bladder Cancer Burden in the European Union, Environ. Health Perspect. 128 (n.d.) 017001. https://doi.org/10.1289/EHP4495.
[66] G. Fantuzzi, G. Aggazzotti, E. Righi, G. Predieri, P. Giacobazzi, S. Kanitz, F. Barbone, G. Sansebastiano, C. Ricci, V. Leoni, Exposure to organic halogen compounds in drinking water of 9 Italian regions: exposure to chlorites, chlorates, thrihalomethanes, trichloroethylene and tetrachloroethylene, Ann. Ig. Med. Prev. E Comunita. 19 (2007) 345.

[67] U. Von Gunten, Ozonation of drinking water: Part II. Disinfection and by-product formation in presence of bromide, iodide or chlorine, Water Res. 37 (2003) 1469–1487.
[68] European Chemicals Agency., Guidance on the Biocidal Products Regulation. Volume V, Guidance on disinfection by-products., Publications Office, LU, 2017. https://data.europa.eu/doi/10.2823/72847 (accessed November 30, 2020).
[69] P. Jarvis, B. Jefferson, S.A. Parsons, Floc structural characteristics using conventional coagulation for a high doc, low alkalinity surface water source, Water Res. 40 (2006) 2727–2737. https://doi.org/10.1016/j.watres.2006.04.024.
[70] E.L. Sharp, S.A. Parsons, B. Jefferson, Seasonal variations in natural organic matter and its impact on coagulation in water treatment, Sci. Total Environ. 363 (2006) 183–194. https://doi.org/10.1016/j.scitotenv.2005.05.032.
[71] J. Duan, J. Gregory, Coagulation by hydrolysing metal salts, Adv. Colloid Interface Sci. 100–102 (2003) 475–502. https://doi.org/10.1016/S0001-8686(02)00067-2.
[72] B. Bolto, J. Gregory, Organic polyelectrolytes in water treatment, Water Res. 41 (2007) 2301–2324. https://doi.org/10.1016/j.watres.2007.03.012.
[73] A.W. Mohammad, Y.H. Teow, W.L. Ang, Y.T. Chung, D.L. Oatley-Radcliffe, N. Hilal, Nanofiltration membranes review: Recent advances and future prospects, Desalination. 356 (2015) 226–254. https://doi.org/10.1016/j.desal.2014.10.043.
[74] M.F.A. Goosen, S.S. Sablani, H. Al-Hinai, S. Al-Obeidani, R. Al-Belushi, D. Jackson, Fouling of Reverse Osmosis and Ultrafiltration Membranes: A Critical Review, Sep. Sci. Technol. 39 (2005) 2261–2297. https://doi.org/10.1081/SS-120039343.
[75] R. Bergamasco, L.C. Konradt-Moraes, M.F. Vieira, M.R. Fagundes-Klen, A.M.S. Vieira, Performance of a coagulation–ultrafiltration hybrid process for water supply treatment, Chem. Eng. J. 166 (2011) 483–489. https://doi.org/10.1016/j.cej.2010.10.076.
[76] M. Li, G. Wu, Y. Guan, X. Zhang, Treatment of river water by a hybrid coagulation and ceramic membrane process, Desalination. 280 (2011) 114–119. https://doi.org/10.1016/j.desal.2011.06.059.
[77] X. Shen, B. Gao, X. Huang, F. Bu, Q. Yue, R. Li, B. Jin, Effect of the dosage ratio and the viscosity of PAC/PDMDAAC on coagulation performance and membrane fouling in a hybrid coagulation-ultrafiltration process, Chemosphere. 173 (2017) 288–298. https://doi.org/10.1016/j.chemosphere.2017.01.074.
[78] S.J. Köhler, E. Lavonen, A. Keucken, P. Schmitt-Kopplin, T. Spanjer, K. Persson, Upgrading coagulation with hollow-fibre nanofiltration for improved organic matter removal during surface water treatment, Water Res. 89 (2016) 232–240. https://doi.org/10.1016/j.watres.2015.11.048.
[79] M.T. Alresheedi, B. Barbeau, O.D. Basu, Comparisons of NOM fouling and cleaning of ceramic and polymeric membranes during water treatment, Sep. Purif. Technol. 209 (2019) 452–460. https://doi.org/10.1016/j.seppur.2018.07.070.
[80] S.-J. Lee, J.-H. Kim, Differential natural organic matter fouling of ceramic versus polymeric ultrafiltration membranes, Water Res. 48 (2014) 43–51. https://doi.org/10.1016/j.watres.2013.08.038.
[81] G. Rao, Q. Zhang, H. Zhao, J. Chen, Y. Li, Novel titanium dioxide/iron (III) oxide/graphene oxide photocatalytic membrane for enhanced humic acid removal from water, Chem. Eng. J. 302 (2016) 633–640. https://doi.org/10.1016/j.cej.2016.05.095.
[82] F.E. Bortot Coelho, C. Gionco, M.C. Paganini, P. Calza, G. Magnacca, Control of Membrane Fouling in Organics Filtration Using Ce-Doped Zirconia and Visible Light, Nanomaterials. 9 (2019) 534. https://doi.org/10.3390/nano9040534.
[83] Z. Zhou, X. Liu, K. Sun, C. Lin, J. Ma, M. He, W. Ouyang, Persulfate-based advanced oxidation processes (AOPs) for organic-contaminated soil remediation: A review, Chem. Eng. J. 372 (2019) 836–851. https://doi.org/10.1016/j.cej.2019.04.213.
[84] S. Giannakis, K.-Y.A. Lin, F. Ghanbari, A review of the recent advances on the treatment of industrial wastewaters by Sulfate Radical-based Advanced Oxidation Processes (SR-AOPs), Chem. Eng. J. 406 (2021) 127083. https://doi.org/10.1016/j.cej.2020.127083.

[85] K. Zhou, Z. Wang, X. Wang, G. Jiao, Y. Li, S.-P. Sun, X.D. Chen, Degradation of emerging pharmaceutical micropollutants in municipal secondary effluents by low-pressure UVC-activated HSO5− and S2O82− AOPs, Chem. Eng. J. 393 (2020) 124712. https://doi.org/10.1016/j.cej.2020.124712.
[86] F.-X. Tian, W.-K. Ye, B. Xu, X.-J. Hu, S.-X. Ma, F. Lai, Y.-Q. Gao, H.-B. Xing, W.-H. Xia, B. Wang, Comparison of UV-induced AOPs (UV/Cl2, UV/NH2Cl, UV/ClO2 and UV/H2O2) in the degradation of iopamidol: Kinetics, energy requirements and DBPs-related toxicity in sequential disinfection processes, Chem. Eng. J. 398 (2020) 125570. https://doi.org/10.1016/j.cej.2020.125570.
[87] M. Fukushima, K. Tatsumi, S. Nagao, Degradation characteristics of humic acid during photo-Fenton processes, Environ. Sci. Technol. 35 (2001) 3683–3690.
[88] W.H. Glaze, F. Beltran, T. Tuhkanen, J.-W. Kang, Chemical Models of Advanced Oxidation Processes, Water Qual. Res. J. 27 (1992) 23–42. https://doi.org/10.2166/wqrj.1992.002.
[89] O. Legrini, E. Oliveros, A.M. Braun, Photochemical processes for water treatment, Chem. Rev. 93 (1993) 671–698. https://doi.org/10.1021/cr00018a003.
[90] W.H. GLAZE, J.-W. KANG, D.H. CHAPIN, The chemistry of water treatment processes involving ozone, hydrogen peroxide and ultraviolet radiation, Chem. Water Treat. Process. Involv. Ozone Hydrog. Peroxide Ultrav. Radiat. 9 (1987) 335–352.
[91] A. Matilainen, M. Sillanpää, Removal of natural organic matter from drinking water by advanced oxidation processes, Chemosphere. 80 (2010) 351–365. https://doi.org/10.1016/j.chemosphere.2010.04.067.
[92] K. Pirkanniemi, S. Metsärinne, M. Sillanpää, Degradation of EDTA and novel complexing agents in pulp and paper mill process and waste waters by Fenton's reagent, J. Hazard. Mater. 147 (2007) 556–561.
[93] C. Comninellis, A. Kapalka, S. Malato, S.A. Parsons, I. Poulios, D. Mantzavinos, Advanced oxidation processes for water treatment: advances and trends for R&D, J. Chem. Technol. Biotechnol. 83 (2008) 769–776. https://doi.org/10.1002/jctb.1873.
[94] S. Parsons, Advanced oxidation processes for water and wastewater treatment, IWA publishing, 2004.
[95] G. Kleiser, F.H. Frimmel, Removal of precursors for disinfection by-products (DBPs)—differences between ozone-and OH-radical-induced oxidation, Sci. Total Environ. 256 (2000) 1–9.
[96] S. Chen, M.Z. Hoffman, Rate Constants for the Reaction of the Carbonate Radical with Compounds of Biochemical Interest in Neutral Aqueous Solution, Radiat. Res. 56 (1973) 40–47. https://doi.org/10.2307/3573789.
[97] P. Westerhoff, S.P. Mezyk, W.J. Cooper, D. Minakata, Electron Pulse Radiolysis Determination of Hydroxyl Radical Rate Constants with Suwannee River Fulvic Acid and Other Dissolved Organic Matter Isolates, Environ. Sci. Technol. 41 (2007) 4640–4646. https://doi.org/10.1021/es062529n.
[98] R. Albrektienė, M. Rimeika, E. Zalieckienė, V. Šaulys, A. Zagorskis, Determination of Organic Matter by UV Absorption in the Ground Water, J. Environ. Eng. Landsc. Manag. - J Env. ENG LANDSC MANAG. 20 (2012) 163–167. https://doi.org/10.3846/16486897.2012.674039.
[99] PINGQING FU, F. WU, C.-Q. LIU, Z. WEI, Y. BAI, H. LIAO, Spectroscopic characterization and molecular weight distribution of dissolved organic matter in sediment porewaters from Lake Erhai, Southwest China, Spectrosc. Charact. Mol. Weight Distrib. Dissolved Org. Matter Sediment Porewaters Lake Erhai Southwest China. 81 (2006) 179–189.
[100] L. Yang, W. Chen, W.-E. Zhuang, Q. Cheng, W. Li, H. Wang, W. Guo, C.-T.A. Chen, M. Liu, Characterization and bioavailability of rainwater dissolved organic matter at the southeast coast of China using absorption spectroscopy and fluorescence EEM-PARAFAC, Estuar. Coast. Shelf Sci. 217 (2019) 45–55. https://doi.org/10.1016/j.ecss.2018.11.002.
[101] E.H. Goslan, F. Gurses, J. Banks, S.A. Parsons, An investigation into reservoir NOM reduction by UV photolysis and advanced oxidation processes, Chemosphere. 65 (2006) 1113–1119.
[102] Sanly, M. Lim, K. Chiang, R. Amal, R. Fabris, C. Chow, M. Drikas, A Study on the Removal of Humic Acid Using Advanced Oxidation Processes, Sep. Sci. Technol. 42 (2007) 1391–1404. https://doi.org/10.1080/01496390701289799.

[103] A. Moncayo-Lasso, C. Pulgarin, N. Benítez, Degradation of DBPs' precursors in river water before and after slow sand filtration by photo-Fenton process at pH 5 in a solar CPC reactor, Water Res. 42 (2008) 4125–4132. https://doi.org/10.1016/j.watres.2008.07.014.
[104] L.A.T. Espinoza, F.H. Frimmel, A simple simulation of the degradation of natural organic matter in homogeneous and heterogeneous advanced oxidation processes, Water Res. 43 (2009) 3902–3909.
[105] R.P. Schwarzenbach, P.M. Gschwend, D.M. Imboden, Direct Photolysis, in: Environ. Org. Chem., John Wiley & Sons, Ltd, 2002: pp. 611–654. https://doi.org/10.1002/0471649643.ch15.
[106] W. Song, V. Ravindran, M. Pirbazari, Process optimization using a kinetic model for the ultraviolet radiation-hydrogen peroxide decomposition of natural and synthetic organic compounds in groundwater, Chem. Eng. Sci. 63 (2008) 3249–3270.
[107] J. Fu, M. Ji, Y. Zhao, L. Wang, Kinetics of aqueous photocatalytic oxidation of fulvic acids in a photocatalysis–ultrafiltration reactor (PUR), Sep. Purif. Technol. 50 (2006) 107–113. https://doi.org/10.1016/j.seppur.2005.11.017.
[108] S. Liu, M. Lim, R. Fabris, C. Chow, M. Drikas, R. Amal, TiO2 Photocatalysis of Natural Organic Matter in Surface Water: Impact on Trihalomethane and Haloacetic Acid Formation Potential, Environ. Sci. Technol. 42 (2008) 6218–6223. https://doi.org/10.1021/es800887s.
[109] S. Dobrović, H. Juretić, N. Ružinski, Photodegradation of Natural Organic Matter in Water with UV Irradiation at 185 and 254 nm: Importance of Hydrodynamic Conditions on the Decomposition Rate, Sep. Sci. Technol. 42 (2007) 1421–1432. https://doi.org/10.1080/01496390701289849.
[110] W. Buchanan, F. Roddick, N. Porter, Formation of hazardous by-products resulting from the irradiation of natural organic matter: Comparison between UV and VUV irradiation, Chemosphere. 63 (2006) 1130–1141. https://doi.org/10.1016/j.chemosphere.2005.09.040.
[111] T. Bond, E.H. Goslan, B. Jefferson, F. Roddick, L. Fan, S.A. Parsons, Chemical and biological oxidation of NOM surrogates and effect on HAA formation, Water Res. 43 (2009) 2615–2622.
[112] T.M. Hashem, M. Zirlewagen, A.M. Braun, Simultaneous photochemical generation of ozone in the gas phase and photolysis of aqueous reaction systems using one VUV light source, Oxid. Technol. Water Wastewater Treat. 35 (1997) 41–48. https://doi.org/10.1016/S0273-1223(97)00007-3.
[113] S.R. Sarathy, M. Mohseni, The Impact of UV/H2O2 Advanced Oxidation on Molecular Size Distribution of Chromophoric Natural Organic Matter, Environ. Sci. Technol. 41 (2007) 8315–8320. https://doi.org/10.1021/es071602m.
[114] J.C. Kruithof, P.C. Kamp, B.J. Martijn, UV/H2O2 Treatment: A Practical Solution for Organic Contaminant Control and Primary Disinfection, Ozone Sci. Eng. 29 (2007) 273–280. https://doi.org/10.1080/01919510701459311.
[115] G.-S. Wang, C.-H. Liao, H.-W. Chen, H.-C. Yang, Characteristics of Natural Organic Matter Degradation in Water by UV/H2O2 Treatment, Environ. Technol. 27 (2006) 277–287. https://doi.org/10.1080/09593332708618638.
[116] B. Langlais, D.A. Reckhow, D.R. Brink, Ozone in Water Treatment: Application and Engineering, Routledge, 2019.
[117] R. Criegee, Mechanismus der Ozonolyse, Angew. Chem. 87 (1975) 765–771. https://doi.org/10.1002/ange.19750872104.
[118] J. Hoigné, Chemistry of aqueous ozone and transformation of pollutants by ozonation and advanced oxidation processes, in: Qual. Treat. Drink. Water II, Springer, 1998: pp. 83–141.
[119] B. Langlais, D.A. Reckhow, D.R. Brink, Ozone in Water Treatment: Application and Engineering, Routledge, 2019.
[120] W.D. McGrath, R.G.W. Norrish, Studies of the reactions of excited oxygen atoms and molecules produced in the flash photolysis of ozone, Proc. R. Soc. Lond. Ser. Math. Phys. Sci. 254 (1960) 317–326. https://doi.org/10.1098/rspa.1960.0022.
[121] K.E. Black, P.R. Bérubé, Rate and extent NOM removal during oxidation and biofiltration, Water Res. 52 (2014) 40–50. https://doi.org/10.1016/j.watres.2013.12.017.

[122] P. Westerhoff, J. Debroux, G. Aiken, G. Amy, Ozone-induced changes in natural organic matter (nom) structure, Ozone Sci. Eng. 21 (1999) 551–570. https://doi.org/10.1080/01919512.1999.10382893.
[123] A. Chin, P.R. Bérubé, Removal of disinfection by-product precursors with ozone-UV advanced oxidation process, Water Res. 39 (2005) 2136–2144. https://doi.org/10.1016/j.watres.2005.03.021.
[124] P. Zhang, L. Jian, Ozone-enhanced photocatalytic degradation of natural organic matter in water, Water Supply. 6 (2006) 53–61. https://doi.org/10.2166/ws.2006.730.
[125] M. Bekbölet, G. Özkösemen, A preliminary investigation on the photocatalytic degradation of a model humic acid, Hazard Assess. Control Environ. Contam. Water. 33 (1996) 189–194. https://doi.org/10.1016/0273-1223(96)00302-2.
[126] M.R. Hoffmann, S.T. Martin, W. Choi, D.W. Bahnemann, Environmental applications of semiconductor photocatalysis, Chem. Rev. 95 (1995) 69–96.
[127] K. Pirkanniemi, M. Sillanpää, Heterogeneous water phase catalysis as an environmental application: a review, Chemosphere. 48 (2002) 1047–1060. https://doi.org/10.1016/S0045-6535(02)00168-6.
[128] X. Huang, M. Leal, Q. Li, Degradation of natural organic matter by TiO2 photocatalytic oxidation and its effect on fouling of low-pressure membranes, Water Res. 42 (2008) 1142–1150. https://doi.org/10.1016/j.watres.2007.08.030.
[129] J. Wiszniowski, D. Robert, J. Surmacz-Gorska, K. Miksch, J.-V. Weber, Photocatalytic decomposition of humic acids on TiO2: Part I: Discussion of adsorption and mechanism, J. Photochem. Photobiol. Chem. 152 (2002) 267–273. https://doi.org/10.1016/S1010-6030(02)00022-9.
[130] R. Martinez-Haya, M.A. Miranda, M.L. Marin, Metal-Free Photocatalytic Reductive Dehalogenation Using Visible-Light: A Time-Resolved Mechanistic Study, Eur. J. Org. Chem. 2017 (2017) 2164–2169. https://doi.org/10.1002/ejoc.201601494.
[131] G.R. Stratton, F. Dai, C.L. Bellona, T.M. Holsen, E.R.V. Dickenson, S. Mededovic Thagard, Plasma-Based Water Treatment: Efficient Transformation of Perfluoroalkyl Substances in Prepared Solutions and Contaminated Groundwater, Environ. Sci. Technol. 51 (2017) 1643–1648. https://doi.org/10.1021/acs.est.6b04215.
[132] M. Saleem, O. Biondo, G. Sretenović, G. Tomei, M. Magarotto, D. Pavarin, E. Marotta, C. Paradisi, Comparative performance assessment of plasma reactors for the treatment of PFOA; reactor design, kinetics, mineralization and energy yield, Chem. Eng. J. 382 (2020) 123031. https://doi.org/10.1016/j.cej.2019.123031.
[133] M. Trojanowicz, A. Bojanowska-Czajka, I. Bartosiewicz, K. Kulisa, Advanced Oxidation/Reduction Processes treatment for aqueous perfluorooctanoate (PFOA) and perfluorooctanesulfonate (PFOS) – A review of recent advances, Chem. Eng. J. 336 (2018) 170–199. https://doi.org/10.1016/j.cej.2017.10.153.
[134] I. Panorel, I. Kornev, H. Hatakka, S. Preis, Pulsed corona discharge for degradation of aqueous humic substances, Water Supply. 11 (2011) 238–245. https://doi.org/10.2166/ws.2011.045.
[135] H. De Haan, T. De Boer, Applicability of light absorbance and fluorescence as measures of concentration and molecular size of dissolved organic carbon in humic Lake Tjeukemeer, Water Res. 21 (1987) 731–734. https://doi.org/10.1016/0043-1354(87)90086-8.
[136] J.R. Helms, A. Stubbins, J.D. Ritchie, E.C. Minor, D.J. Kieber, K. Mopper, Absorption spectral slopes and slope ratios as indicators of molecular weight, source, and photobleaching of chromophoric dissolved organic matter, Limnol. Oceanogr. 53 (2008) 955–969. https://doi.org/10.4319/lo.2008.53.3.0955.
[137] M.S. Twardowski, E. Boss, J.M. Sullivan, P.L. Donaghay, Modeling the spectral shape of absorption by chromophoric dissolved organic matter, Mar. Chem. 89 (2004) 69–88. https://doi.org/10.1016/j.marchem.2004.02.008.
[138] Y. Chen, N. Senesi, M. Schnitzer, Information Provided on Humic Substances by E4/E6 Ratios, Soil Sci. Soc. Am. J. 41 (1977) 352–358. https://doi.org/10.2136/sssaj1977.03615995004100020037x.

[139] R.S. Summers, P.K. Cornel, P.V. Roberts, Molecular size distribution and spectroscopic characterization of humic substances, Sci. Total Environ. 62 (1987) 27–37. https://doi.org/10.1016/0048-9697(87)90478-5.
[140] J.L. Weishaar, G.R. Aiken, B.A. Bergamaschi, M.S. Fram, R. Fujii, K. Mopper, Evaluation of Specific Ultraviolet Absorbance as an Indicator of the Chemical Composition and Reactivity of Dissolved Organic Carbon, Environ. Sci. Technol. 37 (2003) 4702–4708. https://doi.org/10.1021/es030360x.
[141] S.J. Traina, J. Novak, N.E. Smeck, An Ultraviolet Absorbance Method of Estimating the Percent Aromatic Carbon Content of Humic Acids, J. Environ. Qual. 19 (1990) 151–153. https://doi.org/10.2134/jeq1990.00472425001900010023x.
[142] E. Parlanti, K. Wörz, L. Geoffroy, M. Lamotte, Dissolved organic matter fluorescence spectroscopy as a tool to estimate biological activity in a coastal zone submitted to anthropogenic inputs, Org. Geochem. 31 (2000) 1765–1781. https://doi.org/10.1016/S0146-6380(00)00124-8.
[143] P.G. Coble, Characterization of marine and terrestrial DOM in seawater using excitation-emission matrix spectroscopy, Mar. Chem. 51 (1996) 325–346. https://doi.org/10.1016/0304-4203(95)00062-3.
[144] O.S. WOLFBEIS, The fluorescence of organic natural products, Mol. Lumin. Spectrosc. Methods Appl. (1985) 167–370.
[145] P.E. García, R.D. García, C. Soto Cárdenas, M. Gerea, M. Reissig, G.L. Pérez, L.G. De Stefano, D. Gianello, C. Queimaliños, M.C. Diéguez, Fluorescence components of natural dissolved organic matter (DOM) from aquatic systems of an Andean Patagonian catchment: Applying different data restriction criteria for PARAFAC modelling, Spectrochim. Acta. A. Mol. Biomol. Spectrosc. 229 (2020) 117957. https://doi.org/10.1016/j.saa.2019.117957.
[146] K.R. Murphy, C.A. Stedmon, D. Graeber, R. Bro, Fluorescence spectroscopy and multi-way techniques. PARAFAC, Anal. Methods. 5 (2013) 6557–6566. https://doi.org/10.1039/C3AY41160E.
[147] D.M. McKnight, E.W. Boyer, P.K. Westerhoff, P.T. Doran, T. Kulbe, D.T. Andersen, Spectrofluorometric characterization of dissolved organic matter for indication of precursor organic material and aromaticity, Limnol. Oceanogr. 46 (2001) 38–48. https://doi.org/10.4319/lo.2001.46.1.0038.
[148] A. Zsolnay, E. Baigar, M. Jimenez, B. Steinweg, F. Saccomandi, Differentiating with fluorescence spectroscopy the sources of dissolved organic matter in soils subjected to drying, Chemosphere. 38 (1999) 45–50. https://doi.org/10.1016/S0045-6535(98)00166-0.
[149] A. Huguet, L. Vacher, S. Relexans, S. Saubusse, J.M. Froidefond, E. Parlanti, Properties of fluorescent dissolved organic matter in the Gironde Estuary, Org. Geochem. 40 (2009) 706–719. https://doi.org/10.1016/j.orggeochem.2009.03.002.
[150] R.L. Cook, Coupling NMR to NOM, Anal. Bioanal. Chem. 378 (2004) 1484–1503. https://doi.org/10.1007/s00216-003-2422-z.
[151] C.M. Preston, Applications of NMR to soil organic matter analysis: history and prospects, Soil Sci. 161 (1996) 144–166.
[152] A. Sardana, B. Cottrell, D. Soulsby, T.N. Aziz, Dissolved organic matter processing and photoreactivity in a wastewater treatment constructed wetland, Sci. Total Environ. 648 (2019) 923–934. https://doi.org/10.1016/j.scitotenv.2018.08.138.
[153] G.C. Woods, M.J. Simpson, B.P. Kelleher, M. McCaul, W.L. Kingery, A.J. Simpson, Online high-performance size exclusion chromatography− nuclear magnetic resonance for the characterization of dissolved organic matter, Environ. Sci. Technol. 44 (2010) 624–630.
[154] T. Riedel, M. Zark, A.V. Vähätalo, J. Niggemann, R.G. Spencer, P.J. Hernes, T. Dittmar, Molecular signatures of biogeochemical transformations in dissolved organic matter from ten world rivers, Front. Earth Sci. 4 (2016) 85.
[155] J.A. Hawkes, N. Radoman, J. Bergquist, M.B. Wallin, L.J. Tranvik, S. Löfgren, Regional diversity of complex dissolved organic matter across forested hemiboreal headwater streams, Sci. Rep. 8 (2018) 16060. https://doi.org/10.1038/s41598-018-34272-3.

[156] V. Yuthawong, I. Kasuga, F. Kurisu, H. Furumai, Molecular-Level Changes in Dissolved Organic Matter Compositions in Lake Inba Water during $KMnO_4$ Oxidation: Assessment by Orbitrap Mass Spectrometry, J. Water Environ. Technol. 17 (2019) 27–39. https://doi.org/10.2965/jwet.18-043.
[157] E.E. Lavonen, M. Gonsior, L.J. Tranvik, P. Schmitt-Kopplin, S.J. Köhler, Selective Chlorination of Natural Organic Matter: Identification of Previously Unknown Disinfection Byproducts, Environ. Sci. Technol. 47 (2013) 2264–2271. https://doi.org/10.1021/es304669p.
[158] S. Kim, R.W. Kramer, P.G. Hatcher, Graphical method for analysis of ultrahigh-resolution broadband mass spectra of natural organic matter, the van Krevelen diagram, Anal. Chem. 75 (2003) 5336–5344.
[159] O.E. Trubetskaya, C. Richard, S.V. Patsaeva, O.A. Trubetskoj, Evaluation of aliphatic/aromatic compounds and fluorophores in dissolved organic matter of contrasting natural waters by SEC-HPLC with multi-wavelength absorbance and fluorescence detections, Spectrochim. Acta. A. Mol. Biomol. Spectrosc. 238 (2020) 118450. https://doi.org/10.1016/j.saa.2020.118450.
[160] W.A. Arnold, K. McNeill, Chapter 3.2 Transformation of pharmaceuticals in the environment: Photolysis and other abiotic processes, in: M. Petrović, D. Barceló (Eds.), Compr. Anal. Chem., Elsevier, 2007: pp. 361–385. https://doi.org/10.1016/S0166-526X(07)50011-5.
[161] S.A. Green, N.V. Blough, Optical absorption and fluorescence properties of chromophoric dissolved organic matter in natural waters, Limnol. Oceanogr. 39 (1994) 1903–1916. https://doi.org/10.4319/lo.1994.39.8.1903.
[162] C. Richard, S. Canonica, Aquatic Phototransformation of Organic Contaminants Induced by Coloured Dissolved Natural Organic Matter, Environ. Photochem. Part II. 2 (2005) 299.
[163] S. Canonica, U. Jans, K. Stemmler, J. Hoigne, Transformation kinetics of phenols in water: photosensitization by dissolved natural organic material and aromatic ketones, Environ. Sci. Technol. 29 (1995) 1822–1831. https://doi.org/10.1021/es00007a020.
[164] K. McNeill, S. Canonica, Triplet state dissolved organic matter in aquatic photochemistry: reaction mechanisms, substrate scope, and photophysical properties, Environ. Sci. Process. Impacts. 18 (2016) 1381–1399. https://doi.org/10.1039/C6EM00408C.
[165] W. Stumm, Aquatic chemical kinetics: reaction rates of processes in natural waters, Wiley, New York, 1990.
[166] B. Sulzberger, S. Canonica, T. Egli, W. Giger, J. Klausen, U. von Gunten, Oxidative transformations of contaminants in natural and in technical systems, Chimia. (1997) 900–907.
[167] C.J. Miller, A.L. Rose, T.D. Waite, Hydroxyl radical production by H2O2-mediated oxidation of Fe(II) complexed by suwannee river fulvic acid under circumneutral freshwater conditions, Environ. Sci. Technol. 47 (2013) 829–835. https://doi.org/10.1021/es303876h.
[168] W.-U. Palm, Oxygen dependence in the photoreaction of the pesticide metamitron, J. Photochem. Photobiol. Chem. 347 (2017) 138–145. https://doi.org/10.1016/j.jphotochem.2017.07.033.
[169] S. Kouras-Hadef, P. de Sainte-Claire, A. ter Halle, A. Amine-Khodja, C. Richard, The Role of Triplet State Keto–Enol Tautomerism in the Photodeamination of Metamitron, J. Phys. Chem. A. 115 (2011) 14397–14406. https://doi.org/10.1021/jp208907f.
[170] G. Mckay, W. Huang, C. Romera-Castillo, J.E. Crouch, F.L. Rosario-Ortiz, R. Jaffé, Predicting Reactive Intermediate Quantum Yields from Dissolved Organic Matter Photolysis Using Optical Properties and Antioxidant Capacity, Environ. Sci. Technol. 51 (2017) 5404–5413. https://doi.org/10.1021/acs.est.6b06372.
[171] W.L. Miller, D.R. Kester, Hydrogen peroxide measurement in seawater by (p-hydroxyphenyl)acetic acid dimerization, Anal. Chem. 60 (1988) 2711–2715. https://doi.org/10.1021/ac00175a014.
[172] E.S. Boyle, N. Guerriero, A. Thiallet, R.D. Vecchio, N.V. Blough, Optical Properties of Humic Substances and CDOM: Relation to Structure, Environ. Sci. Technol. 43 (2009) 2262–2268. https://doi.org/10.1021/es803264g.
[173] R.M. Cory, D.M. McKnight, Fluorescence Spectroscopy Reveals Ubiquitous Presence of Oxidized and Reduced Quinones in Dissolved Organic Matter, Environ. Sci. Technol. 39 (2005) 8142–8149. https://doi.org/10.1021/es0506962.

[174] D. Vione, V. Maurino, C. Minero, M. Lucchiari, E. Pelizzetti, Nitration and hydroxylation of benzene in the presence of nitrite/nitrous acid in aqueous solution, Chemosphere. 56 (2004) 1049–1059. https://doi.org/10.1016/j.chemosphere.2004.05.027.